DISCLAIMER

This report was prepared as an account of work sponsored by an agency of the United States Government. Neither the United States Government nor any agency thereof, nor any of their employees, makes any warranty, express or implied, or assumes any legal liability or responsibility for the accuracy, completeness, or usefulness of any information, apparatus, product, or process disclosed, or represents that its use would not infringe privately owned rights. Reference herein to any specific commercial product, process, or service by trade name, trademark, manufacturer, or otherwise does not necessarily constitute or imply its endorsement, recommendation, or favoring by the United States Government or any agency thereof. The views and opinions of authors expressed herein do not necessarily state or reflect those of the United States Government or any agency thereof. Reference herein to any social initiative (including but not limited to Diversity, Equity, and Inclusion (DEI); Community Benefits Plans (CBP); Justice 40; etc.) is made by the Author independent of any current requirement by the United States Government and does not constitute or imply endorsement, recommendation, or support by the United States Government or any agency thereof.

Final Technical Report
Project Period: 9/01/2021 – 12/31/2024
Date of Submission of Report: April 30, 2025

Federal Agency/ Organization Element:	DOE/EERE/ Advanced Manufacturing Office (AMO)
FOA Name and Number:	FY20 Advanced Manufacturing Office Multi-Topic DE-FOA-0002252
Award Number:	DE-EE0009402
Award Type:	Cooperative Agreement
Project Title:	Robot-based Additive Manufacturing of Lego-type Modular Molds for Wind Blades
Budget Period	12/01/2023 – 08/31/2024
Project Period:	9/01/2021 – 8/31/2024 (no cost time extension)
Recipient Organization:	University of Michigan (UM)
Recipient Type:	Education
UEI:	GNJ7BBP73WE9
Principal Investigator	Miki Banu, mbanu@umich.edu
Business Contact:	Kellie Buss, klbuss@umich.edu
Partners:	TPI Composites Raytheon Technologies Penn State University
DOE Technology Manager:	Blake Marshall, blake.marshall@ee.doe.gov
DOE Project Officer:	Gibson Asuquo, gibson.asuquo@ee.doe.gov
DOE Project Monitor:	John Hodges, john.hodges@ee.doe.gov
DOE Grants Specialist:	Mary Murray, Mary.Murray@ee.doe.gov
Submitting Official:	Kellie Buss, Sr. Project Representative, klbuss@umich.edu (734) 936-1364

The Submitting Official certifies that the information provided in the Research Performance Progress Report is accurate and complete as of the date shown

Acknowledgment:

“This material is based upon work supported by the U.S. Department of Energy’s Office of Energy Efficiency and Renewable Energy (EERE) under the Advanced Materials and Manufacturing Technologies Office (AMMTO), Award Number DE-EE0009402.”

Executive Summary

The objective of this project is to reduce the cost and lead time of horizontal wind turbine blade mold tooling and blade transportation, while maintaining the highest standards of blade quality. The solution involves a smart-design family of modular molds that are easily transportable to fabrication sites near the place of service. Key innovations include the use of additive manufacturing (AM) to integrate conformal thermal management channels, offering enhanced control over the thermal profiles tailored to specific blade materials. This approach enables in-situ quality assurance during mold fabrication, significantly improves mold life, and allows for reuse across multiple production cycles. Ultimately, the solution aims to optimize both tooling and transportation costs, contributing to the scalability of wind turbine blade production. A significant barrier to scaling up the production of large wind turbine blades lies in the high costs associated with tooling and the transportation of blades. Traditional molds are expensive, bulky, and difficult to transport, adding considerable lead time and cost to the overall manufacturing process. Additionally, transporting blades to distant locations for final assembly further exacerbates these challenges. The project aims to address these inefficiencies by demonstrating a modularized, additive-manufactured mold that meets all necessary blade specification requirements, specifically for blade lengths between 120m and 150m.

The key performance targets for this project are as follows:

1. **Cost Savings**: Achieve a 30% reduction in the cost of fabricating a 120m blade mold when compared to traditional polymer composite additive-manufactured molds.
2. **Reduced Lead Time**: Cut mold fabrication time and time to market by 50%, accelerating the overall manufacturing process and enhancing supply chain efficiency.
3. **Transportation Cost Reduction**: Lower mold and blade transportation costs by 30% through the development of modular molds that are easier and more cost-effective to transport.
4. **Lightweighting of Molds**: Achieve a 25% reduction in the weight of the mold compared to existing traditional molds, which will help to reduce material costs and improve overall mold handling.
5. **Extended Mold Life and Reusability**: Improve mold durability, enabling its reuse across various blade configurations, which will allow for the amortization of mold costs over a larger production volume, further reducing per-unit costs.

The integration of additive manufacturing (AM) for mold fabrication is the central innovation of this project. AM allows for the creation of complex mold geometries, including conformal cooling channels, which provide the ability to fine-tune thermal management throughout the mold. This flexibility enhances blade quality, reduces defects, and speeds up curing times, ultimately leading to better overall performance. Additionally, the modular nature of the molds makes them easier to transport and reconfigure, driving further cost savings and reducing the carbon footprint of transportation logistics.

Conclusion

This project represents a significant step forward in reducing the costs and time associated with wind turbine blade production. By addressing the challenges of tooling, transportation, and mold durability through innovative solutions such as additive manufacturing and modular mold designs, the project has the potential to revolutionize large-scale wind turbine production, making it more cost-effective and sustainable. The successful implementation of these solutions will help scale production capacity, ultimately contributing to the broader adoption of renewable energy sources.

Table of content

1. Introduction: Modular Blade Family with Modular Sections

A family consisting of a 120m, 140m, and 150m blade was designed by scaling a public-domain 100m blade model from Sandia National Laboratory by applying uniform scaling for the blade span and the chord length and twist angles at each station using Qblade software. These individually designed blades, shown in Figure 1.1, are used as the baseline for the evaluation of the aerodynamic performance for a common modular section. Candidates for common sections were identified as <10% difference in the number of stations and the maximum chord length. A 20m mid-section was identified as an acceptable common modular section within all three blades.

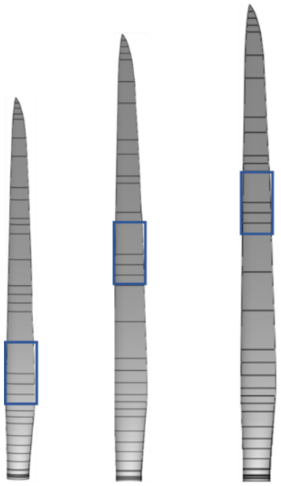

Figure 1.1 A blade family design with common section outlined in blue.

The aerodynamic power coefficient of each blade with the common modular section was predicted using QBlade. The maximum power coefficient Cp_{max} for the individual blades and its ratio to the baseline is summarized in Table 1.1 for all blade lengths using the common modular section. These designs meet the design criteria of 95-98% of the Cp_{max} baseline. This common modular section was selected for the modular mold design.

It was determined in consultation with TPI that defining the exact specification for the thermoset resin and glass fiber for the turbine blade family was unnecessary for the purpose of mold design as only the blade surface geometry defines the aerodynamic performances. Nor would the design of the internal structural reinforcements be necessary for mold design. Therefore, they were left unspecified.

Table 1.1 Comparison of aerodynamic power coefficient Cp_{max}

Blade Model	$C_{p_{max}}$	***Relative*** $C_{p_{max}}$
SNL120	0.4417	1.0
CM120	0.4178	0.95
SNL140	0.4204	1.0
CM-140	0.4100	0.98
SNL150	0.4090	1.0
CM150	0.3899	0.95

2. Topological Optimization, Design, and Analysis of the Modular Mold Structure

The objective of the topological optimization of the modular mold structure was to determine the best shape for the conformal thermal management channels that can control the thermal profile on the mold's airfoil profile surface with minimum thermal distortion of that surface. The fluidic medium selected to provide heat transfer within the channels was air. Over the course of this program, the approach to the design of the conformal channels evolved as experience was gained in their performance and through the fabrication of the molds. The initial approach was to determine channels that provided uniform temperatures with acceptable distortion at the airfoil profile by optimally deducting material from a solid block. The later refined approach used the same criteria but started with a shell of the airfoil profile and optimized the structure for thermal uniformity and minimal distortion.

2.1. Preliminary small-scale mold structure optimization

A preliminary modular mold was designed using an uncoupled thermal-fluidic and structural topology optimization (TO) of the conformal fluid channels using COMSOL and Matlab. At each optimization iteration, the software runs a coupled thermal-fluidic simulation to calculate the temperature distribution of the structure under a thermal and fluidic boundary condition and a structural simulation to calculate the compliance of the structure under a structural boundary condition. This uncoupled thermal-fluidic and structural simulation does not explicitly calculate the surface distortion due to thermal expansion but does achieve implicit reduction of the distortion by bounding the structural compliance. In addition, a Darcy flow model was adopted for fluid flow.

The design domain for the topology optimization (TO) at full scale was approximately 20×10×5 m with three holes each for the conformal channel inlet and outlet. The major parameters for the topology optimization were:

- Mold material: 6061-RAM2 Aluminum Alloy
- Heating fluid: air with velocity = 0.1m/s, inlet temperature = 348K
- Initial temperature for the mold = 293K
- Convection on the mold surface ($h = 10 W/m^2 K$) to model heat dissipation to the blade
- Fixed supports of the bottom surface and the mold interfaces.
- A 1000N load on the mold surface to model the blade material weight
- Target temperature of the mold surface: 343K
- Target volume fraction of fluid channel = 30%
- Target pressure drop between inlet and outlet = 1.5 Pa

Preliminary verification of the TO results using a fully coupled thermal-fluidic-structural simulation are summarized in Table 2.1.1. The temperature distribution and fluid flow are illustrated in Figure 2.1.1. A CAD solid model generated from the TO result provided a print-ready STL file. This design provided a weight reduction of approximately 30% from the solid aluminum mold thanks to the conformal channel.

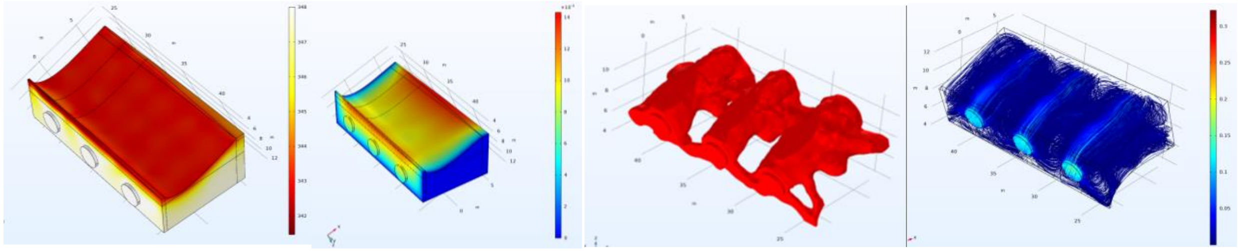
(a) (b) (c) (d)

Figure 2.1.1 Topology optimization results. (a) surface temperature (70±1°C), (b) surface displacement (max. 14 mm), (c) optimized air channel, and (d) air velocity in air channel.

Table 2.1.1 Summary of verification results from TO analysis

Design Requirements	***Target***	***Verification***	***Result***
Temperature on mold surface	≤ ±5°C at 70±5°C	343±1K (70±1°C)	≤ ±1 °C at 70°C
Displacement on mold surface	≤ 1% of chord length (10 m)	14 mm (max)	≤ 0.14 % of chord length

The topology optimized mold model was then passed to the RTRC team for further validation using computational fluid dynamics and finite element modeling. A coupled thermal/fluid (ANSYS *Mechanical/Fluent*) model was run to confirm the TO results with aluminum thermal properties of Al 6061 RAM 2 applied to the thermal model. The model geometry of the conformal channels was meshed using a refined parasolid tetrahedron mesh to simulate the inner surface and its fluid/structure interface. Model assumptions included: solid parameters do not vary with temperature; the fluid flow is stable both in inlet and outlet; hot air delivery is stable and uniform and air has temperature-dependent properties; the influence of the mold-supporting objects on the heat transfer is neglected; and the flow of fluid across the inner and outer cavities of the mold is taken into consideration. Boundary conditions of model were**:**

- 0.1 m/s inlet velocity
- 10 W/m^2 applied to blade airfoil profile
- All other walls are adiabatic, and the surfaces are non-slip.
- The inlet regulates the air temperature. The temperature changes over time until it reaches the curing curve temperature as specified by $T = 0.025 \times t + 29$ K, with an initial temperature of room temperature.
- The outlet regulates the boundary condition of pressure with the default as the hydrostatic pressure.

The *Fluent* model showed the air flowing into the mold increases its velocity when encountering the narrow zones in the mold's solid topography, Figure 2.1.2. The velocity of air near the top of the mold is minimum and the velocity decreases as to approaches the outlet side. This confirmed practical expectations. The profile temperature distribution at the top of the inner surface of the mold module (the inner surface represents the fluid/structure interface) is higher than that in the other positions inside the profile. The lowest and highest temperature observed was around 70°C near the inlet 80^{o}C near the outlet, respectively, with temperature varying about +/- 5 ^{o}C. The *Fluent* model results showed the TO structure of the mold was robust and provided better temperature distribution.

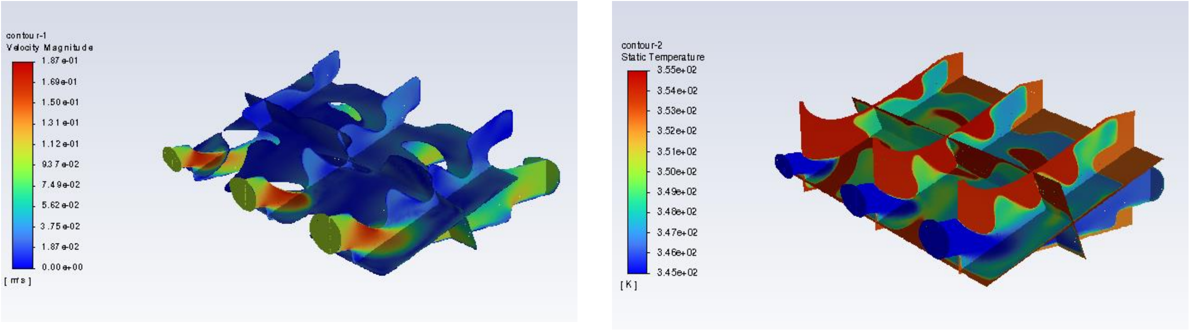

(a) modified velocity magnitude
(conformal channel cross-section)

(b) steady-state temperature distribution
(structural cross-sections)

Figure 2.1.2 Fluent Simulation Results

Steady-state thermal-mechanical analysis was carried out in the ANSYS mechanical module to predict the temperature distribution on the mold surface. The *Fluent* model steady-state temperature boundary conditions were imported into ANSYS and mapped as the fluid/structure interface on the interior surfaces of the mold. A constant heat flow of 10 W/m^{2} was applied to the mold's airfoil profile and was also subjected to the internal temperature distribution obtained from the fluent analysis and convection conditions. The results presented in Figure 2.1.3 illustrate the effect of mold meshing parameters on the uniformity of the predicted temperature distribution. It was determined a fine mesh with element length scale ½ of the coarse mesh predicts a temperature range of ±3.66°C, substantially the same as the coarse mesh temperature range of ±3.89°C. The predicted temperature variation across the mold surfaces in both analyses are within specification, with the predicted temperature distribution more uniform for the fine mesh case.

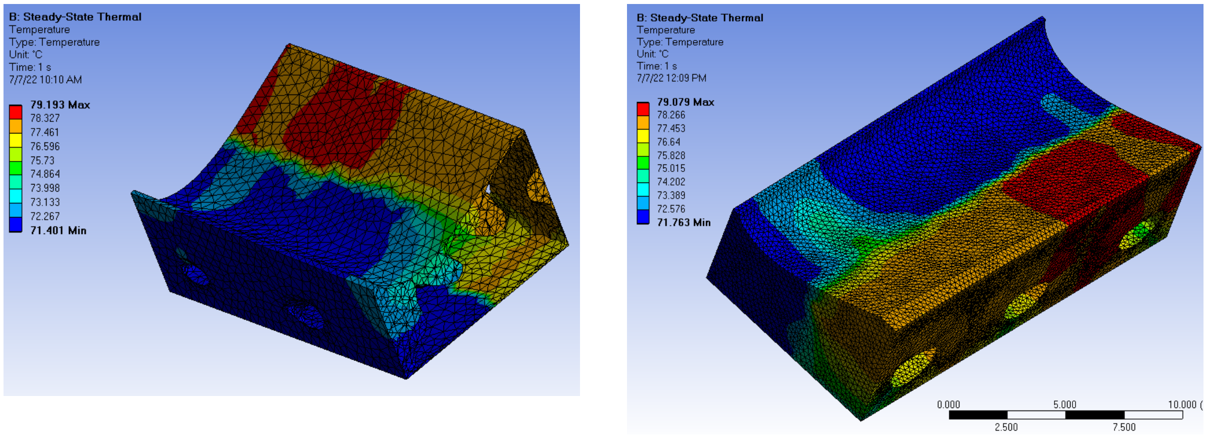

(a) Coarse mesh (sectioned to reveal interior)
(temperature range ±3.89°C)

(b) Fine mesh
(temperature range ±3.66°C)

Figure 2.1.3 Effect of Mesh Size on Temperature Distribution

2.2. Prototype Version 1 modular mold structure optimization and validation

Leveraging the experience gained from modeling the preliminary mold, additional weight reduction was achieved by performing a fully coupled thermal-fluidic-structural topology optimization (TO) using COMSOL and MATLAB. In this version, a blade skin was simulated to better reflect the boundary conditions the mold module will experience during blade fabrication, including blade weight and heat transfer at the mold-part interface. Fig. 14 shows the mold module without conformal channels in full scale (approximately 20×10×5 m), which defines the design domain for TO. The parameters for the topological optimization were updated from the earlier model:

- Mold material: 6061-RAM2 Aluminum Alloy
- Blade skin material glass fiber epoxy (density = 1.95 g/cm^3, thermal conductivity = 0.288 $W/m^2/K$)
- Blade skin thickness = 0.54m
- Heating fluid: air with velocity = 0.1m/s, inlet temperature = 348K
- Initial temperature for the mold = 293K
- Convection on the blade skin top surface (h = 10W/m^2 K) to model heat dissipation to the surrounding.
- Fixed support at grid points on the bottom surface to model support from an egg crate.
- Roller support at mold sides to model support from neighboring mold module.
- Objective: minimize mold volume
- Target temperature of the mold surface: 343K
- Target pressure drop between inlet and outlet = 1 Pa

Figure 2.2.1 shows the COMSOL-optimized geometry in various views, where TO successfully removed 62% of the weight from the solid aluminum block. The additional weight reduction was obtained by setting the TO boundary conditions to entice the mold to be hollow rather than simply create an air passage from the inlet to the outlet. The RTRC validated the thermal performance of this new geometry with a fully turbulent flow model and found a temperature uniformity its airfoil profile to be $75 \pm 5^{\circ}C$.

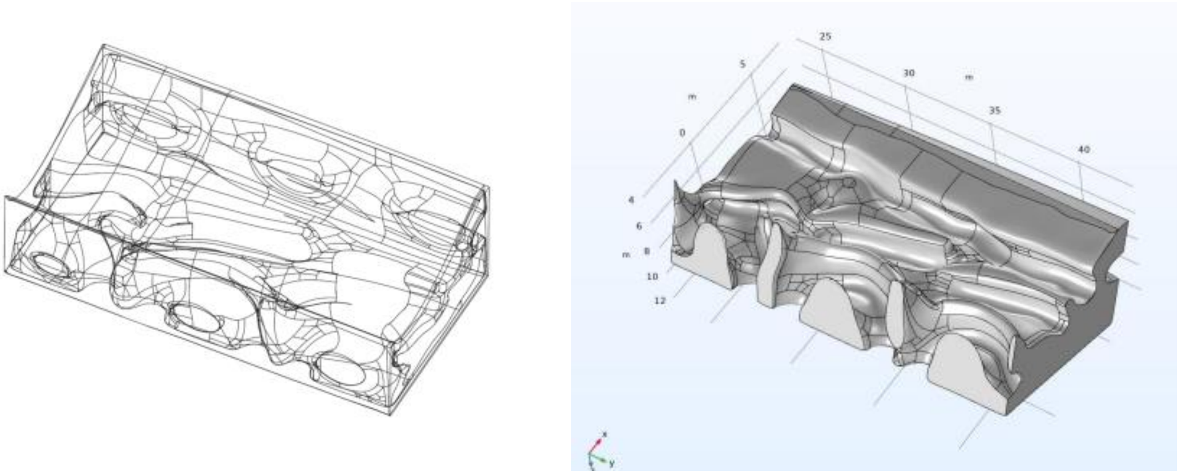

(a) mold module with hidden lines (b) topo-optimized air channel (void)

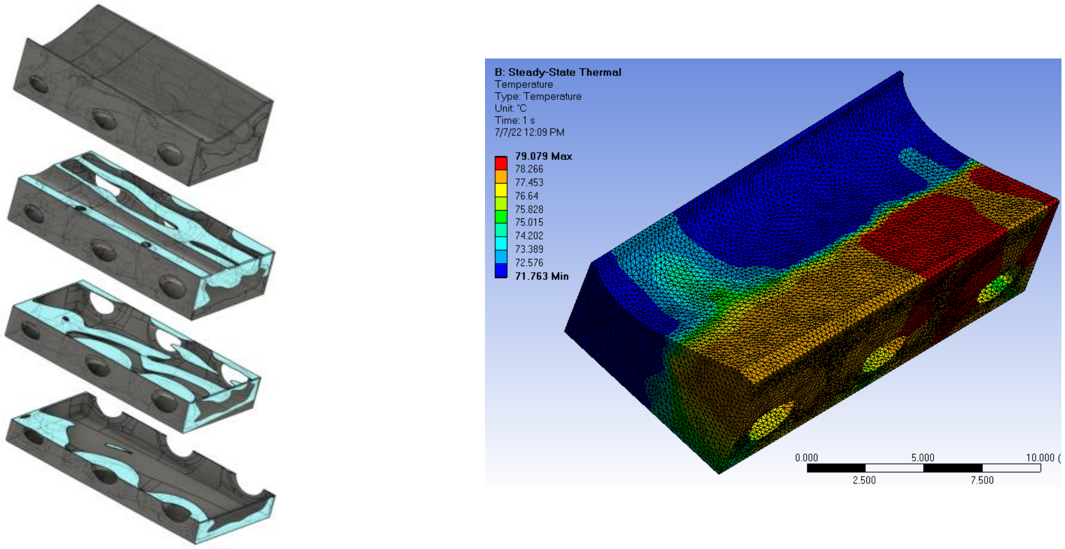

(c) section views of the mold module with air channels (d) ANSYS thermal analysis with turbulent model

Figure 2.2.1 Topology optimization to further reduce weight

The TO-optimized geometry was then reviewed and post-processed by DM3D, the additive manufacturing (AM) vendor, to improve manufacturability within their additive manufacturing process. A structural TO with overhang constraints analysis, available on ANSYS, was utilized by setting up the structural-only TO with a fictitious load in the prescribed build direction. Several build directions were explored to identify the build direction that would result in the most reduction of overhangs that were greater than 60°. The negative y-direction, shown by the yellow arrow in Figure 2.2.2(a), was chosen as the build direction. Fig. 2.2.2(b) is after the overhand reduction by ANSYS. Autodesk *Meshmixer* was then used to add support structures to the remaining overhangs, Figure 2.2.2(c). The post-processed geometry was sent to RTRC for performance validation modeling.

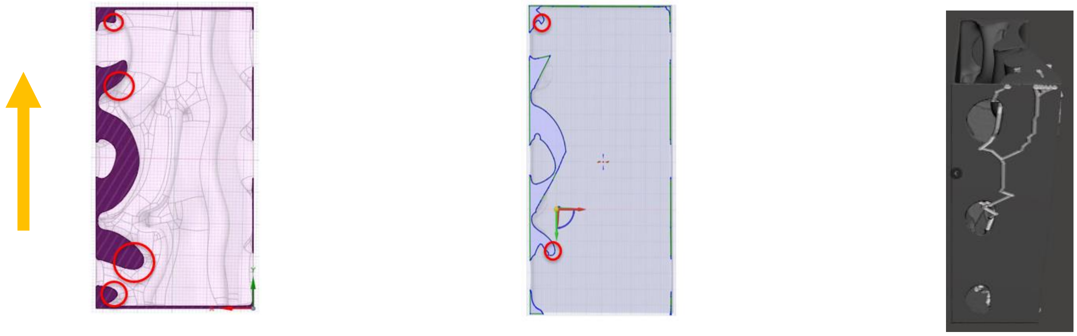

(a) before ANSYS optimization

(b) after ANSYS optimization

(c) after ANSYS optimization with example support structures

Figure 2.2.2 Example section of topology optimization with overhand constraints to improve manufacturability

The Version 1 design was validated using thermo-mechanical finite element models built using an extra step of lattice generation. Three different meshes that correspond to the solid, the void/channel, and the combined part of the mold module were provided from the TO. The solid mesh and the void mesh with lattices are independently generated in ANSYS *SpaceClaim* and then combined in Autodesk Mesh mixer to create the combined mesh, Figure 2.2.3. The lattice fill percentages before the combination are 70% for the solid and 10% for the channel. The lattice is denser in the solid region and looser in the channel region. The reduced size mesh was selected to save computational cost and not for any engineering considerations on the thermal/structural performance model.

The model building process entails dividing the space in the mold into sufficiently small subdomains and determining their locations and control volumes. Mathematical model in the fluid region representing the fluid flow and heat transfer is usually dominated by three physical laws: mass conservation, momentum conservation, and conservation of energy[1]. The governing

---

[1] Zhan CH, Liang X, Wang Y (2011) Rules of impact of autoclave environment on frame mold temperature field of advanced composites. J Mater Sci Eng 29:547–553

equations of the fluid flow and heat transfer can be solved in these pre-determined sub-domains, which must not overlap. An unstructured mesh was selected for grid generation because of the complex organic structure of the mold, and to ensure that the generated grid model well-reflected the geometric model and would form good boundary layer. A detailed view of the model mesh density difference is given in Figure 2.2.4, while a cross-sectional view of the full-size mold solid meshing is given in Figure 2.2.5.

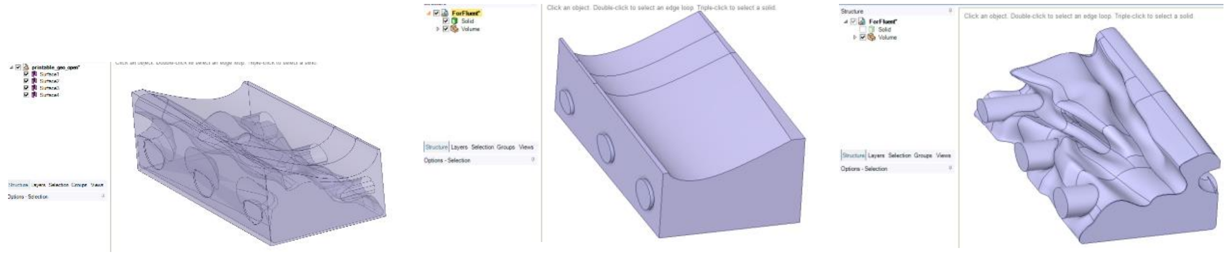

(a) geometry of the topology optimized die (initial)

(b) mold structure modified in *SpaceClaim* to create the fluid volume for Fluent CFD analysis

(c) interior fluid volume for *Fluent* meshing & analysis (post manufacturability review)

Figure 2.2.3 Version 1 lattice generation from solid and fluid components

The mesh condition of the fluid–solid conjugated interface directly controls the simulation accuracy. The grid near fluid–solid conjugated interface, shown in Figure 2.2.4, should be dense. But to reduce computation time, the density of grid should be gradually decreased at the fluid–solid conjugated interface. For the complex geometrical shapes like shown in Figure 2.2.5, coinciding with mesh model needs to be ensured, therefore the mesh of solid should also increase grid density[2]. Heat transfer in fluidic region was governed by the equations listed in reference 2. The governing equation of the solid zone is mainly heat conduction, which was also modeled using the conduction equation listed in reference 2.

---

[2] Zhang CH, Zhang B, Wang Y (2010) Refined simulation on curing temperature field of composites structures. Dev Appl Mater 6:41–46

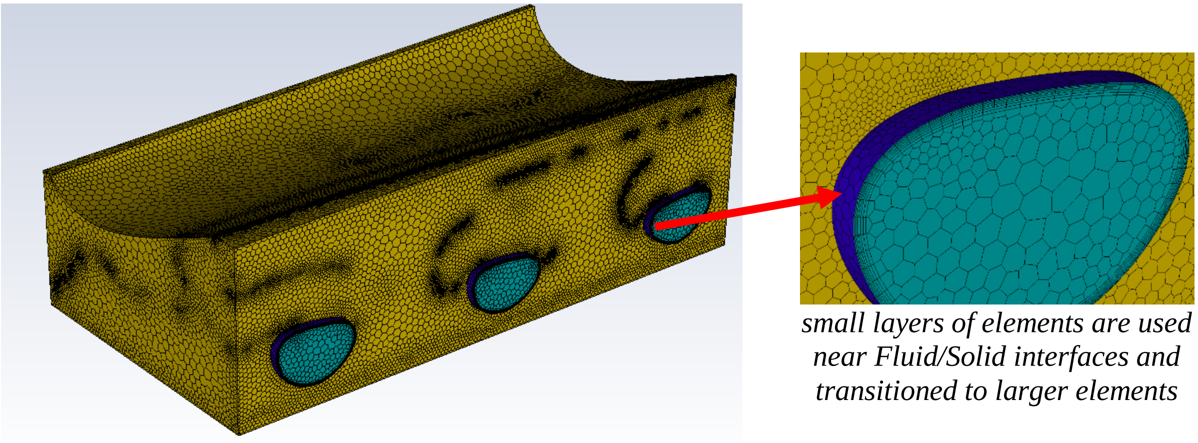

small layers of elements are used near Fluid/Solid interfaces and transitioned to larger elements

Figure 2.2.4 Version 1 mold meshed within *Fluent* in using Polyhedron Mesh

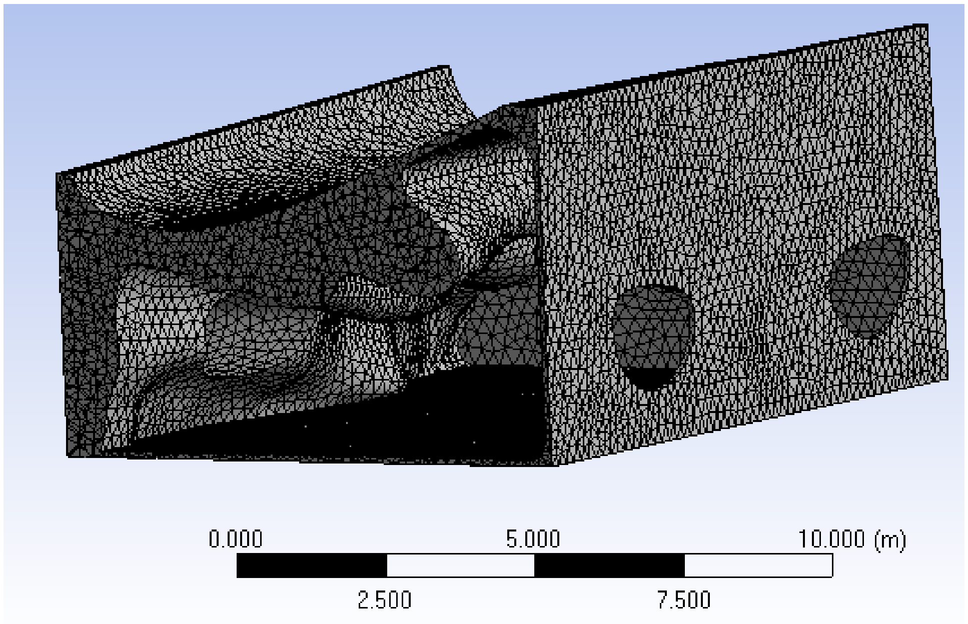

Figure 2.2.5 Version 1 mold design sectioned to illustrate its internal features. This tetrahedron mesh was selected for the mechanical steady-state thermal analysis in ANSYS

Modeling assumptions are: the solid parameters do not vary with temperature; the fluid flow is stable both in the inlet and outlet; hot air delivery is stable and uniform and has temperature-dependent properties; the influence on heat transfer of the mold's support structure is neglected; and the flow of fluid across the inner and outer cavities of the mold is taken into consideration. Boundary conditions of model:

- The inlet is a regulated boundary condition with a 0.1 m/s velocity
- A heat flux of 10 W/m^2 applied to top profile surface

- All other walls are adiabatic and no-slip
- The air temperature changes over time and reaches a final temperature following a curing curve (T = 0.025 × t + 29 K)
- The default initial temperature is room temperature
- The outlet is a regulated boundary condition of pressure whose default is the hydrostatic pressure

Figure 2.2.6(a) shows cross-sections of the air flow through the mold from the inlet to the outlet as shaped by the mold's solid topography. Air velocity increases in the narrower zones of the mold, with minimum velocity near the top of the channels, and lower velocity at the outlet than the inlet, confirming expectations. The temperature distribution is highest at the top of the inner surface of the mold module, shown in Figure 2.2.6(b), (the inner surface represents the fluid/structure interface), reaching a maximum temperature of around 80 ^{o}C. The lowest temperatures are near the inlet and outlet at about 70 ^{o}C. The overall variation in temperature is +/- 5 ^{o}C on the airfoil profile surface, meeting the specification. These *Fluent* model results showed the Version 1 mold is robust enough and provides better temperature distribution. The *Fluent* results will be imposed as boundary conditions on the ANSYS thermo-mechanical analysis.

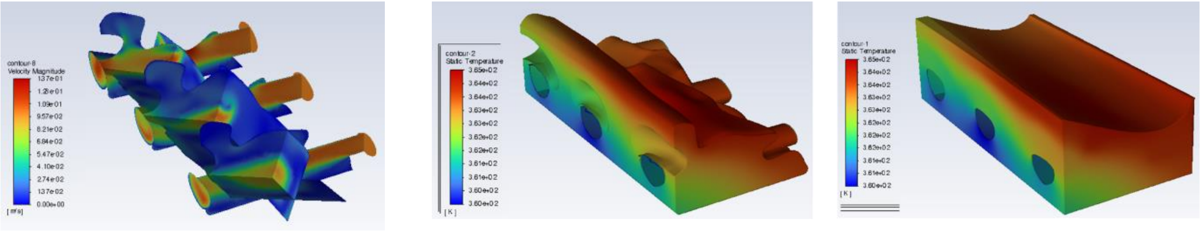

(a) velocity profile cross-sections

(b) temperature distribution of air section

(c) temperature distribution of solid section

Figure 2.2.6 Predicted steady-state flow and temperature of Version 1 mold model using *Fluent* simulation

Steady-state thermal-mechanical analysis was carried out using the ANSYS mechanical module. The model geometry was imported and refined to use a tetrahedron mesh and the steady-state *Fluent* model results were imported whereby the fluid domain was mapped onto the fluid/structure interface. A constant Heat Flow 10 W/m^2 was applied to the airfoil profile surface. The ANSYS steady-state thermal model was used to evaluate the Version 1 mold design's thermal loading condition when subjected to the constant heat flow on the airfoil profile surface and the internal temperatures distribution obtained from *Fluent* analysis. Figure 2.2.7 shows the predicted temperature variation is ±0.2°C with the refined mesh, meeting the design specification. The temperature uniformity is much better in Version 1 mold design than that of the preliminary mold design.

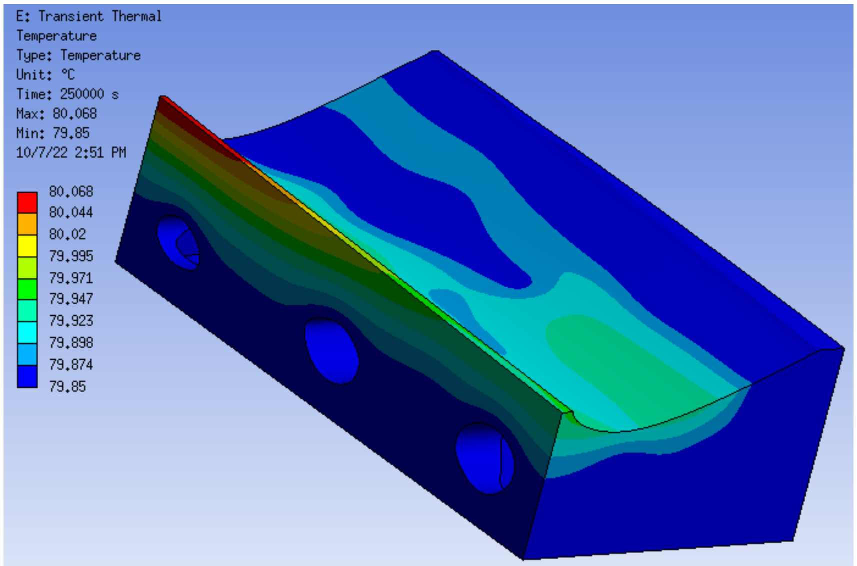

Figure 2.2.7 Version 1 mold temperature prediction. A more uniform temperature distribution was observed with a temperature range of ±0.2°C

A transient thermal analysis was also conducted to estimate the mold heating time. The transient thermal analysis provides a temperature profile over time that is also used as input for the structural analyses as it transitions to its steady-state. Figure 2.2.8 illustrates the transient thermal temperature from 25k s (point A) to 2.5e5 s (point B). Figure 2.2.9(a) & (b) shows the temperature distribution on the mold at these respective times, while Figure 2.2.9(c) & (d) shows the dimensional distortion at 25k s. The maximum Z-deformation was observed to be 0.011 mm, while the maximum total deformation was observed to be 0.040 mm. In general, the Version 1 mold design requires ~69.5 hours to heat up to a uniform temperature distribution.

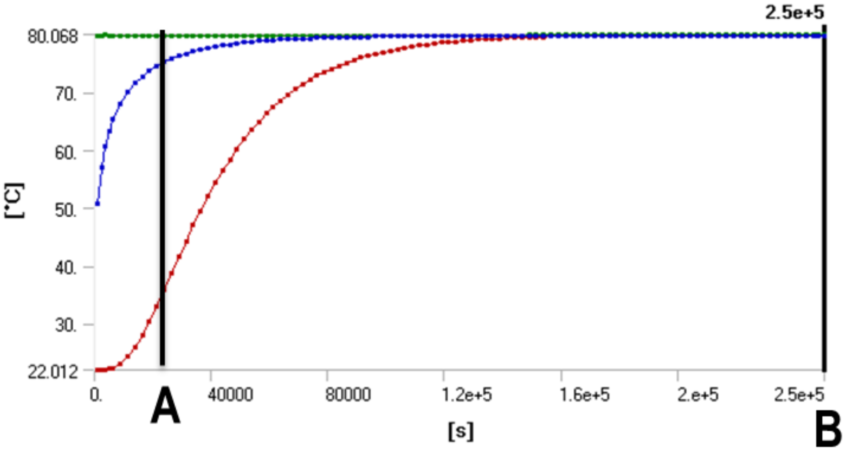

Figure 2.2.8 Transient heating temperature as a function of time

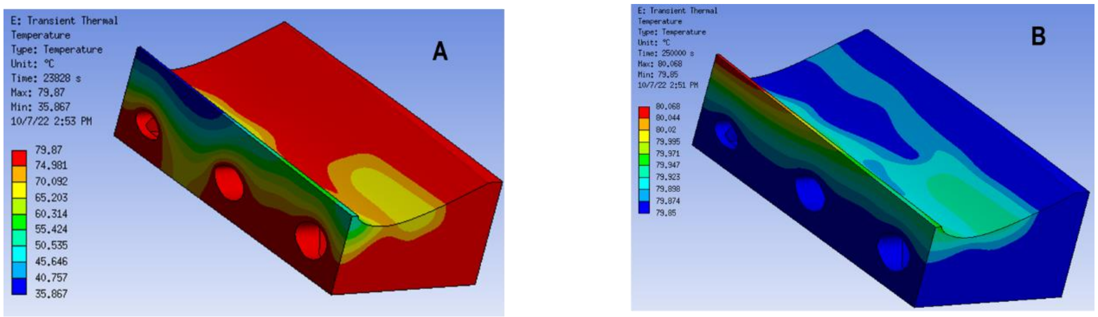

(a) temperature distribution at 25k s (b) temperature distribution at 2.5e5 s

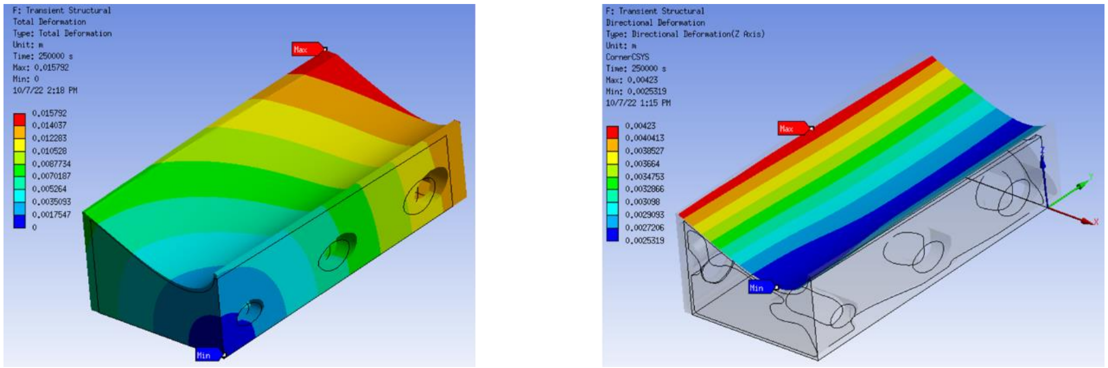

(c) total deformation at 25k s (scaled 88x) (d) Z-deformation at 25k s (scaled 88x)

Figure 2.2.9 Version 1 mold temperature distribution at time A and B during heat-up. ANSYS transient structural analysis subject to thermal expansion

In summary, the thermo-mechanical analysis for the validation of the Version 1 mold design indicates that the temperature distribution is more uniform with minimum variation and lower deformation than the preliminary mold design. However, a heating time at close to 3 days is unacceptable. A new version of the mold will be designed and analyzed to address this deficiency.

2.2.1. Lessons Learned from the Version 1 mold design and analysis

While an uncoupled thermal-fluidic simulation of the temperature distribution and a structural simulation for the structural compliance does not explicitly calculate the surface distortion due to thermal expansion, the topological optimizer can achieve an implicit reduction of the distortion by bounding the structural compliance. This provides the benefit of a significant gain in computational speed. For further reduction of computational time, a Darcy flow model for fluid flow (a model of choice in the literature on thermo-fluidic TO for heat exchangers) should be adopted.

Validation analysis workflow on the topology optimized mold design was significantly improved by modeling the air flow channels (the void) and the solid structure as separate objects that can be combined into one model. This improved the efficiency of meshing feature-sensitive geometries and imposing boundary conditions on the appropriate surfaces.

2.3. Prototype Version 2 modular mold structure optimization and validation

Consultation with experts at TPI Composites indicated that the Version 1 mold design would be excessively costly to 3D print and be too heavy at full scale to be feasibly transported. In addition, the time-transient analysis required an unrealistically long time for the mold to reach the target temperature. Therefore, another design iteration was undertaken to further reduce the weight of the design, referred to here as the Version 2 mold design. Major changes from the Version 1 mold design are listed as follows:

- The design domain for topology optimization was reduced from a 20m x 10m x 5m design space claim to a 20m x 10m x 1m shell of the same blade section. The shell is further split into two adjacent 10 x 10 x 1m modules, so the geometry can fit within DM3D's printing envelope when scaled to 1:20 for prototype fabrication, Figure 2.3.1(a).
- The fluid inlet and outlet are now specified as rectangular openings occupying the entire leading and trailing edges of the top mold surfaces.
- The bottom surface of the mold approximately conforms to the top surface and is formed by attaching a sheet steel to the printed mold with screws, Figure 2.3.1(b). This allows the fluid channels to be "bottomless" in the printed part of the mold. This dramatically reduces the overhang geometry that posed a significant challenge to manufacturability in the Version 1 design.
- Instead of the fully-coupled thermal-fluidic-structural topology optimization used for the Version 1 design, a structural-only topology optimization by ANSYS was used to take advantage of its built-in overhang constraints. The resulting topology was then verified with a steady-state thermal-structural finite element analysis (FEA) for thermal uniformity and rigidity of the airfoil profile surface.

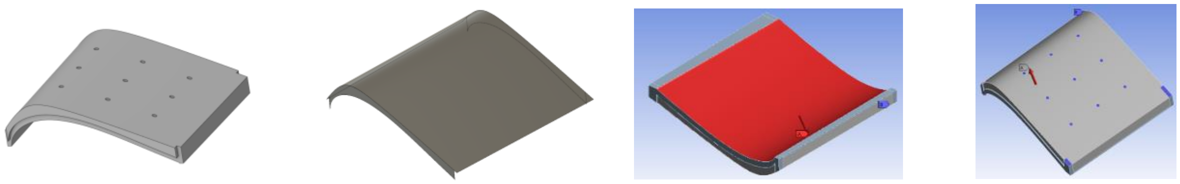

(a) design domain (b) steel sheet for the bottom surface (c) pressure on top surface (d) fixed supports at corners and pillars

Figure 2.3.1 Version 2 mold module space claim before topology optimization

For the structure-only topological optimization with ANSYS, a uniform pressure of 1000 Pa was applied to the top mold surface, Figure 2.3.1(c), and the mold is fixed at the corners and pillars to be screwed on to the steel sheet forming the bottom surface, Figure 2.3.1(d). The non-design regions specified during the topology optimization included a thin layer defining the airfoil profile surface at the top mold surface and fixed corners and pillars defining the support interface points. The optimization objective was to minimize the volume of the structure subject to constraints on structural compliance (<= 0.1 J), overhang in Z-direction (<= 60 deg), and feature size (> 0.25

cm). The upper bound of the compliance was used as a tuning parameter to adjust the degree of weight reduction. The material was the same 6061-RAM2 aluminum alloy used in the Version 1 design.

Figure 2.3.2(a) shows the optimized mold half, denoted Module A, without the steel sheet. The volume is reduced to 22% of the design domain. Figure 2.3.2(b) shows the thermal deformation when the top surface is subject to a heat source of 70°C. The maxium deformation is 0.01m, about 0.12% of the chord (8.31m). As an approximation of the steady-state thermal deformation by heated fluid, the resulting thermal deformation verifes the design has sufficient stiffness justifying further detailed analysis. Since the mold requires machining on the top surface to remove the support structures generated during printing, an additional FEA was conducted to check surface deformation during milling. A 500N point load was applied to the top surface at a location where there was no supporting pillar nearby. The resulting displacement and von-mises stress are shown in Figure 2.3.2 (c) and (d). The maximum displacement and stress was on the order of 10^{-6}m and 10^{5} Pa, orders of magnitude smaller than the chord length and the yield stress, respectively.

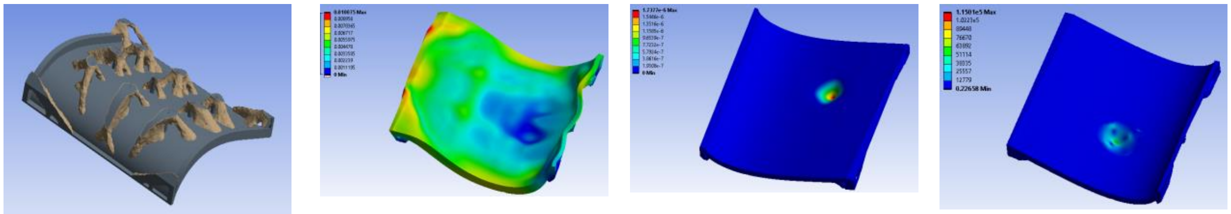

(a) optimized design

(b) thermal deformation of top surface

(c) displacement with point load on the top surface

(d) stress with point load on the top surface

Figure 2.3.2 Topology optimization and verification.

The second half of the 20m mold shell, denoted Module B, was designed using the same workflow and the total weight of the two halves was estimated at 123,460 kg, including the sheet steel air plenum housing, which is 16.2% of the v1 mold design. Figure 2.3.3 compares the weights of the two design versions. Figure 2.3.3 (b) and (c) shows the topologically optimized underside of the two mold halves that provides rigidity and conformal channels. These two modular mold segments, divided along the axis of the turbine blade, are used to demonstrate proof of concept of mold module joint at 1:20 scale.

Following experimentation with the 1:100 scale prototype (see Sections 2.4 and 5.1), the Version 2 geometry was modified for prototype fabrication at a 1:20 scale. Minor adjustments were made to improve the mold-frame connection and mold-mold interface joint, as illustrated in Figure 2.3.4. The changes made included leveling the support structures to the same height for easier assembly of the bottom sheet metal enclosure, improving the assembly, and leveling the side ribs to facilitate the assembly of the sheet metal enclosure to the mold side. The additional side rib material also provided machining stock to implement an O-ring groove to better seal the mold-to-mold joint.

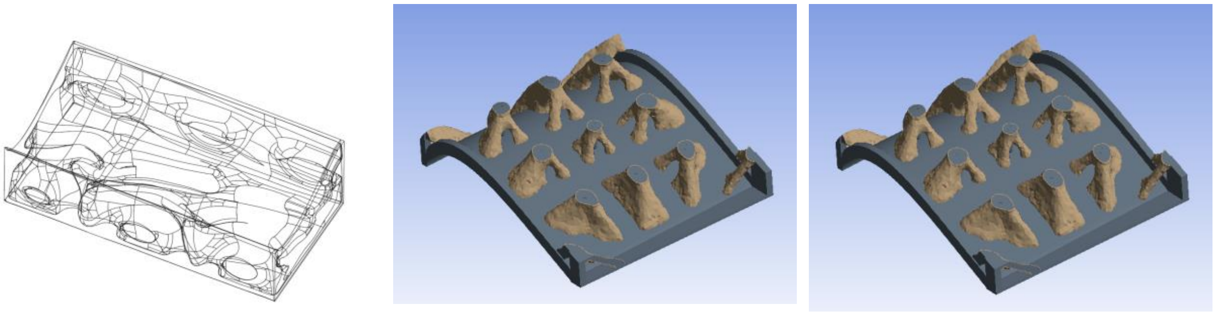

(a) mold Version 1

(b) mold Version 2
Module A

(c) mold Version 2
Module B

Version 1 weight (kg)	Version 2 weight (kg)				Weight Reduction
	Module A	Module B	2 sheets steel	total	
764,100	58,050	62,910	2,500	123,460	84%

Figure 2.3.3 Comparison of the full size mold versions and design weights.

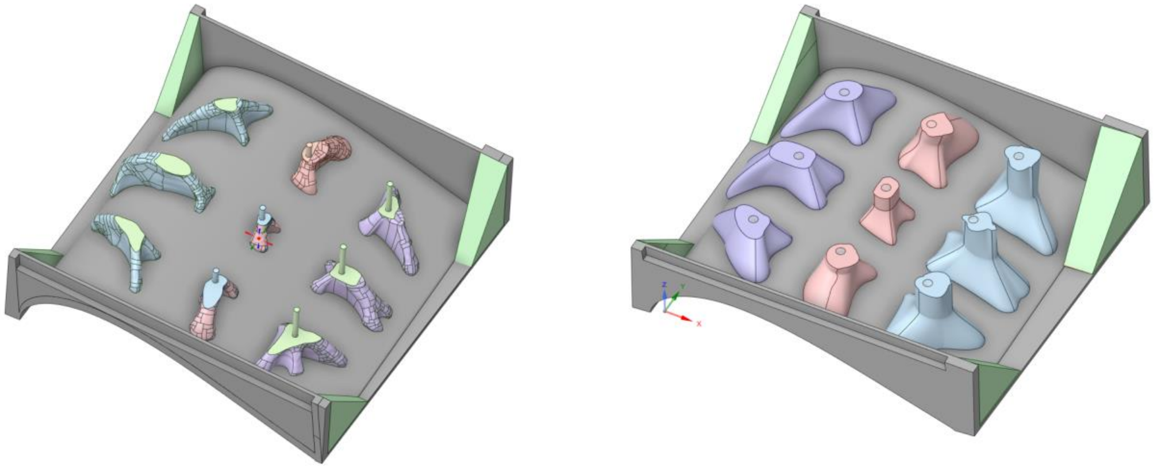

(a) 1:20 Scale mold Version 2
Module A

- XYZ Bounding Box: 492mm x 500mm x 140mm
- Volume: 3.21E-3 m^3
- Weight: 8.67 kg (26% of baseline)

(b) 1:20 Scale mold Version 2
Module B (mating mold)

- XYZ Bounding Box: 492mm x 478mm x 137mm
- Volume: 4.59 E-3 m^3
- Weight: 12.4 kg (35% of baseline)

Figure 2.3.4 Mold Version 2 1:20 scale model design

Note that the modifications made for easier assembly increased the weight of the modules compared to the original design. However, both modules still meet the <75% of baseline weight target.

A manufacturability review for Mold A with DM3D was conducted prior to their 3D printing. Simplifying the design resulted in the support structures in the 1:20 molds being leveled and the side wall support replaced with a separately machined trianglar bracket, allowing for easier assembly. The corner support brackets also reduce print volume. To retrofit Mold A, spacers are installed to level all the supports to the same plane. A small step at the side walls ensures the sheet metal is flush with the mold and provides additional lateral support. The assembly procedure for the 1:20 molds is shown in Figure 2.3.5. Since these minor modifications were anticipated to have a minimal effect on the mold modules' structural and thermal TO performance, the Version 2 design was sent to RTRC for thermal-fluidic-structural FEA validation analysis.

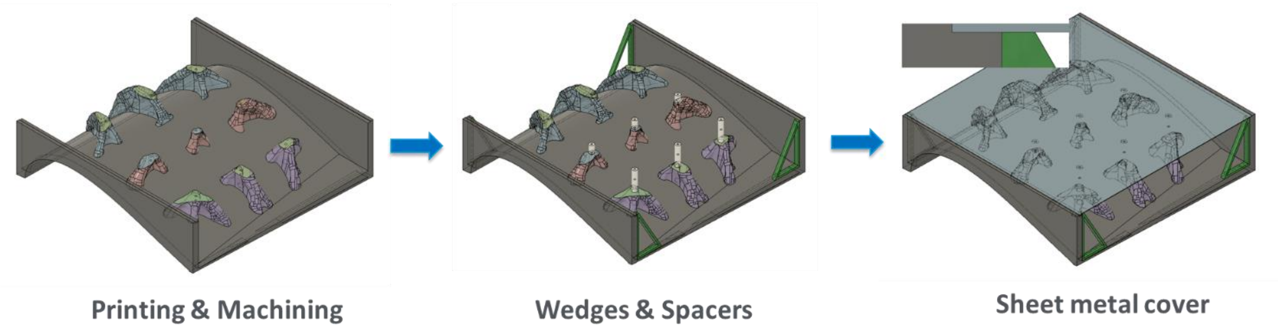

(a) (b) (c)

Figure 2.3.5 1:20 scale model assembly procedure: (a) printed and machined mold, (b) mold with corner brackets (green) and spacers (white), and (c) mold with sheet metal closure (blue).

A review with DM3D experts of the mold Module A post-fabrication found there were a few overhangs and sharp corners causing manufacturability issues. Therefore, the mold Module B design was slightly modified with some addition changes in consideration of the mold-frame connections. The changes were:

- Support material was added to remove overhangs
- The nine support pillars on the backside of the mold module were grouped by their chord-wise location and each group was set to the same height. Threaded holes were added to these pillars for mold-frame connections
- Fillets are added to eliminate sharp corners to provide a minimum machining radius

Since the changes were small compared to the size of the mold modules, they were expected to have little impact on the structural and thermal performance of the FEA verifications run on the mold modules.

2.4. Version 2 mold thermo-mechanical modeling for validation at 1:100 and 1:20 scale

The RTRC Team developed a coupled thermal/fluid model to validate the topology of the 1:100 scale prototype since it was the first model to be physically tested. To verify the temperature field on the airfoil profile surface was within specification, a model was built with ANSYS Workbench 2021R2 (ANSYS Mechanical/Fluent). A polyhedral mesh of both the fluid and solid domains was created to run a conjugate heat transfer analysis. The mesh, shown in Figure 2.4.1, has the fluid mesh shown in blue and the solid mesh shown in gray. Three cells were included in the boundary layer.

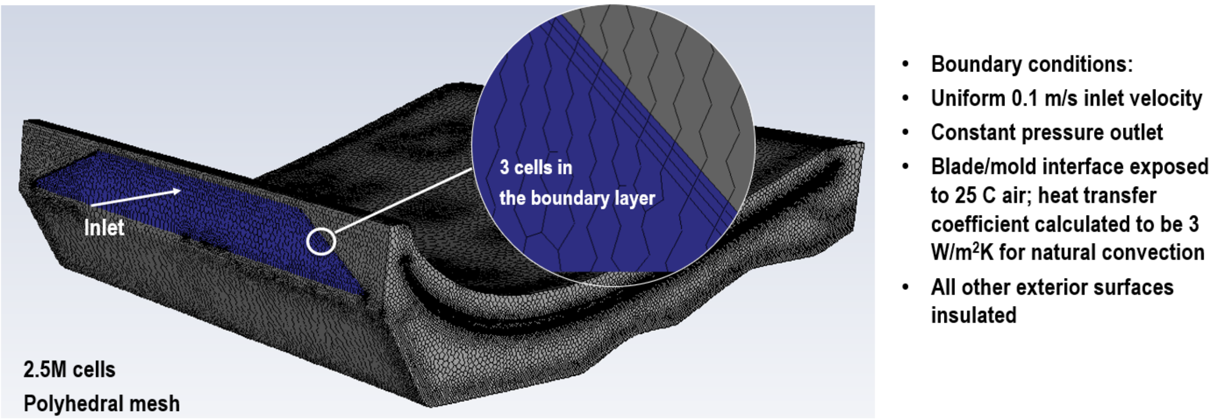

- **Boundary conditions:**
- **Uniform 0.1 m/s inlet velocity**
- **Constant pressure outlet**
- **Blade/mold interface exposed to 25 C air; heat transfer coefficient calculated to be 3 W/m^{2}K for natural convection**
- **All other exterior surfaces insulated**

Figure 2.4.1 Version 2 mold fluent validation mesh and boundary conditions

The simulation conditions were an inlet velocity of 0.1 m/s at 75C, the airfoil profile surface (the blade-mold interface) was exposed to air at 25C, while all other surfaces were insulated. To match the experimental conditions, the modeling conditions were iterated to find the correct balance between the heat transfer coefficient and the temperature difference between the blade-mold interface and ambient, which converged to a temperature delta of approximately 34C yielding a heat transfer coefficient of 3.5 W/m^{2}K. Figure 2.4.2(a) displays the pathlines through the fluid domain of the conjugate heat transfer simulation as they navigate the topological optimized features. The pathlines are colored by temperature. Although the flowlines show a preference through the open passageways, some mixing is evident between the optimized features. Figure 2.4.2(b) shows the temperature distribution along the blade-mold interface. Little variation in temperature is seen along the airfoil profile surface, with the temperature closest to the fluid inlet at 59.9C and the temperature closest to the outlet is 59.3C.

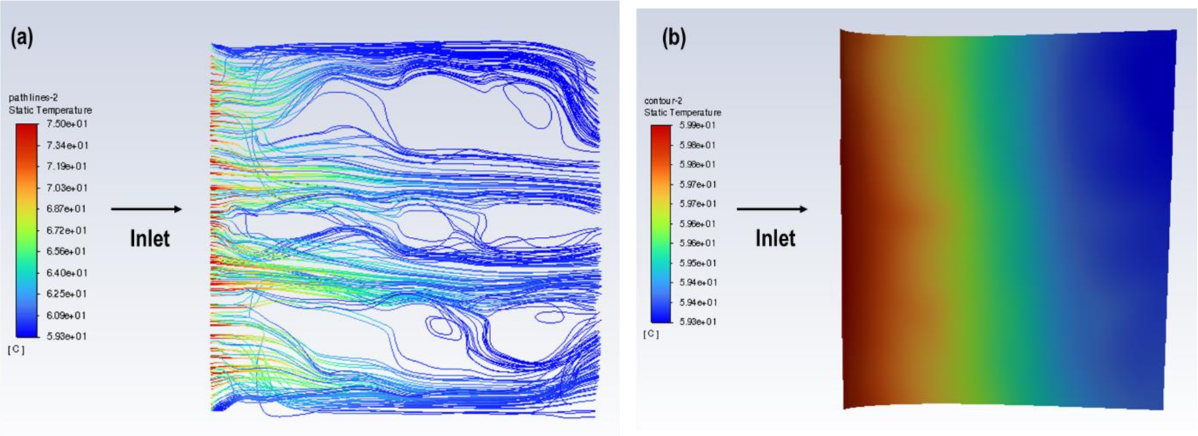

Figure 2.4.2 Version 2 mold coupled thermos/fluid simulation results. (a) Path lines colored by temperature through the fluid domain; (b) Temperature of the blade/mold interface.

A transient thermal analysis of the 1:100 scale topology-optimized geometry was also conducted. Boundary conditions were established using an initial temperature of 25C and the temperature boundary condition imported from a Fluent analysis to the inner fluid-solid interface. The airfoil profile surface was exposed to atmosphere utilizing a convection coefficient of 3 W/m^2*K. The analysis was iterated to find the time to reach steady-state temperature assuming that the heated fluid domain had already reached steady-state. For this small 1:100 scale geometry, steady-state temperature is achieved in about 4.4 seconds with a ~0.5°C range of temperature along the airfoil profile surface as shown in Figure 2.4.3. This time to reach steady-state will differ with both scale and larger temperature differences between the initial and final temperatures. Increasing the air inlet velocity, as shown in Figure 2.4.4, reduces the time to reach steady-state to about 3.0 seconds as mass of the mold module is low. A higher steady state temperature of 59-60C with temperature uniformity within 1C was also achieved. The results were verified experimentally (Section 4.3) and were observed to have close agreement between prediction and measurement.

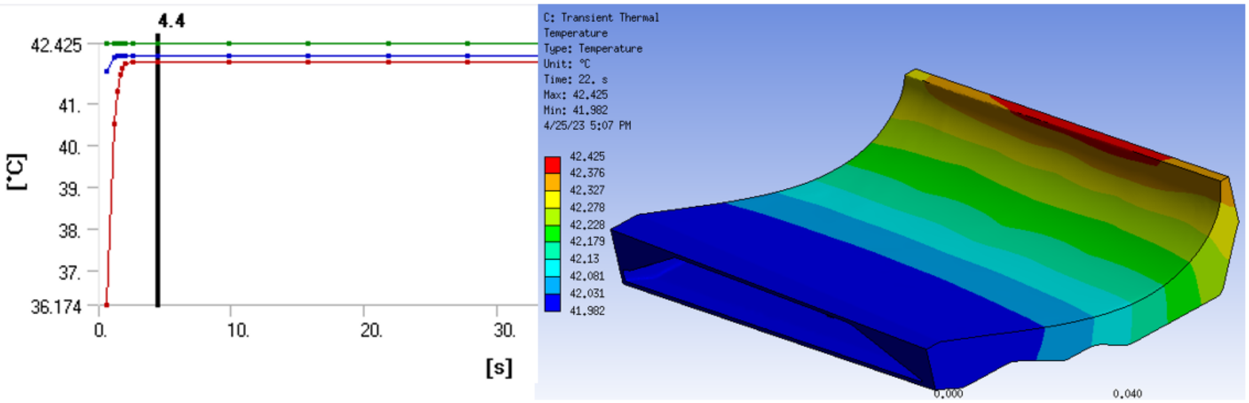

Figure 2.4.3 Transient thermal results where the heated air velocity is 0.1 mm/s

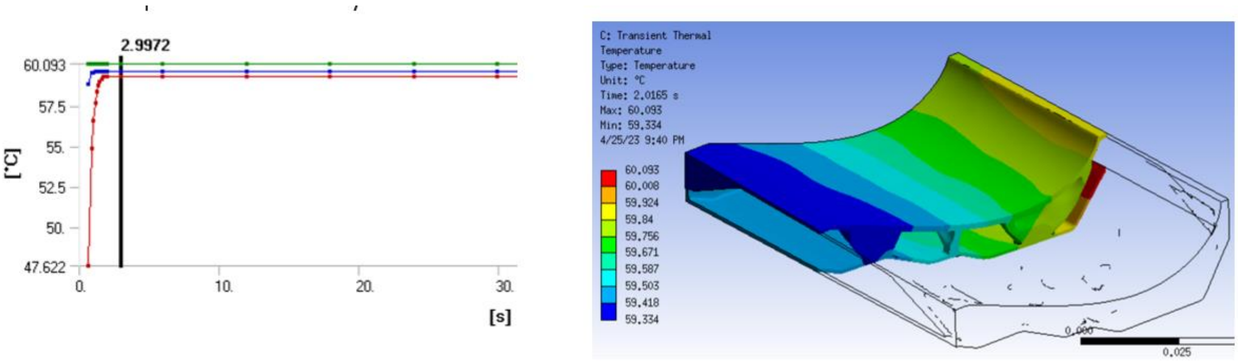

Figure 2.4.4 Transient thermal results where the heated air velocity is 100 mm/s

The next step was for the RTRC team to develop a thermal mechanical model at 1:20 scale and predict the mold deformation, stress distribution due to the thermal load, and estimate its heating time. First, to better represent the boundary conditions on the airfoil profile surface, the thermochemical properties of the resin that will be used must be understood. TPI Composites had already thoroughly characterized their resin and created an Arrhenius style reaction rate model equation for it. This model was incorporated into a software package from Convergent Manufacturing Technologies (CMT) called Raven and several isothermal simulation runs were conducted between 60°C and 85°C with intervals of 5°C to compare against known results of the model as shown in Figure 2.4.5.

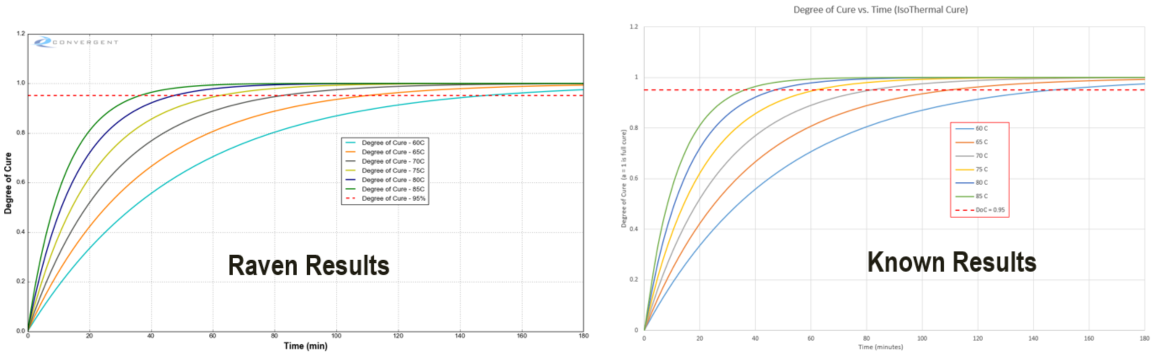

(a) Raven model results

(b) TPI model results

Figure 2.4.5 Comparison of reaction rate model confirming correct implementation in Raven software.

With the resin model validated, a thermal model for the composite material was developed in Raven by combining the resin model with generic carbon fiber properties hereby referred to as the *TPI composite*. A heat flow model for the entire stack of materials forming the turbine blade on the mold's airfoil profile surface was developed assuming a common sandwich structure starting with a laminate of TPI composite placed onto the mold. On top of the first laminate is a honeycomb core material, then a second laminate of TPI composite, followed lastly with a layer of breather cloth used to provide some thermal insulation.

This material layer stack with their relative thicknesses is illustrated in Figure 2.4.6. This figure also summarizes the boundary conditions for this 1D thermal analysis: the top surface is exposed to a convective heat transfer coefficient of 3 W/m^2*K, representing natural convection to room temperature and atmosphere; and the bottom surface is exposed to the heating from within the mold. The heating temperature ramps from 20C to 80C at a rate of 1.5C/minute and is then held at 80C for 240 minutes before cooling. The curing resin has thermal conductivity that is dependent on degree of cure and temperature and varies during the process as shown in Figure 2.4.7.

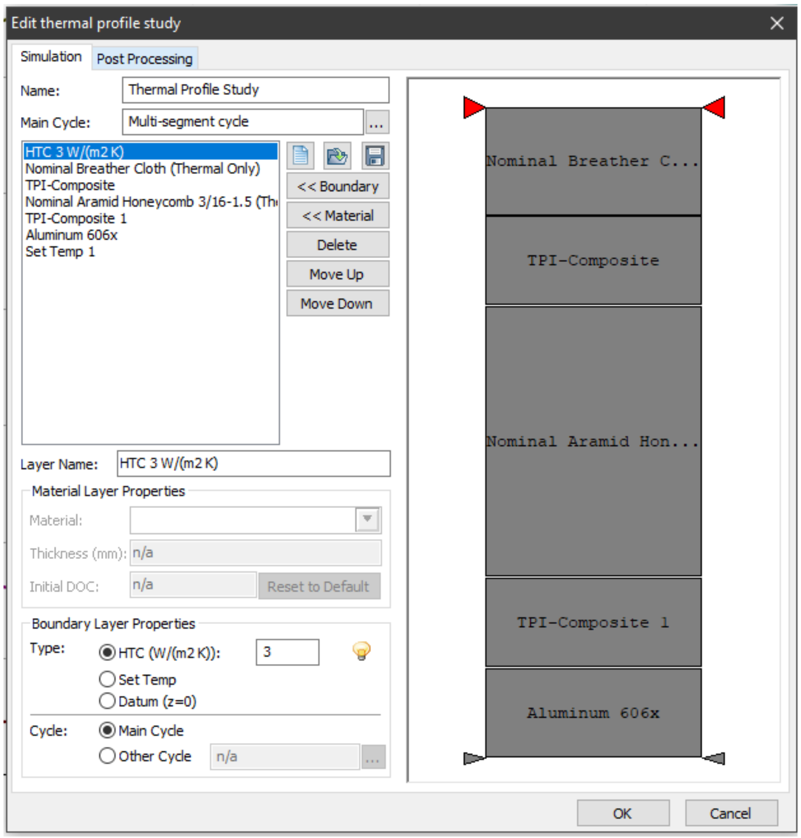

Name: Thermal Profile Study

Main Cycle: Multi-segment cycle

HTC 3 W/(m2 K)
Nominal Breather Cloth (Thermal Only)
TPI-Composite
Nominal Aramid Honeycomb 3/16-1.5 (Th
TPI-Composite 1
Aluminum 606x
Set Temp 1

Layer Name: HTC 3 W/(m2 K)

Material Layer Properties
Material:
Thickness (mm): n/a
Initial DOC: n/a

Boundary Layer Properties
Type: ● HTC (W/(m2 K)): 3
○ Set Temp
○ Datum (z=0)
Cycle: ● Main Cycle
○ Other Cycle n/a

Figure 2.4.6. Raven analysis setup of the material stack up for 1D thermal analysis.

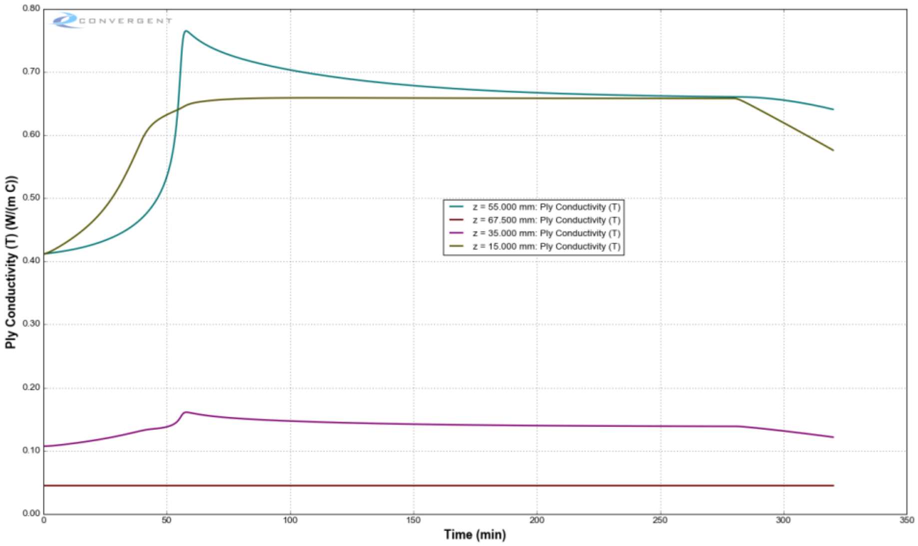

Figure 2.4.7. Thermal conductivity evaluation of the stack at 4 height positions which represent the middle of each layer, i.e., the upper/lower TPI composite layers, the honeycomb core layer, and the breather cloth layer

In Figure 2.4.7, the two top lines represent the thermal conductivity of the two TPI composite layers. Thermal conductivity varies as the curing temperature varies, further driving the curing reaction. As time goes on, the degree of cure in both composite layers become similar. The two lower lines in Figure 2.4.7 are for the honeycomb core and breather cloth, which largely don't change with temperature. The evaluation was done for the specific heat of each material layer establishing the thermal conductivity properties summarized in Table 2.4.1.

Table 2.4.1: Critical thermal properties of each material in the stack up.

Material	***Thermal Conductivity (W/mK)***	***Specific Heat (J/kgK)***
TPI composite	0.65	1030
Honeycomb Core	0.14	1250
Breather Cloth	0.045	1300

The layers were grouped together to create a bulk thermal resistance for the CFD model. Figure 2.4.8 shows the grouped model with the fluid volume in translucent blue, the mold in gray, and the bulk material at the blade/mold interface in solid blue. The 1D resistance network used to calculate the bulk thermal resistance is shown for reference. As in previous simulations, the model includes a convection coefficient at the interface with the ambient air to mimic heat loss to the environment.

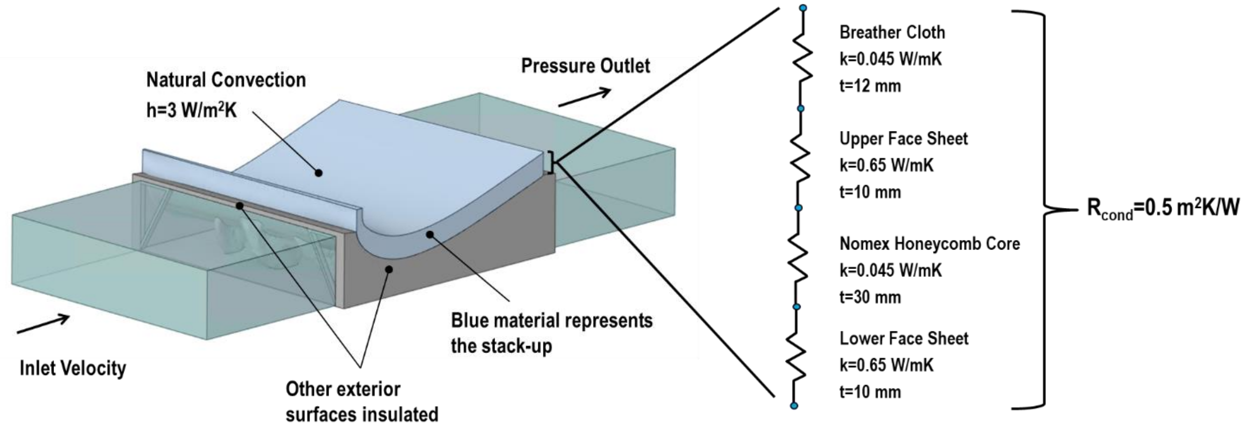

Figure 2.4.8 CFD model showing fluid volume, mold, and bulk representation of face sheet, core, and breather cloth stack-up

A computational fluid dynamics (CFD) simulation was run with three inlet velocities of 0.1 m/s, 0.5 m/s, and 1 m/s. For each simulation, the inlet temperature was adjusted such that the temperature at the blade/mold interface reached approximately 80C. Table 2.4.2 shows the boundary conditions and resultant temperatures of the three simulations. As expected, the material stack insulated the mold leaving the temperature of the exposed surface relatively constant across the three simulations.

Table 2.4.2 Boundary conditions and temperatures for the three CFD simulations

Inlet Velocity	***Inlet Temperature***	***Blade/mold Interface Temperature***	***Outer Surface Temperature***
0.1 m/s	90 C	81 C	47.8 C
0.5 m/s	83 C	79.9 C	47.3 C
0.1 m/s	90 C	81 C	47.8 C

Figure 2.4.9 shows the velocity flowlines as the fluid progresses through the mold colored by their temperature. While the flow shows preference through the open passageways, some mixing is evident between the optimized features. Little variation in temperature is seen, with the temperature closest to the fluid inlet at 59.9^{o}C and outlet at 59.3C.

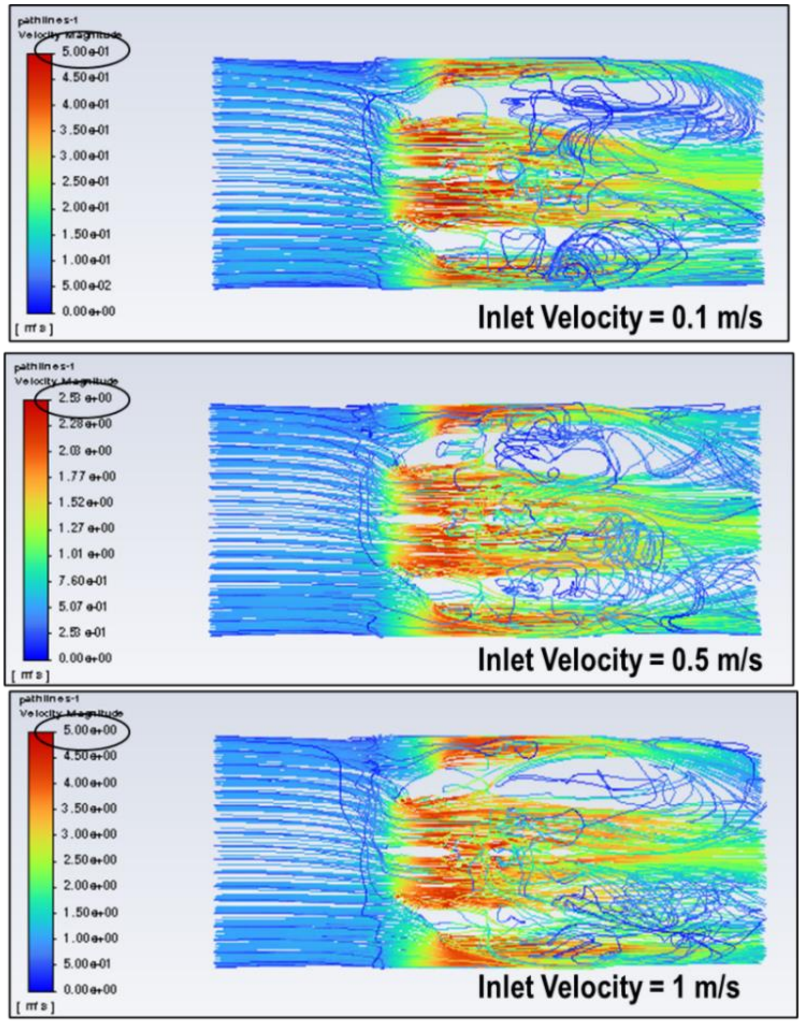

Figure 2.4.9 Velocity flowlines through the mold, colored by velocity magnitude. Due to the different inlet velocities, the contour levels for each image are at different scales.

The results from the Fluent CFD models were imported as boundary conditions into ANSYS for the three inlet velocity cases. While the range of temperature is quite similar, the distribution of temperature in each case is unique because the flow patterns are different at each velocity condition. Note the inlet temperature was adjusted for each velocity to achieve the desired 80C temperature at the mold/composite interface. The ANSYS model included the composite stack at the mold airfoil profile surface and a natural convection boundary condition for heat loss to the atmosphere on the top surface of the insulation blanket of 3 W/m^{2}K.

The transient thermal analysis and time to reach steady-state time for the 1:20 scale topology optimized geometry was then estimated. The solid domain mesh was imported from the same geometry used in the Fluent CFD ANSYS. External boundary conditions were established using an initial temperature of 25°C. The internal temperature boundary conditions were imported from the Fluent analysis and applied to the inner fluid-solid interface. The time estimated to reach a steady-state temperature was about 2-3 hours with approximately 0.5C temperature variance on the airfoil profile surface, as shown in Figure 2.4.10. The time to reach steady-state temperature at different heated fluid velocities is about the same because of the mold module mass. Compared to the 1:100 scale mold module simulation, the steady-state temperature is considerably higher, in the range of 70C, with a temperature uniformity within ~1.5°C. The time to reach the steady-state is likely to increase as both the scale and temperature differences between the initial and final temperatures get larger.

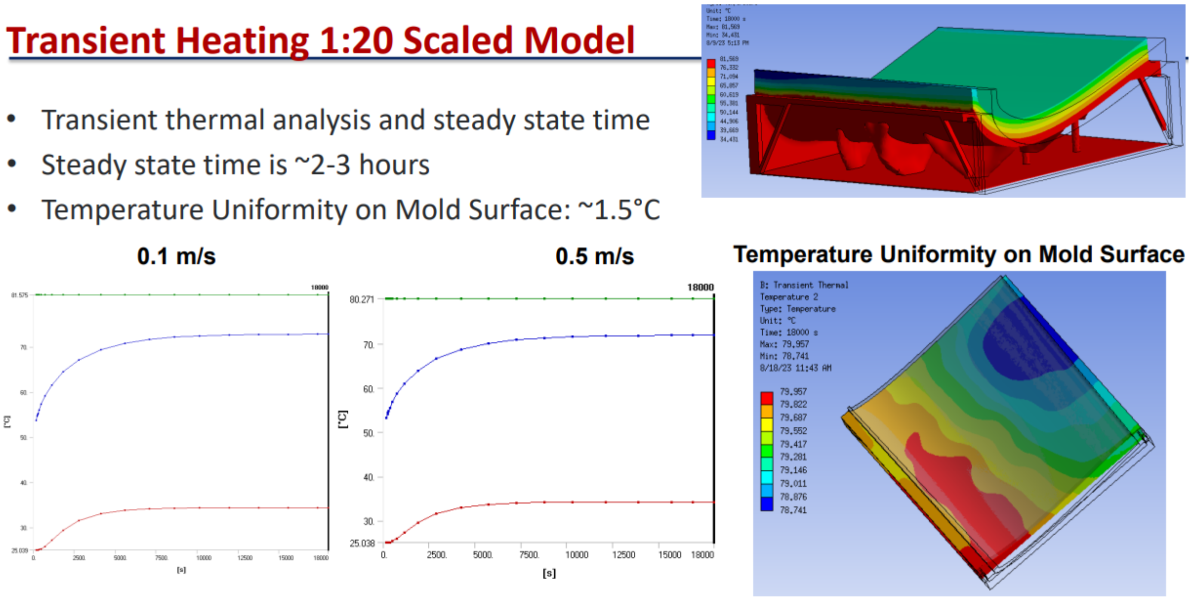

Transient Heating 1:20 Scaled Model

- Transient thermal analysis and steady state time
- Steady state time is ~2-3 hours
- Temperature Uniformity on Mold Surface: ~1.5°C

0.1 m/s

0.5 m/s

Temperature Uniformity on Mold Surface

B: Transient Thermal
Temperature 2
Type: Temperature
Unit: °C
Time: 18000 s
Max: 79.957
Min: 78.741
8/18/23 11:43 AM

Figure 2.4.10 Transient thermal results where the heated air velocity is 0.1 and 0.5 m/s

The thermal results from the CFD model were incorporated into a mechanical analysis to analyze how the temperature changes affects the structural integrity of the mold and predict thermal stresses, deformation, and fatigue life. The thermo-mechanical analysis for the validation of the 1:20 scale TO mold design indicates that the temperature distribution is more uniform with minimum variation. Figure 2.4.11 shows the ANSYS transient structural analysis (thermal expansion) deformation results driven by CTE. The Z-deformation shows a small deformation in the center of module with an absolute value of ~0.15 mm.

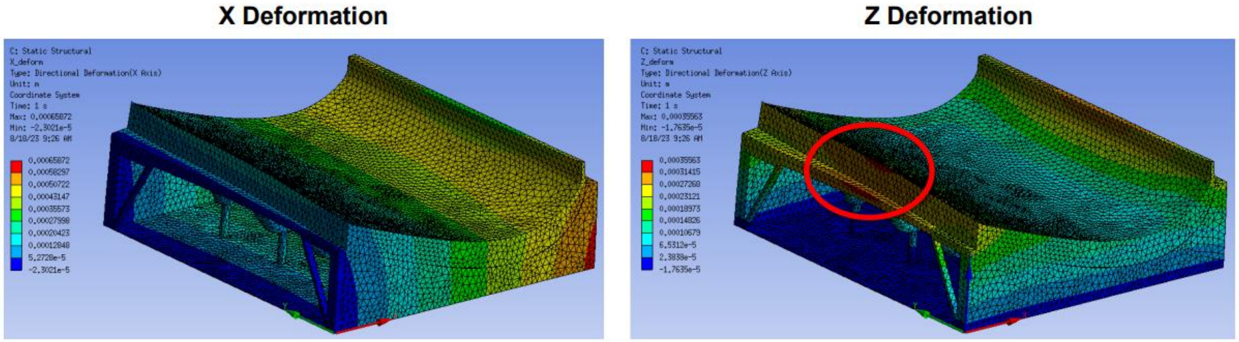

Figure 2.4.11 ANSYS Transient Structural Analysis (Thermal Expansion). The maximum Z deformation is 0.15 mm

Additional thermal sensitivity studies were conducted on the 1:20 scale mold. A simulation with a more realistic bottom insulation boundary condition predicted the airfoil profile surface temperature range to be 79.6 to 80.3C. Figure 2.4.12. As expected, overall cooler surfaces were observed because of the additional heat loss through bottom. With perfect insulation on the bottom, however, the predicted temperature range was 80.3 to 81.6C. In general, this relatively insignificant effect can be addressed by inlet temperature control. Inlet air temperature sensitivity was also studied to investigate the sensitivity of airfoil profile surface temperature variation. A +/-10% variation in the inlet temperature was simulated with an inlet velocity of 0.5 m/s. An 83C inlet temperature achieved 80C at the airfoil profile surface, while a 91 °C inlet temperature predicted 86C at this surface. The results indicate that the temperature sensitivity is roughly proportion to the inlet temperature.

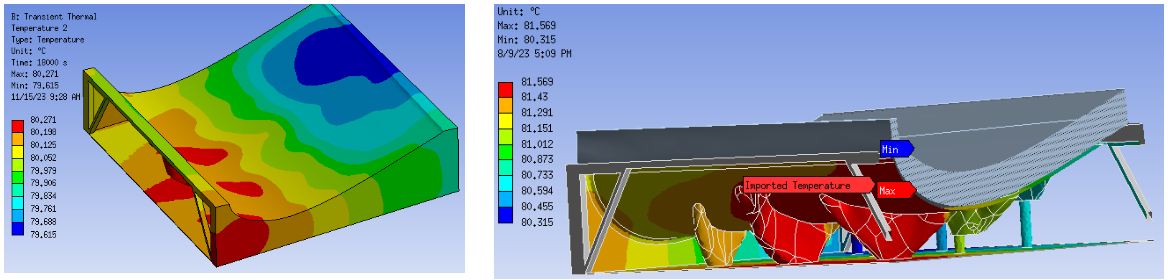

Figure 2.4.12 Transient thermal results where the heated air velocity is 1 m/s for bottom surface convection.

2.5. *Third prototype Version 2 modular mold design*

A third 1:20 scale mold module, denoted Module C, was designed to provide a full prototype assembly of the modular mold joints. A three-mold-module prototype assembly allows for a more accurate test of module joining and the potential mechanical and thermal distortion. The design team initiated the design for a Version 2 Module C module by selecting a mating geometry to Module A or B, Figure 2.5.1. The new module should capture the changing features of a "root-mid-tip" transitions of the conventional mold of a multi-module assembly. Additionally, the middle module should be subject to the more realistic boundary conditions of a mold-mold interface compared to a two-mold-module assembly where the modules are only in contact with a module on one side. The blade section for the third module was chosen from the same 120m blade that the previous two mold modules were designed. Module C was determined by extending the turbine blade profile from Module A toward the tip of the blade with the same length as Module A. By specifying the new mold module length the same length as an existing module, the support framework design of Module A can be reused with only minor modifications.

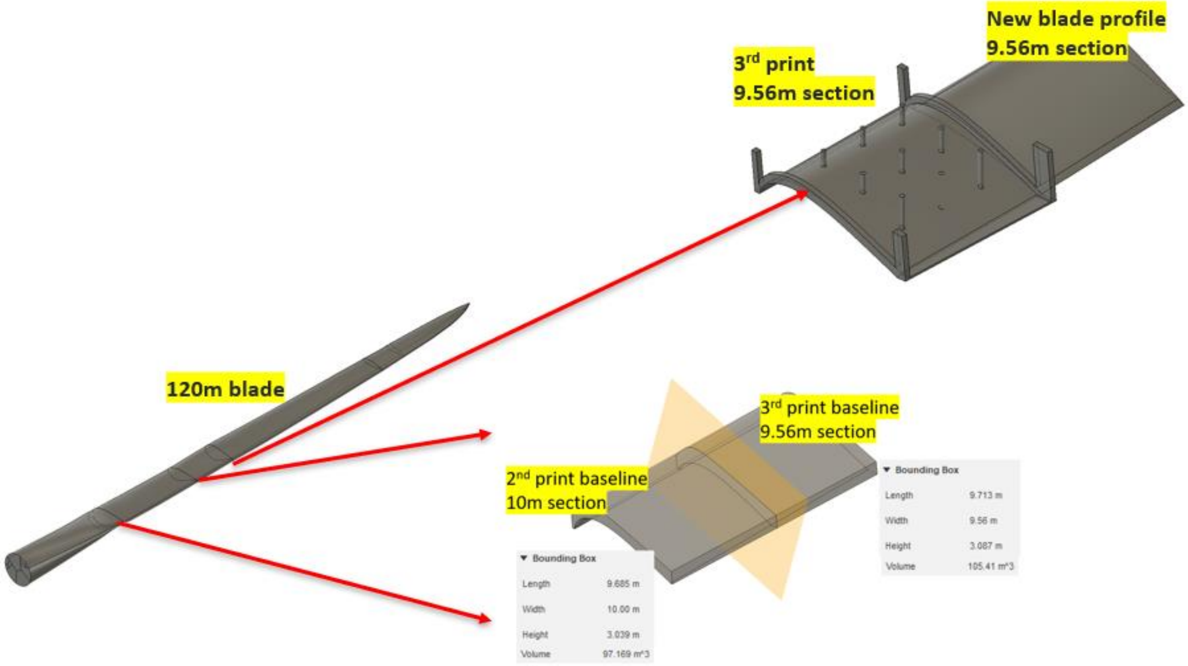

▼ Bounding Box	
Length	9.685 m
Width	10.00 m
Height	3.039 m
Volume	97.169 m^3

▼ Bounding Box	
Length	9.713 m
Width	9.56 m
Height	3.087 m
Volume	105.41 m^3

Figure 2.5.1 New blade section selection

Experience with the distortion of the 1:20 scale Version 2 Modules A and B during the printing process, see Section 4.4, gave an opportunity to further refine the mold design. A post-fabrication review by DM3D found a likely cause of distortion in these earlier modules was the thin mold shell became warped due to thermal stress from its support structures. To address this issue, DM3D proposed increasing the airfoil profile shell's overall thickness and lessening the curvature on the backside's leading edge. Importantly, these changes would not impact on the airfoil profile interface, a critical contour of the molded part. The mold design team worked closely with DM3D to ensure the Module C shell design was optimized for manufacturing before proceeding with topology optimization. The flowchart in Figure 2.5.2 illustrates this collaborative process, and the revised workflow marked a significant improvement over the earlier design process, where the design team independently determined the mold shell geometry and the manufacturing experts at DM3D received the geometry after topology optimization.

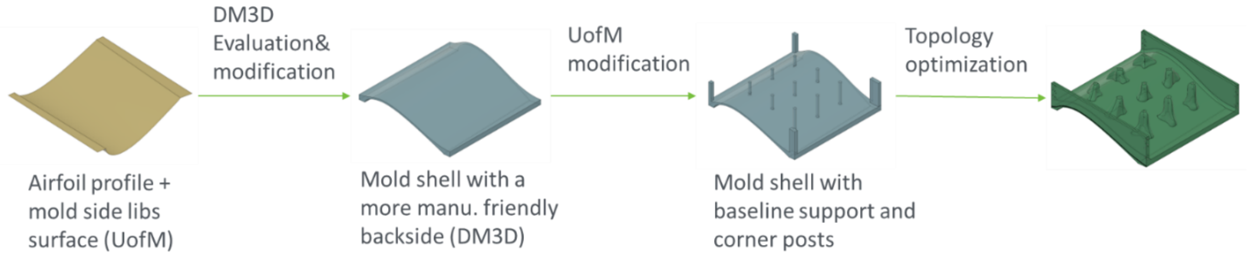

Figure 2.5.2 Design for manufacturability workflow for 1:20 scale Version 2 Module C

2.6. Version 2 modular mold design evolution summary

The differences between the Version 2 module prototype designs and their assembly will be reviewed here to add context to their design evolution. The original 1:20 scale prototype was based on a full-size, 19.56m, section common across the 120, 140, and 150m blade family. The section was cut into two to satisfy the 3D-print envelope constraint during fabrication while maintaining a passive domain at the blade interface that would preserve the airfoil profile. During topological optimization, pillar features were allowed to form providing a continuous connection between the airfoil structure and the support frame. An additional module was added to these original two modules to provide the three modular mold assembly.

The original two modules had thermal distortion during fabrication, so an iterative pre-topology-optimization review was conducted with DM3D to enhance manufacturability, Figure 2.5.2. This resulted in the third module prototype having a thicker mold shell with a smoother backside to reduce potential thermal concentrations. The backside supports whose interface was leveled to the same plane were also added to reduce part count and improve assembly. A comparison of the design features of Modules A through C is given in Figure 2.5.1.

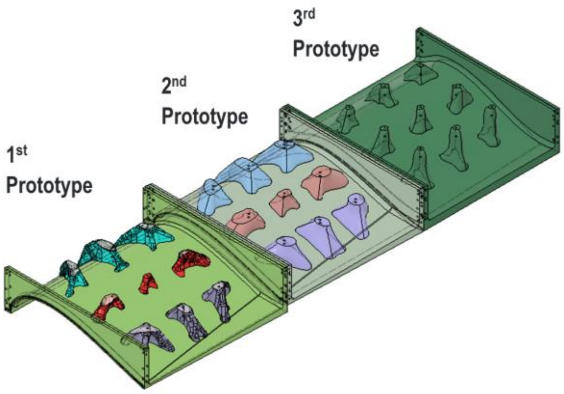

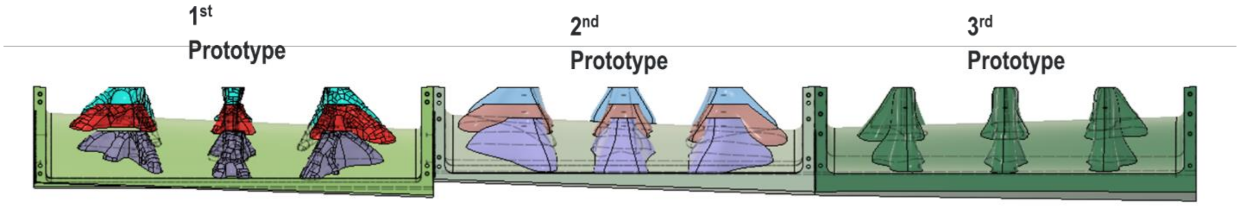

Figure 2.5.1 Mold Iteration Comparison

2.6.1. Lessons learned from Version 2 mold design and analysis

Table 2.6.1 summarizes the performance accomplishments simulated and measured for the Version 2 mold design.

Table 2.6.1 Summary of design performance accomplishments

Goal	***Performance Characteristic***	***Target***	***Performance Achieved***	***Comments***
MRL 4	*Aerodynamic Power Coefficient*	>90%	C_{pmax}=95% on 120m and 150 m & C_{pmax}=98% on 140m	Qblade analysis model
	Max Surface Distortion	<1% of chord (0.08 m)	v.1 0.0042m v.2 0.01m	FEM (Ansys) Transient Structural v.1 conformal channel design v.2 reduced mass
	Surface Temperature Uniformity	< ±5ºC, at 70±5ºC and 15 mbar ambient	±3.66°C (est. 72°C – 82°C ambient air)	v.1 FEM (Ansys) fine mesh
Stretch	*Surface Temperature Uniformity*	±3ºC at 40ºC	±0.2°C	FEA of Topology Optimized Structure (v.1) at steady state
	Max Surface Distortion	<±0.025 inch (±63.5 μm)	mean error ±20 μm	measured on 1:100 scale prototype (laser scanner)
	Vacuum Integrity	10 mbar over 60 minutes	Held <10 mbar loss over 30 minutes	dual o-ring sealing method

2.7. Mold fixtures and ancillary support equipment design and specification

A consultation with the experts at TPI revealed that the steel frames that support the current glass fiber molds are inexpensive and relatively easily assembled on site. Saving materials for the frames, therefore, were unlikely to contribute to the overall cost of mold transportation. Since the Version 2 mold design has a curved bottom surface much like the current glass fiber molds, a frame design similar to the current glass fiber mold was designed, as illustrated in Figure 2.5.1. A sheet steel plenum is bolted on the bottom of the printed part of the molds and attached to the ribs. Each mold module has an independent frame structure that supports it. Adjusting mechanisms, similar to those used in the current mold frames, are implemented between the molds and the frame, and between the frames for adjacent mold modules.

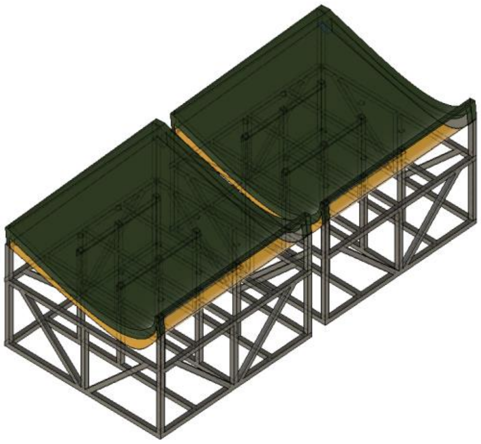

Figure 2.5.1 Mold frame design concept

Alignment mechanisms, inspired by the current mold alignment mechanisms are shown in Figure 2.5.2, and were designed for the Version 2 mold. Each corner of the mold module has a jack screw to provide fine-tune adjustment of the position of the mold chord-wise. In addition, there are nine jack screws located at the bottom of the mold-frame structure for height-wise alignment. Moreover, each mold-to-mold interface is provided with pads that include holes for mold-to-mold joining.

The support framework was specified to use structural grade carbon steel tubes. Specifically, square tubes are used at ground level and the sides. There are also round vertical support tubes at the middle of the support structure. The round support tube’s circular cross-sectional provides uniform resistance against shear load in any direction during mold alignment. While commonality in design was strived for, each mold has a similar but different geometry due to differences in size, twist, and offset of the turbine blade, and therefore the specific details for each mold support structure may be unique.

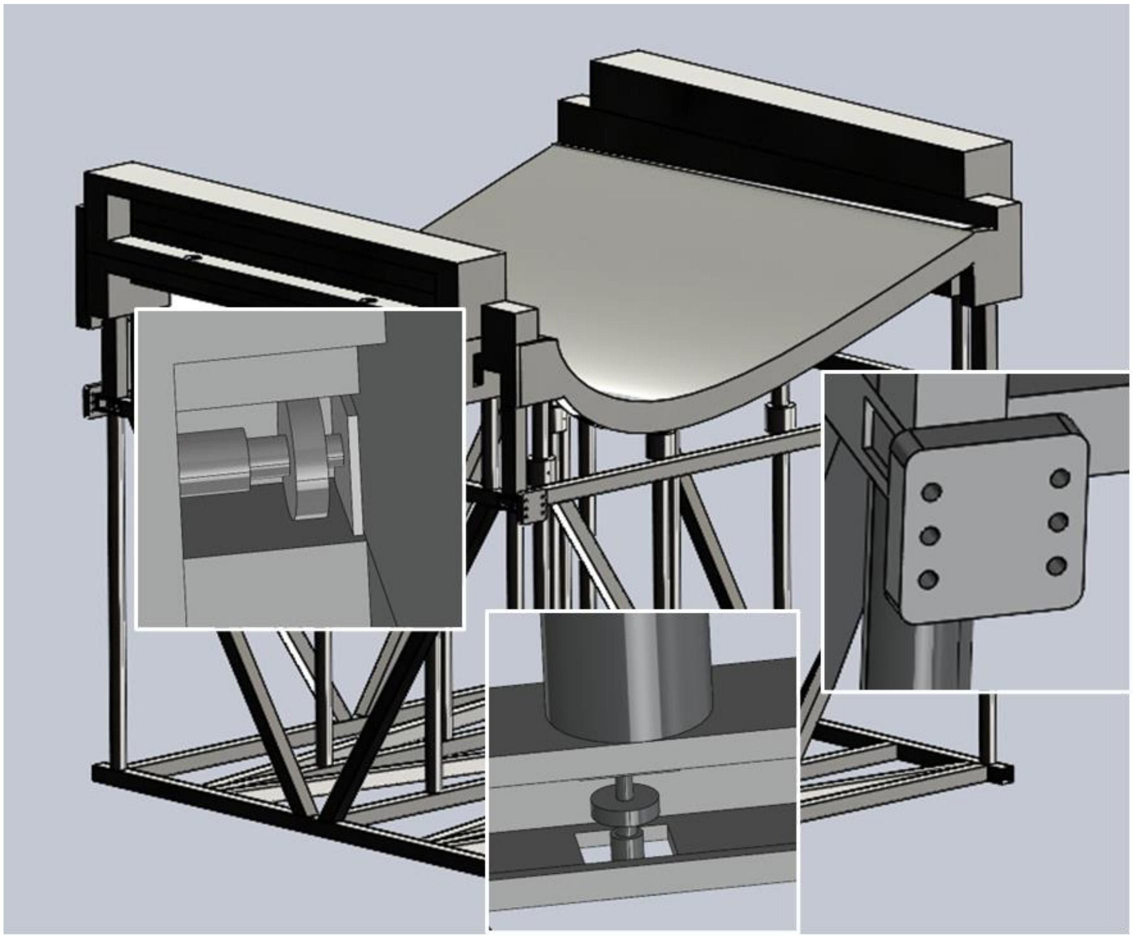

Figure 2.5.2 Mold support framework design (sheet metal hidden). Detail view from left to right: side jack screw for chord-wise alignment, bottom jack screw for height-wise alignment, and load pad with holes for mold-mold joining

Figure 2.5.3 illustrates the mold auxiliary systems that connect to the mold at the heated air inlet and outlets. An inlet air plenum box connects the mold to the heater/blower for hot air entrance, and a similar box is attached to the exit. Threaded holes are also provided for temporary eyebolts for mold lifting. An FEA simulation shown in Figure 2.5.4 models the mold deformation during lifting. Maximum deformation on the mold is 4.86 mm, which satisfies the < 1% of chord (100 mm considering 10m mold) specification. However, local stress concentrates near the mold-eyebolt connection points exceeds the yield stress of Aluminum 6061, leading to potential plastic deformation. Therefore, stress concentration mitigation methods such as relief notches and grooves may be required in the finalized mold design.

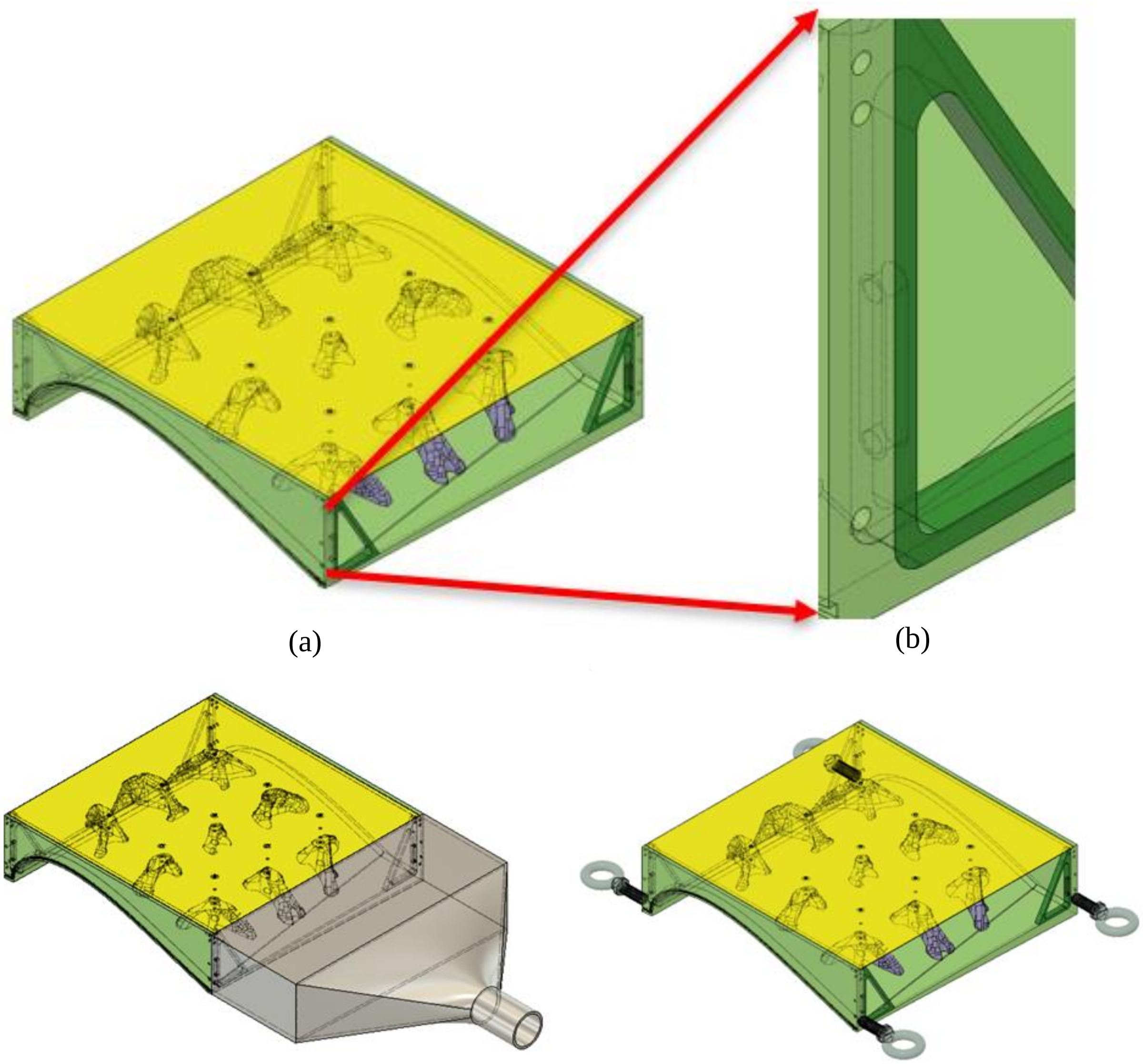

(a) (b)

(c) (d)

Figure 2.5.3 Mold auxiliary system design (1:20 Mold A is shown): (a) 1:20 mold A with (b) detailed view on threaded holes located at inlet/outlet surfaces, (c) register box connecting mold to heater/blower, and (d) lifting eyebolt for mold lifting (not to scale).

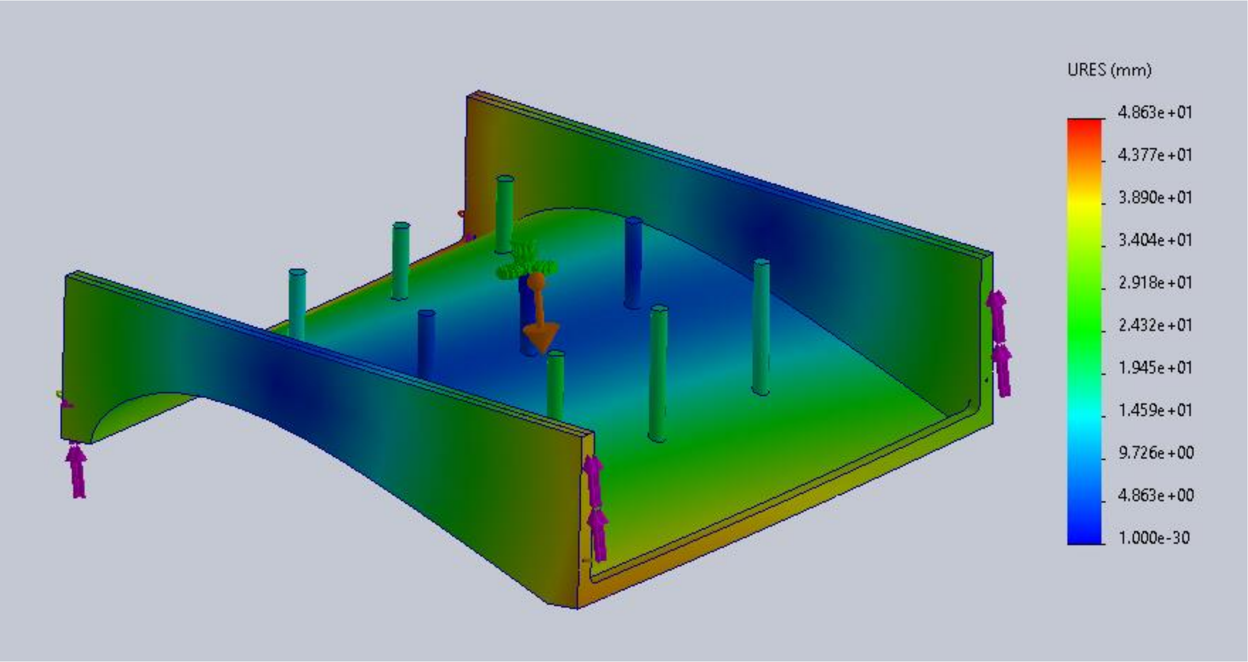

Figure 2.5.4 Structural FEA simulation for mold lifting with eyebolts: the mold is subject to self-weight (brown downward arrow). The lifting eyebolts at four corners have distributed lifting force (purple upward arrows) equal to the weight of the mold.

A refined support structure design, Figure 2.5.5, illustrates two adjacent full scale mold modules resting on their support framework. To determine the mold airfoil profile surface distortion of the assembly, a FEA simulation with gravity was conducted on the assembly, including an exaggerated (10x) blade weight. The FEA results are shown in Figure 2.5.6. The maximum distortion observed at the critical airfoil profile surface was 5mm, well within the specification limit of 100mm. The maximum von-mises stress was observed to be 148 MPa, also less than the yield stress of Aluminum 6061, 276 MPa, yielding a safety factor of 1.86. This simulation result validates the support framework design at full scale.

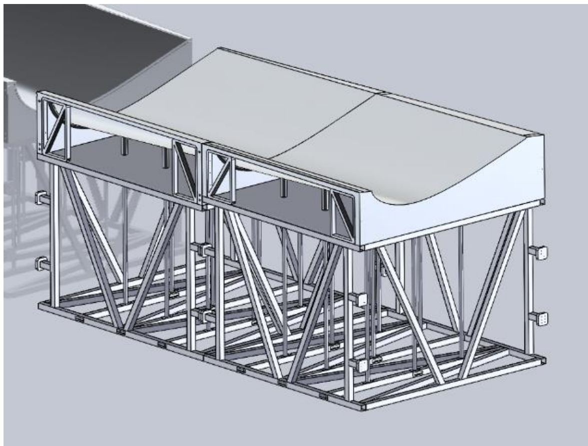

Figure 2.5.5 Assembly of adjacent mold modules on their support frames

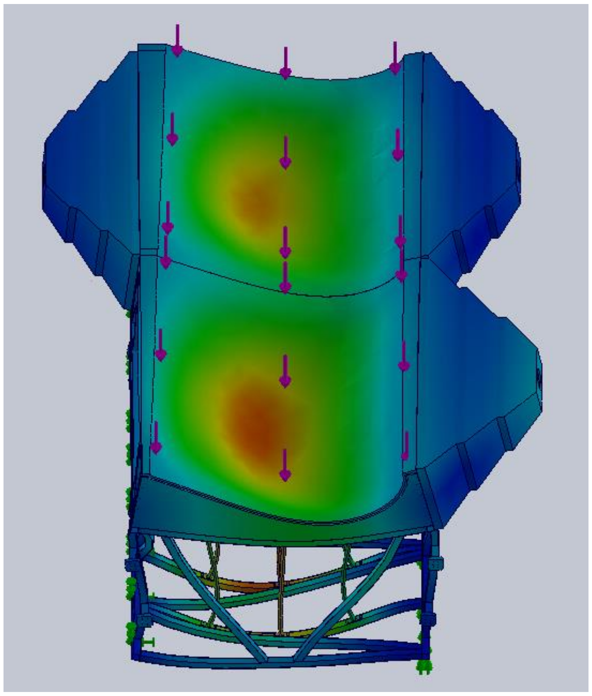

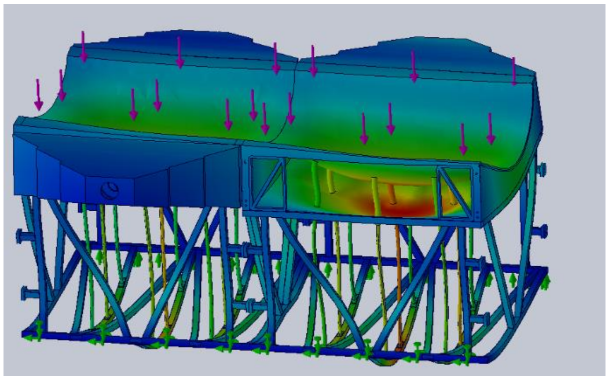

(b) distortion inside mold module

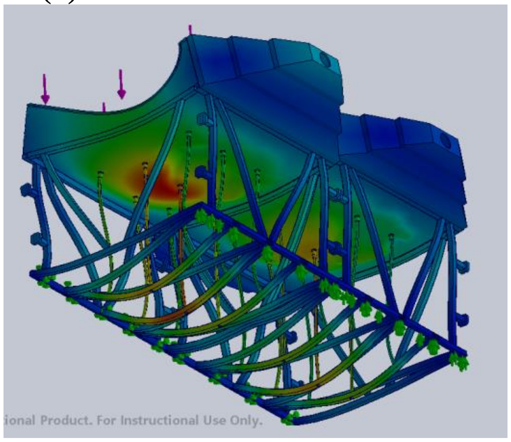

(a) distortion at airfoil profile

(c) maximum distortion at sheet metal for mold-frame connection

Figure 2.5.6 Structural FEA simulation modeling blade manufacturing scenario at full scale (distortion has been exaggerated for illustration).

For the 1:20 scale prototype hot air tests, commercially available heater/blower with built in temperature and air flow controls were procured, as were corner brackets, sheet metal fabrications, and spacers. To ensure that the experimental setup for the prototype would be consistent with the assumptions made during the performance analysis, a baffle plate was designed upstream of the mold inlet to ensure flow uniformity was consistent with the original flow and thermal analysis. Second, a CFD on the mold Module B design was undertaken to provide pretest predictions for the prototype testing.

Given the inlet flow to the mold module was provided by a hot air blower with a 62 mm diameter nozzle, a baffle plate that provided a dynamic pressure head of 10X that at the hot air blower nozzle was designed. At the maximum hot air blower flowrate, the dynamic head at the blower inlet was calculated to be 14 Pa. As such, the baffle plate was designed for a target head loss of 140 Pa, which established a design with 5 mm holes spaced 20 mm apart, as shown in Figure 2.5.7. In the simulation, the blower nozzle was placed 12” upstream of the mold, with the baffle plate 6” downstream of the blower. A CFD simulation, confirmed by hand calculations, showed a pressure drop of 140 Pa across the plate and yielding a mass-weighted uniformity index of 0.91 at the mold inlet. In these simulations the mold itself was not modeled. Instead, a fluid domain downstream of the mold inlet was modeled as a porous media to provide the appropriate back pressure.

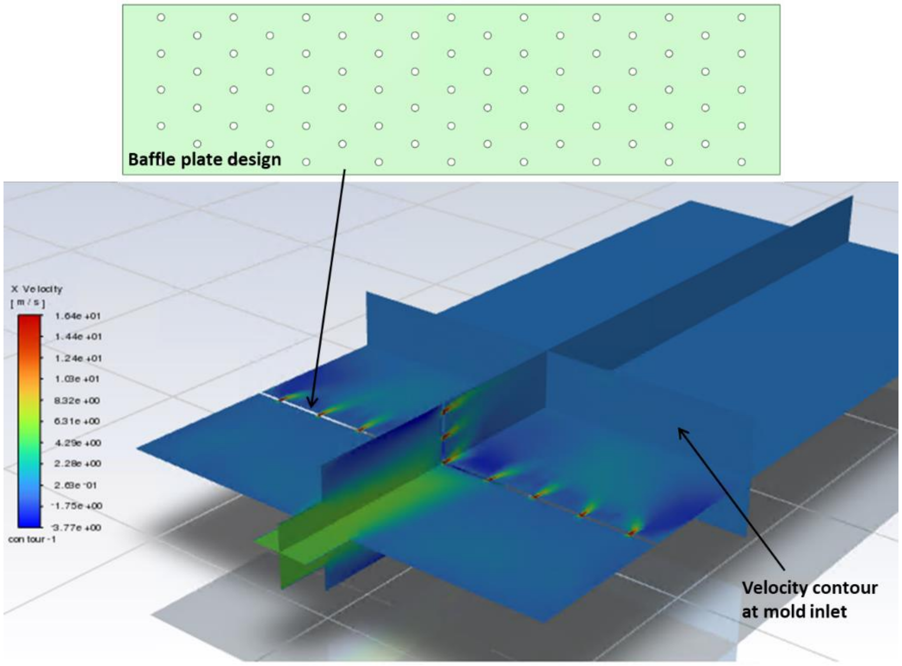

Figure 2.5.7 Baffle plate design showing 5 mm holes spaced 20 mm apart. Velocity contours show adequate flow uniformity at the inlet to the mold.

A CFD analysis of mold Module B and with the baffle plate upstream of the mold was then run with an inlet velocity of 1 m/s and the inlet temperature of 83C, as in previous validation runs. The baffle plate still provided decent flow uniformity to the mold, with a mass-weight uniformity index at the entrance to the mold of 0.89. A contour of the air velocity through the mold is shown in Figure 2.5.8 with a temperature contour of a slice taken from the centerline of the module shown in Figure 2.5.9. As in previous CFD simulations, an insulating layer was modeled on the top of the mold as shown. The temperature at the blade/mold interface was observed to be 79C, while the outer, exposed surface was observed to be 38C.

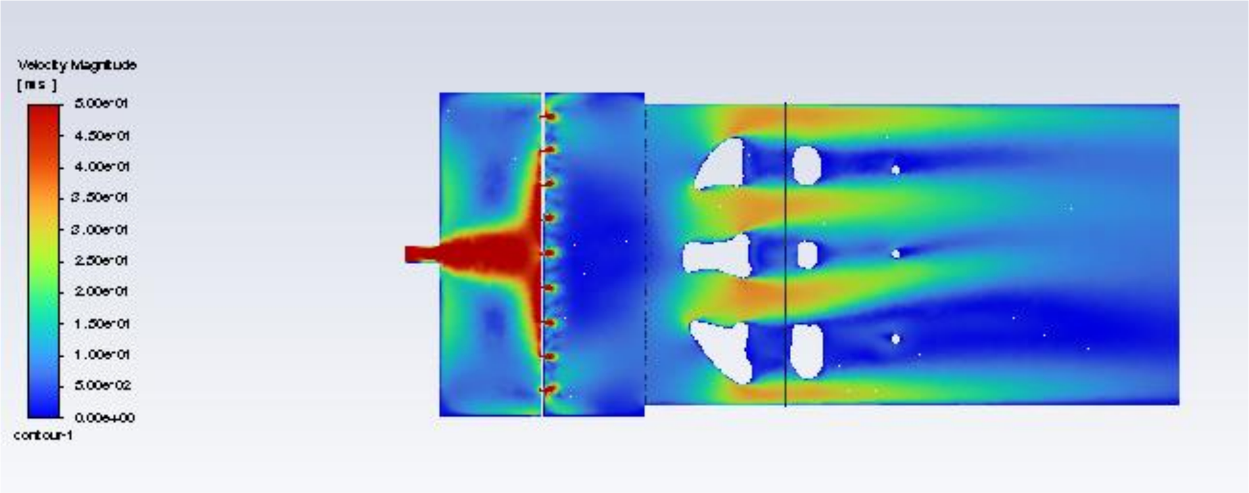

Figure 2.5.8 Air velocity contour through the mold

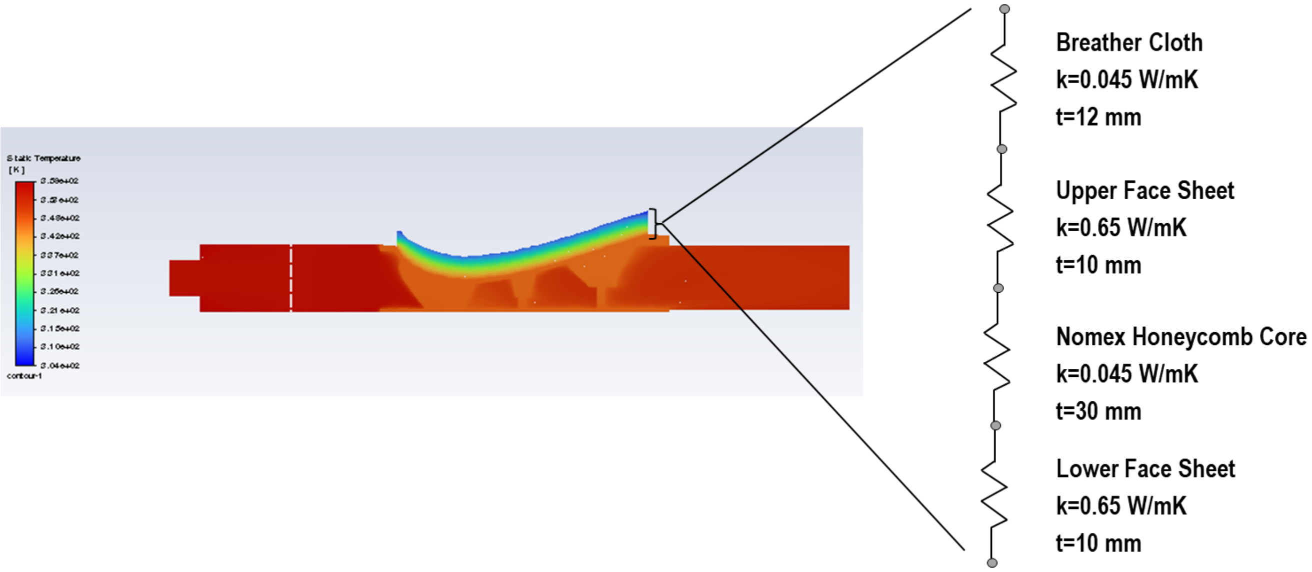

Figure 2.5.9 Temperature contour of the centerline section through the mold.

2.7.1. Lessons learned from the support structure design and analysis

3. Direct Material Deposition Material Characterization, Process Design, and Analysis

Material coupon samples were printed in the laboratory to characterize the physical and chemical composition of the direct material deposition (DMD) process. The objective was to understand the microstructural features that impact process optimization. Protocols for treating the surface of the mirror polished sample with Keller's Reagent, an acid, and a modified Weck's Reagent were developed to preferentially remove material from the grain boundaries and highlight microstructural features such as precipitates and porosity. Optical microscopy of the sample after this treatment, Figure 3.1(a) and (b), allows quick assessment of macroscopic features such as keyhole porosity, sample geometry, cracking, etc. SEM imaging, Figure 3.1(c), is used to view the grain structure, precipitate morphology and distribution, and extent of fusion/gas porosity highlighted by the etching. EDS is also used to view micro-segregation between grains and determine precipitate compositions.

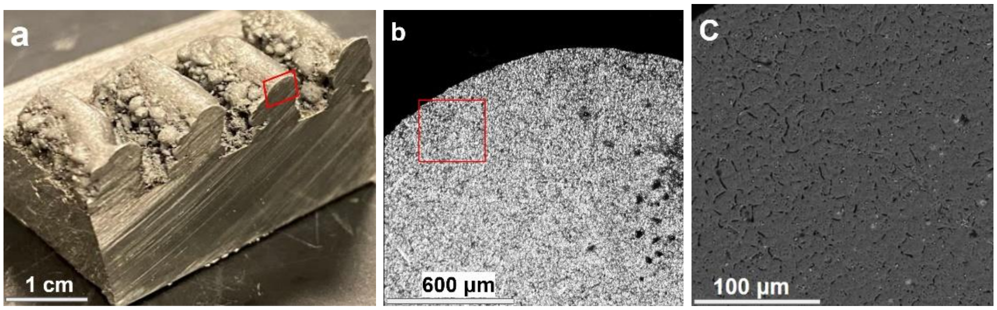

Figure 3.1 A single deposition line's (a) optical microscopy (b) and SEM (c) after deep etching with Keller's Reagent.

3.1. Evaluation of deposition line on test coupons

Solid samples printed with overlapping deposited lines were fabricated for density evaluation. Single and dual layer samples were machined into cuboids by using a 3-axis CNC milling machine to face and remove them from the baseplate, Figure 3.1.1. The density of the cuboids was measured using Archimedes' method, a nondestructive test for determining porosity in bulk solid materials. A study of the deposition trends in cross section geometry based on laser spot diameter was undertaken, Figure 3.1.2. Additionally, the chemical composition of the deposited material was analyzed, Figure 3.1.3. Analysis of single-track 3D prints finds a larger beam diameter will allow larger deposition area with no observed increase in porosity resulting in wider line spacing and a faster print. A one mm laser spot at a slower feed rate results in irregular cross section transverse to the single-track deposition. Microscopic imaging of a cross-section of a single-track identifies the dominant material reinforcing phase as Al_3Ti. Clusters of TiB_2 are present but not as homogenously distributed. The individual phase morphology is expected to change between single-track and bulk prints.

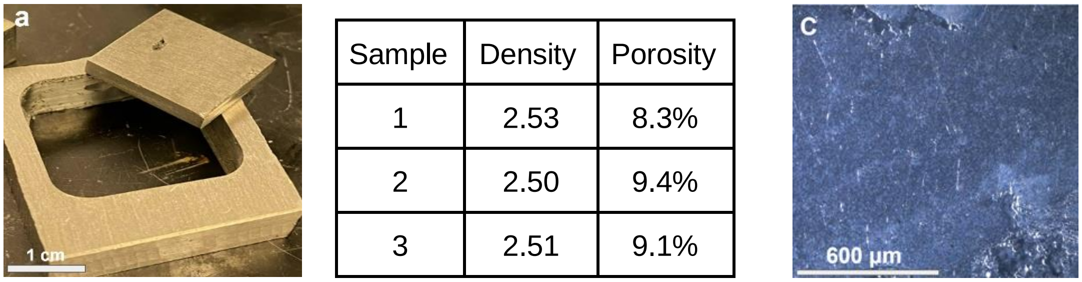

Sample	Density	Porosity
1	2.53	8.3%
2	2.50	9.4%
3	2.51	9.1%

Figure 3.1.1 Solid samples milled into cuboids from the baseplate (a) are used to estimate bulk density and porosity via Archimede’s method (b) and calculate porosity and examine microstructural features on a cross section via optical microscopy (c).

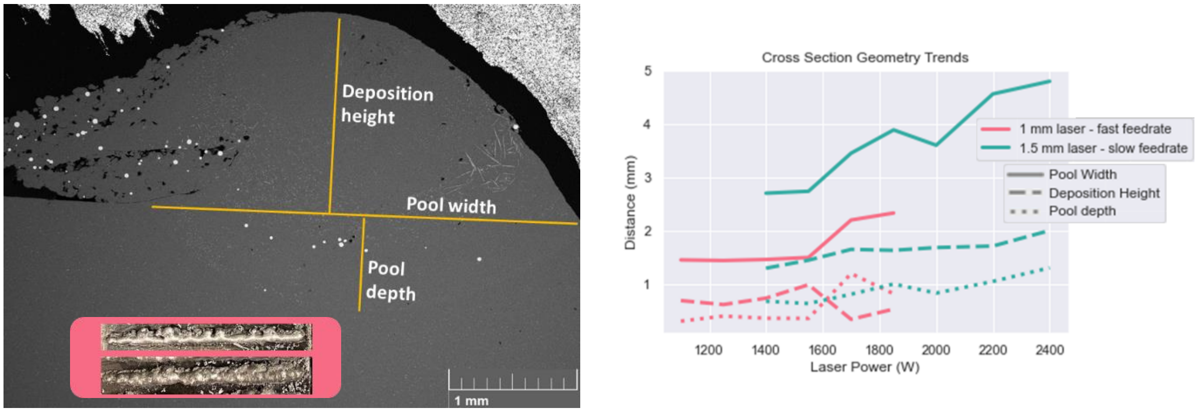

Figure 3.1.2 Analysis of single tracks shows that using a larger beam diameter allows for larger deposition areas with no observed increase in porosity. A one mm laser at a slow feed rate resulted in an irregular cross section.

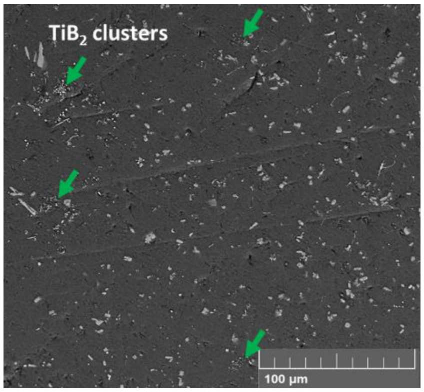

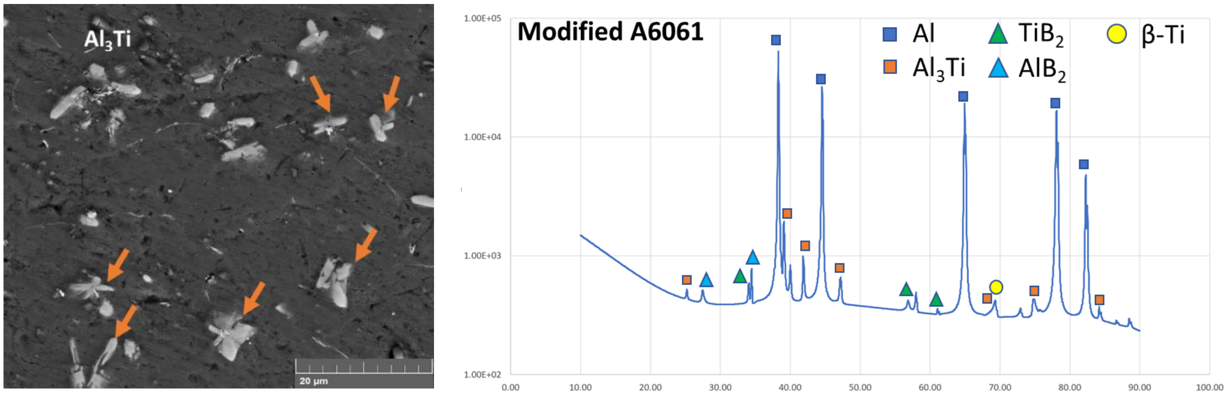

Chemical components identified in printed material.

Figure 3.1.3 Microscopic imaging identifies the dominant reinforcing phase as Al_3Ti with clusters of TiB_2 present but not as homogenously distributed.

3.2. Investigation of defect-free process parameters

The RTRC team modified their proprietary physics-based additive manufacturing (AM) process simulation code for aluminum alloy to help define defect free process parameters for additively manufactured modular molds. The model has been shown in the past to be capable of accurately predicting flaw type, density, and location in 3D printed structures as a function of operational conditions. These models are used to inform experiments to bolster understanding of flaw generation. The models were validated and modified using a design of experiment to calibrate the code with the mold's aluminum alloy. Calculation of the process map for single and multi-hatch, multi-stripes, and multi-layers depends on the prediction of thermal history that is calculated analytically and numerically without the need for external input from sensors or FE analysis. The code also calculates average fluctuations for local defects. In addition, the code calculates the process and 3D defect maps from first principles, no empirical calibration needed. The prediction of the 3D defects map is very fast. The bench marking of the tool is based on empirical correlations between defects and thermal history. Multiple operational conditions are always modeled for process optimization.

Input data was defined for the DED process. The different process parameters range are classified based on their tendency to create a specific type of defects based on defect generation mechanisms. The defect free zone are defined in each case as a function of laser parameters (power, speed, and powder deposition rate). It should be noted that the layer thickness, scanning strategy and supporting structures also influence the as-deposited phase and grain size/lath spacing and the pore content. The expected output results will be based on the following input process parameters:

1. Single track map, which serves as a launch point to develop parameter space for multi-pass and multi-layer builds. In addition to being used as agnostic-to-scan strategy, can readily produce single tracks maps for other laser configurations.
2. For a single strip, this serves as a launch point to develop parameter space for 3D builds.
3. For a cylinder (3D part).

Figures 3.2.1 and 3.2.2 summarize example results for a 3D print that can be obtained with different deposition conditions. The results indicate that the first set of power and speed were on the border between the defect free zone and the keyhole porosity. Figure 3.2.1 shows the existence of keyhole porosity is possible in addition to high surface roughness. Figure 3.2.2 shows the second process conditions were within the defect free zone and no defects were predicted. The modified model is used to define the defect free parameters and to set a detailed design of experiment to validate the results.

Metal 3D printing powders were evaluated for their suitability as a feedstock material. The size distribution, powder shape, and chemical composition were evaluated for a 6061 powder, a 7075 Al alloy supplied by Valimet, and a 6061 crack-prevention formula supplied by Elementum3d. The 6061 powder was unacceptable as its size distribution was not uniform with smaller particles stuck to bigger ones (called satellites) and was observed to include faceted rather than spherical particles. The Valimet powder size was normally distributed but would require sieving to get rid of particles below 20 microns. It also had substantially high satellite formation and was not spherical. The best power was determined to be Elementrum3d whose powder size distribution was normal, its size distribution was desirable, and its shape was visibly more spherical.

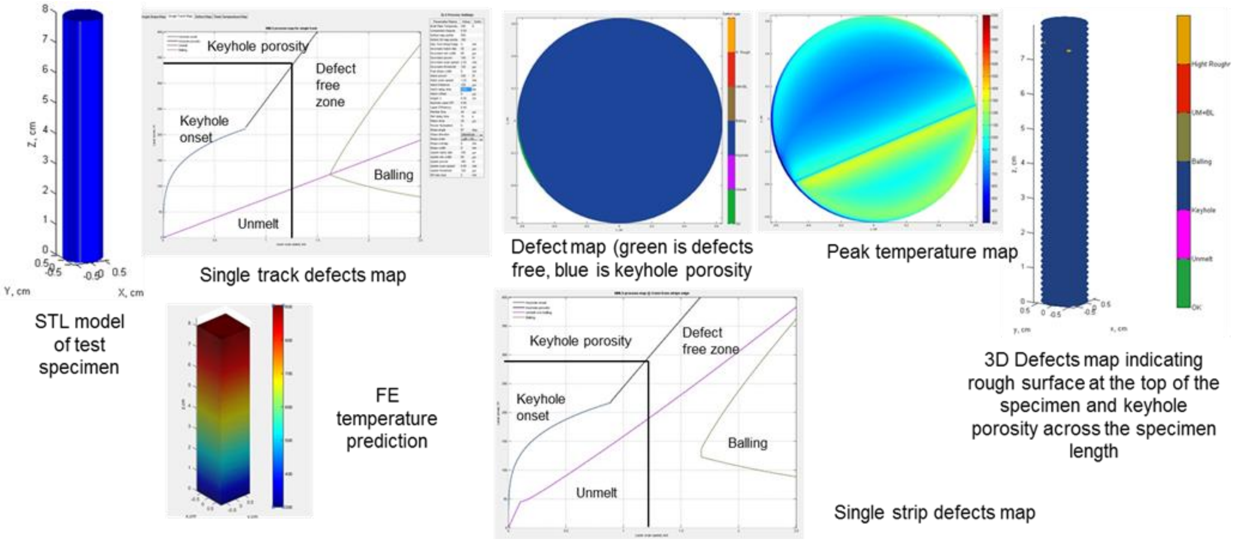

Figure 3.2.1 Process map indicates that the selected process parameters are on the border of keyhole porosity. The 3D analysis was run for depositing a test sample (1cm x 8 cm)

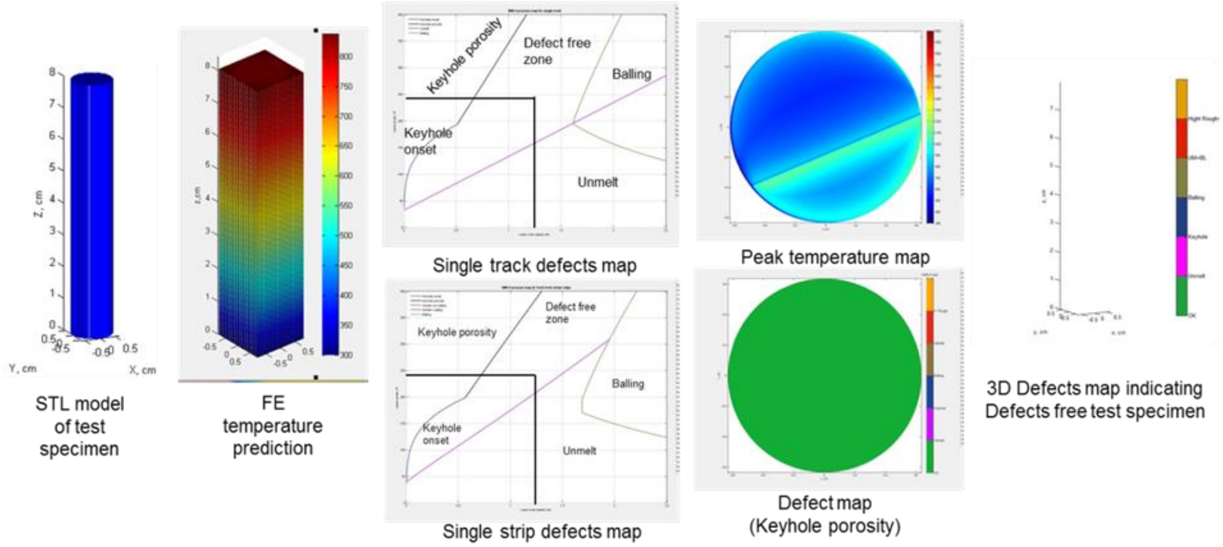

STL model of test specimen

FE temperature prediction

Single track defects map

Single strip defects map

Peak temperature map

Defect map (Keyhole porosity)

3D Defects map indicating Defects free test specimen

Figure 3.2.2 Process map indicates that the selected process parameters are within the defect free zone. The 3D analysis was run for depositing a test sample (1cm diameter x 8 cm height)

The AM melt characteristics the in-house 6061Al alloy powder on a 7075 baseplate and the Elementum3d 6061 powder on a 5052 baseplate were studied for the blade mold. For compatibility between University of Michigan (UofM) laboratory and DM3D, the 6061 alloy was the focus of study of the build material. The 7075 and 5052 Al plates were identified as the best target baseplates, as baseplate should mate well with the build material. Characterization of the materials from printing experiments will inform the finalized build material.

Experiments were conducted in the UofM laboratory using similar process settings to the DM3D process, with a beam diameter of 2±0.5mm. Experiments with printed coupons using various printing parameters in a design of experiment identified the most important parameters are laser power, beam diameter, traverse speed, powdered metal deposition rate, shield gas type and flow rate, and base plate initial temperature. The evaluation criteria was continuity of deposition and deposited metal density, porosity, micro cracking, and layer delamination. It was found on the 6061 in-house alloy on 7075 baseplate some of the high-power experiments returned better layer height, but with undesirable bead shapes. Power levels between 2000-2500W result in better-looking depositions. Conclusions for the 6061 Elementum3D custom alloy depositions on 7075 baseplate generally provided satisfactory deposition at mid power ranges (1400-1800W) with uniform layer height satisfactory continuity.

3.3. Prediction of laser powder directed energy deposition (DED) process map

The following utilizes proprietary RTRC defect code to predict the process map, defect free zone and surface finish to define the defect free process parameters for additively manufacturing the modular molds. An Additive Manufacturing Modeling Framework at RTRC, presented in Figure 3.3.1, illustrates the integrated physics-based simulation of AM processes to predict part level distortion, defects, microstructure and establish correlation to performance. This is used to reduce AM process development time and cost.

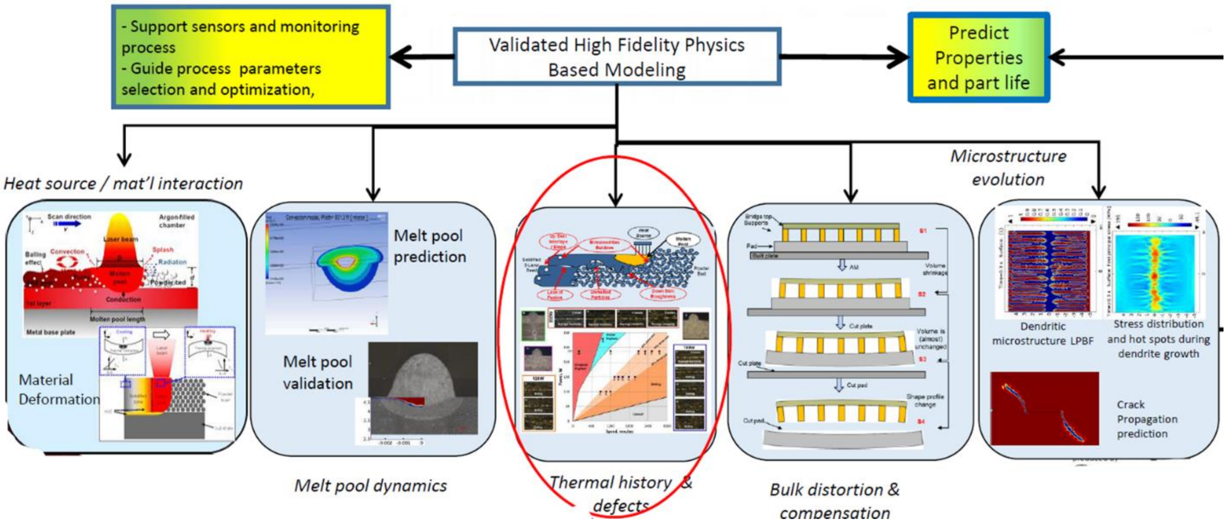

Figure 3.3.1 Additive Manufacturing Modeling Framework Developed at RTRC

The physics-based AM process simulations that have been shown capable to accurately predict flaw type, density, and location in 3D as a function of operational conditions and material thermal properties has been modified to predict process map for L-DED AM process. The thermal history of DED processes controls both the macrostructure, microstructure and defects generated based on the following as illustrated in Figure 3.3.2:

1. Type of DED technology (feedstock and heat source);
2. Build environment (vacuum, inert gas, or ambient);
3. beam-material interactions (rapid and repeated heating–cooling cycles during a layer-by layer deposition that create unique microstructural features, non-equilibrium phases, solidification cracking, directional solidification, residual stresses, porosity, delamination, and warpage. Anisotropy in mechanical properties and heterogeneous microstructures due to the deposition's directional nature);
4. deposition parameters (mainly, laser powder, laser scan speed, hatch spacing, powder feed rate, laser scan strategy);
5. feedstock attributes.

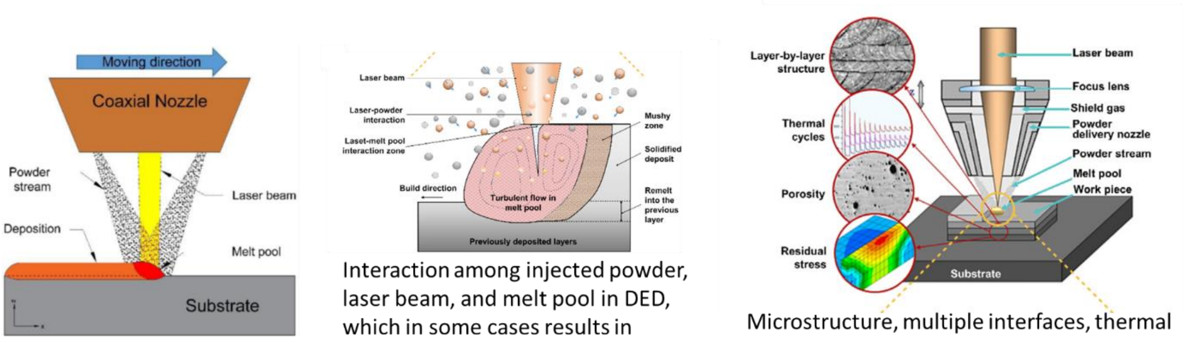

Schematic of DED's

Interaction among injected powder, laser beam, and melt pool in DED, which in some cases results in keyhole formation in the melt pool

Microstructure, multiple interfaces, thermal cycling, defects, and residual stre[1]

Figure 3.3.2 Laser Powder Directed Energy Deposition (DED) System and corresponding defects physics[3]

During DED, defects can occur impacting the quality and integrity of built components. Some of the main defects generated during DED deposition and their analytical modeling framework are shown in Figure 3.3.3. Defects include:

1. **Porosity**: Porosity refers to the presence of voids or gas pockets within the deposited material. It can weaken the structural integrity of the part and reduce its mechanical properties. Porosity can occur due to entrapped gases in the powder feedstock, incomplete fusion, or inadequate shielding gas coverage.
2. **Lack of Fusion**: This defect occurs when the deposited material does not fully fuse with the underlying layers or substrate. It can result from insufficient energy input, improper process parameters, or inadequate material flow.
3. **Cracking**: Cracking can manifest as hot cracks or cold cracks. Hot cracks occur during solidification due to high temperature gradients and thermal stresses, while cold cracks can develop after deposition as the material cools and contracts. Both types of cracks can compromise part integrity.
4. **Inclusions**: Inclusions are foreign particles or contaminants that become trapped in the deposited material. These can originate from impurities in the feedstock powder, contamination of the deposition environment, or other sources. Inclusions can weaken the material and reduce its quality.
5. **Melt Pool Instabilities**: Unstable weld pool behavior can lead to irregular deposition patterns, which may result in uneven layer thickness and surface irregularities. This can occur if the energy source is not properly controlled or if there are fluctuations in process parameters.
6. **Oxidation**: Oxidation happens when the deposited material reacts with oxygen in the atmosphere, leading to the formation of oxides on the surface. Oxidation can weaken the

---

[3] B. Zheng et al., Mater. Sci. Eng., A 764 (2019) 138243, https://doi.org/10.1016/j.msea.2019.138243.

material and negatively impact its properties. Maintaining a controlled atmosphere or using inert shielding gases can mitigate this issue.

7. **Overheating**: Overheating can cause excessive heat input, leading to distortion, warping, and material degradation. It can occur if the process parameters, such as laser power or travel speed, are not properly set.
8. **Geometry Deviations**: DED can create geometric inaccuracies if the deposition path deviates from the intended design due to issues with the control system or other factors.

To minimize these defects in DED processes, it's essential to carefully control and optimize process parameters, ensure proper material quality, maintain a controlled environment, and regularly inspect and monitor the deposition process to detect and address defects promptly. The DED defects analytical modeling framework is presented in Figure 3.3.3.

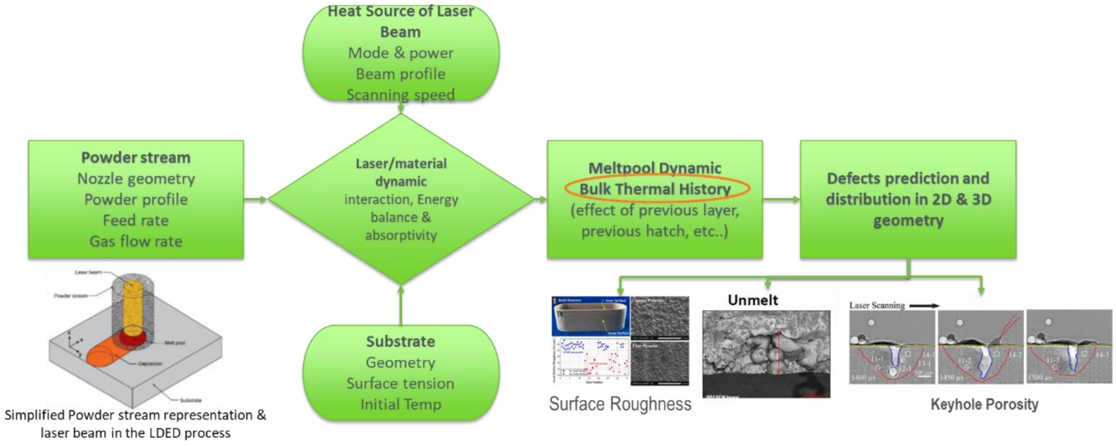

Process Physics to be simulated and corresponding process variables for LDED to be used to modify RTRC models

Figure 3.3.3 DED Defects Analytical Modeling Framework (Fast Acting Matlab Base)

The modification of the analytical code is mainly related to thermal history equations, the boundary conditions of the models and the process parameters range. These modifications will be used to inform experiments to bolster understanding of flaw generation. Analytical modeling of thermal history in L-DED process is based on powder material transportation, powder catchment, energy transfer, laser-material interactions, and thermomechanical behavior of the part. In addition, mechanical and thermal properties of metal powder materials should be function of temperature. The transient temperature field solution at the point of interest $X = (x, y, z)$ of a moving 2D Gaussian laser heat source with a powder feeding rate $\dot{m}$ in the L-DED process is given by Equation 3.3.1:

$$T(X,t) = \frac{2}{\rho_p C_p \pi \sqrt{\pi \alpha_p}} \int_{\tau=0}^{\tau=t} d\tau \left\{ \frac{\frac{\beta_W P_L}{\sqrt{(t-\tau)}}}{R_L^2 + 8\alpha_p(t-\tau)} exp\left[-\frac{2[(x-v\tau)^2+y^2]}{R_L^2+8\alpha_p(t-\tau)} - \frac{z^2}{4\alpha_p(t-\tau)} \right] + \frac{C_p \dot{m}\,(T_0 - T_m)/\sqrt{(t-\tau)}}{r_{avg}^2 + 8\alpha_p(t-\tau)}\ exp\left[-\frac{2\left[[\frac{(x-v\tau)}{sin\varphi}]^2+y^2\right]}{r_{avg}^2+8\alpha_p(t-\tau)} - \frac{z^2}{4\alpha_p(t-\tau)} \right] \right\} + T_0 \tag{3.3.1}$$

where ρ_P is the density, c_p the specific heat, α_P the thermal diffusivity, β_w the dynamic process laser absorptivity (which is function of the absorptivity of the powder material for a flat surface, a_w the Brewster coefficient, h the deposit height and D_L is the laser beam diameter), φ the nozzle angle, r_{avg} the average powder stream radius, T_0 the ambient temperature and eventually T_m is the melting temperature. The laser is turned on at time $\tau = 0$ with laser power P_L , laser radius R_L and moves along the x-axis with speed v. In the built coordinate, x, y and z represent the scanning direction, transverse direction and the deposit height direction, respectively. The derivation of the above solution is elaborated in Eqn 3.3.2, which is developed based on Green's function with the absence of radiative and convective heat losses and had been verified by the single-track and multi-layers multi-tracks experiments. The latent heat of fusion in melting/solidification cycles is not considered since it is much smaller than the energy amount required for melting the metallic powder. The value of thermal conductivity is at least two times larger than the stationary melt conductivity in the presence of thermocapillary flow (Marangoni flow), hence, to predict the thermal history during deposition, the thermocapillary flow is compensated by adding a correction factor μ_M to the initial thermal conductivity.

The melt pool cross-section can be calculated from energy balance assuming that 90% of absorbed laser power is consumed for pool melting. Aluminum enthalpy of melting (ΔH_{fus}) is 10.8 kJ/mol and the Enthalpy of heating ($\Delta H_{heat} = \rho C(T_m - T_0)$ = 8.8×10^8 J/m^3).

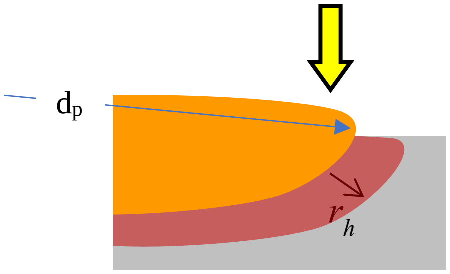

- Energy density equation = β P / v
- Enthalpy of heating + melting $\Delta H = \Delta H_{heat} + \Delta H_{fus}$
- Energy loss due to metal heating adjacent to the pool =
- $$\frac{P_{loss}}{P} = \frac{V}{P} C\rho(T_m - T_0) r_h \frac{\pi d_p}{2}$$
- $$\xi = (1 - P_{loss}/P)$$
- $r_h = 2 \times \alpha_p / v$
- Melt pool periphery S = ζ E / ΔH

An estimate of the defect conditions are:

1. Balling defect condition is calculated from modified Rayleigh condition of instability for melt pool aspect ratio and is function of melt pool diameter, deposited layer thickness, powder size, ΔH_{fus}, ΔH, thermal properties, melting temperature and ambient temperature (Figure 3.3.4).

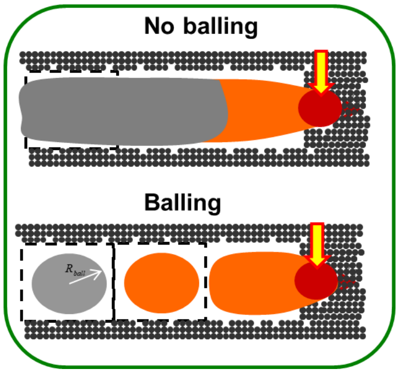

Figure 3.3.4 Origin of balling defect conditions

2. Regular unmelt defect condition depends on regular array of pores predicted at deterministic unmelt conditions function of powder properties and geometry.
3. Non-regular (fluctuation) unmelt defect condition is calculated from fluctuation of large local amount of powder could result in local unmelt in the current layer, or from fluctuation of small local amount of powder could result in local unmelt in the next layer Figure 3.3.5.

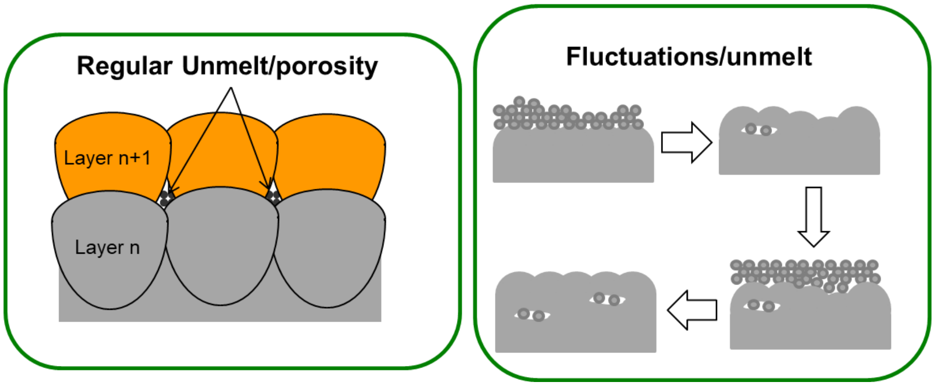

Figure 3.3.5 Origin of unmelt defect conditions.

4. Keyhole/porosity depends on melt pool temperature where force and heat balance in the Marangoni vortex determine flow velocity and maximal temperature under the beam. Deep keyhole is unstable and tends to collapse with bubble formation in the melt pool (Figure 3.3.6).

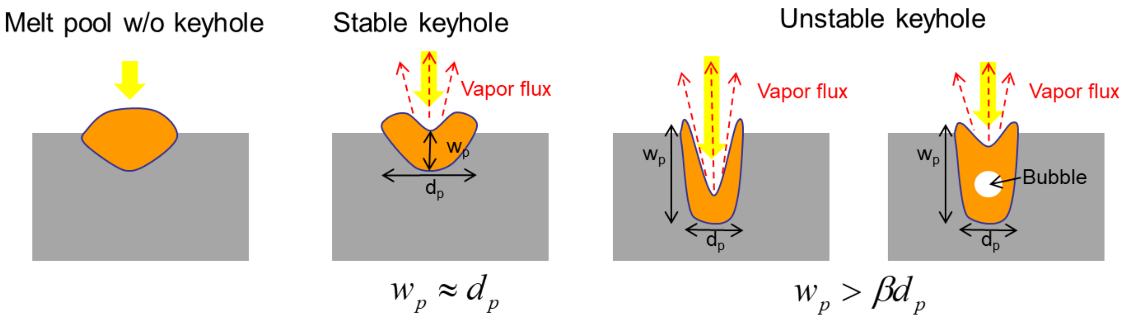

Figure 3.3.6 RTRC code includes modules to predict several keyhole instability criteria.

The modified code was used to investigate the effect of scanning strategy, power, and hatch spacing on defect generation, in addition to hatch spacing and laser spot size on asymptote of unmelt defects, porosities and surface roughness. The real scanning speed is kept within the expected zone of 0.6 m/min max deposition speed. The actual deposition speed used is 0.0762 m/min and 0.231 m/min. The maximum laser power that will be used is 3500 W, while the minimum laser power used is 1100 W. The machine specification was changed to accommodate continuous wave of 1030 nm wavelength. The laser spot diameter used is between 1 mm and 2.5 mm. The melt pool depth was determined experimentally and is considered as an input to the model. The hatch spacing used ranges from 1.0 to 1.8mm. The material properties were determined from data available in open literature to define the 6061-RAM2 aluminum alloy thermal properties. The thermal conductivity and specific heat in addition to density are not available as a function of temperature. In addition, 6061-RAM2 aluminum alloy latent heat, solidus and liquidus, dynamic viscosity, etc., are not available and replaced by Al6061 as shown in Figure 3.3.7. The Al6061 alloy absorptivity was 0.45. Heat convection and radiation emissivity evolution is modified with the correct laser velocity. Most of the heat input is assumed to be transferred by conduction. The RTRC defects code takes into account the fluid motion and Marangoni effect within the melt pool.

Material composition: Proprietary A6061 w/2% ceramic (E3D-T6 Condition)

Theoretical maximum density: 2.74 g/cm³
Printed relative density: > 99.7%
Ultimate tensile strength[1]: 48 ± 3.0 ksi (331 MPa)
Yield strength[1]: 43 ± 2.0 ksi (297 MPa)
Elongation[1]: 12 ± 1.5 %
Hardness[2]: 60 ± 2.0 HRB
Modulus of elasticity[3]: 11.0 ± 0.10 Msi (76 GPa)
Deposition rate[4]: 2.3 in3/hr (10.4 mm3/s)
Wear volume loss[5]: 5.1x10-3 in3 (84 mm3) (Note: Lower volume loss is better)

Thermal conductivity[8]: 162±3 W/m·K (measured in z)
Coefficient of Thermal Expansion (CTE)[9]: 22.4ppm/°C

Latent Heat, kJ/kg	397.0	
Melting Temperature, K	924.85	
Boiling Temperature, K	2730.0	Literature
Dynamic Viscosity, mPa·s	2.0	Literature
dSigma/dT, mPa·m/K	-0.35	Literature
Laser radiation absorptivity	0.45	Experimentally / Melt pool modeling
Keyhole onset factor	0.5	
Keyhole stability factor	3.5	

Thermo-physical property Assumed in the defect model

% T,K	Cp, J/kg K	% T, K	kappa, W/m K	% T,K	rho, kg/m3
297.6		299.8853	162.5	287.004	2645.38
	917.853	375.354	177.25	373.646	2619.2
376.8		477.108	192.75	601.083	2575.72
	978.582	569.903	207	839.35	
478		667.386	223	2529.34	
	1028.489	777.755	253.25	855.596	2441.53
570.4		881.693	70	1001.81	2392.05
	1058.191	974.488	71.25	1207.58	2351.46
676		1080.488	70	1407.94	2264.01
	1078.98	1182.143	72.5	1602.89	2194.12
768.4		2700		1803.25	2112.53
	1133.57		75	1992.78	2033.84
874				2425.99	1873.65
	1230.69			2700	
975.2				1757.11	
	1169.48				
1076.4					
1167.06					
1177.6					
1166.85					
2700					
	1160				

Figure 3.3.7 Al6061 RAM2 Mechanical and Thermal Properties used in the analysis

The effect of scanning strategy on defect generation was investigated, in addition to hatch spacing and laser spot size on the asymptote of unmelt defects, porosity, and surface roughness. Figure 3.3.8 illustrates the effect of process parameters on the single track and single strip defect maps. As shown in the figure, for the single-track map the defect free zone contains a wide range of power and scanning speed, while the single stripe map shows a strong dependence on the hatch spacing and laser spot size. The process parameters used generate unmelt defects for all scanning speeds when using a laser power below 1500 W. Porosity defects can be generated at laser power >1500 W when the scanning speed is less than 0.0005 m/s.

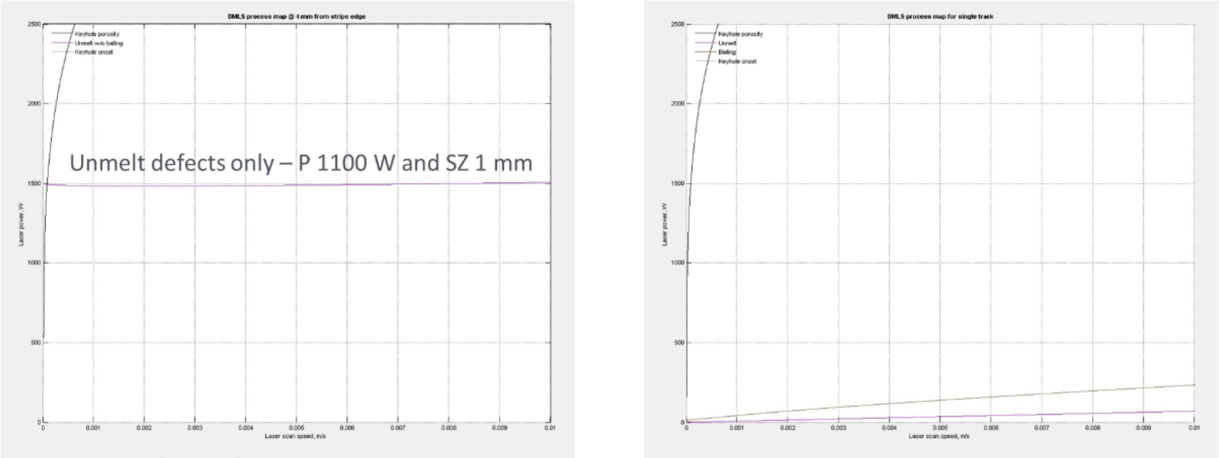

Single Stripe map

Single Stripe map identify effect of hatch spacing and laser spot size on asymptote of unmelt defects and surface roughness

Single Track map

Single Track map identify boundaries for porosities generation during depositions and indicates no unmelt defects are generated for all deposition parameters

Figure 3.3.8 Single track and single stripe for DED of Al6061 RAM2

Hatch spacing strongly affects the defect-free zone. The simulation also shows that a scanning speed >1.00 mm/s is recommended to eliminate any porosity generated as shown in Figure 3.3.9. Several process parameters were selected from those used during single track experiments. These results were used to validate the modified defects model.

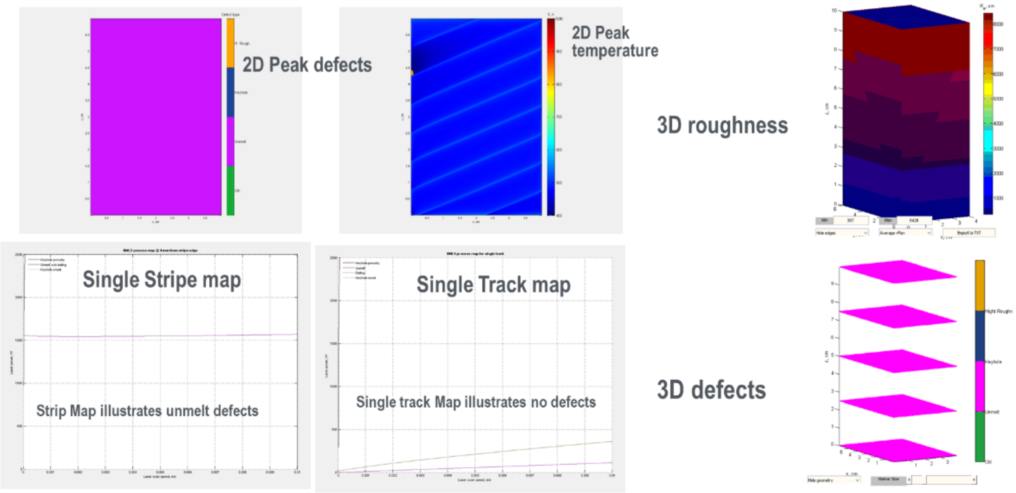

Figure 3.3.9 Unmelt defects prediction for DED Parameters: P1550 W, V0.00127 m/s, SS 1.5 mm, hatch spacing 0.75 mm

The effect of the laser power on the defects density and position are illustrated in Figures 3.3.10 and 3.3.11. Figure 3.3.10 illustrates a reduction of the unmelt defect density and the existence of defect-free area in the build when the laser power used is 1850 W. The surface roughness increased as the power increase and the rougher surface is observed at the highest length of the build. Figure 3.3.11 indicates that for the same spot size and scanning speed, increasing the laser power beyond 2000W reduces the unmelt defects but produces a rougher surface. Also increasing the hatch spacing reduces the unmelt defects.

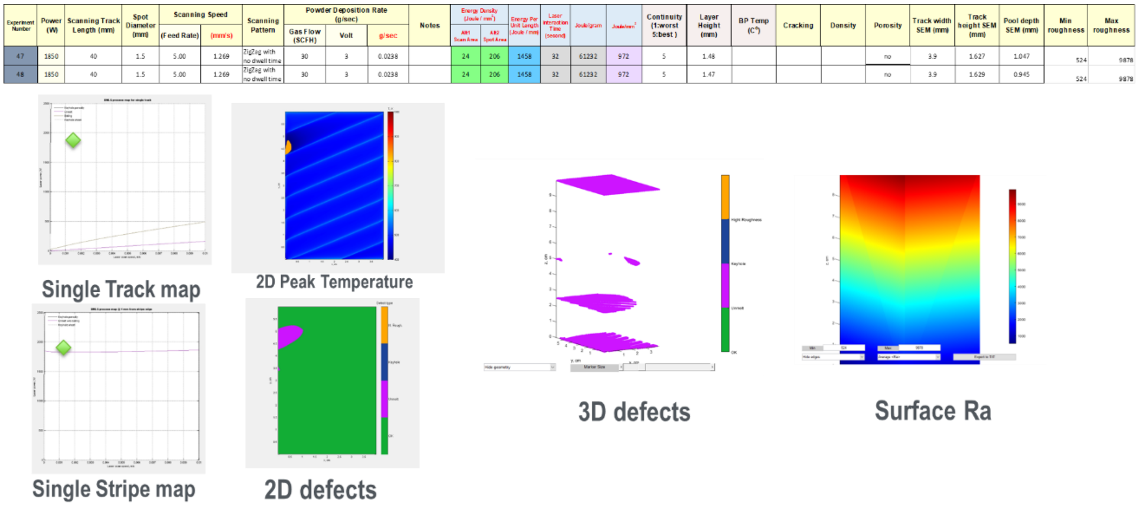

Experiment Number	Power (W)	Scanning Track Length (mm)	Spot Diameter (mm)	Scanning Speed		Scanning Pattern	Powder Deposition Rate (g/sec)			Notes	Energy Density (Joule / mm²)		Energy Per Unit Length (Joule / mm)	Laser interaction Time (second)	Joule/gram	Joule/mm²	Continuity (1:worst 5:best)	Layer Height (mm)	BP Temp (C°)	Cracking	Density	Porosity	Track width SEM (mm)	Track height SEM (mm)	Pool depth SEM (mm)	Min roughness	Max roughness
				(Feed Rate)	(mm/s)		Gas Flow (SCFH)	Volt	g/sec		Alt1 Scan Area	Alt2 Spot Area															
47	1850	40	1.5	5.00	1.269	ZigZag with no dwell time	30	3	0.0238		24	206	1458	32	61232	972	5	1.48				no	3.9	1.627	1.047	524	9878
48	1850	40	1.5	5.00	1.269	ZigZag with no dwell time	30	3	0.0238		24	206	1458	32	61232	972	5	1.47				no	3.9	1.629	0.945	524	9878

Figure 3.3.10 Unmelt defects prediction for DED Parameters: P1850 W, V0.00127 m/s, SS 1.5 mm, hatch spacing 0.75 mm

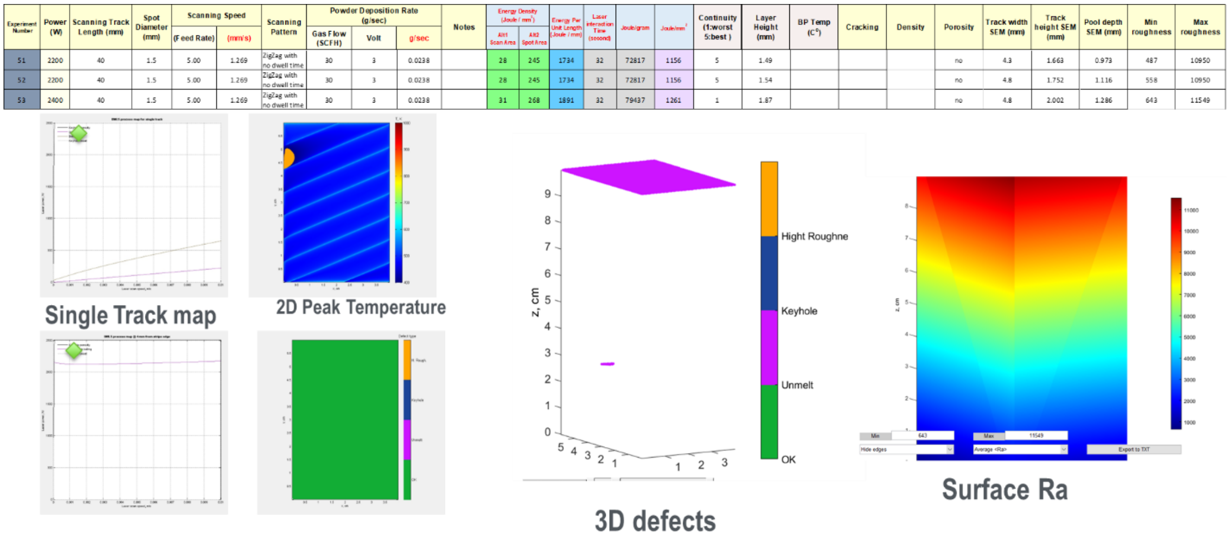

Experiment Number	Power (W)	Scanning Track Length (mm)	Spot Diameter (mm)	Scanning Speed		Scanning Pattern	Powder Deposition Rate (g/sec)			Notes	Energy Density (Joule / mm²)		Energy Per Unit Length (Joule / mm)	Laser interaction Time (second)	Joule/gram	Joule/mm²	Continuity (1:worst 5:best)	Layer Height (mm)	BP Temp (C°)	Cracking	Density	Porosity	Track width SEM (mm)	Track height SEM (mm)	Pool depth SEM (mm)	Min roughness	Max roughness
				(Feed Rate)	(mm/s)		Gas Flow (SCFH)	Volt	g/sec		Alt1 Scan Area	Alt2 Spot Area															
51	2200	40	1.5	5.00	1.269	ZigZag with no dwell time	30	3	0.0238		28	245	1734	32	72817	1156	5	1.49				no	4.3	1.663	0.973	487	10950
52	2200	40	1.5	5.00	1.269	ZigZag with no dwell time	30	3	0.0238		28	245	1734	32	72817	1156	5	1.54				no	4.8	1.752	1.116	558	10950
53	2400	40	1.5	5.00	1.269	ZigZag with no dwell time	30	3	0.0238		31	268	1891	32	79437	1261	1	1.87				no	4.8	2.002	1.286	643	11549

Figure 3.3.11 Unmelt defects prediction for DED Parameters: P2200 W, V0.00127 m/s, SS 1.5 mm, hatch spacing 0.75 mm

One important parameter to be further investigated is the change in the melt pool depth. The smaller depth leads to producing defect-free component. The results presented in Figure 3.3.12 indicate that the process is stochastic in nature.

Experiment Number	Power (W)	Scanning Track Length (mm)	Spot Diameter (mm)	Scanning Speed		Scanning Pattern	Powder Deposition Rate (g/sec)			Notes	Energy Density (Joule / mm³)		Energy Per Unit Length (Joule / mm)	Laser interaction Time (second)	Joule/gram	Joule/mm²	Continuity (1:worst 5:best)	Layer Height (mm)	BP Temp (C°)	Cracking	Density	Porosity	Track width SEM (mm)	Track height SEM (mm)	Pool depth SEM (mm)
				(Feed Rate)	(mm/s)		Gas Flow (SCFH)	Volt	g/sec		Alt1 Scan Area	Alt2 Spot Area													
45	1700	40	1.5	5.00	1.269	ZigZag with no dwell time	30	3	0.0238		22	190	1340	32	56268	893	4	1.59				no	2.9	1.586	0.639
46	1700	40	1.5	5.00	1.269	ZigZag with no dwell time	30	3	0.0238		22	190	1340	32	56268	893	4	1.65				no	4.0	1.705	0.968

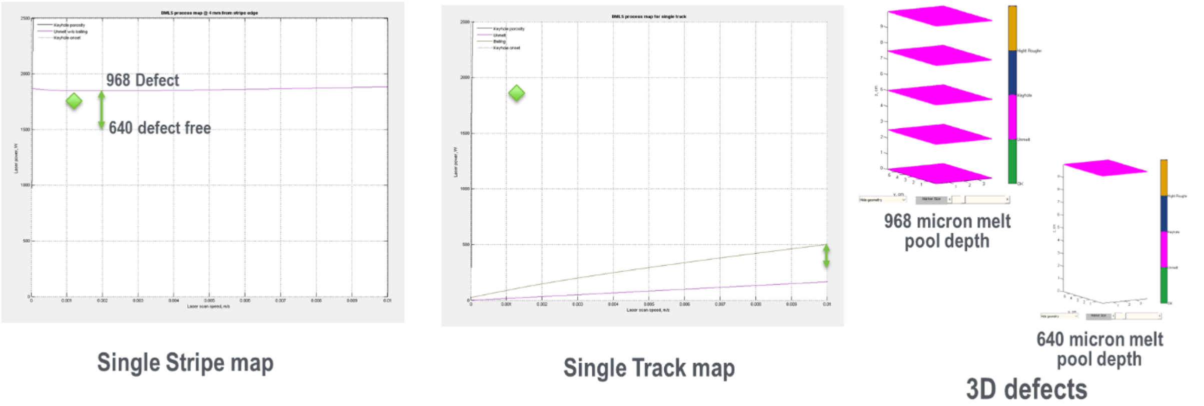

Figure 3.3.1 Effect of melt pool depth on the Unmelt defects generation for same DED Parameters: P1700 W, V0.00127 m/s, SS 1.5 mm, hatch spacing 0.75 mm

The predicted results from running the experimental parameters in the code support the code validation. The predicted defects were compared with the defects observed during the deposition of single-track coupons summarized in Table 3.3.1. The prediction matched the experimental data for the porosity defects, unmelt, and some discontinuity (balling).

Table 3.3.1 Prediction of different defects as a function of varying process parameters

Black : Input Red : Output																	Results								
Experiment Number	Power (W)	Scanning Track Length (mm)	Spot Diameter (mm)	Scanning Speed		Scanning Pattern	Powder Deposition Rate (g/sec)			Hatch spacing microns	Powder size micron	Layer depth	Melt pool depth	Compacting degrees	Substrate temperature oK	Continuity (Balling) (1:worst 5:best)	Max Temp 0K	Unmelt	min Power for defect free W	Min speed for no porosity m/s	Porosity	min Ra micron	max Ra micron
				(Feed Rate)	(mm/s)		Gas Flow (SCFH)	Volt	g/sec														
1	1100	40	1	5.00	1.269	ZigZag with no dwell time	30	3	0.0238	250	45	200	0.287	0.5	300	5	820	minimum	1060	0.0001	No	103	6759
2	1250	40	1	5.00	1.269	ZigZag with no dwell time	30	3	0.0238	250	45	250	0.391	0.5	300	4	820	minimum	1180	0.0001	No	127	7257
3	1400	40	1	5.00	1.269	ZigZag with no dwell time	30	3	0.0238	300	45	300	0.392	0.5	300	4	820	minimum	1340	0.0002	No	152	7692
4	1550	40	1	5.00	1.269	ZigZag with no dwell time	30	3	0.0238	350	45	350	0.351	0.5	300	4	820	minimum	1400	0.00025	No	176	8110
5	1700	40	1	5.00	1.269	ZigZag with no dwell time	30	3	0.0238	400	45	400	1.201	0.5	300	4	820	minimum	1600	0.0003	No	201	8513
6	1850	40	1	5.00	1.269	ZigZag with no dwell time	30	3	0.0238	450	45	500	0.842	0.5	300	4	820	areas of unmelt increase	1780	0.00035	No	251	8903
7	2000	40	1	5.00	1.269	ZigZag with no dwell time	30	3	0.0238	500	45	500	0.825	0.5	300	4	820	areas of unmelt increase	1850	0.00036	No	251.0	9281
8	2200	40	1	5.00	1.269	ZigZag with no dwell time	30	3	0.0238	500	45	550	0.973	0.5	300	4	820	areas of unmelt reduced	1950	0.0004	No	276.0	9805
9	2400	40	1	5.00	1.269	ZigZag with no dwell time	30	3	0.0238	550	45	600	1.286	0.5	300	4	820.00	areas of unmelt reduced	2200	0.0006	No	301.0	10282
10	2600	40	1	5.00	1.269	ZigZag with no dwell time	30	3	0.0238	600	45	700.00	1.5	0.5	300	4	820	areas of unmelt increased	2450	0.001	yes	351	10745
11	2800	40	1	5.00	1.269	ZigZag with no dwell time	30	3	0.0238	650	45	750.00	1.60	0.5	300	4	820	areas of unmelt increased	2600	0.00125	yes	376	11197
12	3000	40	1	5.00	1.269	ZigZag with no dwell time	30	3	0.0238	650	45	750.00	1.70	0.5	300	4	820	areas of unmelt increased	2600	0.002	yes	Error	Error
13	3200	40	1	5.00	1.269	ZigZag with no dwell time	30	3	0.0238	650	45	750.00	1.71	0.5	300								
14	3400	40	1	5.00	1.269	ZigZag with no dwell time	30	3	0.0238	650	45	750.00	1.80	0.5	300								

Overall, the Table 3.3.1 summary identifies the parameters that produce porosity, balling and unmelt defect, and the produced surface roughness. All experimental parameters were run in the code and the predicted results support the code validation. The prediction defects when compared with the defects observed during the deposition of single tracks were very close to the experimental data for the porosity defects, unmelt and some discontinuity (balling).

3.4. Experimental coupon fabrication process analysis

Testing was conducted using a vacuum test to determine if the test coupons with a shaped airfoil profile surface, procured per Section 4.1, had satisfactory porosity and surface finish, and the seal at the modular mold interface would be adequate for resin infusion. After validating the vacuum test setup, Figure 3.4.1, it was determined that a dry interface was insufficient to form a vacuum seal between the test coupons. Experimentation with high vacuum silicon grease applied to the interfaces to fill minor gaps at the joint demonstrated improved vacuum retention, as it only lost the vacuum in <1 min rather than <10 sec, but the setup was not able to pass the vacuum test. The test coupons were then altered to utilize a dual O-ring seal, Figure 3.4.5. This configuration successfully held a vacuum for 30 minutes.

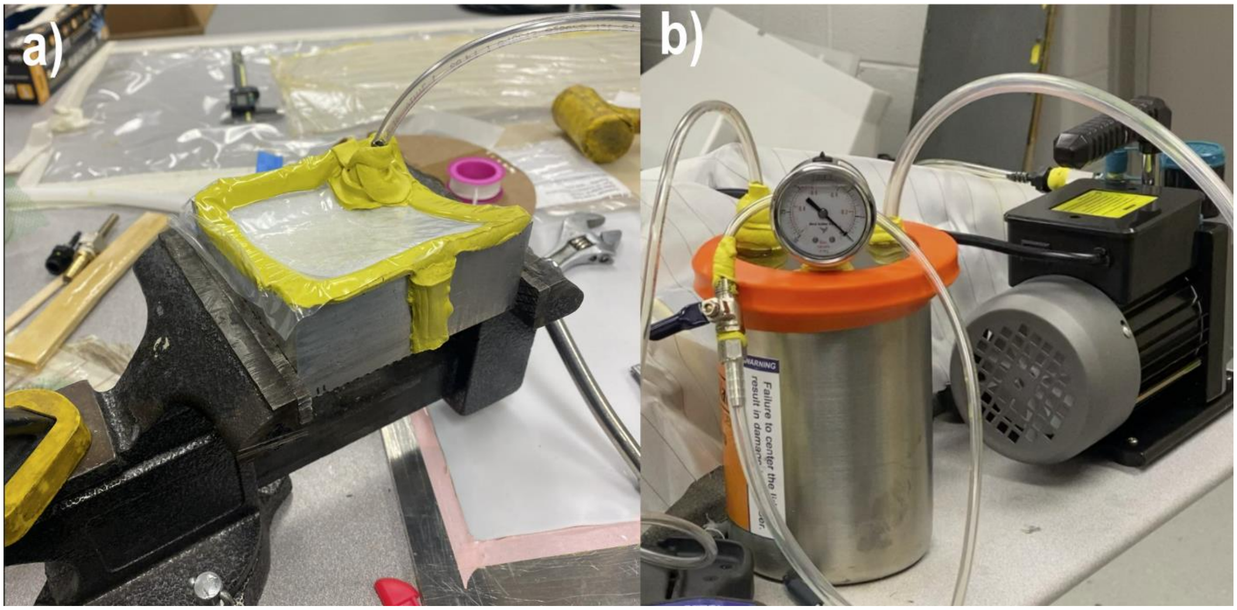

Figure 3.4.1 Vacuum Test Setup (a) The two scale molds are pressed together in a manually tightened vise grip. Sealing putty seals, the vertical seams of the interface and the edges of the top surface (yellow putty on the two mold configuration). The putty forms a seal with a vacuum plastic liner that has a piece of diffusion clothe between it and the mold surface. The vacuum is pulled to the surface using plastic tubing and a diffusion nozzle who's joining features with the mold have been sealed with additional putty (b) the tubing goes from the mold to a vacuum control diaphragm (the cylinder with the orange sealing lip) which is attached to a cutoff valve, vacuum pressure gauge, and vacuum air pump.

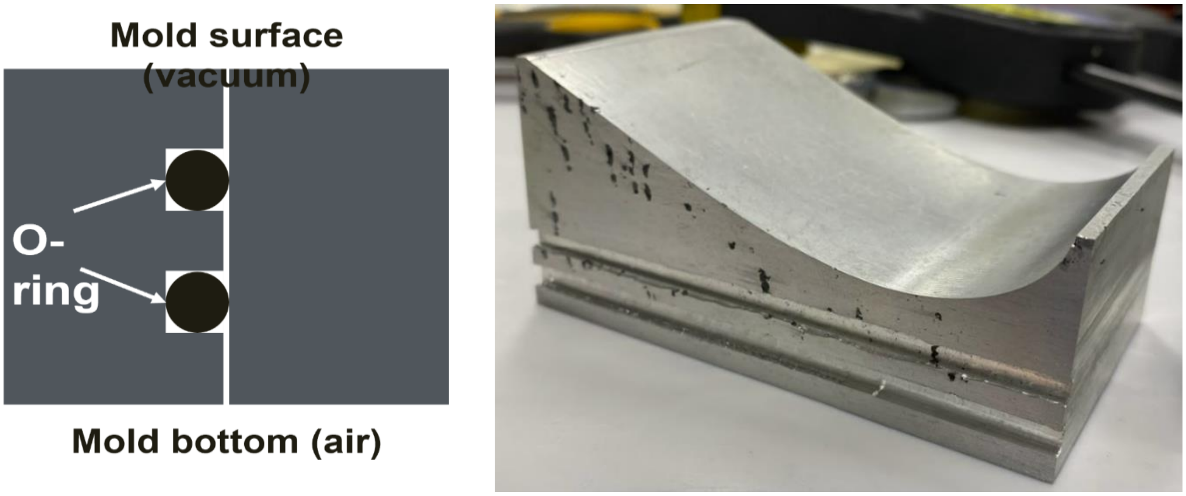

(a) O-ring interface concept

(b) Implementation on test coupon

Figure 3.4.2 Interface cross section showing O-ring in grooves to form a vacuum seal at coupon interface joint

Next, the extent of resin infiltration into the O-ring during the vacuum test was determined. The experimental setup was modified to supply curing resin into the vacuum bag at room temperature, Figure 3.4.3. After the pump removed the air and the resin completed infiltration, the tube was sealed and the resin cured for twenty-four hours. Post-cure analysis showed that the resin fully infiltrated the coupon interface only up to the first O-ring barrier. This indicated that only a single O-ring was necessary, and this information was passed on to the mold design team.

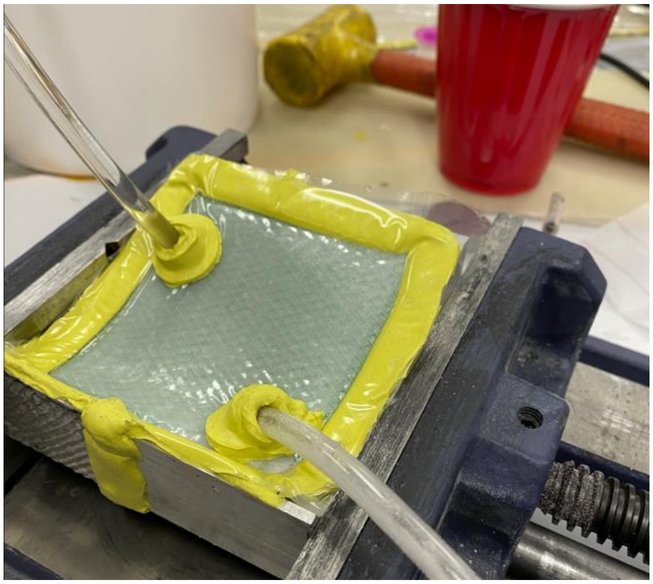

Figure 3.4.3: Scale mold resin infiltration test: The vacuum bag includes stiff plastic mesh and a cotton diffuser layer to allow quick removal of air from the bag and resin infiltration.

3.5. Prototype mold print porosity analysis

A 1:20 scale Version 1 mold design prototype, heat treated using a T6 process, was provided by DM3D for material characterization, Figure 3.5.1. A sample was cut off from the as-printed face, indicated in blue in Figure 3.5.1, allowed an assessment of the material properties over the height of the print. High resolution optical images were taken at different sections of the cutoff piece to determine the change in porosity and other observable features. Overall porosity was calculated at <1%, meeting the specification of >99% density. A slight variance of the average suface porosity from the bottom to top was observed, ranging from 0.61%-0.71% area porosity, corresponding to print direction rather than mold orientation.

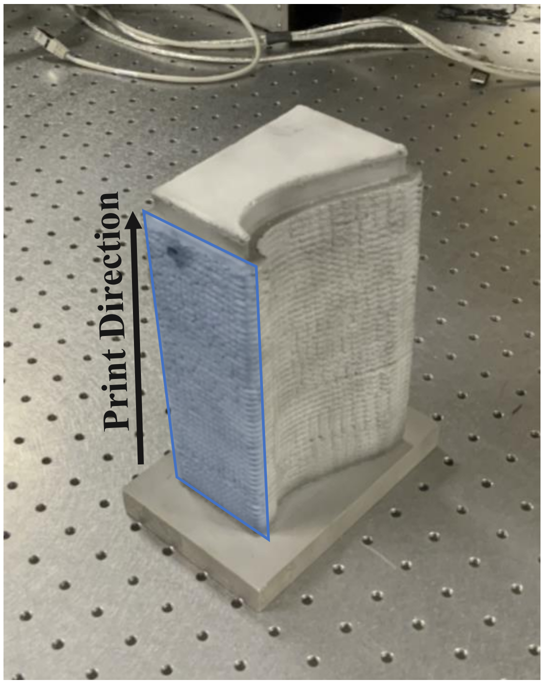

Figure 3.5.1 1:100 scale Version 1 mold prototype. Characterization of the material informs if there are significant changes in properties and microstructure as the mold is printed. The blue rectangle is the cutoff face provided to UofM for characterization.

The material cut off was sent to Zeiss for micro-CT imaging to quantify the porosity characteristics within the volume of the cutoff sample. As the sample included the entire length of the mold along the build direction, the porosity distribution related to the layer depositions could be revealed. The micro-CT scan was performed at a voxel resolution of 64.79 µm over the entire piece, and at a finer voxel resolution of 20.94 µm at the very top of the piece. The overall calculated density target was confirmed at 99.65%. As shown in Figure 3.5.2, spikes in porosity were observed at layer boundaries and regions of porosity also approached 0.8%. Despite these observed spikes, no interlayer cracks were observed in either scan, supporting the effectiveness of the 6061-RAM2 powder at hot crack elimination.

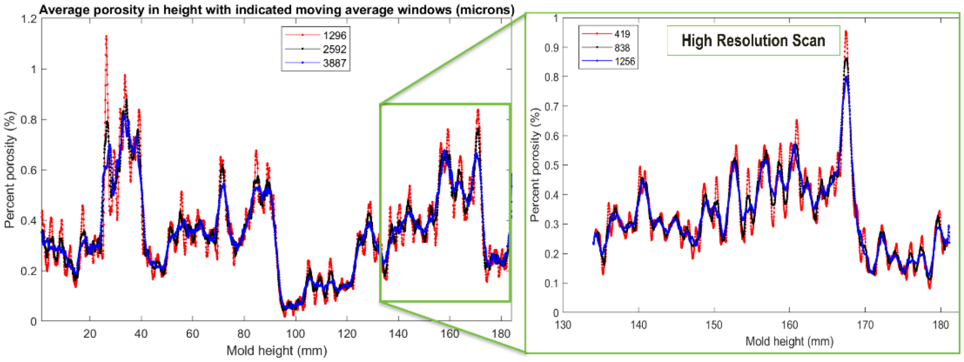

Figure 3.5.2 Porosity distribution in full volume scan. Porosity peak periodicity correlates with predicted layer height (left). Porosity distribution in high resolution scan of the top of the build piece (right).

The porosity size distribution calculated from the high-resolution scan showed that 10% of the pores in the top section of the mold are above 150 µm, Figure 3.5.3. Most of the pores appear to be keyhole pore formations rather than from lack-of-fusion defects despite the higher concentration of pores at layer boundaries. This conclusion was made due to the pores within the piece were observed to be almost exclusively spherical with only infrequent instances of connected porosity.

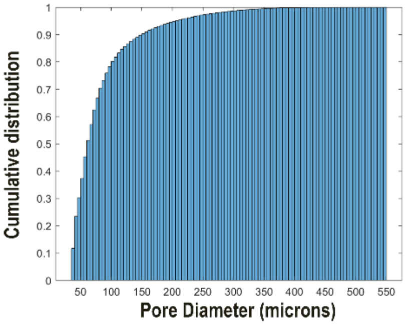

Figure 3.5.3 Cumulative distribution function of the equivalent pore diameter in high resolution scan of the top of the build piece – 90% of pores are below 150 µm.

3.6. *Material quality Inspection of Version 2 mold*

A microstructural analysis of Version 2 Module C material was conducted on non-functional material used to secure the module during machining, Figure 3.6.1. The sample was sectioned, ground, and polished for SEM imaging. An analysis of the microstructure finds it is dominated by unreacted B_4C and elemental Ti powder. The purpose for these alloying additions to the 6061 based powder is for the formation of reinforcements. However, some of the TiB nanoparticles do not completely react in the melt pool, making it difficult to determine the porosity level from these SEM images due to their visual similarity between unreacted B_4C and pores in the print matrix.

However, the objective porosity level is still below the specification limit given that the combined area percentage of the pore and unreacted B_4C particles observed was 0.4%.

The primary reinforcement phase observed in the analyzed material was seen to be Al_3Ti. While TiB particles were present near B_4C rich regions, they were not observed to have been well dispersed throughout the microstructure. The Al_3Ti intermetallic, refined greatly due to the fast-cooling rate inherent to direct energy deposition (DED) process, still provides a substantial reinforcing effect on the printed part. See Figure 3.6.2 and 3.6.4. Nothing observed is expected to affect the function of the mold.

Figure 3.6.1 Material sample removed from the Version 2 Module C print

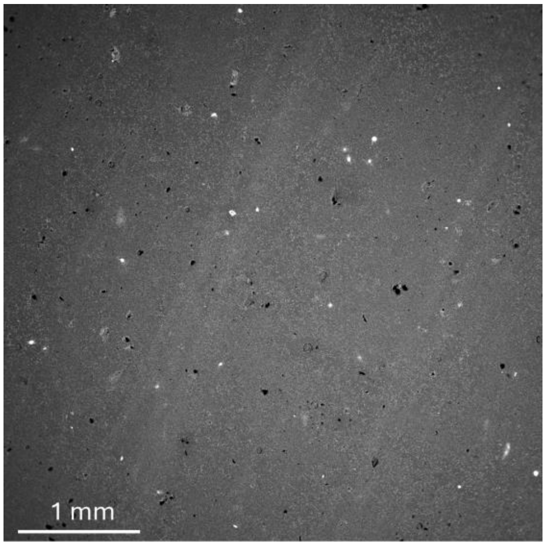

Figure 3.6.2 Macro image of Version 2 Module C cutoff section. Unreacted B_4C (dark phase) and Ti (large bright white phase) are seen dominating the microstructure. The speckled grey phase can be seen near homogeneously distributed in the microstructure as a reinforcing phase. Area percentage B_4C + Pores approximately equal to 0.4%.

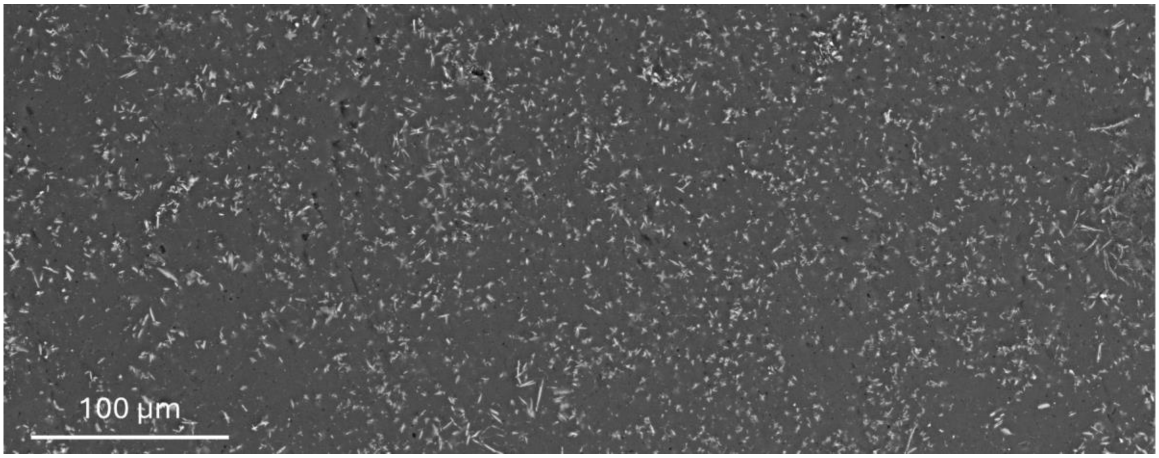

Figure 3.6.3 Reinforced region. High strength intermetallic, Al_3Ti (light grey) can be seen distributed throughout the 6061 microstructure (dark grey). In this view it is difficult to distinguish the presence of TiB nanoparticles

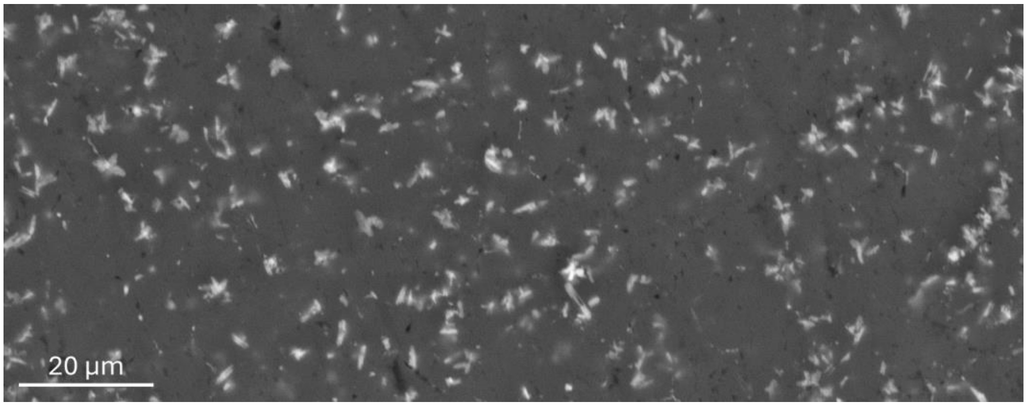

Figure 3.6.4 Reinforced region. High strength intermetallic, Al_3Ti, seen as the faceted and cross-like phase, is the primary reinforcement feature throughout the observed microstructure.

3.7. Lessons learned from the material analysis

4. Fabrication of 1:100 and 1:20 Scale Prototype Coupons and Molds

The development of coupons and molds was undertaken jointly by UM and DM3D, the direct material deposition (DMD, i.e., additive manufacturing) 3D print vendor. Details of the print process were largely proprietary to DM3D and will not be reported. Machining services for printed components were also provided by DM3D according to UM design specifications.

4.1. Shaped experimental coupon fabrication

Two test coupons approximating the airfoil profile shape at a 1:100 scale were printed at DM3D, Figure 4.1.1. The sample was printed in two parts to facilitate evaluation of a joint across the airfoil profile surface once it was machined.

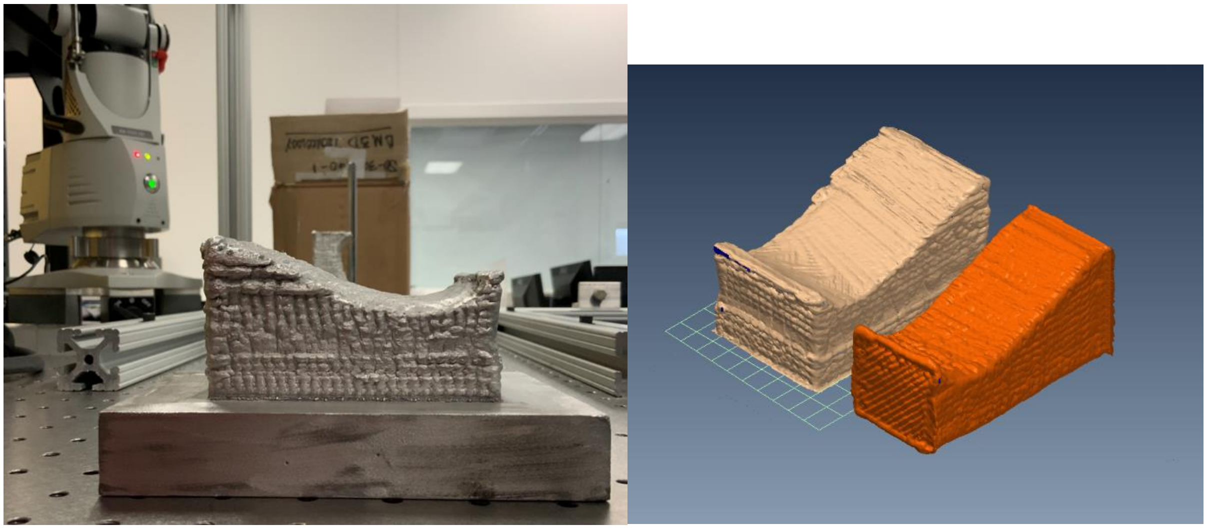

Figure 4.1.1 Unmachined 3D printed preliminary scaled-down mold and laser scan of the of the two mold segments.

To achieve a satisfactory surface finish and reduce post processing cost, the modular molds' interface must align properly and form a seal such that resin does not leak when a vacuum is used during turbine blade fabrication. Initially, the mold design was such that a flat surface between the mold faces could be aligned and form a vacuum seal. Unfortunately, the coupon interface after machining, Figure 4.1.2, had vertical scratches that would prevent the interface from keeping a vacuum. These scratches were determined to be machining artifacts left over from the milling process and had not been removed by grinding. The interfaces were reground to remove the milling artifacts, see Figure 4.1.3, but despite the improved surface, the interface was still not able to hold a vacuum, Section 3.4. These sample coupons were provided to Penn State for their work in developing their surface finishing process.

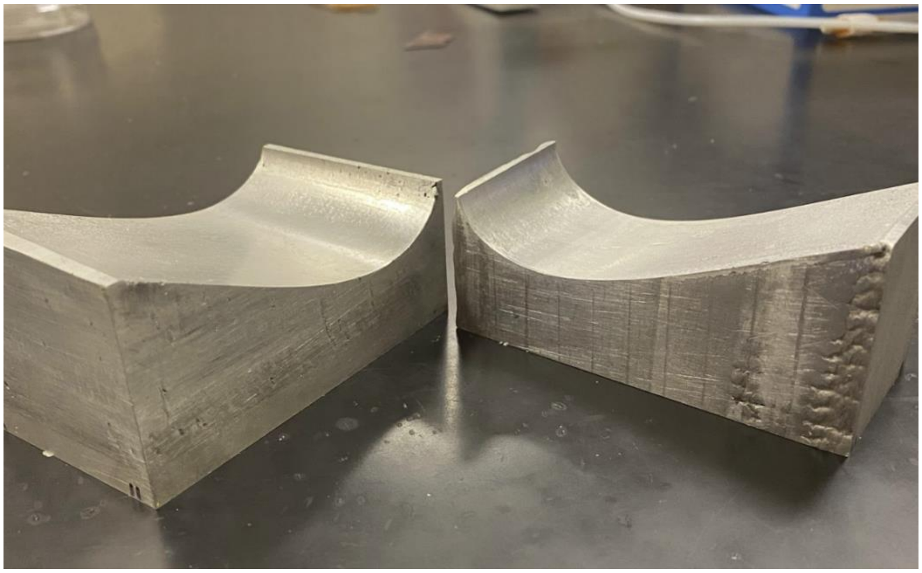

Figure 4.1.2 Mold interface after DMD fabrication and machining

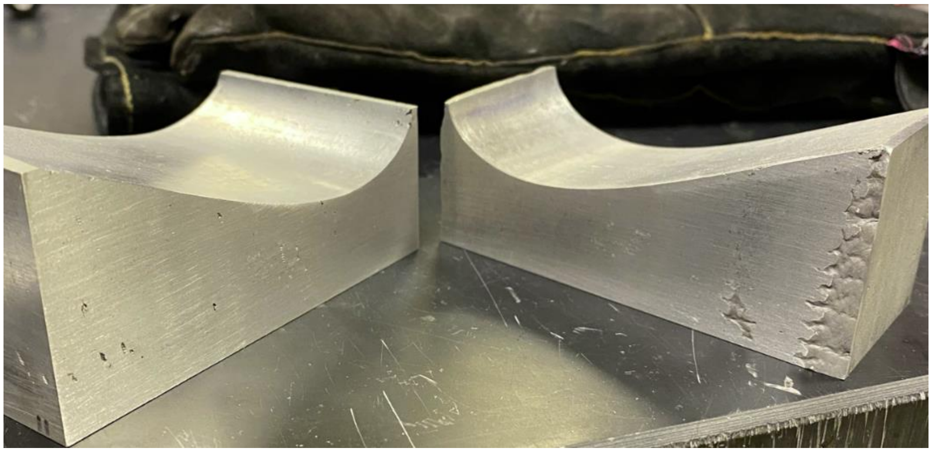

Figure 4.1.3 Mold surfaces after regrinding the interface

4.2. 1:100 scale Version 1 mold fabrication

Following the design manufacturability review for the topologically optimized Version 1 mold, Section 2.2, the additive manufacturing prototype vendor, DM3D, finalized their preliminary direct metal deposition process and printed the molds, Figures 4.2.1 and 4.2.2. The build orientation was chosen to facilitate the formation of the internal structure's organic shapes, avoiding overhang complications. The hollow column was capped off with a separately printed end-cap that eliminated any concerns with unsupported material when enclosing the print. This prototype was then evaluated for print material performance, Section 3.5, and lessons learned during fabrication.

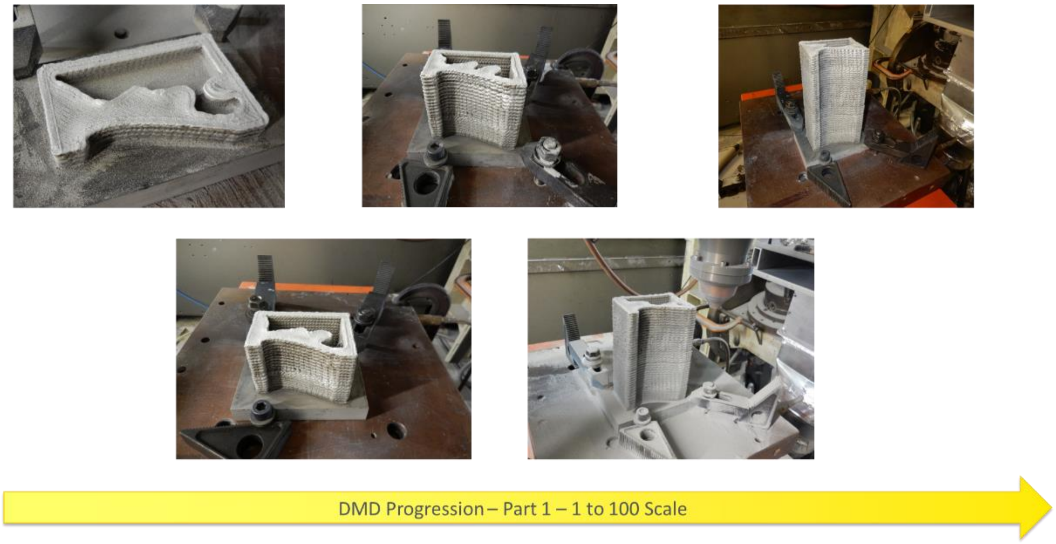

Figure 4.2.1 3D print progression of TO mold Version 1 prototype

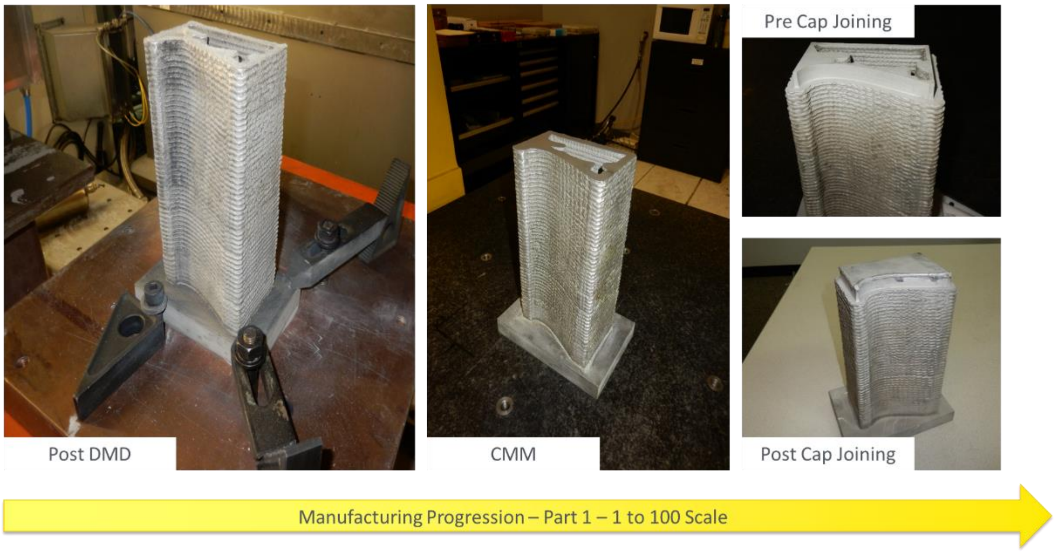

Figure 4.2.2 Assembly of 3D printed components of the TO mold Version 1 prototype

4.3. 1:100 scale Version 2 mold fabrication

Figure 4.3.1 shows the 3D printed 1:100 scale prototype of mold Version 2 prior to machining. The mold was mounted on a baseplate during printing that is removed before machining. The very rough texture was the result of the deposition process and will be removed from the mold by machining. The roughness is an effect of the fabrication scale and will be less prominent at larger scales. Each layer of the build can be clearly seen in the images. See Sections 5.1 and 5.2 for the performance evaluation of these prototypes.

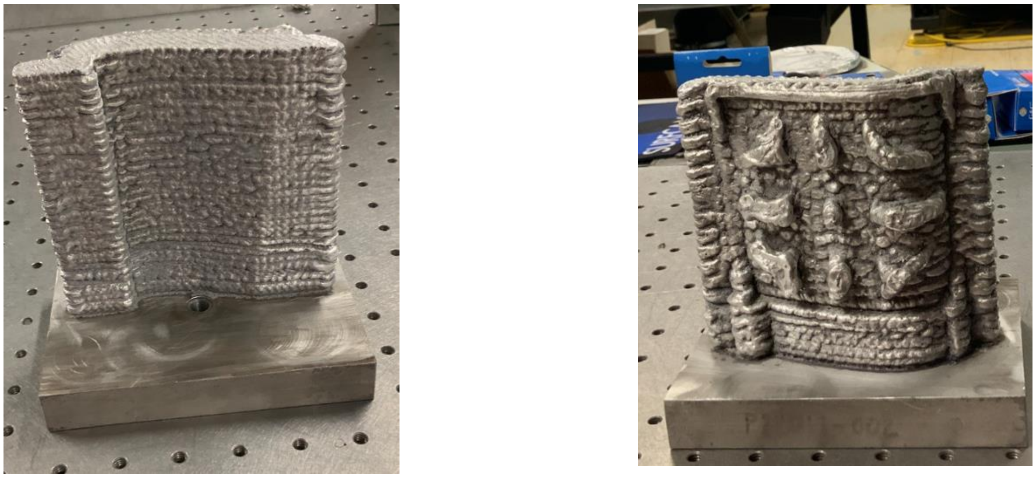

(a) top surface
(b) back surface with conformal channels

Figure 4.3.1 Version 2 1:100 scale mold after 3D printing and before machining

(a) mold surface view showing shell side profile
(b) underside of the mold, showing tapped holes for the support structure

Figure 4.3.2 Version 2 1:100 scale mold after machining

4.4. 1:20 scale Version 2 mold fabrication

Following the manufacturability review and finalization of the design of the Version 2 1:20 scale mold, it was released to the prototype vendor, DM3D, for fabrication using direct laser deposition (DLD). The completed DLD print and machining for Module A is shown in Figure 4.4.1. Its underside is shown in Figure 4.4.2. The change in scale and machining of the bottom deck before printing the pillars in the revised DM3D fabrication process demonstrates a much smoother finish in comparison to the 1:100 scale Version 2 molds. This was expected to provide improved performance by providing a more uniform heat transfer from the hot air to the underside surface.

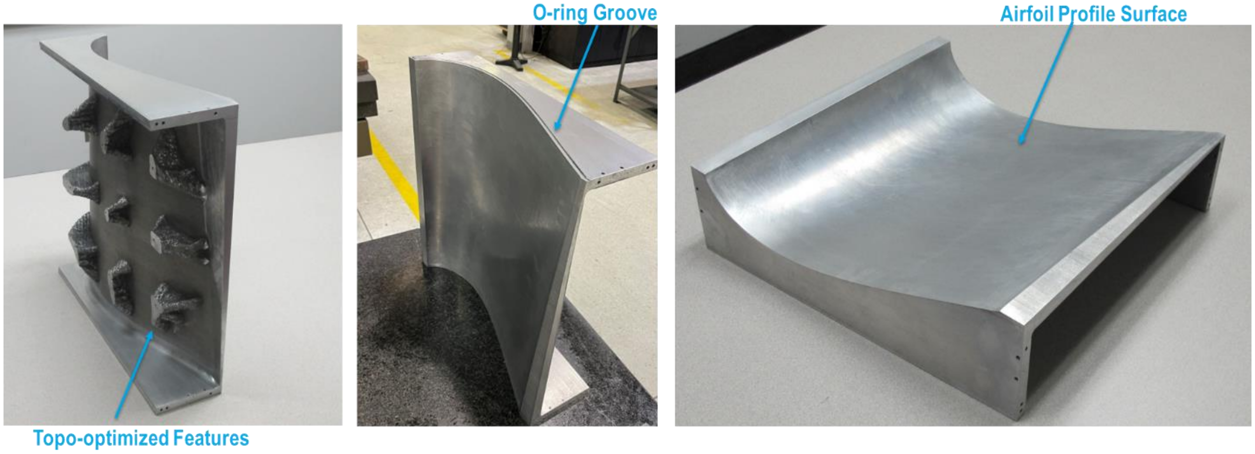

Figure 4.4.1 1:20 scale Version 2 Module A prototype post-machining

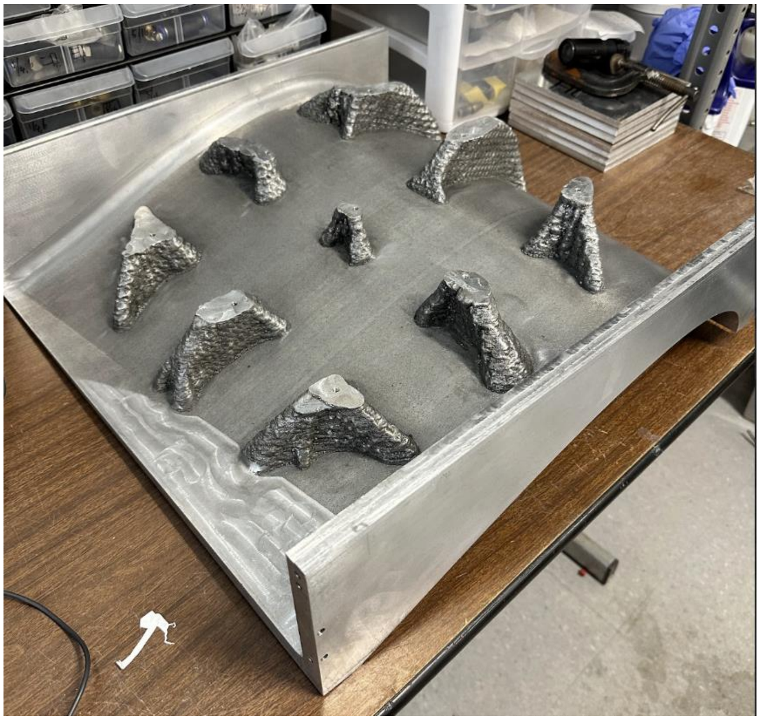

Figure 4.4.2 Underside of Version 2 Module A prototype post-machining.

Challenges encountered for Module A during its fabrication included build-warpage, warpage during heat treatment, and cracking at the mold side wall, Figure 4.4.3. Build-warpage was due to the additional deposition of material at a corner needed due to aggressive curvature at that location. This thicker deposition caused the part to curl pulling the concave surface away and resulting in out-of-tolerance part dimensions at the corner of the concave surface. To correct this condition, the top left corner was machined and redeposited to establish sufficient stock material.

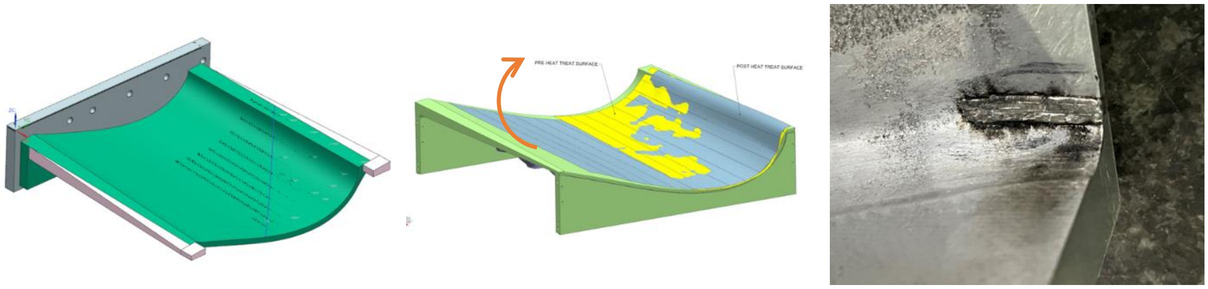

(a) Build warpage (b) Heat treatment warpage (c) Sidewall cracking

Figure 4.4.3 Challenges encountered during Version 2 Module A DMD print

Heat treatment warpage was due to following the recommended guidelines for the aluminum material, which consists of a T4 solution treated procedure following the print that employs a water quench with precipitation hardening (T6). The heat treatment caused curling of the thinner section on airfoil surface which inherently shifted the topologies. As a result, to maintain the concave surface geometry, the hole locations on the bottom side topology features were adjusted by a shift of about 0.125”.

Cracking at the side wall was observed at the corner where the mold wall is thinnest. This crack is believed to be a result of the thermal stress during water quenching from solutioning temperature. To repair, the crack was machined out and laser-micro welded. DM3D recommended altering the heat treatment to air quench instead of water quenching and increasing the sidewall thickness to help overcome these problems in future mold prints.

From this experience, the manufacturability of the Version 2 Module B DLD print was improved by making several changes to the Module B design and fabrication process. Material was added locally to the Module B design at the corners and edges of the mold to mitigate the distortion observed during manufacture of the previous mold module. This design change is illustrated in Figure 4.4.4. In addition, the recommended revised heat treatment plan was approved, as the higher strength and wear resistance of a precipitation hardened mold material was determined to be unnecessary for this application.

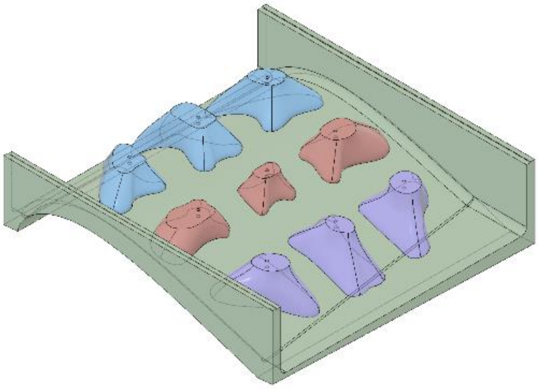

Figure 4.4.4 Updated design for 1:20 scale Version 2 Module B

4.5. 1:20 scale Version 2 Module C mold prototype fabrication

While the design of Version 2 Module C was modified in accordance with the experience gained printing Modules A and B, distortion during fabrication of Version 2 Module C was observed requiring rework. DM3D's post-fabrication manufacturability review indicated the distortion may have been caused by the larger support features of Module C. A Comparison of Module B and Module C is shown in Figure 4.5.1. It is obvious that the support structures of Module C are larger than that of Module B. Investigation into the root causes of the distortion and recommendations to further improve manufacturability will be left to a future project. The final machining of Version 2 Module C prototype is shown in Figure 4.5.2.

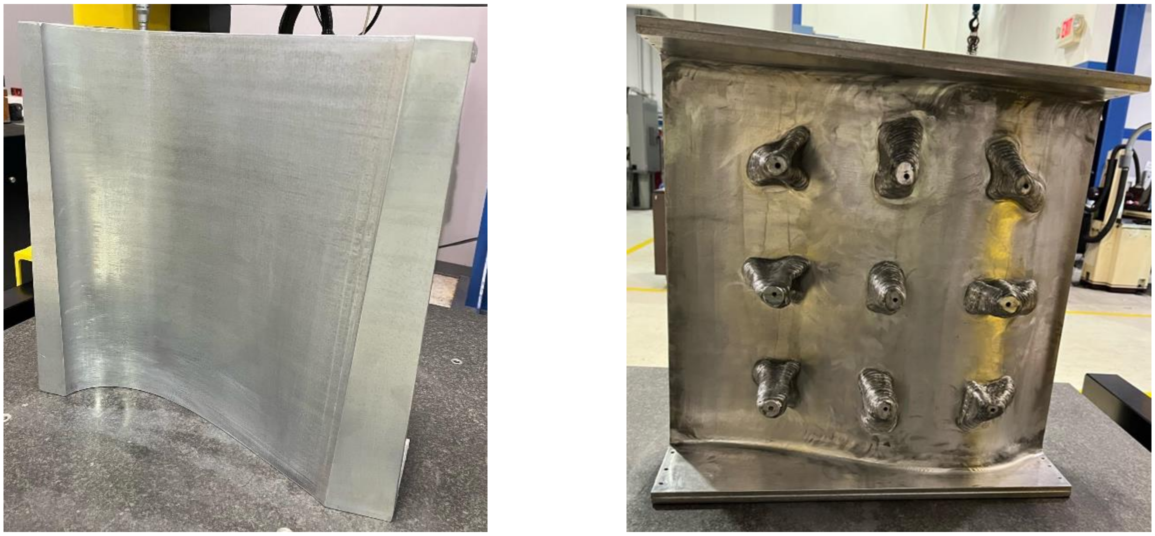

(a) Airfoil surface (b) Underside as machined

Figure 4.5.2 Final machined 3D print of mold Version 2 Module C

4.6. Fabrication and procurement of ancillary equipment for the Version 2 mold assembly

The mold support framework design scaled-down to the 1:20 scale for the Version 2 Module A was reviewed with a machinist. Based on the machinist's feedback, the design was changed to standard tube stock sizes available the local steel supplier. The new design consists of 5/8" by 5/8" by 0.065" square tubes and ½" by 0.065" round tubes. Both dimensions were larger than the original design resulting in a sturdier structure. The tube material, A513, was a weldable carbon steel that met the strength requirements. All part drawings were revised based on the feedback, and assembly drawings and bill of materials (BOM) were created. Examples of the structure's procurement documentation are shown in Figure 4.5.1. A review of the design with the machinists also provided a detailed manufacturing process estimate for the labor hours and cost.

Commercial heater/blowers capable of delivering the specified mold inlet air temperature and flow were also procured. The heater/blower must generate heated air at a minimum of 75C (+5C above the target temperature), but a desired 85C will reduce the curing time. An air circulation system from the outlet back to inlet was considered to reduce energy loss during heat-up and cure but was deemed unnecessary for testing the prototype molds.

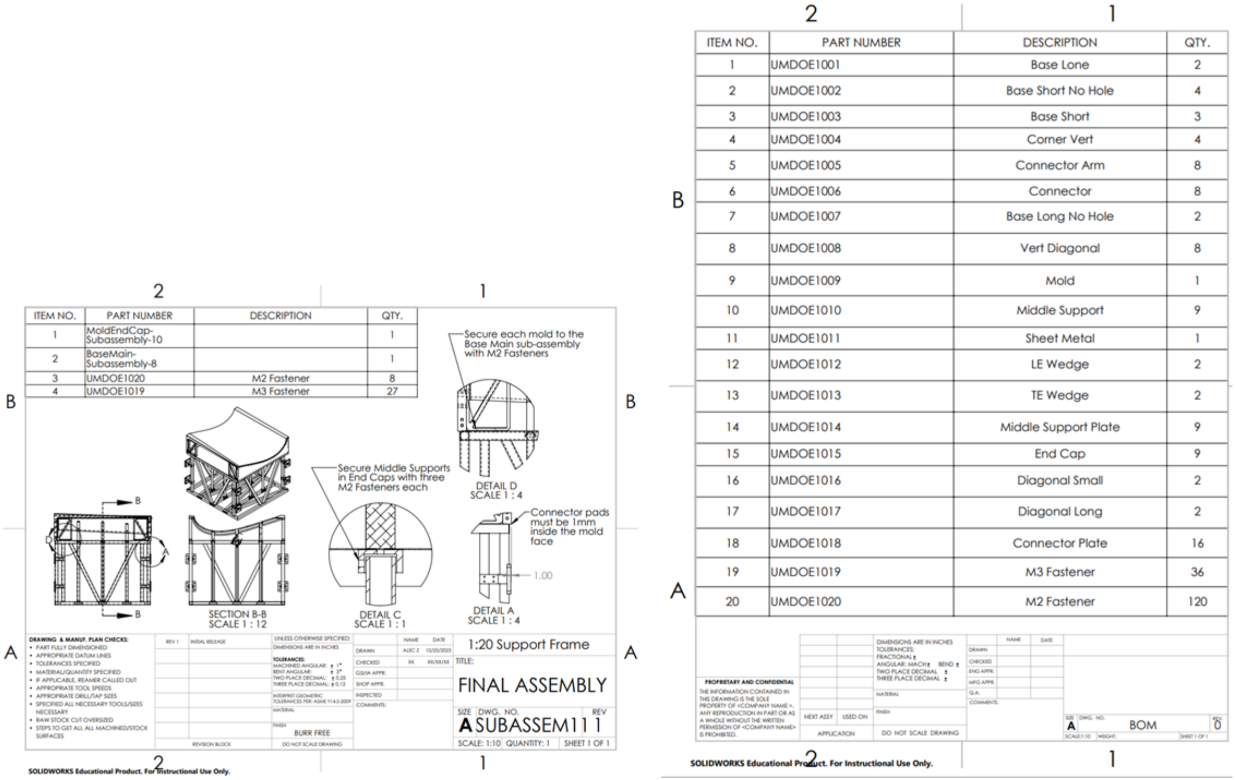

ITEM NO.	PART NUMBER	DESCRIPTION	QTY.
1	MoldEndCap-Subassembly-10		1
2	BaseMain-Subassembly-8		1
3	UMDOE1020	M2 Fastener	8
4	UMDOE1019	M3 Fastener	27

ITEM NO.	PART NUMBER	DESCRIPTION	QTY.
1	UMDOE1001	Base Lone	2
2	UMDOE1002	Base Short No Hole	4
3	UMDOE1003	Base Short	3
4	UMDOE1004	Corner Vert	4
5	UMDOE1005	Connector Arm	8
6	UMDOE1006	Connector	8
7	UMDOE1007	Base Long No Hole	2
8	UMDOE1008	Vert Diagonal	8
9	UMDOE1009	Mold	1
10	UMDOE1010	Middle Support	9
11	UMDOE1011	Sheet Metal	1
12	UMDOE1012	LE Wedge	2
13	UMDOE1013	TE Wedge	2
14	UMDOE1014	Middle Support Plate	9
15	UMDOE1015	End Cap	9
16	UMDOE1016	Diagonal Small	2
17	UMDOE1017	Diagonal Long	2
18	UMDOE1018	Connector Plate	16
19	UMDOE1019	M3 Fastener	36
20	UMDOE1020	M2 Fastener	120

a) full assembly drawing b) bill of materials

Figure 4.5.1 Example engineering documents for procurement of the 1:20 scale support structure

5. Assembly and Testing of Prototype Molds

Mold module prototypes procured from DM3D were laser scanned to check their dimensions both individually and as assemblies. Other tests included vacuum retention of the mold airfoil profile surface and assembly joint, and hot air tests to determine the mold surface temperature distribution.

5.1. 1:100 scale Version 1 mold dimensional analysis and hot air tests

The machined prototype of the Version 1 mold was compared to its CAD model using a 3D point cloud generated with a laser scanner. The critical airfoil profile surface was found to be within 0.0066 inches of design intent, Figure 5.1.1(a). Dimensions on other planar surfaces were within 0.050 inches, Figures 5.1.1(b)-(d). Perpendicularity between machined planes was <0.005 inches, meeting the <0.039 inch target. The Ra surface roughness of the airfoil profile surface ranges from 0.261 to 0.326 µm longitudinally, and 0.280 to 0.377 µm transversely. This confirmed that the printed and machined component met the external specified dimensions.

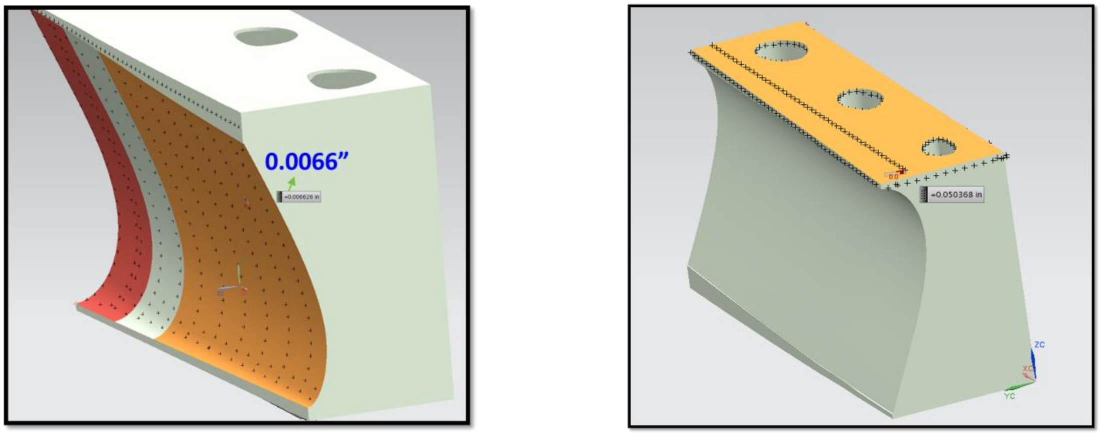

(a) airfoil profile surface

(b) inlet plane

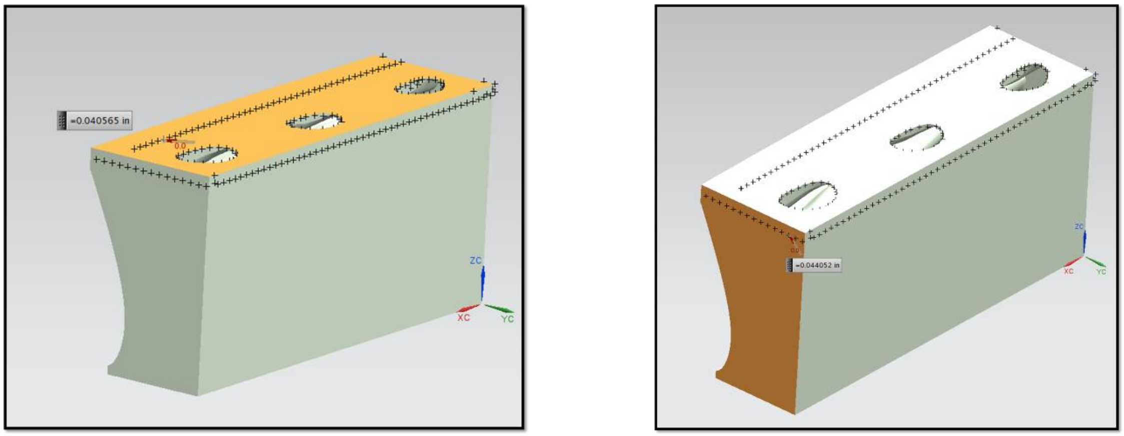

(c) outlet plane

(d) side plane

Figure 5.1.1 Dimensional compliance of Version 1 prototype to CAD model

An attempt was made to validate the Version 1 finite element simulation performed during the design validation phase, Section 2.2. An experiment using hot air replicated the following simulation conditions, Figure 5.1.2:

- Inlet temperature: 75°C
- Inlet air velocity: 0.1 m/s
- Approximately adiabatic mold sides and bottom
- Constant convective heat loss at the mold surface

Despite the inlet temperature being held constant at ~75°C, the mold surface plateaued at ~60C. Insulative cloth was utilized to approximate the adiabatic conditions on the sides and bottom of the mold. Unfortunately, control over the convective heat loss at the mold surface is difficult and likely resulted in the inability to reach the targeted temperature. This exercise helped refine the test protocol for the Version 2 mold prototypes.

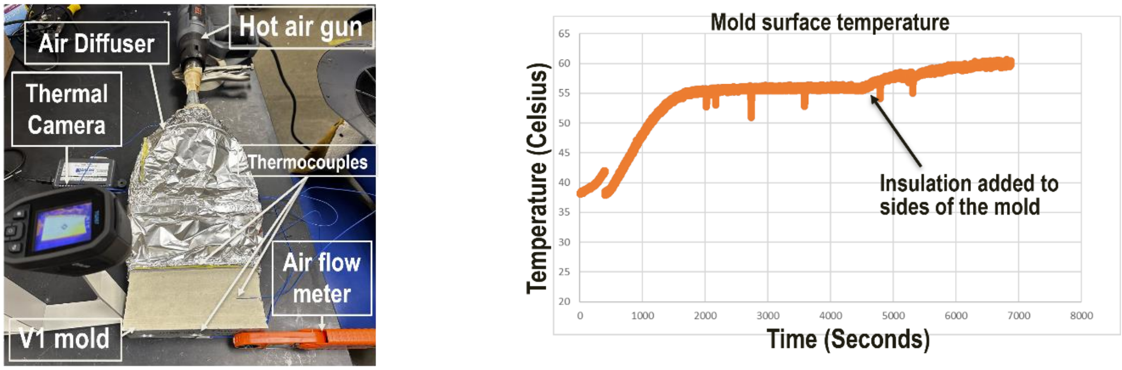

(a) set-up for hot air testing

(b) temperature on airfoil profile surface

Figure 5.1.2 Hot-air test on 1:100 scale Version 1 mold prototype

5.2. 1:100 scale Version 2 mold dimensional analysis and hot air tests

The machined prototype of the Version 2 mold was compared to its CAD model using a 3D point cloud generated with a laser scanner. The critical airfoil profile surface was found to have a machining error between 0.468 to 1.204mm, Figure 5.2.1, above the +/-0.5mm target. This airfoil profile surface error was attributed to the thin profile deck at that scale, in comparison to the Version 1 design whose profile deck had more structural support that was observed to have a machining error of 0.216 to 0.468 mm. This deviation is not anticipated to be a problem when the design is scaled up to full size. Perpendicularity between machined planes was measured to have a range of -0.164 to +0.124mm, meeting the <1mm target.

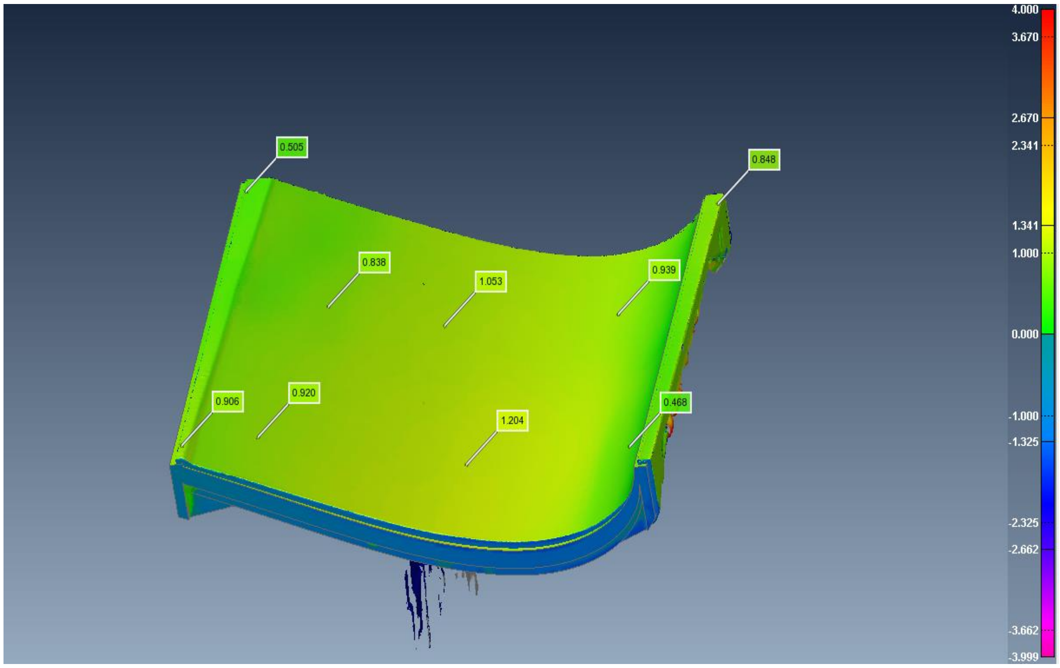

Figure 5.2.1 1:100 scale Version 2 airfoil profile surface machining error

The specification for the gap between two joined molds is <1mm. The two 1:100 scale mold prototypes were manually aligned and clamped together, and the interfacial gap was measured with a high-resolution panorama stitching Olympus DSX Optical Microscope, Figure 5.2.2. Twenty-five points were sampled across the mold gap and the distribution of measurement is shown in Figure 5.2.3. The maximum gap distance of 0.258mm, well below the maximum gap objective.

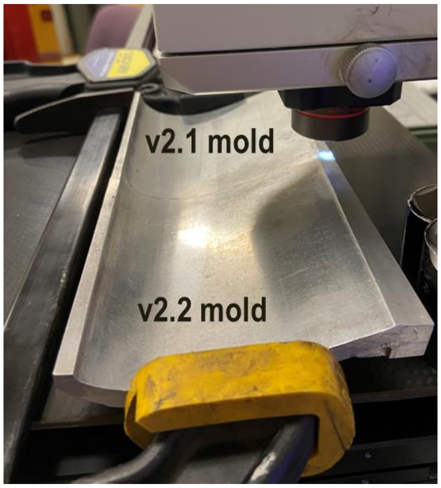

Figure 5.2.2 Mold gap scan configuration

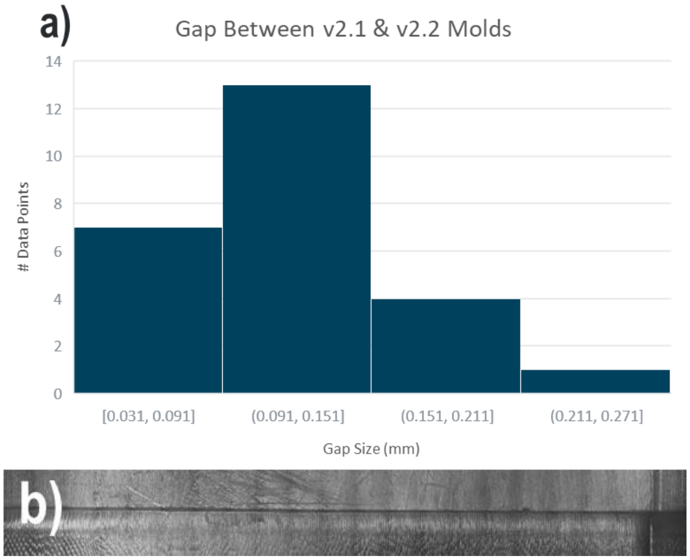

Figure 5.2.3 Interface gap dimensions. a) distribution of measured gap distance
b) high-resolution panorama stitching of the mold interface area

Testing the 1:100 scale mold prototype assembly provided experience toward finalizing the test setup for the 1:20 scale mold testing and to better understand its challenges. For example, experiments determining the thermal steady-state of the mold during hot air testing found that a higher inlet temperature was required, 105°C actual vs 75°C predicted, to reach the targeted 70°C mold surface temperature. At the time, this discrepancy was attributed to different adiabatic assumptions made in the simulation that could not be practically duplicated in the physical experimentation. However, additional testing found that the thermocouple reading at the inlet of the mold was not representative of the inlet temperature profile as there were thermal losses within the inlet air ducts. These losses result in non-uniform temperature distributions that then required higher readings at the thermocouple to achieve the targeted surface temperature.

The prototype assembly can be seen in Figure 5.2.4. The mold assembly was held together by a large hand clamp that held the outer edges of along the longitudinal direction. A hot air test was performed at room temperature and at temperature (70°C) and a laser scan collected dimensional point cloud of the airfoil profile surface. The temperature of the mold inlet and surface was monitored by thermocouples. A baseline surface laser scan was performed at room temperature. After flowing hot air for approximately 35 minutes, the surface of the molds reached the specification temperature, a hot laser scan was taken. Comparing the change in surface position with the chord specifications, Figure 5.2.5 shows thermal distortion was well below the allowable tolerances. The change in surface distortion was found to be less than 1% of chord at all locations in the assembly.

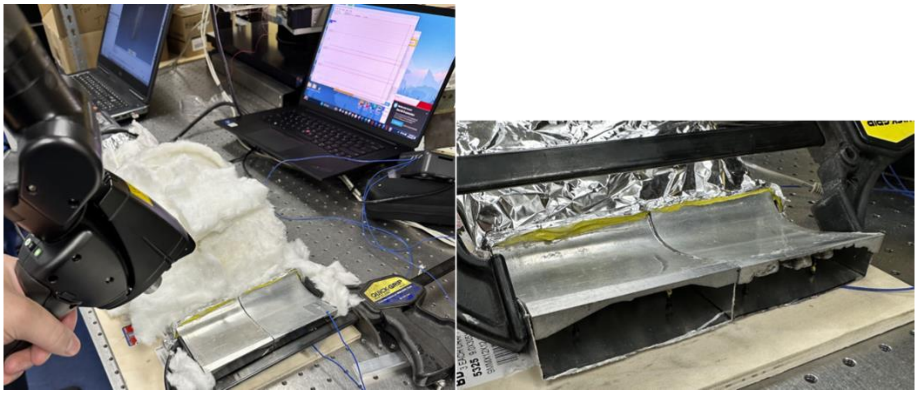

a) laser scan set-up b) mold assembly outlet

Figure 5.2.4 Version 2 mold assembly at 1:100 scale. a) Romer arm laser scan device pictured taking room temperature scans of the mold assembly. Thermal insulation covers the inlet. b) The outlet of the assembly. The clamp holds the molds together after they are aligned by their support pillars.

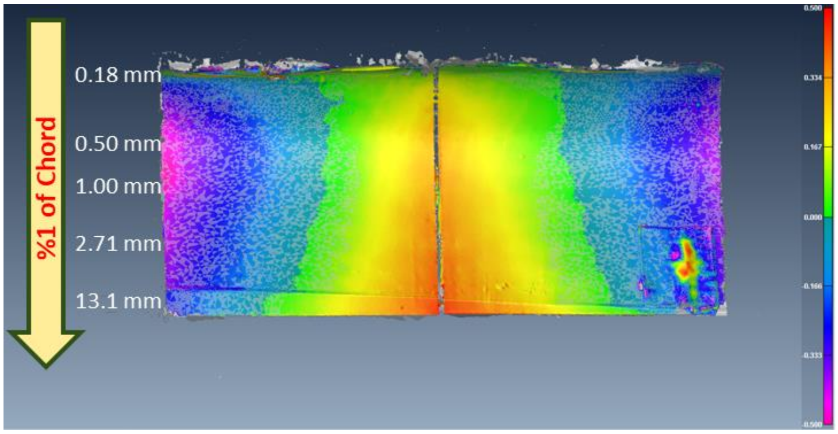

Figure 5.2.5 Version 2 mold assembly 1:100 scale surface deviation from baseline scan at 70°C. More distortion seen at the center of the mold assembly, likely due to “beam” deflection as the mold interface at the center of action to the clamp. The lower right corner of the assembly shows the thermocouple location on the mold surface.

Good insulation of the inlet air ducts was determined to be necessary for uniform thermal profiles. Figure 5.2.6(a). shows the test set-up where ceramic insulation is bundled around the inlet duct to reduce heat loss and increase the uniformity of air temperature as it reaches the mold. Figure 5.2.6(b) shows thermocouple heating profile where an inlet temperature of approximately 80C results in the targeted mold surface temperature of 70C. Using the thermal camera on the inlet, outlet, and surfaces, Figure 5.2.6(c), the mold surface is observed to be emitting heat to the environment at a uniform rate. Note that the dark line on the mold is from the thermocouple wire and not indicative of actual surface temperature distribution. Distribution. The thermal image indicates the mold surface temperature varied by ±0.2C. As shown in Figure 5.2.6(d), some thermal loss is still seen from the side of the mold that FEA simulations assumed to be adiabatic.

The RTRC simulation group was informed of this heat loss so that the 1:20 scale Version 2 mold could better model the thermal loss at the sides and bottom of the mold assembly.

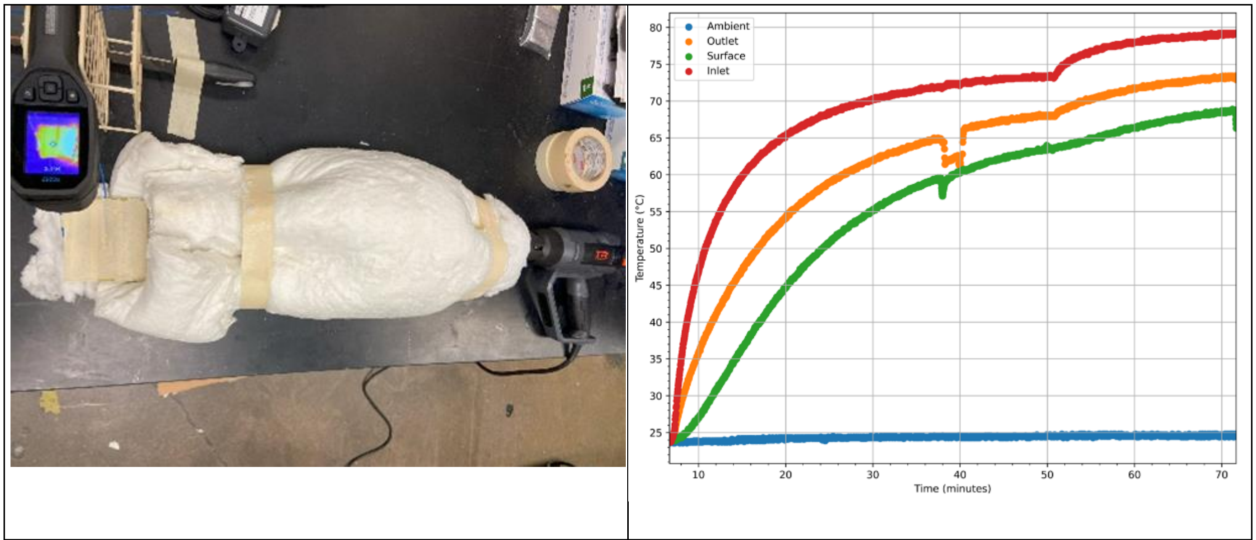

(a) Set-up for hot air testing

(b) Temperature at centerline mold position

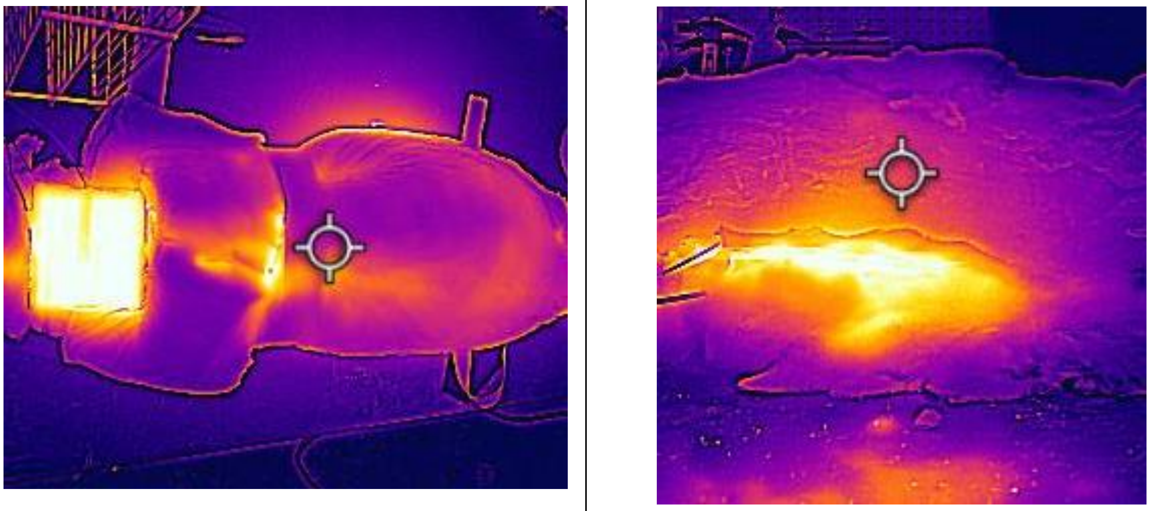

(c) Test set-up with inlet insulation

(d) Thermal camera image of mold side

Figure 5.2.6 Hot-air test on 1:100 scale first generation mold.

Table 5.2.1 summarizes the performance accomplishments measured for the 1:100 scale Version 2 molds, individually and as assemblies.

Table 5.2.1 Summary of 1:100 scale Version 2 prototype testing performance accomplishments

Performance Characteristic	***Target***	***Performance Achieved***	***Comments***
Perpendicularity of mold horizontal base to mold axis 100% Achieved	< 1mm	<0.125mm	Using laser scanning (1:100).
Gap between two assembled modules 100% Achieved	< 1mm	Mean gap: 0.112mm, Minimum gap: 0.032mm, Maximum gap: 0.258mm	Using laser scanning. Second-generation molds (1:100).
Profile surface temperature from module heating circuit 100% Achieved	80±5°C	Analytical: 79.4±0.7°C Experimental: 79.2°C	At profile surface (1:100)
Vacuum integrity of seam line at the mold joint 100% Achieved	10 mbar vacuum for minimum of 60 min at a surface temperature of 80±5°C	Mold 4 stand-alone: <10 mbar loss for 60 minutes at ambient temperature	Using industry standard vacuum bag at mold surface temperature specifications and cure time. Mold versions 2 and 3 (1:100).
Seam line at the mold joint ≤ 1mm 100% Achieved	≤ 1mm	Mean gap: 0.099 mm, Minimum gap: 0.025 mm, Maximum gap: 0.172 mm	In sample material at mold joint under vacuum. Mold versions 2 and 3 (1:100).

5.3. 1:20 scale Version 2 prototype inspection, dimensional analysis, and mold assembly

Prior to the assembly of the 1:20 scale mold with a neighboring module, the Version 2 Module A was dimensionally inspected for its conformance to the CAD models. The dimensional accuracy verification process was standard, using a *Hexagon Romer Absolute Arm*, a red light-based laser scanner as a Coordinate Measuring Machine (CMM). This arm provides a scan area of approximately 50 x 50 cm with a feature resolution as fine as 0.05 mm. Owing to the mold module's substantial size, it was scanned in sections and the scan data was digitally combined in the analysis phase. Figure 5.3.1(a) illustrates the airfoil profile surface dimensional accuracy. The laser scan found that the critical airfoil profile surface conformed to the CAD specification with less than 0.3mm deviation, while the bottom topographically optimized features were within ±5mm, Figure 5.3.2(b).

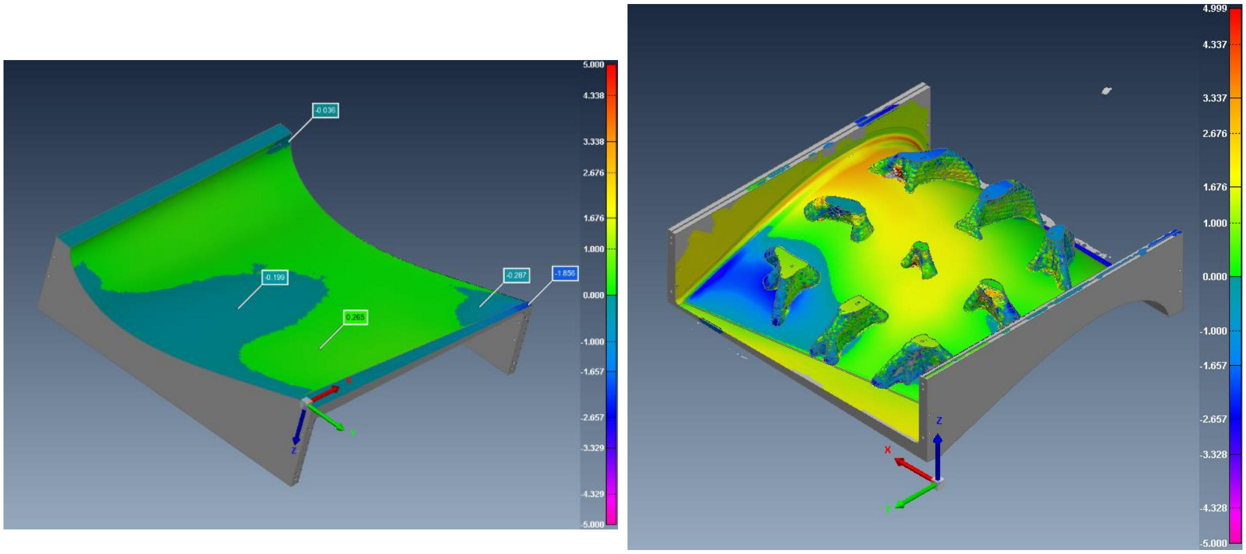

(a) airfoil profile surface (b) TO underside

Figure 5.3.1 1:20 scale Version 2 Module A machined surface conformance to CAD model

The dimensional accuracy of the Version 2 Module B underwent a similar dimensional verification process as Module A with the overall dimensional accuracy of the mold compared to the CAD specifications. The results of this inspection are illustrated in Figures 5.3.2. The color map images use a range of -4 to +4 millimeters, which is less than the 1% cord tolerance specification of the largest cord dimension of Module B, indicating its high precision. The topologically optimized (TO) features on the reverse surface of the were also measured, Figure 5.3.2(c). These non-critical features are not machined and are in their as-printed state. Although slight deviations from their CAD model dimensions were observed, they were not expected to significantly disrupt the airflow or heating-cooling cycle performance of the mold. Moreover, these dimensional deviations are not expected to be observed in a full-size module, as the printed material line width does not scale proportionally with the increase in mold module size. The curvature of the airfoil profile surface where it mates to Modules A and C was compared to the curvature manually extracted from the CAD model. The results observed fell within 1% of design intent, Figure 5.3.3.

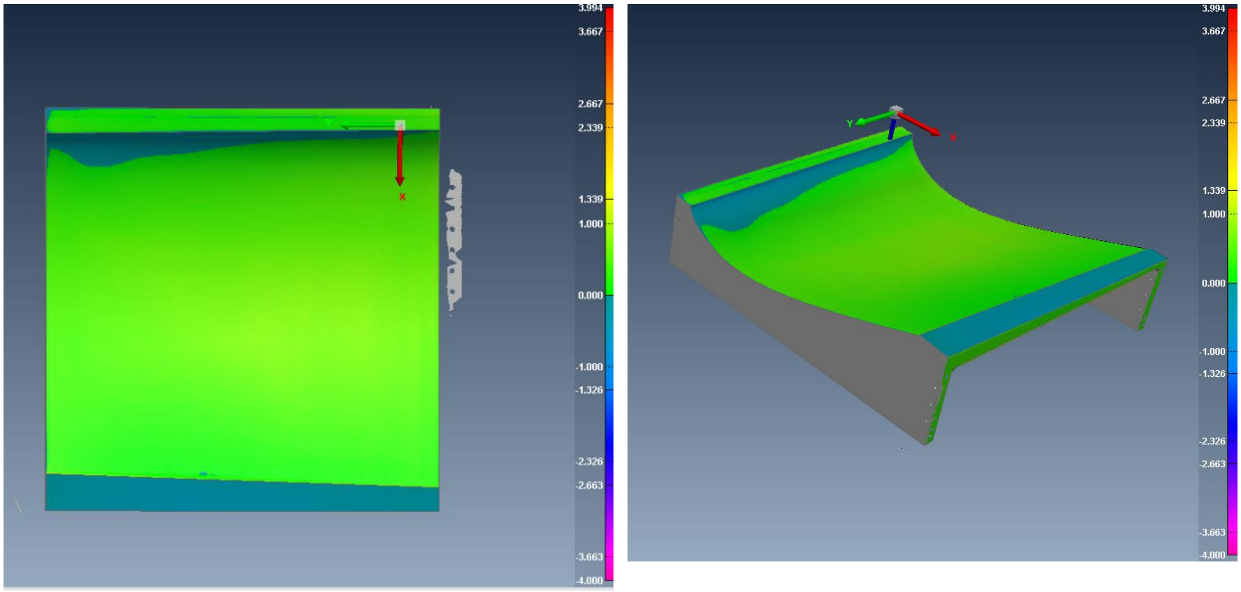

(a) critical airfoil profile surface (b) 3D view airfoil profile surface

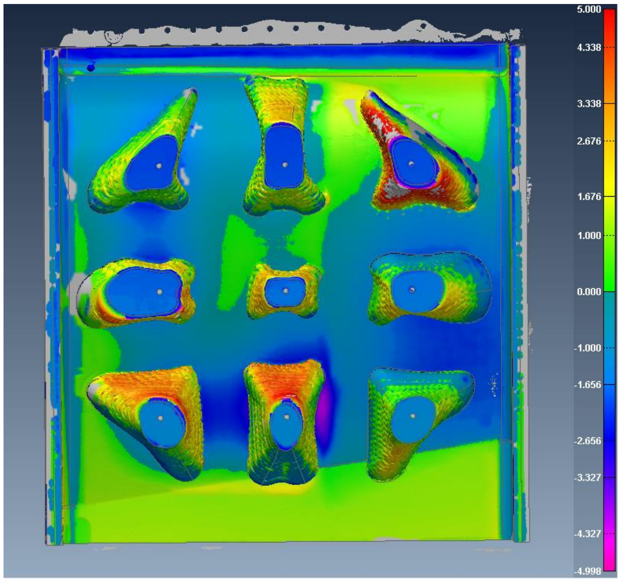

(c) TO underside (feature dimensions are not critical)

Figure 5.3.2 1:20 scale Version 2 Module B airfoil profile surface color map showing deviation from design intent (mm)

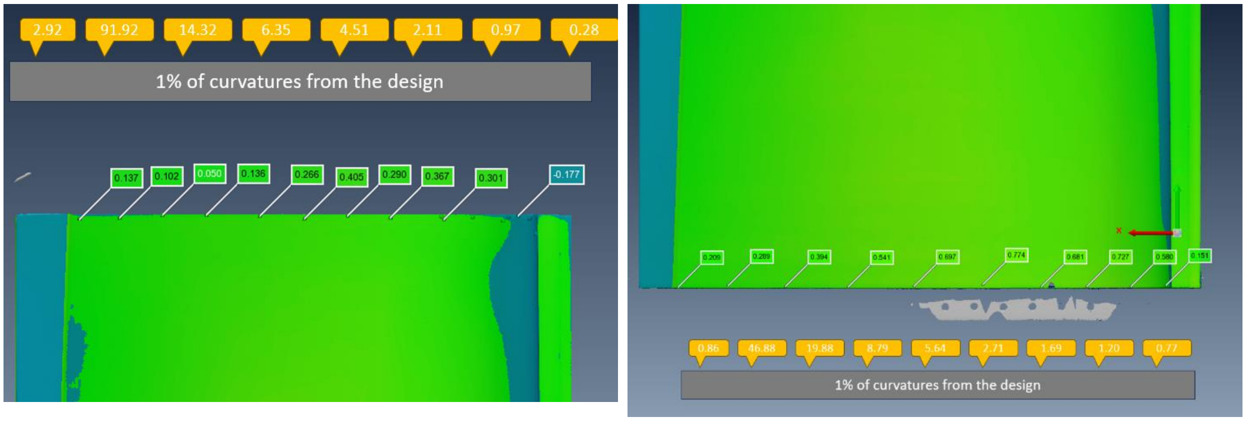

(a) mating end (b) opposite mating end

Figure 5.3.3 1:20 scale Version 2 Module B dimensions of the airfoil profile curve (mm). Expected CAD dimensions are shown in the yellow bubbles.

Visual inspection of the 1:20 scale Version 2 Module A airfoil profile surface indicated the presence of pores after machining, Figure 5.3.4(b). The mold was too large to fit under the optical microscope for precision scans, but all large pores observed were measured with calipers at <1mm. The 1:20 scale Version 2 Module A was vacuum tested before assembly with Module B as an independent module, Figure 5.3.4(a). Module A passed the vacuum tests easily, holding pressure with <10 mbar loss in vacuum over 60 minutes. This indicates that the few surface pores that were found during inspection are not connected through the thickness of the mold. Primary surface roughness appears to be the result of machining and can be remedied by post machining surface polishing or mold sealant and release coatings.

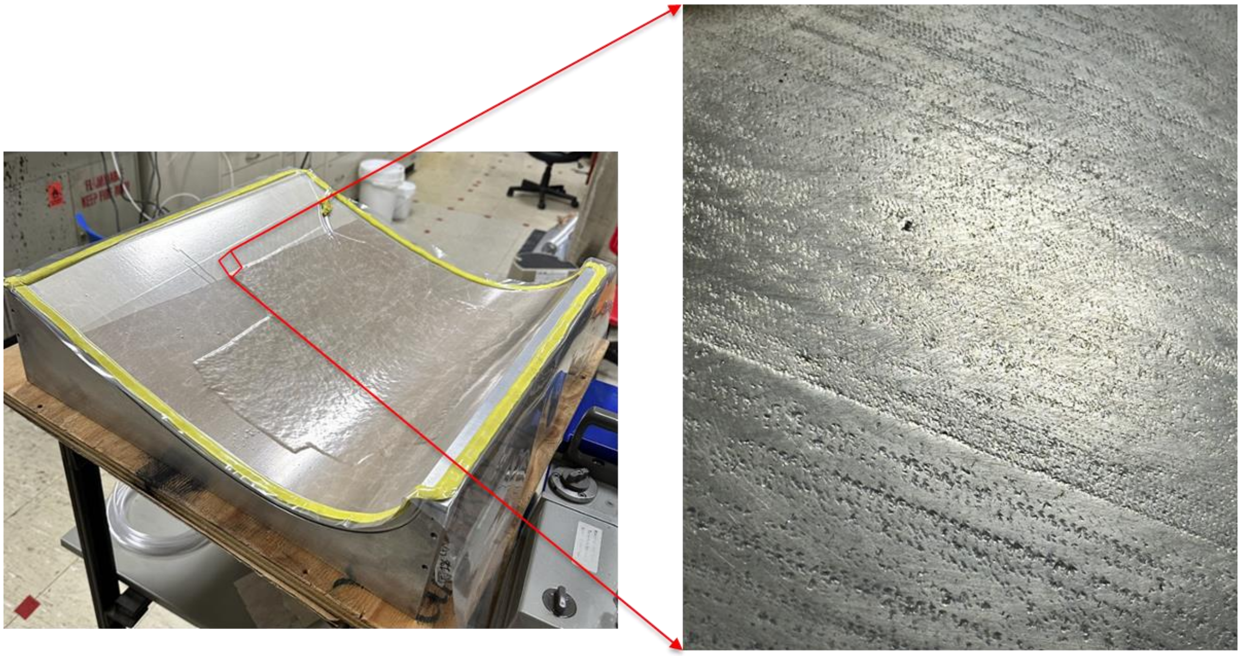

(a) vacuum test of vacuum retention at surface (b) zoomed image of surface finish

Figure 5.3.4 Surface finish and vacuum test of 1:20 scale Module A

An example of the Version 2 mold-to-support frame assembly is shown in Figure 5.3.5. The support frame for Module B differs slightly from the frame for Module A to conform with its airfoil surface variations as well as the printed design features on its underside. However, the Module C support frame and its interface to the mold module was specifically designed to duplicate the frame of Module B to reduce design overhead.

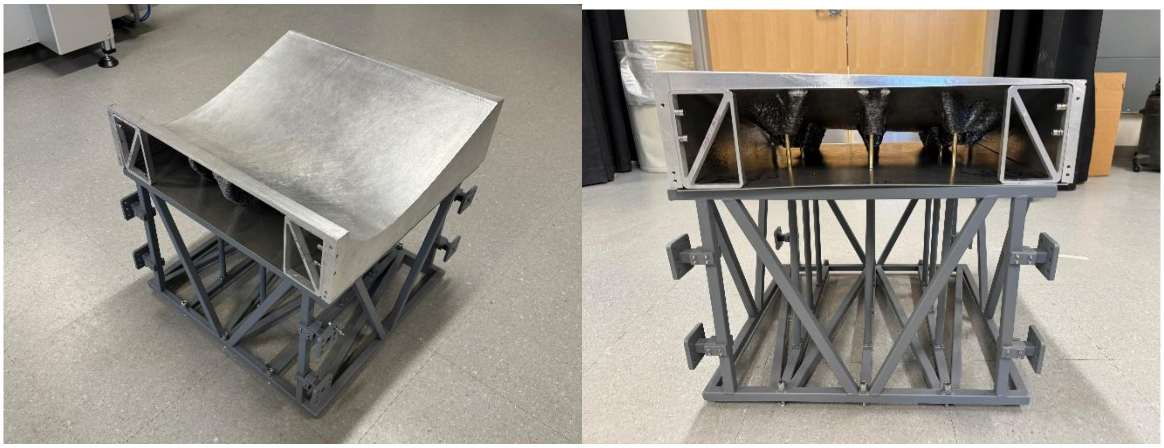

Figure 5.3.5 1:20 scale Version 2 Module A mold and frame assembly. Note the sheet metal enclosure and side-wall stabilization brackets are modular to each mold.

The 1:20 scale Version 2 Modules B and C were mated together on their stands and the difference in height at their joint was measured. The height differential measurement was taken using a horizontal dial test indicator along the joint line at approximately every 5 cm, Figure 5.3.6. The average difference between the two molds at the seam line was 0.1 mm, well within the specification of <0.5mm. The range of observations was 0.0 to 0.2 mm, indicating that the joint differential error is expected to be controllable.

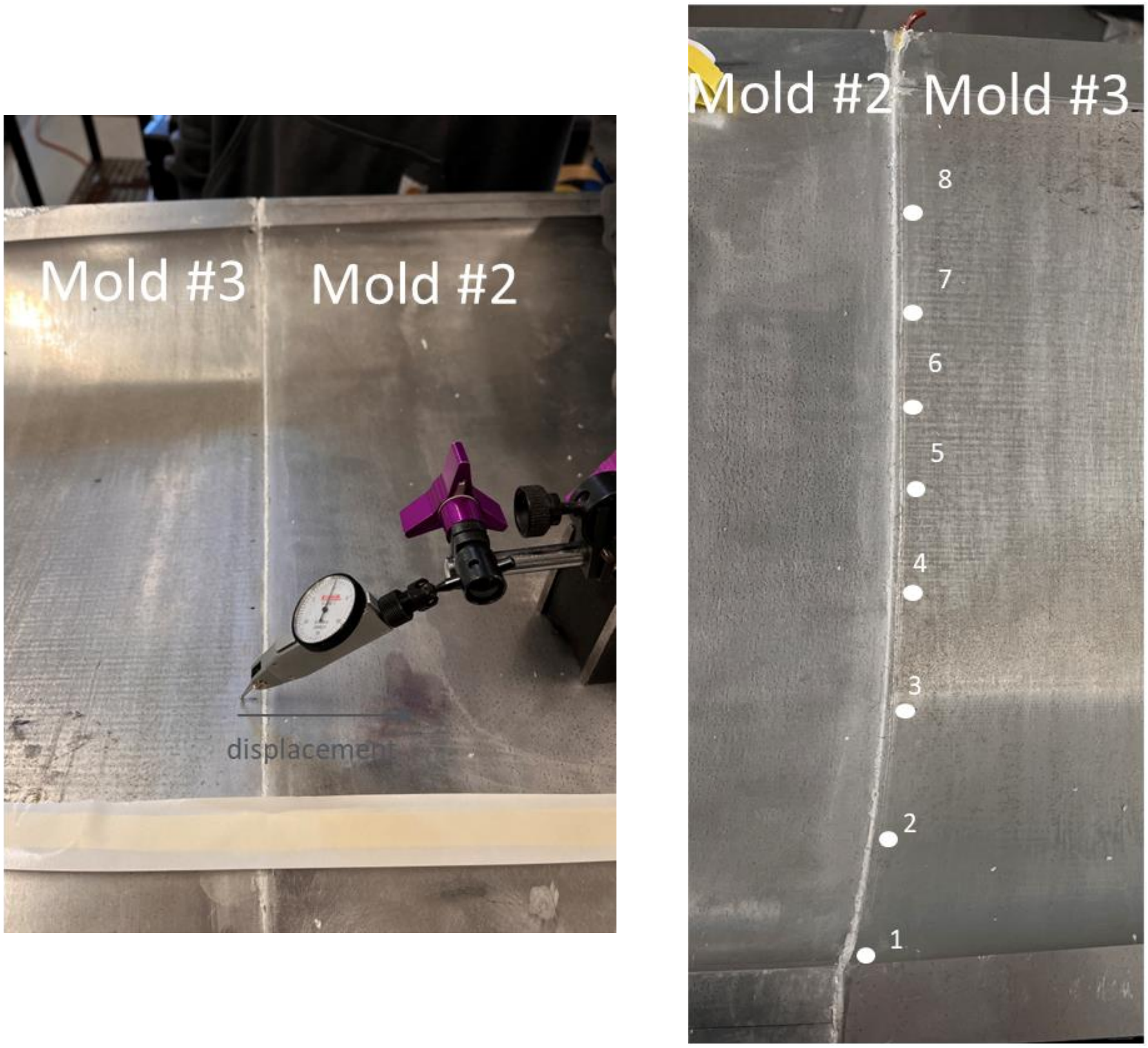

(a) test set-up (b) data collection locations at seamline

Figure 5.3.6 Mold height differential between Version 2 Modules B and C at assembly joint

The three 1:20 scale Version 2 mold assemblies, mated together, then the airfoil profile surface underwent a vacuum test. A vacuum bag consisting of CompositeEnvisions vacuum film and sealant tape was connected to a DMT RS-1 vacuum pump, Figure 5.3.7. A steady vacuum pressure of 88 kPa was held successfully for 240 minutes with no leakage observed, exceeding the 10 millibars for one hour specification requirement.

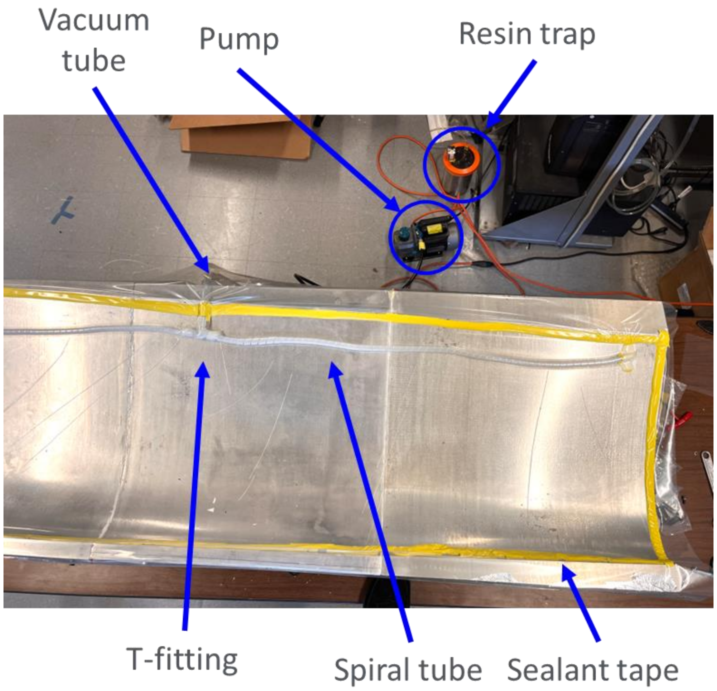

Figure 5.3.7 Test set-up for thee mold 1:20 scale Version 2 assembly vacuum test

5.4. 1:20 scale Version 2 prototype hot air test

Before assembly of the three molds, individual mold's temperature profile were independently tested on its support stand to observe if any anomalies were present. Mold Module B was typical of these tests and will be presented here. Figure 5.4.1(a) shows the location of the thermocouple placement for mold Module B, which was approximately the same for the other two modules. A temperature range of 75-80C was observed on mold Module A's airfoil surface, with 75-79C on Module B, and 75-78C on Module C, respectively. The thermal camera, measuring the ambient temperature on the thermal batting surface, had a range of about 21-28C, Figure 5.4.1(b), with a hotspot of 43C observed on the airfoil batting surface of Module C. Heating of the individual molds was similar, with steady-state being achieved in about two hours. A significant amount of variance was observed in the thermocouple temperature, but this can be attributed to the mounting of the thermocouple wires, which grounded out on the mold surface. Figure 5.4.2 shows the variance in the raw data of mold Module B, and the temperature trend when filtering the temperature signal using a moving average with a window size 15.

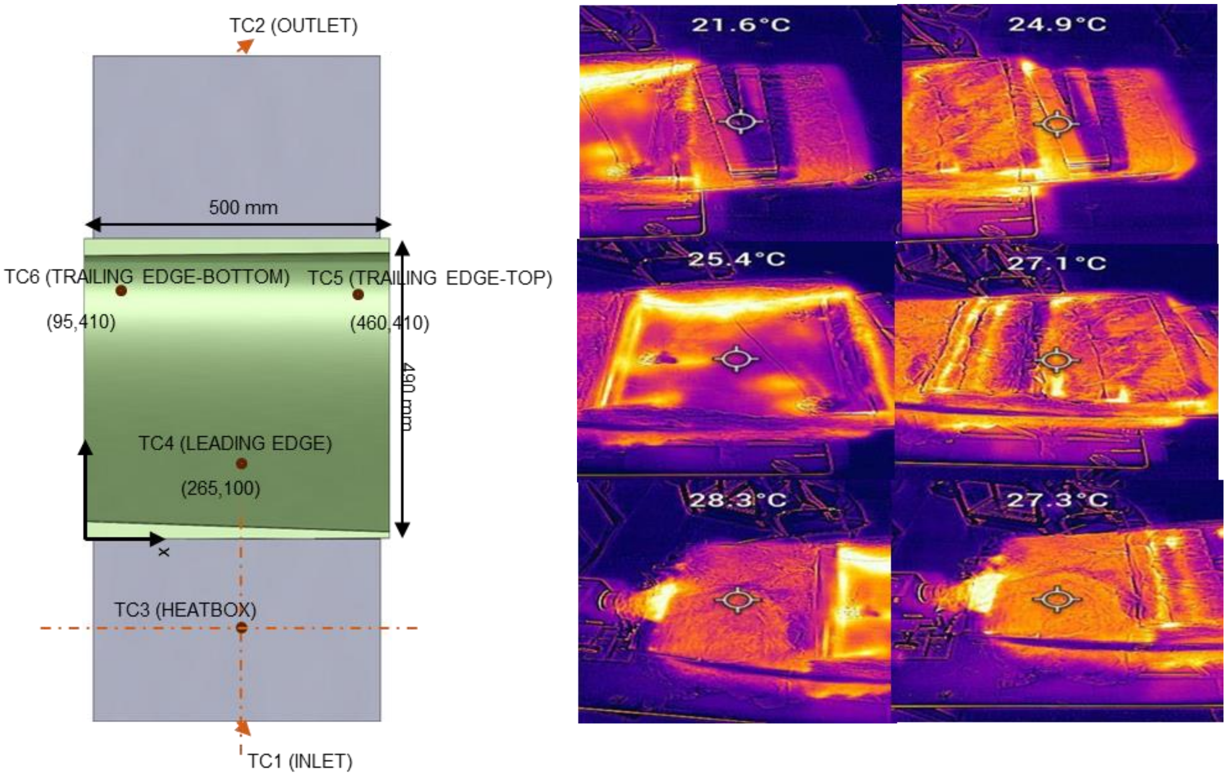

(a) thermocouple locations

(b) thermal camera temperature profile on insulative batting (ambient temp shown)

Figure 5.4.1 Thermocouple locations and temperature profile of the 1:20 scale Version 2 Module B

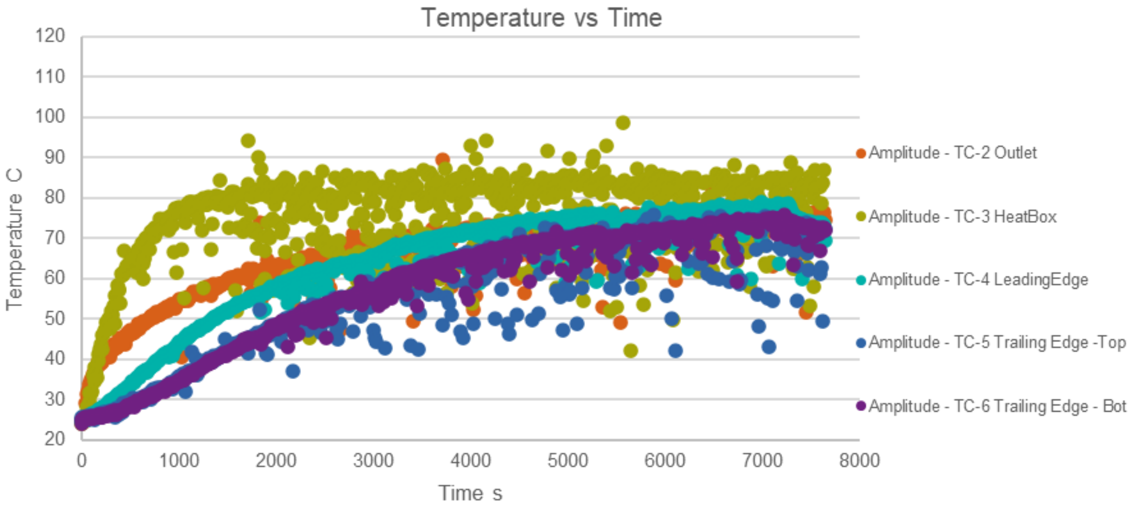

(a) Raw temperature data showing data variance

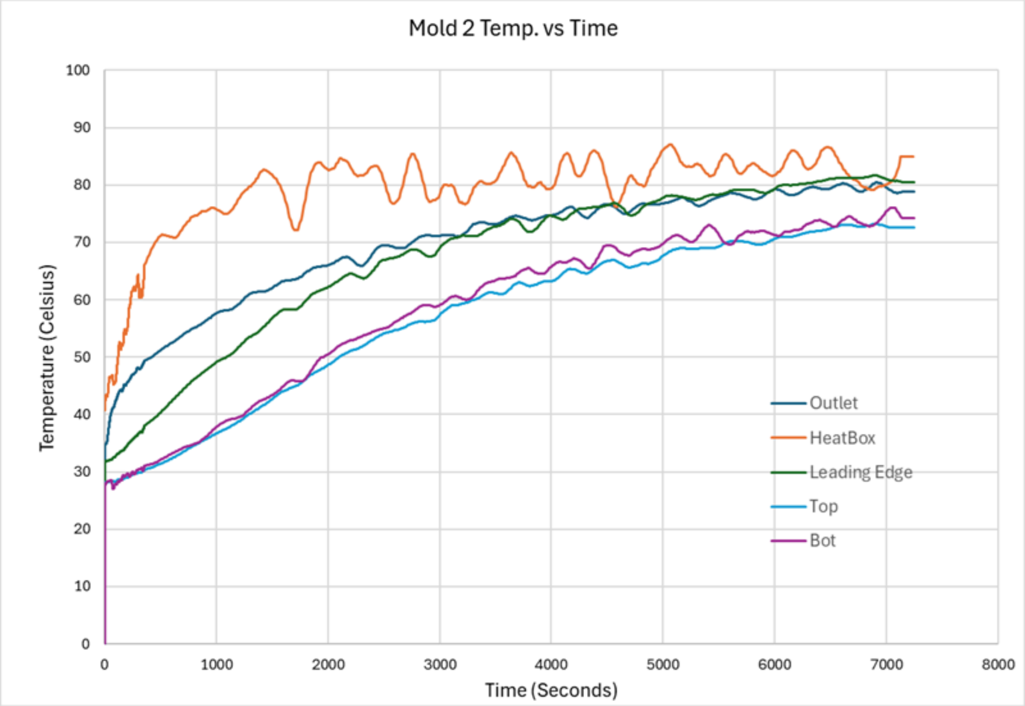

(b) Filtered temperature data showing trend

Figure 5.4.2 Temperature profile of Version 2 Module B during heat-up

The three 1:20 scale Version 2 prototype molds were assembled with their support stands and their inlet and outlet plenums for prototype testing, Figure 5.4.3. The thermal insulation batting pads on the inlet and outlet plenums and the top, bottom, and sides of all molds were secured using 3M aluminum insulation tape. The airfoil profile surface was insulated using removable pads so that it could be exposed when necessary for the thermal camera when taking surface temperature profiles. Thermocouples were adhered to the airfoil profile surface using foil insulation tape. The inlet and outlets and other significant points were also instrumented for temperature. A summary of the test equipment and conditions is given in Table 5.4.1

Table 5.4.1 Test Equipment and Conditions

Test Equipment	***Equipment Specification***	***Test Conditions***
Data acquisition software	National Instruments USB-6343	Room temperature: 20.5 C
Thermocouple	Type-K	Humidity: 54%
Insulation pads	McMaster Fiberglass	Inlet velocity target: 6 m/s
Temperature camera	FLIR-TG267	Inlet heater temp target: 95 C
Anemometer	EXTECH 45118	
Heat blower	HERZ	

(a) top view with insulation removed (b) top view with top insulation in place

Figure 5.4.3 1:20 scale Version 2 three mold assembly test set-up

Thermocouple temperature measurements were taken for the three-mold assembly. Each mold had a separate heat source that was independently and manually controlled. The temperature range observed for the three-mold assembly was 75-80C. Mold Module C, which incorporated the lessons learn from fabricating the first two molds, had a temperature range +/-3C, meeting the target range target. Demonstrating the evolution in the design and fabrication of the three molds, mold Module A had a temperature range of 5C, while mold Module B had a temperature range of 4C. Possible causes for surface temperature deviation between the molds include design differences of internal structure leading to different heat conduction, and variation in the porosity within a mold that may cause uneven thermal conductivity and heat retention. Figure 5.4.4 shows the thermocouple locations. Figure 5.4.5 shows the dynamic temperature profile during heating (filtered) of the three-mold assembly.

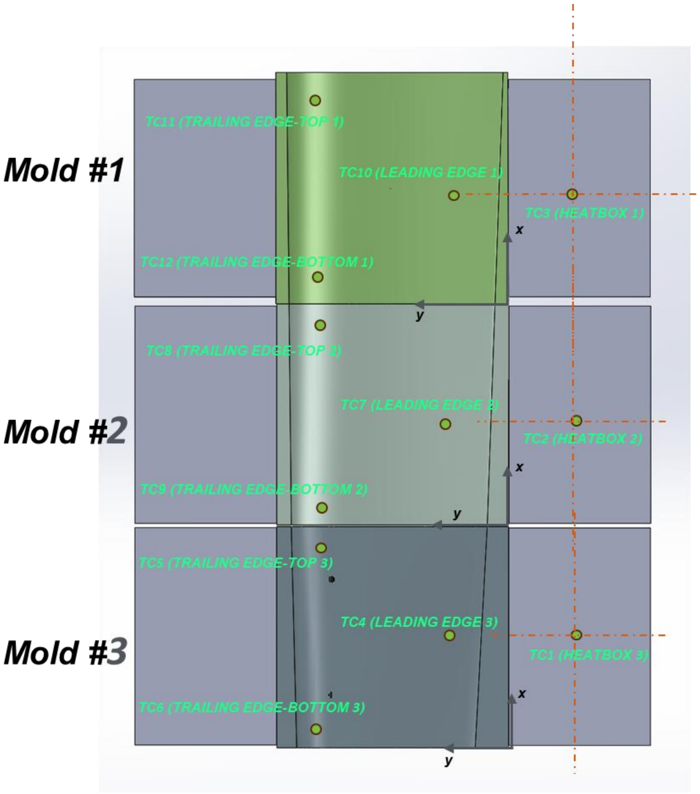

Figure 5.4.4 1:20 scale Version 2 three mold assembly thermocouple locations

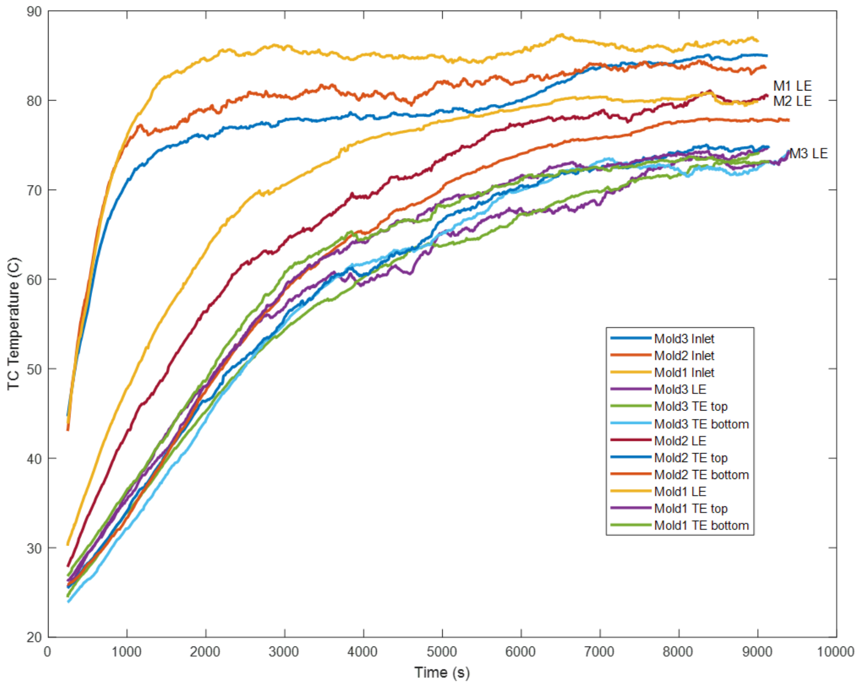

Figure 5.4.5 1:20 scale Version 2 three mold assembly temperature trend during heat-up (filtered using a moving average window size of 100)

Figure 5.4.6 shows the temperature profile detected by the thermal camera both without (top three images) and with the insulative batting. As can be seen, the temperature is fairly uniform except at the mold assembly joints. This is likely due to the side walls acting as fins, but it is expected that at steady-state the non-uniform temperature at the joint will dissipate. Additional study will be required to adjust the mold structure to even out the heat conduction at the joints during heating.

The results of the hot air test were compared to the RTRC FEA simulation to ensure that the experimental setup for the prototype was consistent with the assumptions made during the performance analysis. RTRC concluded that the experimental set-up and their simulation have some differences in detail but overall are similar. For example, the RTRC Fluent CFD simulation was run as a static steady-state, which assumes that the time to reach steady-state for the inner surface topology is significantly less for the entire tool. Thermal simulation comparison to the experimental set-up for a single mold are given in Table 5.4.2. Given the assumptions on the boundary conditions, the simulation and experiment agree quite well, with the experimental results suggesting there is more heat loss than modeled but that the results compare very well.

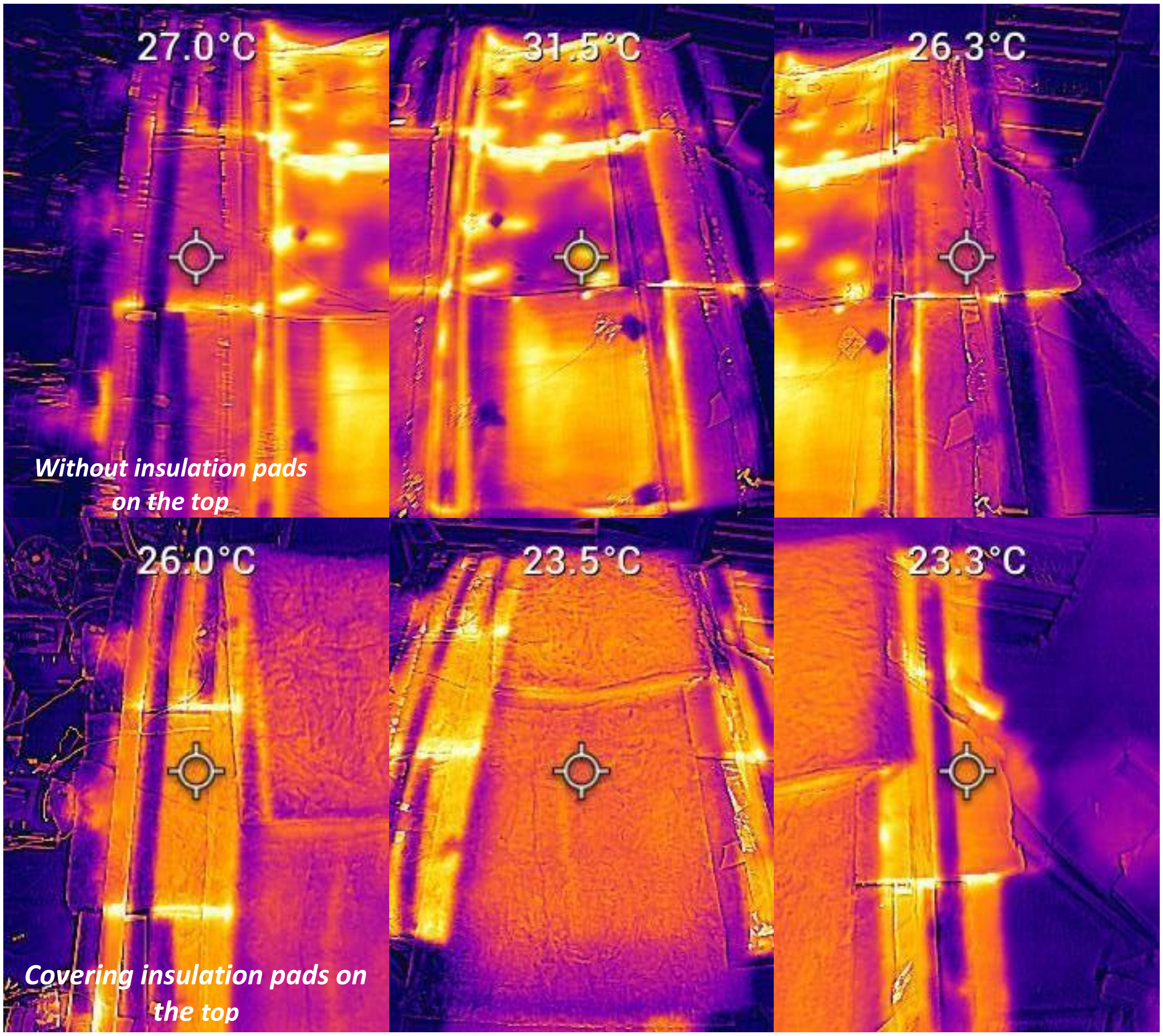

Figure 5.4.6 Thermal camera temperature profile for three-mold assembly (ambient temperature noted)

Table 5.4.2 Comparison of simulation to experimental result for Version 2 Module A

Thermal Property	***Simulation Result***	***Experimental Result***
Mold Temperature Range	72 – 75°C	73 – 78°C
Temperature Variation	1 - 3°C (depending on which simulation)	~4°C
Temperature on top of airfoil insulation	27 – 31°C	36 – 38°C
Time to Steady-State Temperature	~2 hrs (whole mold) 0.66 hrs (tool temperature)	~2 hrs

5.5. 1:20 scale Version 2 prototype carbon fiber reinforced resin impregnation test

A demonstration of the glass fiber reinforced matrix with vacuum impregnated resin was performed on the 1:20 scale Version 2 three mold assembly. The fiber was a plain weave fabric with a non-woven mat having a total volume of 3.51e-4 m^3. The resin value was determined from the fraction ratio at 2.34e-4 m^3. Figure 5.5.1 illustrates the mat orientation and assembly into the vacuum bag. The process took 30-40 minutes to infuse the resin, two hours to heat up to 75C, and 40-60 minutes to cure, validating the curing rate for the 1:20 scale Version 2 mold with conformal channels. The glass fiber shell, extracted from mold, is presented in Figure 5.5.2.

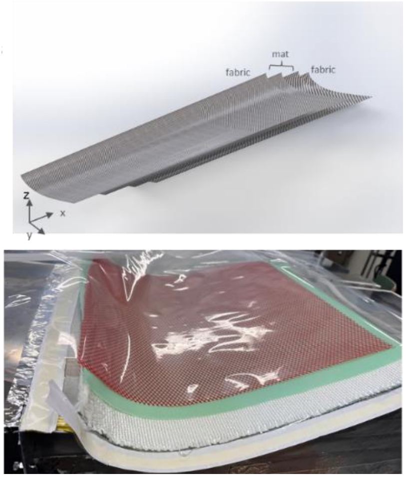

Figure 5.5.1 Fabrication of a composite shell on the 1:20 scale Version 2 three mold-module assembly

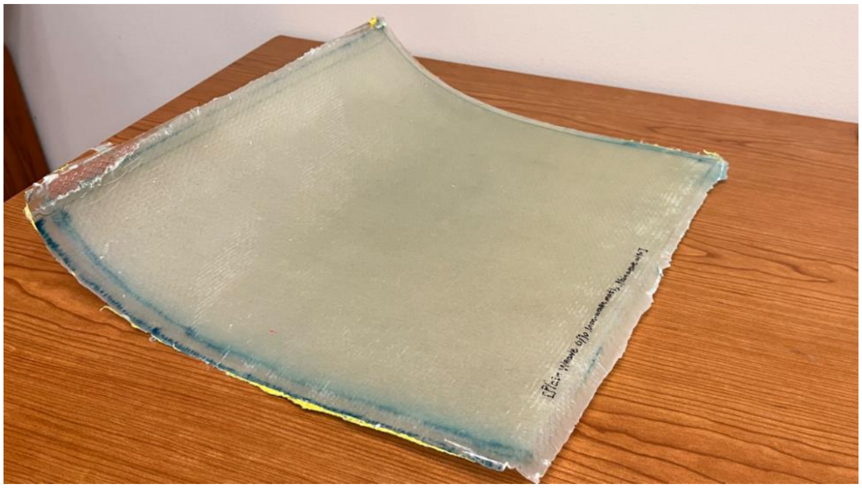

Figure 5.5.3 Glass fiber composite shell extracted from the Version 2 modular mold assembly

6. Design and Analysis of Superfinishing Method using Electro-Chemical Machining

The work carried out in this task was split between the execution of bi-directional flow PECM experiments and the continuation of surface texture evolution experiments using previously developed apparatus. The results of each are discussed separately.

6.1. Bidirectional flow PECM experiments

The Bi-Directional Flow PECM was successfully assembled, connected to the ISSEL 3-axis gantry system and CoolPulse 1000 PECM machine tool, and used to process 1:100 scale mold specimens. The entire system is illustrated in Figure 6.1.1(a). A close up view of the PECM cell with protruding 1:100 scale mold specimen and bi-directional flow valves is shown in Figure 6.1.1(b).

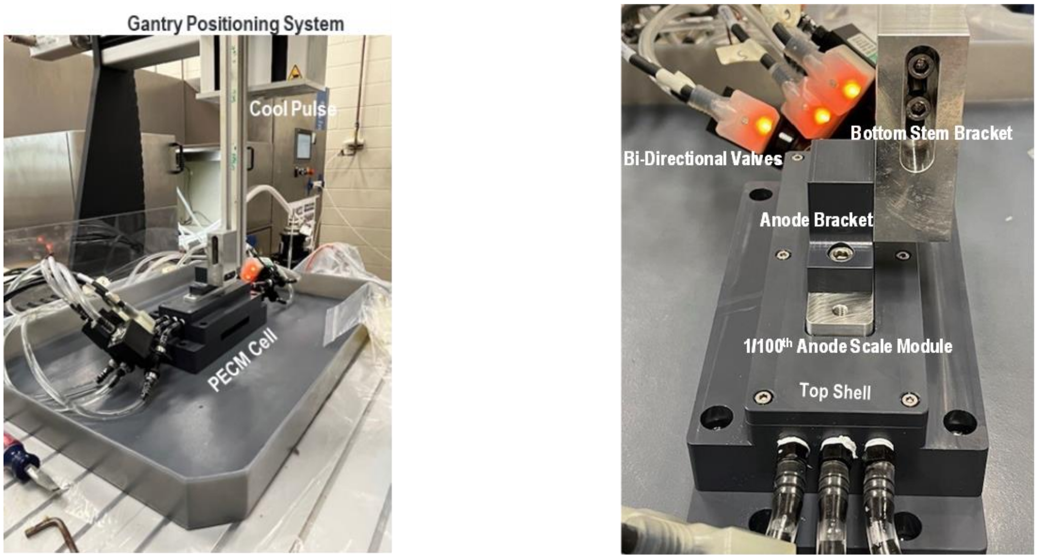

(a) View of the CoolPulse 1000-Gantry System-PECM Cell

(b) Close Up View of the Bi-Directional Flow PECM Cell

Figure 6.1.1 Bi-direction flow PECM system

Chilled and filtered electrolyte was supplied from the CoolPulse 1000 to the PECM cell using the CoolPulse table pump. Heated electrolyte exiting the PECM cell dropped down into a sump container, and in return was transferred back to the CoolPulse main tank using a sump pump.

Figure 6.1.2 shows a close-up view of the interface surface of the mold specimen. This specimen design was used for all experiments. The dimensions of the interface surface were 100 mm x 25 mm. To facilitate texture measurement using contact profilometry, the surface was designed to be flat. The interface surface was finish machined with a 5.556 mm ball nose end mill at a step over of 0.198 mm. This left the surface with a nominal roughness of R_a 6μm.

Figure 6.1.2 1:100 scale mold module flat (100 mm x 25 mm) ball nose end-milled surface

Bi-directional flow experiments were run using a 1 mm interelectrode gap distance (IEGD), and a nominal IEG potential of 30V. However, the electrolyte flow rate was varied from near stagnant up to 1 liter/min. Effort was made to achieve 4 liter/min, the value used for the original bi-directional flow rate experiments that were carried out within the CoolPulse working tank. Unfortunately, this could not be achieved due to the much larger flow path resistance associated with moving electrolyte to and from the CoolPulse and the PECM cell.

During a PECM experiment, the specimen was pulled from the PECM cell for measurement. A Mitutoyo SJ 410 contact profilometer was used to measure and record surface texture profiles and compute texture statistics. A Hexagon CMM with an analog contact probe was used to measure the geometry of the processed surface, store measured point data, and compute surface flatness error.

Figure 6.1.3 shows the evolution of the specimen surface during a typical experiment. Before processing, the surface had a flatness error of 0.02 mm and a roughness of R_a 7.53 μm. Midway through processing after an average of 0.457 mm had been removed from the surface, the roughness was reduced to R_a 1.14 μm, but the flatness error increased to 0.118 mm. At the end of processing, a total of 0.621 mm had been removed from the surface. The resultant roughness was R_a 0.44 μm and the resultant flatness error was 0.079 mm.

Figure 6.1.4 shows the typical distribution of material removal from a processed surface. The independent axes represent the electrolyte flow and cross flow directions. Note the consistent variation in the flow direction. This variation is opposite to what was originally expected. In general, local material removal rate is proportional to local electrolyte conductivity. In turn, this is primarily sensitive to electrolyte temperature. Specifically, conductivity increases with temperature. However, it is also to a much lesser extent sensitive to aluminum hydroxide build-up in the electrolyte, which decreases it.

A separate but related factor is the deposition and build-up of aluminum hydroxide on the anode surface. This is also known to retard local dissolution. It occurs when there is insufficient electrolyte flow to mechanically sweep the deposits from the surface. The depth removal patterns observed in these experiments indicate that aluminum hydroxide build-up on the anode surface maybe the dominant factor. In this case, the regions of lowest flow rate are the ones expected to have the least processing. In the case of the bi-directional flow experiments, for which the inlet flow rates were lower than in the past, the mid region of specimen should be the area of least flow and hence less processing.

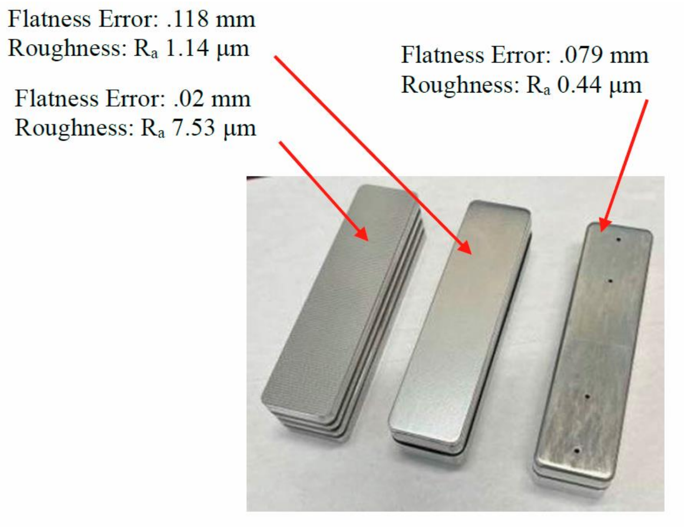

Figure 6.1.3 Observed machining progression of 1:100 scale mold module using bi-directional flow PECM system. Left: No PECM, Middle: 0.457 mm Removed Thickness. Right: 0.621 mm Removed Thickness

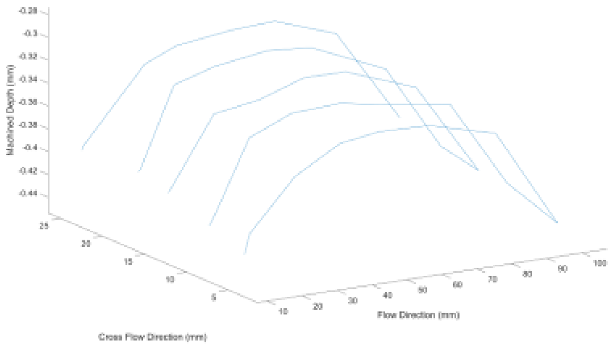

Figure 6.1.4 Machined depth profile of 1:100 scale mold module after 300 s of steady-state PECM

The principal conclusions that were drawn from these experiments are as follows:

- The PECM process removed metal from the specimen surface and in the process of doing so created a new surface with roughness close to the desired value of R_a 0.2 µm and an average flatness error of 100 µm. While the flatness error was substantially larger than that left behind by the proceeding milling process, it was still substantially smaller than the allowable tolerance of 1000 µm (1% of chord length) which was a target of this project.
- The experiments revealed the challenges of achieving a high electrolyte flow rate through a 1 mm high by 100 mm long IEG. Yet despite this fact, the process worked. However, the material removal rate was significantly lower than what was previously achieved at high

flow rates. This is relevant, because achieving a high flow rate through a 1 mm high by 10 m long IEG is most likely impossible. In this scenario, processing will need to be done in near stagnant flow conditions.

6.2. Surface texture evolution experiments

For this project, PECM is being developed and evaluated as a means to finish machine the interface surface of a mold module. The starting texture of this surface will originate by a ball nose end milling process. Previous surface texture evolution experiments were limited to surfaces that were created using a 5.556 mm diameter mill at respective step overs of 0.198 mm and 0.102 mm. In turn, this left behind textures with corresponding theoretical roughness values of R_a 6 μm and R_a 3 μm respectively. These experiments demonstrated that as the surface dissolves during PECM, its measurable roughness decreases at an exponential rate in response to surface profile loss. Furthermore, these experiments indicated that the rate exponent increased with decreased IEGD distance and larger starting roughness.

As insightful as these experiments were, a full-scale mold module will most likely be milled with a ball nose end mill as large as 25.4 mm, based on information provided by Symmetrix Composite Tooling, the current fabricator of tooling used by TPI. To understand the influence this may have on surface texture evolution during PECM, an expanded set of surface texture evolution experiments were carried out using the apparatus and samples shown in Figure 6.2.1.

(a) view of the Phase II PECM cell on the CoolPulse 1000 table

(b) specimen with textured surfaces that were processed using PECM

Figure 6.2.1 Phase II PECM system

These were identical to those used for the original study, however different textures were created using a variety of different mill diameters and step overs. The complete experimental design is shown in Table 6.2.2. The intent of this design was to maintain equivalent values of starting roughness while varying the actual geometry of the texture. Note that the original set of experiments were included in this design.

Table 6.2.1 End milling processes used to create surfaces for PECM experiments

Test	Mill Dia. (mm)	Step Over (mm)	Theo Ra (µm)
1	**25.4**	**1.542**	**6**
2	**25.4**	**1.090**	**3**
3	**12.7**	**1.090**	**6**
4	**12.7**	**.772**	**3**
5	**9.525**	**.945**	**6**
6	**9.525**	**.668**	**3**
7	**5.556**	**.198**	**6**
8	**5.556**	**.102**	**3**

Figure 6.2.2 shows the results of these experiments. These results indicate that the roughness dissolution rate is extremely sensitive to the diameter of the mill used to generate the surface texture, not just its starting roughness. Specifically, the dissolution rate diminishes rapidly with an increase in mill diameter.

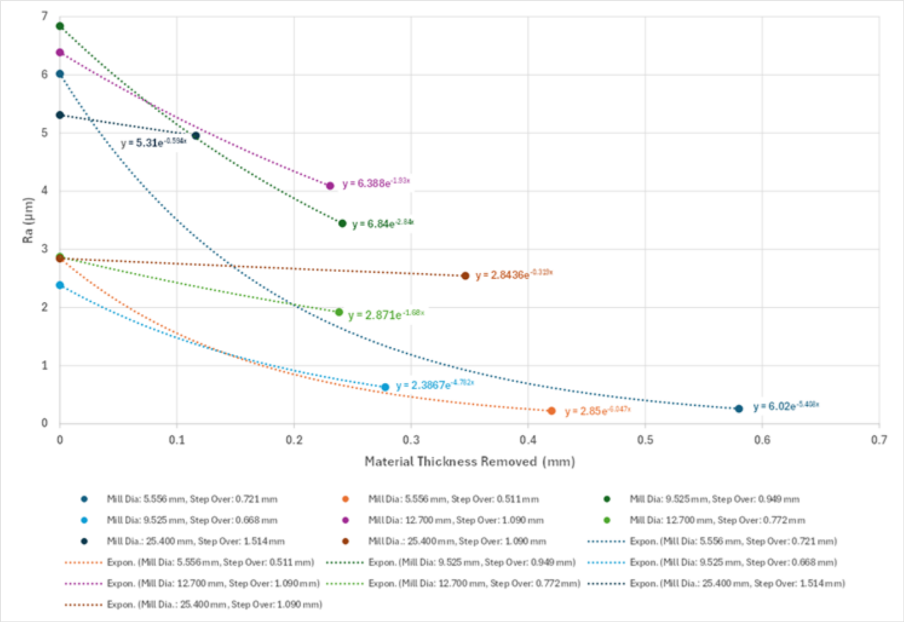

Figure 6.2.2 Influence of ball nose end mill diameter and step-over on the dissolution rate of surface roughness during PECM using a 1 mm IEGD

We hypothesize that these results are due to the distribution of material within the scallop and its spatial relationship to the cathode. Figure 6.2.3 shows the cross section (shown in gray) of a theoretical scallop left behind by a ball nose end milling process. While a single scallop is illustrated, the same geometry repeats itself along the entire milled surface. The root limit line is defined by the lowest points in each scallop. Below the root limit line is solid workpiece material.

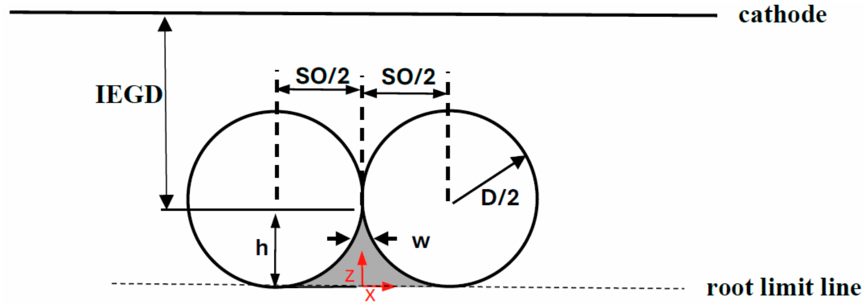

Figure 6.2.3 Scallop geometry in relation to the cathode and ball nose end milling parameters that influence it

For convenience, a x-z reference frame is drawn on the root limit line, directly below the peak. The two circles represent the cutting envelopes of the ball nose end mill when it creates the scallop. The two variables that dictate the scallop shape and peak-to-valley height (h) are the mill diameter (D) and the mill step over (SO). Note that the cutting envelopes are not drawn to scale relative to the scallop. Typical values of D are 250 to 1000 times larger than h. Likewise, values of SO are 10 to 40 times larger. Lastly, the cathode is also shown. Theoretically, the starting interelectrode gap distance (IEGD) is between the scallop peak and cathode. Similar to D and SO, the IEGD is also not drawn to scale, since it is typically 10 to 40 times larger than h.

What drives electro anodic dissolution is the electrostatic field between the cathode and workpiece surface. Since the voltage between the two is held constant, the closer the surface is to the cathode, the stronger the field strength. Consequently, while the entire scallop surface is subject to a localized field, it is slightly stronger at the peak than surrounding valleys. Hence it dissolves at a faster rate.

With this in mind, a scallop that has starting geometry with a smaller fraction of metal near the peak (e.g. sharper peak) will differentially dissolve at a greater rate. One way of characterizing sharpness is the dimension shown in Figure 6.2.3. This dimension changes as a function of z. This dimension takes it minimum value of 0 at the peak (z= h) and its maximum value of SO at the valley (z = 0). Furthermore, it continuously increases as z progresses from z = h to z = 0. The rate of change ($\dot{w}$) of w with respect to z maybe expressed as:

$$\dot{w} = \frac{4z-2SO}{\sqrt{-4z^2+4zSO}} \text{ for } 0 \le z \le h \qquad \text{(Eqn 6.2.1)}$$

The value of $\dot{w}$ is negative for all values of z. The value of $|\dot{w}|$ approaches infinity as z approaches 0. It takes on its minimum value at z = h. Lastly, it is known that the relationship between h, SO and D is to a very fine approximation:

$$h = \frac{SO^2}{4D} \qquad \text{(Eqn 6.2.2)}$$

Likewise, the relationship between h and the theoretical roughness Ra of the scallop geometry is:

$$R_a = \frac{h}{4} = \frac{SO^2}{16D} \qquad \text{(Eqn 6.2.3)}$$

The sharpness of a peak may thus be expressed as the value of ($\dot{w}$) at z = h. A sharper peak has a smaller value of $|\dot{w}|$ at z = h. But it also has $|\dot{w}|$ grow at a smaller rate as z approaches 0.

With this in mind, an examination of Figure 6.2.3 in combination with Equations (6.2.1) – (6.2.3) reveal the following:

- For fixed SO, increasing D has the effect of reducing both h and peak sharpness
- For fixed D, increasing SO has the effect of increasing both h and peak sharpness
- Different combinations of D and SO may yield the same value of R_a, but not the same values of peak sharpness

Figure 6.2.4 illustrates the relationship between scallop peak sharpness for the milling diameters used in this study and for varying values of R_a. Two important observations from this plot are as follows. First, the relative sharpness of the peaks remains essentially the same for any value of R_a. For example, the ratio of $\dot{w}$ (D = 5.556 mm) to $\dot{w}$ (D = 25.4 mm) remains approximately 0.46 throughout the range of R_a. This indicates that a scallop created by a smaller mill will always be sharper and easier to dissolve away than the scallop created by a larger mill. The second observation is that as the starting value of R_a decreases, the peak sharpness decreases at a disproportionally larger rate. As a consequence, the initial dissolution rate of shallow scallops is much smaller than the initial dissolution rate of steeper scallops. Both of these observations help explain the trends shown in Figure 6.2.2.

On a final note, it was previously reported that the roughness dissolution rates predicted using a multi-physics simulation model of the PECM process were substantially larger than those observed during the actual PECM experiments. For reference, Figure 6.2.5 shows the dissolution rate curves that derived from the simulations for a starting texture created by a 5.556 mm ball nose end mill at step overs of 0.696 mm and 0.493 mm. The corresponding starting roughness values of these simulated surfaces are 5.68 μm and 2.82 μm respectively. These values are close to the starting values associated with the same mill in Figure 6.2.2. Yet the dissolution rates are much greater. Specifically, the roughness dissolution exponent derived from the simulated data are -13.07 and -8.45 for the starting roughness values of 5.68 μm and 2.82 μm respectively. In contrast, the exponents derived from the corresponding experimental data are -6.05 and -5.41 respectively.

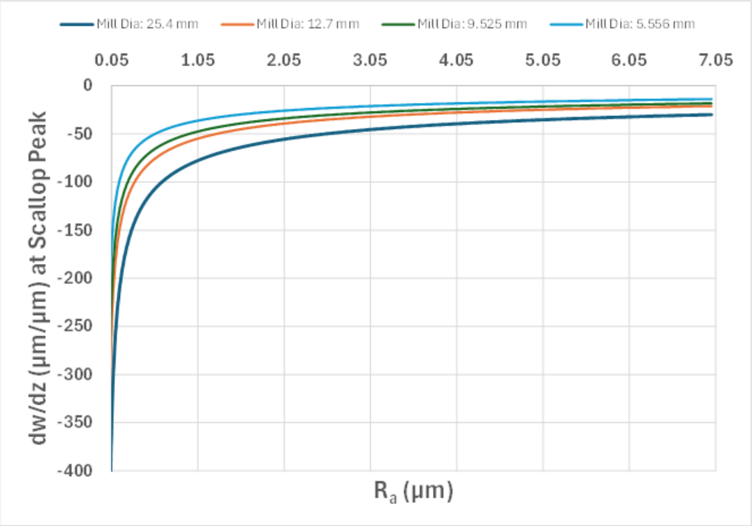

Figure 6.2.4 Rate of Change of Scallop Peak Width as a Function of Ra and Mill Diameter

At the time of this previous report, it was hypothesized that the PECM process inherently roughens the anode surface to a small extent via flow mark formation and preferential alloy dissolution while it simultaneously dissolves scallops. Since this roughening effect was not captured in the simulation, it led to the discrepancy in the results.

However, an additional effect has been observed. Figure 6.2.6 shows the predicted dissolution of the scallops. It should be noted that the dissolution occurs uniformly across the scallop flanks. This results in essentially no change in the pitch between the scallop peaks. Figure 6.2.7 shows profilometry data taken from a specimen with essentially the same starting texture and that was subjected to the actual PECM process. Here, it can be seen that the dissolution of the scallops is not uniform, with greater amounts of dissolution occurring along selective flanks and valleys. This nonhomogeneous dissolution will retard the diminishment of measurable R_a because it increases the relative peak-to-valley height of select regions.

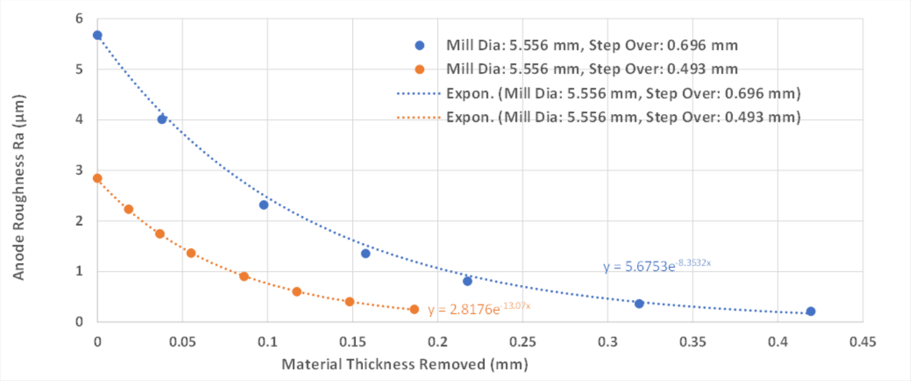

Figure 6.2.5 Surface Roughness Dissolution Predicted from Multi-Physics Simulation of PECM Using 1 mm IEGD and Anode Surface Previously Milled with a 5.556 mm Diameter Ball Nose End Mill and Step Over of 0.493 mm and 0.696 mm

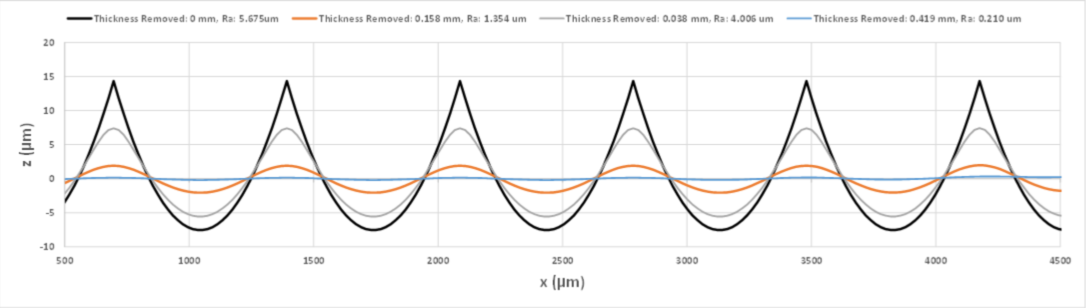

Figure 6.2.6 Surface Roughness Dissolution Predicted from Multi-Physics Simulation of PECM Using 1 mm IEGD and Anode Surface Previously Milled with a 5.556 mm Diameter Ball Nose End Mill at a Step Over of 0.696 mm

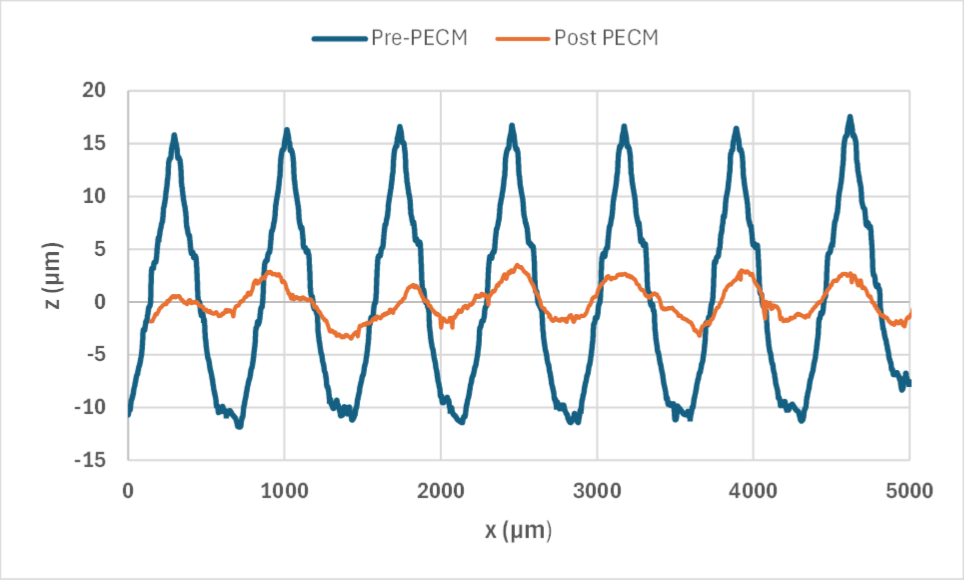

Figure 6.2.7 Surface Roughness Dissolution from PECM Using 1 mm IEGD and Anode Surface Previously Milled with a 5.556 mm Diameter Ball Nose End Mill at a Step Over of 0.721 mm

6.3. Finish polish surface of 1:20 scale and full scale mold modules

The aim of this task is to identify how PECM may be applied to a full-scale module to remove tool marks from the interface surface that are leftover by ball-nose end milling. Based on the variety of experimental investigations and analyses that were carried out previously, the following design considerations were identified:

- PECM is a machining process, not a polishing process. The geometric error induced by PECM during dissolution and the necessary stock removal must be considered as well as texture evolution.
- The mold interface surface must be machined by an enveloping cathode and a strong electric field to avoid corrosion and excessive geometric error

- All other mold surfaces must be protected from electrolyte to avoid corrosion
- Bi-directional flow is effective at maintaining uniform dissolution if electrolyte velocity is high (30 mm/s), but loses effectiveness at much lower velocities. Good results however are still achievable with near stagnant flow velocities: Specifically, at the 1:100 scale, PECM was able to reduce the roughness of a surface from R_a 7.8 µm to R_a 0.3 µm while inducing an average form error of 100 µm (0.1% Chord Length).
- A full-scale mold module or 1:20 scale mold module needs to be processed at near stagnant flow velocities due to large flow path-to-IEG height ratio and the associated flow resistance.
- The IEGD must be made as small as possible in order to minimize the amount of stock that needs to be removed from the mold module to achieve the desired R_a value as well as minimize electrical power consumption and Ohmic heating
- The transfer of heat and aluminum hydroxide generated within the IEG during processing is critical to success

With this in mind, a PECM system capable of machining a full-scale mold module will require three major sub-systems. These are the PECM cell, a three-axis gantry, and a PECM station. These will be discussed separately.

6.4. PECM cell

The PECM cell necessary to process a full-scale mold module will resemble that shown in Figure 6.4.1 and 6.4.2. It is a relatively simplistic system consisting of a mold module holder and a cathode holder. These will be fabricated from a light weight, non-conductive, electrolyte resistant material such as Nylon. As the name implies, the mold module holder will be used to hold and position the mold module relative to the PECM process. In this particular case, the mold interface surface will be facing upwards. The holder will be mounted to the floor of the three-axis gantry.

It should also be noted that the module holder will have an extended inlet port and outlet port for allowing electrolyte and coolant to pass through the system. These ports will be connected to manifolds (not shown) that will allow both fluids to traverse to and from the PECM station.

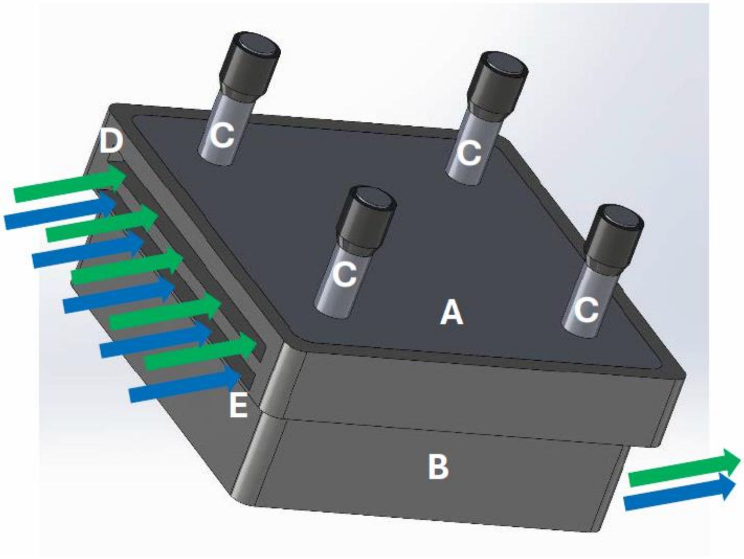

Figure 6.4.1 Closed PECM cell with elements
A) Cathode Holder, B) Mold Module Holder, C) Connecting Shafts to X-Y-Z Stage, D) Inlet Port for Electrolyte, E) Inlet Port for Mold Module Coolant

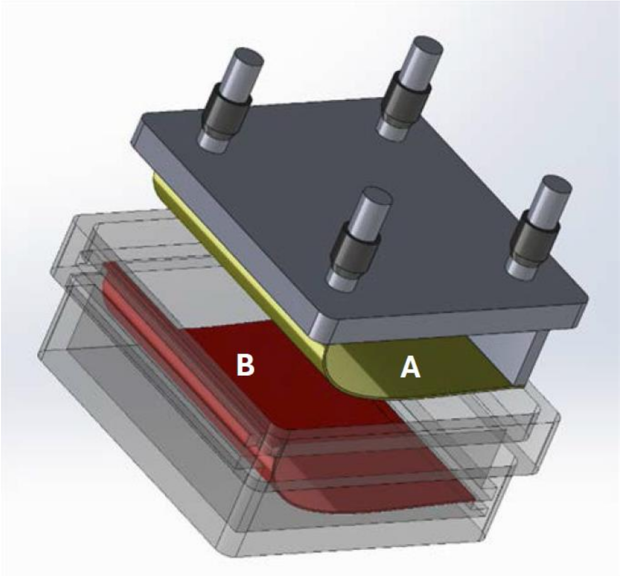

Figure 6.4.2 Open PECM cell with elements
A) Cathode, B) Mold Module

The cathode holder will hold the cathode. It will have attachment points for mounting to the gantry, which will be used to position it relative to the module holder. Since major size fluctuations between module designs is not anticipated, it is believed that both holders will be general purpose and thus capable of accommodating all modules designs within a family as well as their respective cathodes. Some customization will be necessary, but that can be handled with localized hard contact elements and clamps at the attachment points within each. These elements are not shown. Nor are the seals that will need to be in place to prevent electrolyte from bypassing the cathode and coolant from bypassing the mold module.

The cathode will be a thin sheet fabricated from a corrosion resistant metal such as stainless steel or alternatively it will be aluminum coated with a conductive, corrosion resistant layer. Out of necessity, the IEG surface of the cathode will need to be the negative image of the mold module interface surface. As a consequence, it will be dedicated to a specific module design.

The manner in which the mold module will need to be processed is different than what we have previously experimented with directly at Penn State. The issue is the length of the IEG that the electrolyte must travel through from inlet to outlet. This distance is approximately 10m, whereas the IEGD will be small (1mm to 2 mm). Small IEGD is desired to minimize the amount of stock that will need to be stripped away from a starting surface with rough texture and transition it to a finished surface with a roughness of $\approx R_a$ 2 µm. It is also desired to minimize Ohmic resistance and heat generation the IEG.

With such a long travel path and small IEGD, the electrolyte flow velocity is going to be very slow, even if the inlet pressure is very high. As a consequence, the electrolyte will quickly heat up and accumulate aluminum hydroxide during the machining cycle. Furthermore, it may be too low to properly sweep away aluminum hydroxide from accumulating on the surface. The solution to this problem is to couple motion of the cathode with the down phase of the pulsed voltage cycle.

Prior to the beginning of the machining cycle, the gantry system will displace the cathode holder assembly toward the module interface surface as shown in Figure 6.4.3. During this motion, the electrolyte flow between the cathode and module continuously decreases as the flow resistance increases. Once the cathode is positioned such that the IEGD is at its desired value, the flow rate will decrease to near stagnation. At this point, the IEG is energized while the electrical current is monitored.

Due to the low electrolyte flow rate, the electrolyte temperature and conductivity will quickly rise along with material removal rate, power consumption, and heat generation. To keep the process from thermal run-away, the voltage will correspondingly be reduced to keep the electrical current below an upper limit. Throughout the machining cycle, aluminum hydroxide will quickly build up in the electrolyte and a top the interface surface. At this stage, the IEG will be deenergized and the electrolyte flush cycle will begin.

At the beginning of the flush cycle, the gantry system will displace the cathode holder assembly away from the module interface surface as shown in Fig 6.4.4. As this happens, the electrolyte flow rate within the IEG will increase significantly. This will remove accumulated heat and aluminum hydroxide from it. After a time period, the flush cycle will stop and the cathode assembly will be positioned back toward the module interface surface.

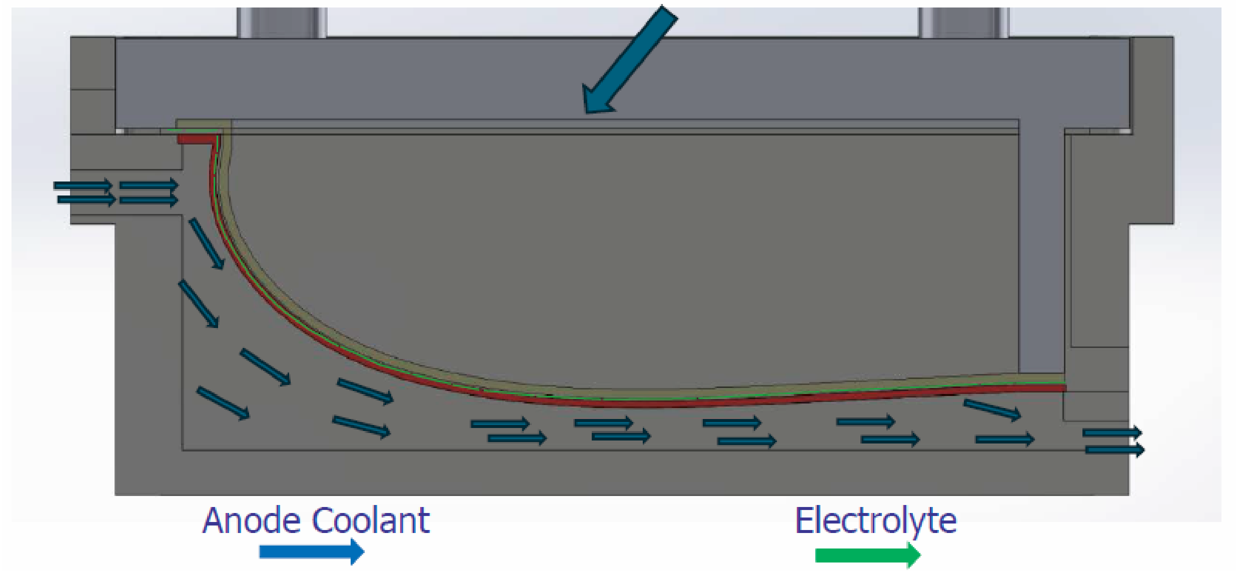

Figure 6.4.3 PECM cell during machining cycle

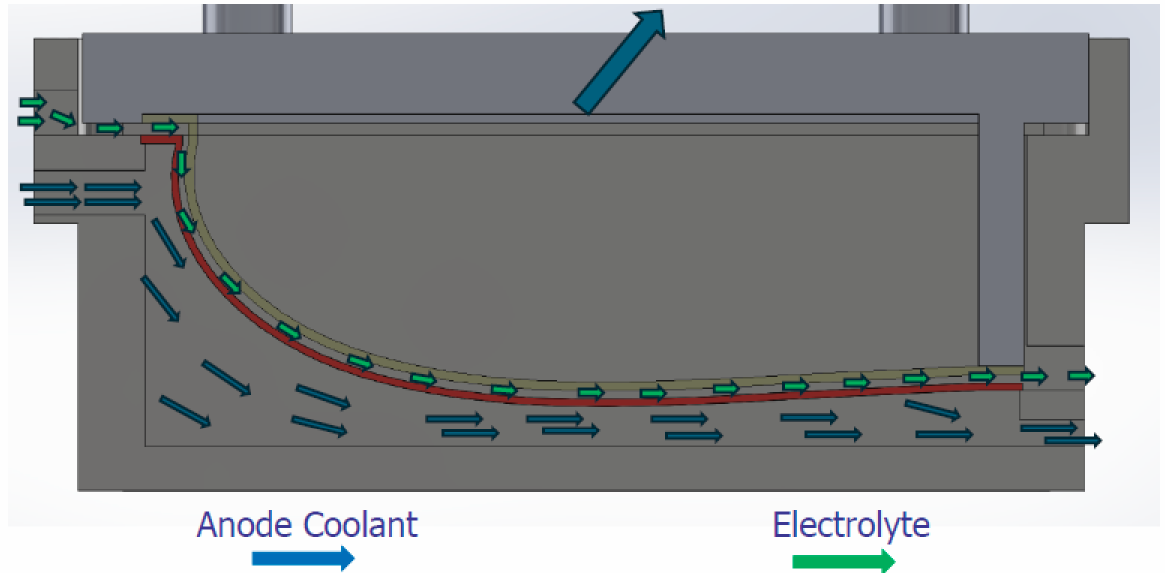

Figure 6.4.4 PECM cell during electrolyte flush cycle

The flush cycle alone will not be sufficient to remote heat from the IEG and surrounding conductors. Because of this fact, it is anticipated that a separate anode coolant system will be required. As shown in Figures 6.4.3 and 6.4.4, this system will run chilled anode coolant through the mold module holder directly underneath the mold module. This flow will be continuous throughout both cycles. Note that it is technically feasible to run an equivalent system for the cathode to directly extract heat from it as well.

No direct prototype of this system has yet to be built and tested at Penn State. However, the principal concept on which it is hinged was discovered by accident during the execution of the Bi-directional flow PECM experiments. Specifically, the PECM was allowed to continue for 300 seconds with minimal flow rate through the IEG. This resulted in thermal runaway and rapid dissolution of the module interface surface. Yet, the resultant surface exhibited good (not great) form error and smooth texture. This suggests that the same principle maybe applied to the proposed concept.

The key to realizing this concept, is the development of the automatic controls needed to keep the system stable. This will require a means to monitor electrolyte temperature close to the IEG and electrical current passing through the IEG. In turn, this system will actively control the voltage applied to the IEG. It will also control the gantry to control the IEGD. The latter will be controlled by the gantry system. This will be carried out as future work.

6.5. Gantry system and PECM station

Figure 6.5.1 shows an image of how the PECM cell would be positioned within the three-axis gantry system. To accommodate the cell, the gantry will require a range of 15 m of travel in the X axis, 20 mm of travel in the Y axis, and 6m of travel in the Z axis. This range is needed to allow clearance for cell assembly as well as positioning of the cathode holder.

Figure 6.5.2 illustrates the principal functionality of the PECM station and its connectivity to the PECM cell and gantry system. These functions are:

- Electrical Power Supply
- Electrolyte Circulation
- Coolant Circulation
- Controls

The electrical power supply will consist of the voltage wave generator and its electrical power supply. This system will deliver a peak voltage of 12.84V and a peak current of 6M amps across the IEG during a pulse cycle. The pulse cycle will have a 20% duty phase. During the duty phase, the power supply will need to deliver 77 MW of power, with the vast majority of this being lost to Ohmic heating.

The electrolyte circulation system will circulate an estimated 1M liters of electrolyte through a combination of three circuits. These transport electrolyte from the reservoir to the PECM cell, electrolyte chiller, and electrolyte filtration system and back again respectively. During the flush cycle, it is estimated that the volumetric flow rate will be 1100 liters/min. The coolant circulation system is intended to be the primary means by which to extract heat from the IEG. It is expected to circulate 2 M liters through a combination of two circuits.

Figure 6.5.1 PECM cell within three-axis gantry system

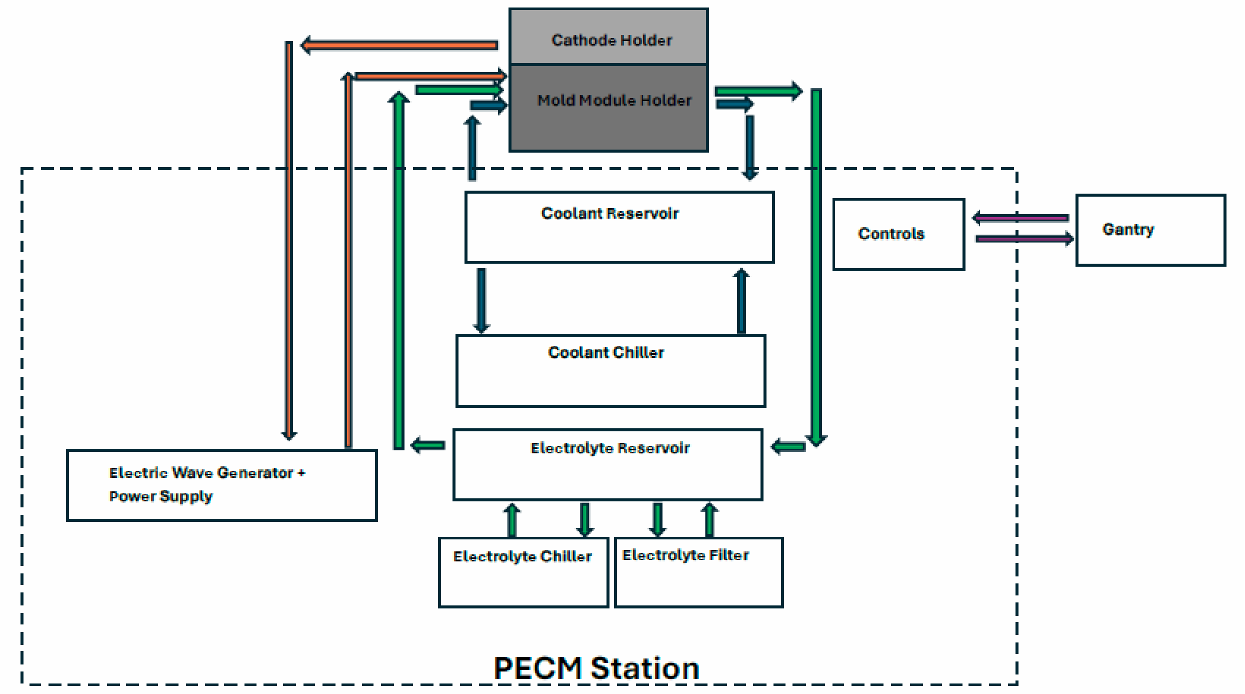

Figure 6.5.2 PECM station and linkages to PECM cell and gantry system

6.6. *Comparative analysis of techno-economic challenges for scaling up mold fabrication*

The objective of this task was to investigate the feasibility of using PECM to remove milling scallops from blade interface surface of a mold module. Technical feasibility was verified on a 1:100 scale mold module originated from wrought 6061 aluminum. Furthermore, a PECM concept has been presented that is believed to be technically feasible at the full scale. However, the question remains whether it is commercially advantageous to use this concept. To answer this question, an analysis was carried out to compare the use of this concept to that of directly milling the surface to a finish of approximately R_a 0.2µm.

Related to this is the feasibility of actually achieving a finish of R_a 0.2µm or less on 6061 aluminum that is printed using the Direct Energy Deposition process. Here the principal concern is porosity. To investigate this, a separate study was conducted. The results of these studies are described next.

After printing, a full-scale mold module will be placed in a five-axis, gantry machining center, where all of its functional surfaces will be machined in two distinct operations. Assuming that the blade interface surface is the last feature to be machined on the module, two options are available to create a mold interface surface with a form error less than or equal to 10 cm (1% chord length) and a roughness of R_a 0.2µm or less.

The first option (see Figure 6.6.1) is to complete the last roughing pass and the finishing pass with a ball nose end mill. Logically, this should be done with the largest end mill available to minimize processing time. In this analysis, this is assumed to be 25.4 mm, which is a tool diameter commonly used to machine large free form surfaces. Furthermore, as will be discussed, this option was determined to be marginally feasible, at least on a small-scale level.

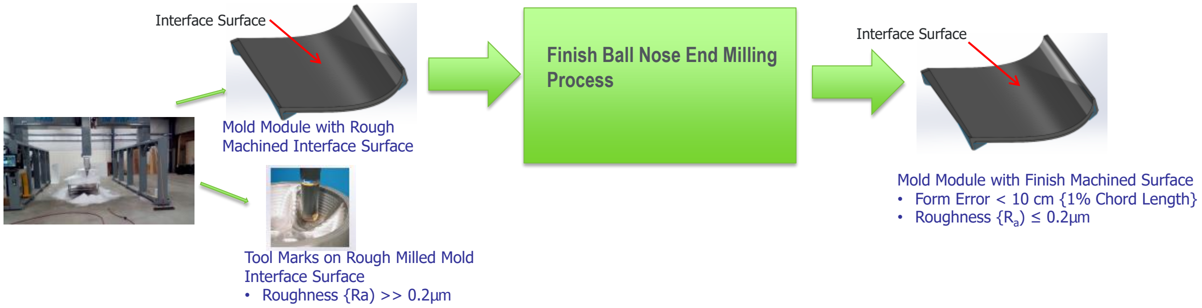

Figure 6.6.1 Option 1: Use ball nose end milling with a 25.4 mm diameter mill at a step over of 1.542 mm to rough machine a surface to a roughness of Ra 6.0µm and reduce the step over to 0.199 mm to finish machine the interface surface to a form error < 10 cm and a theoretical roughness equal to Ra 0.2µm

It is assumed that the roughing process uses a step over of 1.542 mm, which theoretically should leave behind a surface with roughness equal to R_a 6.0µm. Likewise, it is assumed to use a step over of 0.199 mm for the finishing process, which was shown experimentally to leave behind a surface finish close to R_a 0.2 µm.

The second option (see Figure 6.6.2) is to use a ball nose end milling process to rough mill the surface to a theoretical roughness of R_a 6.0µm, remove the mold module from the machining center, transfer it to the Pulse Electrochemical Machining Cell shown in Figure 6.4.2, and then use PECM to create the finished interface surface that will have a form error less than or equal 10 cm and a surface finish of approximately R_a 0.2 µm.

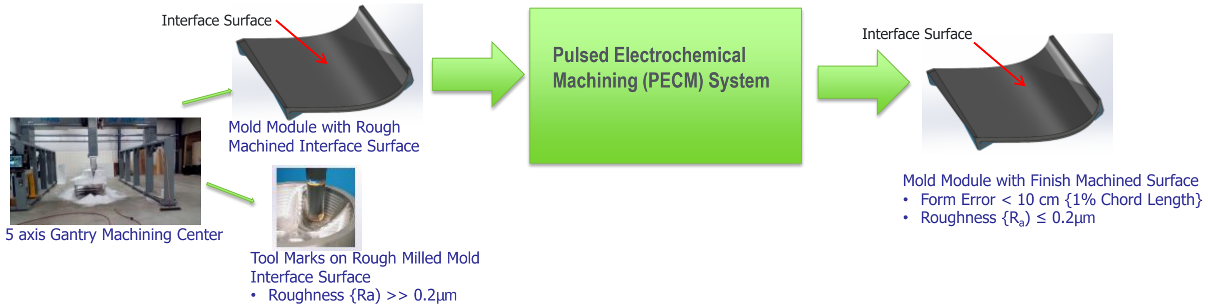

Figure 6.6.2 Option 2: use ball nose end milling to rough machine a surface to a roughness of R_a 6.0µm, remove the mold module from the machining center and transfer to the PECM cell, and use pulsed electrochemical machining to create a finished interface surface with form error < 10 cm and theoretical roughness equal to R_a 0.2µm

In this scenario one of four end mill-step over combinations is used to rough mill the interface surface in the machining center. These are: 25.4 mm diameter-1.542 mm step over, 12.7 mm diameter-1.090 mm step over, 9.525 mm diameter-0.944 mm step over, and 5.556 mm diameter-0.721 mm step over. The amount of material thickness that must be removed is determined using the curves in Figure 6.2.2.

The underlying assumptions of this analysis are as follows:

- The five-axis gantry machining center has a maximum spindle velocity of 7000 rpm and a maximum linear feed rate of 10,000 mm/min.
- The rough milling process used for either option is carried out with a four flute, carbide mill
- The specific cutting energy of the milling process is 0.32 J/mm^3.
- The machining cycle of the PECM process is assumed to operate at a current efficiency of 75%, and the IEGD is maintained at 1mm. Furthermore, during this cycle, the voltage across the IEG is 12.84 V, the average current density across the mold interface is 6 A/cm^2, and the average electrolyte conductivity is 0.4673 S/m. The aluminum molar weight is 26.98 g/mol, the aluminum valence is 3, and the aluminum density is .0027 g/mm^3.
- Due to the time required to move the cathode assembly as well as the additional time required to flush out the IEG, the machining cycle will only comprise 20% of the total cycle time (i.e. machining cycle time + flush cycle time).
- With regard to energy consumption, only the energy necessary to directly remove aluminum is considered. Energy for moving positioning axes or circulating electrolyte or coolant are not considered. Thus, for machining, only the energy necessary for chip formation and shearing is computed. For pulsed electro-chemical machining, only the energy lost through Ohmic heating within the IEG is computed. This energy loss is known to dwarf that associated with the chemical reactions that occur.

For Option 1, the time required to rough mill the interface surface is predicted to be 6,287 min. The time required to finish mill the surface is predicted to be 87,624 min. The total machining time is predicted to be 93,911 minutes.

Table 6.6.1 lists the predicted milling process time and predicted milling energy consumption associated with option 2. The first column identifies the combination of mill diameter and mill step over that will leave the rough milled surface with a theoretical roughness of R_a 6.0 µm. The third column is the time necessary for the mill to raster across the rough interface surface at the prescribed step over. The third column identifies the necessary layer thickness to be left over for the PECM process. This is the minimum thickness that must be removed by PECM to achieve a theoretical roughness of R_a 0.2 µm. The fourth column identifies the energy that would be consumed by the milling process to this stock in lieu of the PECM process.

Table 6.6.1 Predicted milling processing time and milling energy consumption for Option 2

Mill Dia. (mm)/Step Over (mm)	***Roughing Pass Time (min)***	***Stock (mm) left Over for PECM Process to Remove***	***Milling Process Energy that would need to be Expended to Remove Remaining Stock (J) if PECM were not Used***
25.4/1.542	6,287	5.520	171,731,357
12.7/1.090	8,892	1.795	55,831,434
0.9525/0.944	10,267	1.244	38,690,341
0.556/0.721	13,443	0.630	19,583,154

Table 6.6.2 lists the predicted PECM time and predicted PECM energy consumption associated with Option 2. The first two columns identify the milling process parameters used to create the starting surface as well as the required stock to be removed by the PECM process. The third column lists the time needed by the PECM process to remove the layer. The fourth column lists the total processing time associated with rough milling the surface and subsequent PECM. The last column lists the energy consumed by the PECM process to remove the remaining stock.

Table 6.6.2 Predicted PECM Processing Time and PECM Energy Consumption for Option 2

Mill Dia. (mm)/Step Over (mm) for Rough Milling Process	***Stock (mm) to be Removed by PECM to Achieve R_a 0.2µm***	***PECM Processing Time (min)***	***Total Milling and PECM Processing Time (min)***	***PECM Process Energy Expended to Remove Stock (J)***
25.4/1.542	5.520	296	6,583	273,753,550,619
12.7/1.090	1.795	96	8,988	88,999,782,131
9.525/0.944	1.244	67	10,334	61,675,505,119
5.556/0.721	0.630	24	13,467	31,217,118,656

The following three conclusions can be drawn from this analysis.

- The PECM processing time and the total processing time for option 2 are sensitive to the mill diameter used to previously rough the interface surface. However, their sensitivity is opposite of one another.
- The required energy consumption necessary for the PECM process to finish machine the surface is extremely sensitive to the mill diameter used to rough it. Whereas increasing the mill diameter favorably reduces total processing time, it results in significant growth in the required PECM energy consumption. This is due to the increasing amount of stock that must be removed.
- In terms of processing time alone, any one of the four choices of mill diameter in Option 2 is far superior to Option 1. Alternatively, in terms of energy consumption, anyone of the four choices of mill diameter in Option 2 is far inferior to Option 1.

A word of caution regarding the comparison of processing time. This analysis does not factor in the time required to remove the mold module from the fixture within the five-axis gantry machining center, transport and mounting to the PECM cell, and set up of the PECM process. This is too difficult to predict reliably at this point of time.

This comparative analysis does not also factor in cost. Currently, five-axis gantry machining centers are commercially available to machine a full-scale mold module to completion. In contrast, the PECM system is not. It will need to be developed. However, what is developed will be a general-purpose system capable of processing the complete family of mold modules. The one exception is the cathode, which must be dedicated to each mold module design. Obviously, if only one of each module design is to be machined, Option 2 will not be attractive. Nor will it be if the cost of electrical energy is high.

6.7. Machinability Analysis

Mold surface texture and porosity affect part quality during resin transfer molding processes. The two principal concerns are:

- mechanical interlock between the mold surface texture and the solidified resin on the outside skin of the composite part
- air within the mold texture pits and valleys may become trapped by the liquid resin

Resin interlock at the mold interface will increase the external forces necessary to remove the part from the mold and likewise lead to a greater number of stress concentrations on the part skin. In tandem, this will increase the likelihood of cracks developing in the part. Air trapped below liquid resin at the mold interface can expand when the mold is heated. This will drive air bubbles into the solidifying resin causing porosity defects in the part subsurface. For these reasons, mold surfaces are typically fine polished to R_a 0.03 μm after machining and sanding.

One of the characteristics of DED printing, is its propensity to introduce porosity into the part. This porosity is due to gas bubble formation and lack of fusion defects. As it relates to this project, the principal concern is the potential effect of porosity on the ability of the printed aluminum to hold a vacuum. However, a secondary concern is its effect on the ability of the printed aluminum to be finely polished to R_a 0.03 μm.

To investigate this, samples of 6061 aluminum were fine machined and sanded. One of the samples was derived from wrought 6061 aluminum bar stock. This aluminum served as a reference, since it is known that wrought aluminum contains the least amount of porosity. A second set of samples were derived from printed aluminum taken from the 1:100 scale module prototype, see Figure 6.7.1(a), created by DM3D. The third set was derived from metal supports that were printed with 1:20 scale module prototype, see Figure 6.7.1(b). According to DM3D, a much coarser pitch was used for this printing than the 1:100 scale module. As such, it was expected to contain a larger fraction of porosity defects.

(a) 1:100 scale shaped coupon

(b) printed support material from a 1:20 scale mold module print

Figure 6.7.1 Sources of direct energy deposited aluminum samples

The samples were first machined into rectangular bars. The top surface of each sample was subsequently ball nose end milled with a 25.4 mm diameter, four flute, carbide end mill at a step over of 0.199 mm. This should have resulted in a theoretical roughness of R_a 0.1 μm. Each sample was subsequently hand sanded with 1000 grit sandpaper followed by 2000 grit sandpaper.

Two different profilometry technologies were used to measure the surface of each sample. A Mitutoyo SJ410 contact profilometer with a 1 μm radius stylus tip, see Figure 6.7.2(a), was used to obtain multiple line traces across each sample. A Gaussian filter was applied to the data with a cut-off width of 0.80 mm. The evaluation length was 1.25 mm. The roughness metric R_a was computed for each trace.

A Keyence VK-X3100 laser confocal microscope, see Figure 6.7.2(b), was used to obtain a surface scan at 20X magnification yielding a 0.617 mm x 0.617mm image for each. The roughness metric S_a was computed for each scan. No filtering was applied to the scan.

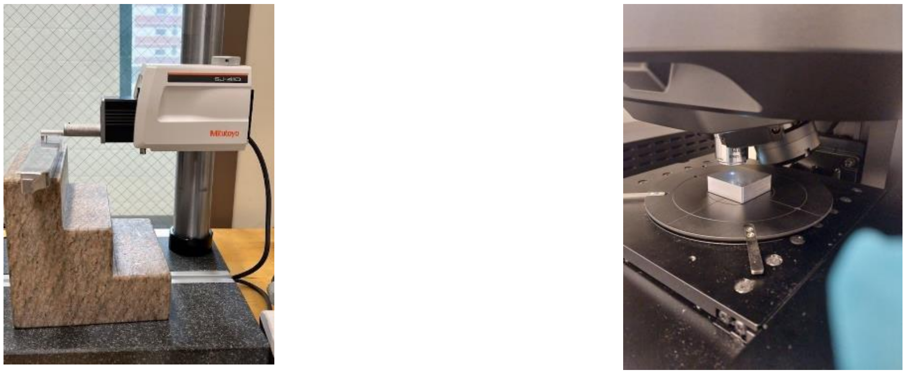

(a) Mitutoyo contact profilometer (b) Keyence laser confocal microscope

Figure 6.7.2 Profilometry technologies employed in study

Tables 6.7.1 through 6.7.3 summarize the statistics derived from each family of aluminum samples as derived from the two measurement technologies. They also show images derived from the laser confocal microscope. What appear as dark patches in the images are regions of porosity or severe scratches left behind by the sanding processes. The conclusions that are drawn from these results are the following:

- All samples exhibit porosity pits at 20X magnification. However, their frequency and visible surface area increases dramatically from the wrought aluminum to the DED aluminum taken from the 1:100 scale prototype to the DED aluminum taken from the 1:20 scale prototype. The porosity pits in the DED aluminum are visible to the naked eye.
- The R_a values derived from the contact profilometer are noticeably smaller than the S_a values derived from the laser confocal microscope. This is because S_a is a measure of roughness for a surface patch, whereas R_a is a measure of roughness from a line element within the same patch. It inherently has to be smaller than or equal to the value of Sa, depending on the directionality of the trace relative to dominant directions of roughness.
- None of the milling processes were able to achieve a texture of R_a 0.2μm, despite the fact that the small stepover should have led to a theoretical roughness of R_a 0.1μm. The reason for this discrepancy is the imperfect chip formation behavior that results from the zero to near-zero cutting velocity that occurs at the tip of the mill. This deformation more closely resembles a scratch test rather than true peripheral milling. Rather than shearing cleanly, a fraction of this aluminum being machine gets squeezed upward into the texture peaks and subsequently pushed outward. This being said, milling the wrought aluminum resulted in a respectable R_a 0.319 μm.
- The sanding processes were able to significantly reduce the roughness left behind by the milling process for all three aluminum sample types.
- Porosity clearly influences measured roughness. Wrought aluminum, which had the least
- porosity, yielded significantly lower measured roughness than either printed aluminum. The 1:20 scale aluminum, which yielded the greatest porosity, had the greatest measured roughness.

Table 6.7.1 Profilometry Results for Wrought 6061 Aluminum

Finishing Process	***Ball Nose End Milling***	***Sanding and Paste Polishing***
Image from Laser Confocal Microscope		
Measured Roughness (R_a/µm) using Contact Profilometer (1.25 mm Trace)	Avg: 0.319 Max: 0.333 Min: 0.285	Avg: 0.143 Max: 0.162 Min: 0.109
Measured Roughness (S_a/µm) using Laser Confocal Microscope (0.627 mm x 0.627 mm scan)	Avg: 0.326 Max: 0.340 Min: 0.304	Avg: 0.146 Max: 0.253 Min: 0.092

Table 6.7.2 Profilometry Results for DED 1:100 Scale 6061Aluminum

Finishing Process	***Ball Nose End Milling***	***Sanding and Paste Polishing***
Image from Laser Confocal Microscope		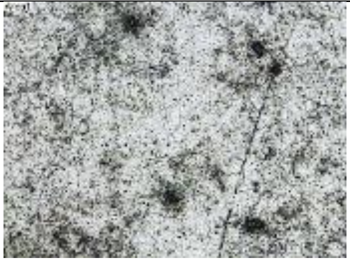
Measured Roughness (R_a/µm) using Contact Profilometer (1.25 mm Trace)	Avg: 0.372 Max: 0.497 Min: 0.287	Avg: 0.200 Max: 0.253 Min: 0.133
Measured Roughness (S_a/µm) using Laser Confocal Microscope (0.627 mm x 0.627 mm scan)	Avg: 0.539 Max: 0.623 Min: 0.535	Avg: 0.238 Max: 0.272 Min: 0.204

Table 6.7.3 Profilometry Results for DED 1:20 Scale 6061Aluminum

Finishing Process	***Ball Nose End Milling***	***Sanding and Paste Polishing***
Image from Laser Confocal Microscope		
Measured Roughness (R_a/µm) using Contact Profilometer (1.25 mm Trace)	Avg: 0.412 Max: 0.462 Min: 0.382	Avg: 0.214 Max: 0.293 Min: 0.152
Measured Roughness (S_a/µm) using Laser Confocal Microscope (0.627 mm x 0.627 mm scan)	Avg: 0.607 Max: 0.678 Min: 0.560	Avg: 0.279 Max: 0.391 Min: 0.217

These results indicate that it is doubtful that aluminum consisting of this much porosity can be fine polished to roughness as low as R_a 0.03 µm. Steps certainly can be taken to reduce the volume fraction of porosity it however. For example, during the build of a full scale mold module, a coarse pitch laser scan can be used to fabricate the bulk volume of the module. In turn, a fine pitch laser scan can be used to fabricate the outer layers with the intent of reducing lack of fusion defects. If necessary, a laser remelt scan without powder deposition maybe applied to these outer layers to reduce this porosity even further.

However, even in the absence of these measures, the porosity encountered in DED aluminum should not prohibit its use for the fabrication of a composite mold. Their existence can be countered by the application of a polymer sealant to the semi-finished mold surface prior to fine polishing. The use of such sealants is routine in composite manufacturing.

6.8. Refined PECM economic analysis

A superfinishing economic analysis was conducted the UM team by creating a model to investigate the time, energy requirements, and cost of superfinishing full scale modules. Our colleagues at Penn State provided the UM team with data from the PECM process they are currently refining. The data provided started at a surface roughness of six microns and superfinished the surface to less than 0.3 microns. Laser powder bed fusion machines can achieve a surface roughness of 5-35 microns. Our assumption is that DED would be able to reach a surface roughness of six microns given the similar process to L-PBF, therefore the PSU data was used to create this model. The model was then extrapolated to determine the time and energy requirements for a full-scale module for a modular mold. Some ways to decrease machining time using PECM is to increase the current density, increase the size of tool, Figure 6.9.1, or increase the number of tools Figure 6.8.2.

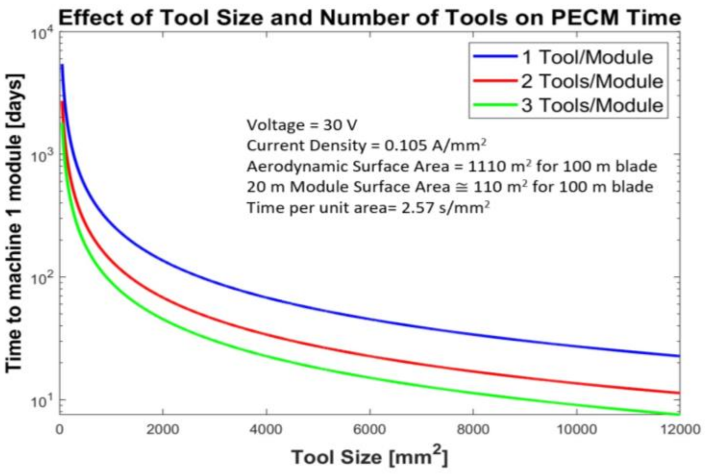

Figure 6.8.1 Effect of tool size and number of tools on PECM time

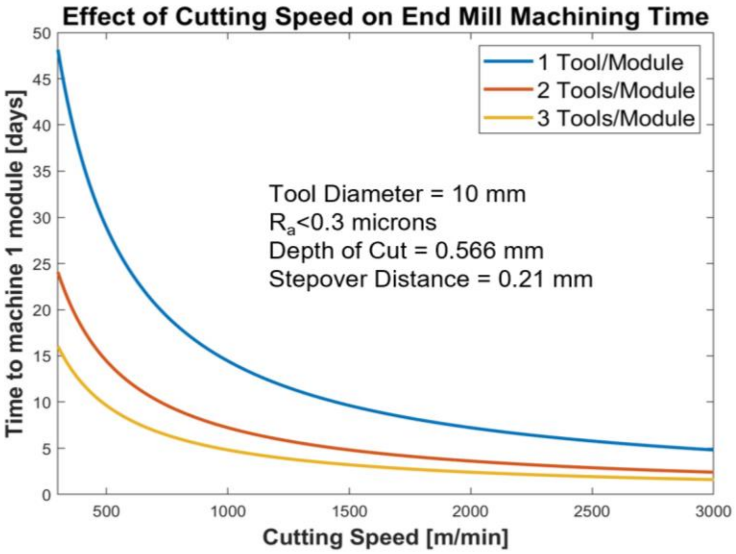

Figure 6.8.2 Effect of cutting speed on end mill machining time

A conventional end mill machining model was also created to compare the PECM machining process to a more conventional machining process. For this end mill machining model, the surface roughness achieved by PECM was met along the “floor” of the ball end mill and perpendicular to the feed rate along the scallops created by the ball end mill. This required a separate model to calculate the theoretical stepover required to meet the surface roughness required. This model was also then extrapolated to a full-scale module. Some ways to decrease the machining time for end milling is to increase the cutting speed or to increase the number of tools.

The overall goal of the PECM and end mill machining models is to compare the impacts of either PECM OR end milling to machine the entire module (time, cost, primary energy). The PECM

Model has been designed to be very broad to integrate any future changes that might be suggested by PSU. The current PECM data on relationship between time, energy, surface roughness, etc. (provided by PSU) was derived experimentally from an aluminum surface that reduced surface roughness from 6 microns (starting from a unique scalloped surface) to <0.3 microns using PECM. Some shortcomingof the current PECM model, Figure 6.8.3, is that this data would not apply to a surface with scallops from a different sized ball end mill and the model assumes the PECM time/energy/surface roughness relationship is invariant to different surface roughness geometries (e.g. different size ball end mills). More experiments are required to understand the limits of this assumption.

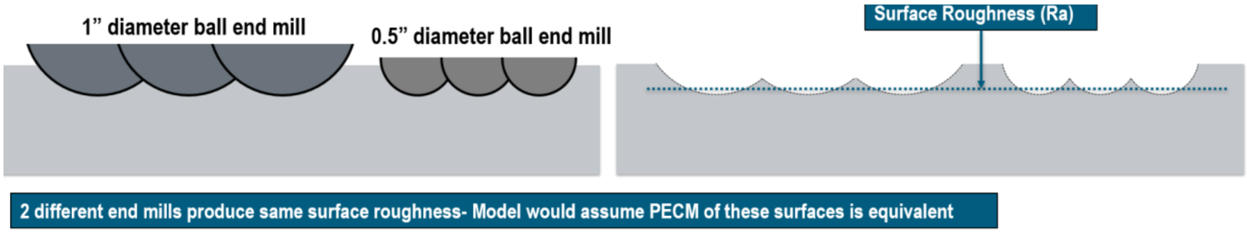

Figure 6.8.3 Shortcoming of PECM model

The current model can be seen below in Equation (6.8.1), where A is the area to be machined, N is the number of tools, T is the tool area, OF is the overlap factor (akin to stepover for end mill model), V is the voltage applied, and I is the current density.

$$Machining\ Time = \frac{A}{N * T * (1 - OF)} * \frac{Energy\ Density/Unit\ Area}{V * I_d} \tag{6.8.1}$$

The effect of tool size and number of tools on the PECM processing time for a module with a surface area of 110 m^2 can be seen in Figure 6.8.4, assuming an overlap factor of 0, and the processing data from PSU. It can be seen that increasing both the number of tools and the size of tool will decrease the processing time to machine the module, with both the moving cathode and fixed cathode concepts proposed by PSU seen on the graph.

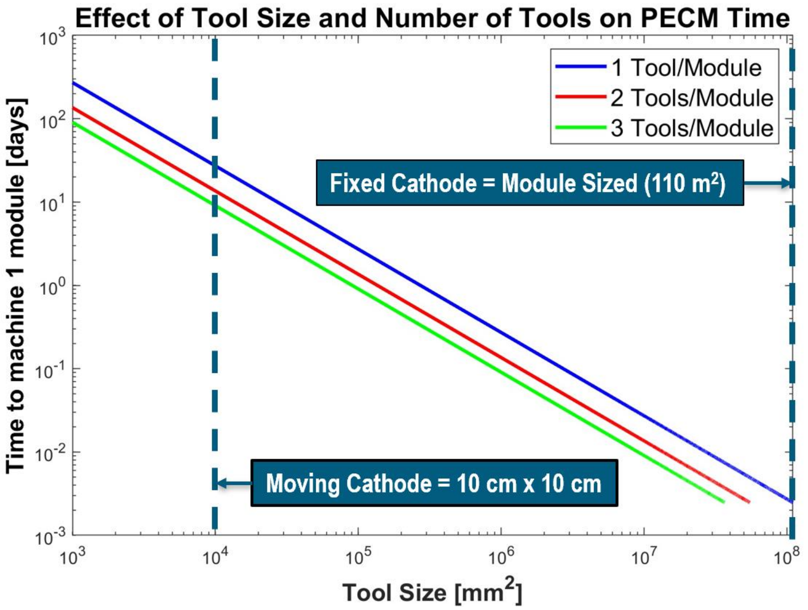

Figure 6.8.4 Effect of tool size and number of tools on PECM processing time

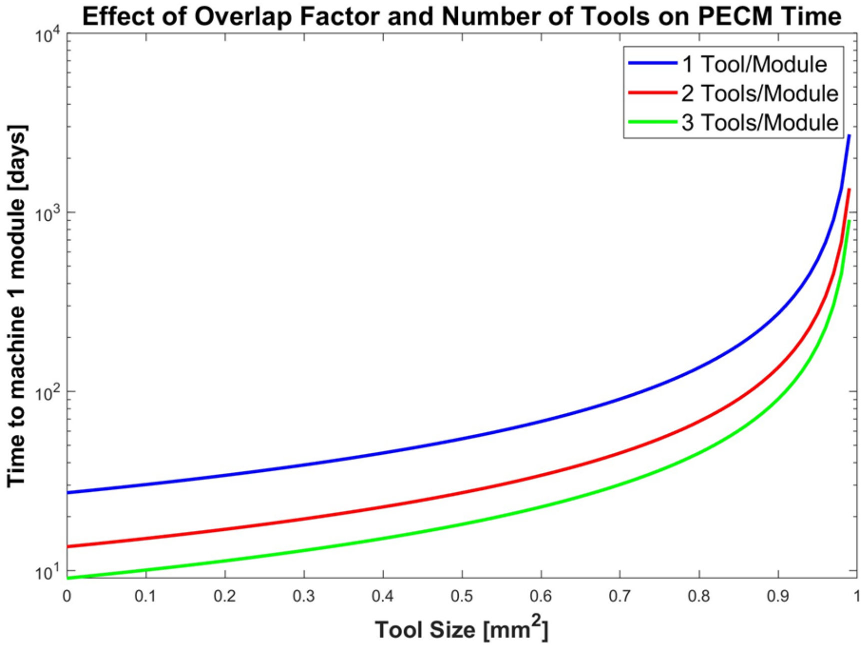

Figure 6.8.5 Effect of overlap factor on PECM processing time

The overlap factor can also be used to decrease the PECM processing time, as seen in Figure 3 (assuming a 10 cm x 10 cm moving cathode concept). The overlap factor can be defined as the percentage of stepover from one machining path to the next.

$$Energy\ at\ "tooltip" = Energy\ Density/Unit\ Area * A * 1/(1 - OF) \tag{6.8.2}$$

$$Machine\ Energy = Energy\ at\ "tooltip" + (Baseload\ Power * Processing\ Time) \tag{6.8.3}$$

$$Energy\ cost = Machine\ Energy * 0.0775\ \$/kWh \tag{6.8.4}$$

The models to calculate PECM cost and energy can be seen in Equations (6.8.2)-(6.8.4). This is where we believe the most uncertainty exists when calculating the impacts of PECM on modular molds. The baseload power assumption is bold and needs to be updated with new PECM data, and we are also exploring whether wire EDM efficiency (delivered power vs. baseload power ratio) is a reasonable proxy for PECM.

6.9. Lessons learned from the development of the PECM process

The following knowledge gained from this task will have a profound impact on the commercial use of PECM to process metal surfaces.

- PECM is not a direct substitute for sanding. Sanding is a process that reduces measurable roughness by mainly subtracting from texture peaks, and which requires little surface profile loss to reduce roughness. PECM dissolves metal from the peaks and valleys with small preference given to the peaks. As such, considerably more profile loss is required to achieve a surface that is both geometrically accurate and smooth.
- The rate at which measurable roughness diminishes for given profile loss is a direct function of the interelectrode gap distance (IEGD) and the geometry of the surface texture. Diminishment rate increases with deceasing IEGD. It also increases if the texture geometry is dominated by small wavelengths rather than large wavelengths. Regardless of their amplitude, small wavelength contributions are quickly erased whereas long wave contributions take substantial profile loss to erase.
- When applying PECM to finish machine a surface that was previously rough milled by ball nose end milling, the amount of material that must be removed by PECM/ECM to create a finished surface with reduced roughness is heavily influenced by the diameter of the mill that was used to rough the surface. Given two surfaces of equivalent measured roughness, the one that was milled with the smaller mill diameter will require less material to be removed by PECM/ECM to achieve the desired roughness.
- When applying PECM to a metal surface, especially an aluminum surface, an enveloping cathode that is the mirror image of the surface must be used. A small geometry, moving cathode cannot be used because metal surrounding the cathode and exposed to electrolyte will be subject to a weak electrostatic field that will generate unwanted corrosion and pitting. Excluding the surface to be processed, all other part surfaces need to be protected from contact with the electrolyte to prevent weak field dissolution, corrosion, and pitting.
- Ideally, when applying PECM to finish machine a rough milled surface, the IEGD should be made as small as possible while maintaining high electrolyte velocity flow across the IEG. It should also be coupled with bi-directional electrolyte flow to insure uniformity in average electrolyte temperature across the workpiece surface. This will ensure the highest machined surface quality while at the same time minimizing Ohmic power loss across the

IEG. This will also minimize corresponding heat generation and the costs for mitigating it. This project has demonstrated that this can be achieved at the 1:100 module scale, but it is doubtful that this can be achieved at the full scale. This is due to the challenge of achieving a high electrolyte flow rate through an IEG with a large length-to-cross section area.

- To apply PECM to finish machine a surface as large as the blade interface surface of a full-scale mold module, it must be modified to include a machining cycle and a flush cycle. Prior to the machining cycle, the cathode must be moved to within a close proximity of the workpiece surface. During the machining cycle, electrolyte flow will be close to stagnant, causing electrolyte temperature, electrolyte conductivity, anodic dissolution, hydrogen gas formation, and metal hydroxide formation to rapidly increase via thermal runaway. However, the machining cycle will be monitored and terminated before the electrolyte reaches the boiling point or before the electrical current is allowed to surpass a limit. At this time, a flush cycle will commence where the cathode is moved away from the workpiece surface to allow high volume electrolyte flow through the IEG. This will flush away heat and unwanted products.

7. Market Benefits and Process Commercialization - Cost, Time, and Energy Analysis

A cost model was developed that was divided into three categories: inputs, data analysis, and outputs. Inputs include global inputs which apply to all three mold manufacturing techniques and specific inputs which apply to each process separately. The inputs are used in different sections of data analysis which include plug materials, plug manufacturing, mold materials, mold manufacturing, blade materials, blade manufacturing, and transportation. These models include equations used to determine costs for each step of the process. The model outputs costs for each of these steps along with a total cost for each mold manufacturing process. The cost model organization is shown in Figure 7.1.

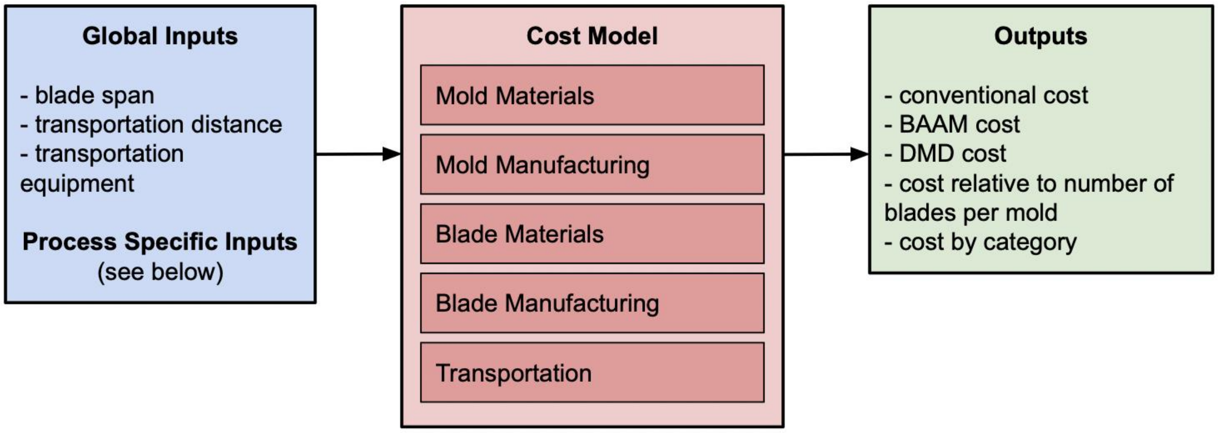

Figure 7.1 Flow of information in cost model including inputs, process subsections, and outputs

7.1. Inputs to cost model

This section will cover the independent variables used in the cost model. They are separated by mold manufacturing process. Global inputs apply to each of the processes while conventional, BAAM, and DMD inputs apply to their respective processes, Figure 7.1.1.

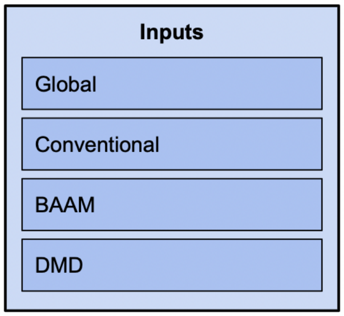

Figure 7.1.1 Overview of how inputs are organized in the cost model

7.1.1. Global inputs

Input parameters to the cost model that apply to each of the different manufacturing processes are in this global input section. These variables, corresponding units, and values are found in Table 7.1.1 below.

Table 7.1.1 Global input parameters for the cost model

Decision Variable	***Units***	***Input Value***
Blade span	m	100
Blade outer aerodynamic area	m^2	1010
Single blade production time	day	1
Electricity cost	$\$/kWh$	0.06
Conventional: transportation distance for plug	km	1862
Conventional: transportation distance for mold	km	0
Conventional: transportation distance for blade	km	3700
BAAM and DMD: transportation distance for mold	km	3792
BAAM and DMD: transportation distance for blade	km	448

The industry standard for single blade production time once in full production is 24 hours according to TPI. The value for blade span was decided from a Sandia Technical Report as a baseline and constant to compare between manufacturing processes (Griffith, 2013). The outer aerodynamic area was subsequently calculated based on blade span, root diameter of 6 m, maximum chord length of 7.63 m, and location of maximum chord length at 33.6% of blade span. These values are in the Sandia Report as well. The formulas used for aerodynamic area calculations are shown as Equations 7.1.1-7.1.3.

$$SS_1 = Bs \times (C/100) \times (A_r \times A_c)/2 \tag{7.1.1}$$

Where SS_1 is surface section one area in m^2, Bs is blade span in m, C is location of maximum chord length as percent of blade span, A_r is area at the root in m^2, and A_c is area at the location of maximum chord in m^2.

$$SS_2 = Bs \times (1 - C/100) \times A_c/2 \tag{7.1.2}$$

Where SS_2 is the surface section two area in m^2.

$$A = SS_1 + SS_2 \tag{7.1.3}$$

Where A is the total blade aerodynamic area. These formulas come from communications with ORNL.

The transportation distances for each part are dependent on where each is produced and the blade destination. For the conventional manufacturing model, it is assumed that the plug is produced in Minden, NV and transported to Juarez, Mexico where the mold is produced. The blade is produced in Juarez as well and sent to Burlington, VT. For BAAM and DMD manufacturing, the mold is produced in Juarez, Mexico and transported to Warren, RI where the blade is made. The blade is then sent to Burlington, VT. The decision for Burlington, VT as a final destination is based on a Sandia Report (*Cost Study for Large Wind Turbine Blades: WindPACT Blade System Design Studies, 2003*). The locations of the plug, mold, and blade manufacturing facilities are based on current TPI facilities and communication with TPI members. Keep in mind that all locations are parameters subject to change and the model has built in adaptability to allow for this.

7.1.2. Conventional inputs

Input parameters that apply to the conventional blade manufacturing process are included in this section. Table 7.1.2 shows these parameters as well as units and values used.

Table 7.1.2: Conventional input parameters for the cost model

Decision Variable	***Units***	***Input Value***
Plug segment length	m	20
Mold segment length	m	50

Both plug and mold segment length influence how many segments of each are needed to produce a blade and therefore transportation cost. These values come from communication with TPI.

7.1.3. BAAM inputs

Input parameters that apply to the BAAM blade manufacturing process are included in this section. Table 7.1.3 shows these parameters as well as units and values used.

Table 7.1.3: BAAM input parameters for the cost model

Decision Variable	*Units*	*Input Value*
Number of mold segments per blade	-	104
Mold shell thickness	m	0.21
Mold material price	$\$/kg$	9.55

Mold material density	kg/m^3	1,140
Deposition rate	kg/h	36
Energy intensity	kWh/kg	1.17

The number of mold segments per blade is calculated from the maximum build size of the BAAM machine (1.8288m) and the blade span. This value is doubled to account for both halves of the mold. All the variables in this section are referenced from ORNL communication and documentation (Love, 2015).

7.1.4. DMD inputs

Input parameters that apply to the DMD manufacturing process are included in this section. Table 7.1.4 lists these parameters, units, and values used.

Table 7.1.4 DMD input parameters for the cost model

Decision Variable	***Units***	***Input Value***
Mold material price	$\$/kg$	190
Mold material density	kg/m^3	2740
Deposition rate per head	kg/h	2.5
Argon gas consumption rate per head	m^3/h	1.89
Argon gas price	$\$/m^3$	0.78
Energy intensity	kWh/kg	1051
Mold shell thickness	m	0.0023
Machines in parallel	-	1
Scrap price	$\$/kg$	0.77
Machining removal thickness	m	0.0002

The mold material price and density are for the Al6061-RAM2 aluminum alloy as proposed (*A6061-RAM2 Brochure*, 2021). The deposition rate of the machine is based on the current industry value for wire fed DMD. This is quicker than powder fed DMD which has a deposition rate of 2.25 kg/hour (*Quick Guide to Metal AM*, n.d.). The energy consumption rate is sourced from a paper regarding general DMD cost modeling (Abel Passos Dos Santos, 2018). Mold shell thickness assumes 75% lightweighting relative to conventional molds. Increasing machines in parallel decreases time of manufacturing at the expense of upfront capital costs. Scrap price is used for calculating monetary gains from mold disposal as proposed. Machining removal thickness is the amount of material traditional finishing procedures remove after DMD production. The decision to model traditional machining and not the large-scale pulsed electro-chemical machining (PECM) process being developed for the project was made because PECM is still in preliminary stages of testing. As more progress is made by our colleagues at Penn State University, this information will be updated.

7.2. Mold material/manufacturing

This section will cover the costs for plug and mold materials and manufacturing. Each subsection covers a different mold manufacturing process. Costs such as materials, fixtures, labor, overhead, and energy are included. This is shown in Figure 7.2.1.

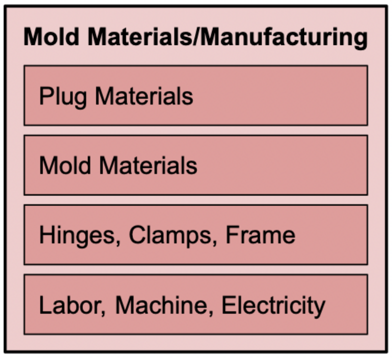

Figure 7.2.1 Overview of what is included in the mold materials and manufacturing section of the cost model

7.2.1. Conventional mold materials/manufacturing

Mold material cost for conventional mold manufacturing, Mat_{con}, is determined by both area prices and unit prices in Equation 7.2.1.

$$Mat_{con} = (P + S) \times A + H \times N_H + C \times N_C + F \tag{7.2.1}$$

Where P is plug material cost in $\$/m^2$, S is the mold shell material cost in $\$/m^2$, A is blade aerodynamic area in m^2, H is cost per hinge, N_H is the number of hinges, C is the cost per clamp, N_C is the number of clamps, and F is the frame cost.

The area for plug materials (steel frame, glass laminate, epoxy) and shell materials (resin, glass, consumable, insulation, heating, and controls) is determined by the blade outer aerodynamic area. The standard unit prices of $2,500/$m^2$ for plug materials, $400/$m^2$ shell materials, and $500/$m^2$ heating and controls are based on TPI communications. It is assumed that 8 hinges ($71,417 per hinge) are used for a 100 m blade and clamps ($937 per clamp) are spaced every two meters on each side along the length of the blade. This gives 100 clamps for a 100 m blade span. The frame cost is assumed to be 25% of the shell cost. These values are based on TPI elicitation.

Mold manufacturing cost, Man_{con}, is a function of unit labor cost (\$600/m^2) and blade aerodynamic area based on TPI communications. This unit labor cost includes overhead, machine cost, energy, and building/lease cost. Equation 7.2.2 shows the formula for calculating mold manufacturing cost for the conventional process.

$$Man_{con} = L \times A \tag{7.2.2}$$

Where L is unit labor cost in \$/m^2 and A is blade aerodynamic area in m^2. Total cost for conventional mold materials and manufacturing is determined by adding the material and manufacturing costs.

7.2.2. BAAM mold materials/manufacturing

Mold material cost for BAAM mold manufacturing, Mat_{BAAM}, is also determined by both area prices and unit prices in Equation 7.2.3.

$$Mat_{BAAM} = S \times A + H \times N_H + C \times N_C + Sh \times N_{Sh} + F \tag{7.2.3}$$

Where S is shell material cost in \$/m^2, A is blade aerodynamic area in m^2, H is cost per hinge, N_H is the number of hinges, C is the cost per clamp, N_C is the number of clamps, Sh is cost per build sheet, N_{Sh} is the number of build sheets, and F is the frame cost.

The area for shell materials (thermoplastic with carbon fiber reinforcement) is determined by the blade outer aerodynamic area. The standard unit price for shell materials is \$2,288.74/m^2 which is calculated from ORNL provided \$/kg cost, shell material density, and mold thickness. The need for plug manufacturing is eliminated due to the nature of the printing process. Similarly, the need for heating system costs is removed due to built-in heating channels taking the place of traditional wiring. The cost of hinges, clamps, and frame are identical to that of conventional manufacturing. There are 12 build sheets needed at \$60 each. These sheets are the surface which is built upon during the BAAM process. These values are based on a BAAM cost model provided by ORNL.

Mold manufacturing cost, Man_{BAAM}, includes design time, amortized machine cost, energy cost, labor, assembly, and set-up costs. This is shown in Equation 7.2.4.

$$Man_{BAAM} = D \times C_D + M \times C_M + Mass \times E \times C_E + (L + A + S) \times C_L \tag{7.2.4}$$

Where D is design labor time in hours, C_D is design unit labor cost in \$/hour, M is hours of machine operation, C_M is amortized machine cost in \$/hour, $Mass$ is mass of the BAAM mold in kg, E is energy intensity in kWh/kg, C_E is electricity cost in \$/kWh, L is machine labor time in hours, A is mold assembly time in hours, S is machine set-up time in hours, and C_L is labor cost in \$/hour.

The printing time is calculated based on blade aerodynamic area, shell thickness, material density, and deposition rate. The design time cost comes from labor time of 40 hours and unit labor cost of

$50/hour. The amortized machine cost is the printing time multiplied by unit cost of $100/hour. The labor, assembly, and set-up unit costs are all $30/hour. The energy cost is calculated from mold mass, process energy intensity, and electricity cost. The mass is calculated from blade aerodynamic area, mold thickness, and material density. All values are based on the BAAM cost model provided by ORNL.

7.2.3. DMD mold materials/manufacturing

Mold material cost for DMD mold manufacturing, Mat_{DMD}, is also determined by both area prices and unit prices in Equation 7.2.5.

$$Mat_{DMD} = (S - Sc) \times A + H \times N_H + C \times N_C + F \tag{7.2.5}$$

Where S is shell material cost in $\$/m^2$, Sc is scrap cost in $\$/m^2$, A is blade aerodynamic area in m^2, H is cost per hinge, N_H is the number of hinges, C is the cost per clamp, N_C is the number of clamps, and F is the frame cost.

The area for shell materials (Al6061-RAM2) and scrap cost is determined by the blade outer aerodynamic area. The standard unit price for shell materials is $\$1197.38/m^2$ from material price, density, and DMD mold thickness. The standard unit price for scrap is $\$5.82/m^2$ from scrap price, density, and mold thickness. This scrap cost is subtracted from the material cost as it represents a future income. The cost of hinges, clamps, and frame are identical to that of conventional manufacturing.

To model manufacturing cost (Man_{DMD}), design time, build process, and finishing were considered. Design time cost comes from labor time of 40 hours and unit labor cost of $28.4/hour. These values come from TPI communications. The build process cost includes electrical energy cost, gas consumption cost, machine cost, maintenance cost, and labor cost. The printing time is calculated based on blade aerodynamic area, shell thickness, material density, and deposition rate. An electrical energy consumption rate of 1051 kWh/kg and electricity cost of $0.06/kWh were used. An argon gas consumption rate of 1.89 m^3/h for shielding and gas price of $\$0.78/m^3$ were used (Abel Passos Dos Santos, 2018). Machine cost was calculated from an initial upfront cost of $900,000 over ten years of operation to determine a price of $12.88/hour. This number comes from inter-team communication. Machine cost in $/hour is shown in Equation 7.2.6. Maintenance cost is assumed to be 20% of machine cost. Hourly labor cost is $20/hour which is multiplied by build time (Abel Passos Dos Santos, 2018). Using mass of material to be removed (from blade aerodynamic area and machining depth), material removal rate of 7.5 kg/h (based on traditional machining), and labor costs of $20/hour gives the cost for traditional machining.

$$C_M = U \,/\, (H \times 0.8) \tag{7.2.6}$$

Where C_M is machine cost in $/hour, U is upfront DMD machine cost in $, H is lifespan in hours, and 0.8 represents utilization rate. Total manufacturing cost for DMD mold production is shown in Equation 7.2.7.

$$Man_{DMD} = D \times C_D + Mass \times E \times C_E + G \times C_G + M \times C_M \times 1.2 + L \times C_L + (Mass_R/R \times C_L) \tag{7.2.7}$$

Where D is design labor time in hours, C_D is design unit labor cost in \$/hour, $Mass$ is mass of DMD mold in kg, E is energy intensity in kWh/kg, C_E is electricity cost in \$/kWh, G is argon gas consumption in m^3/h, C_G is argon gas price in \$/m^3, M is hours to build mold, L is machine labor time in hours, C_L is labor cost in \$/hour, $Mass_R$ is mass of material to be removed during finishing in kg, and R is material removal rate in kg/h.

7.3. Blade material/manufacturing

This section will cover the costs for the blade materials and manufacturing. Costs such as materials and labor are included. This is shown in Figure 7.3.1.

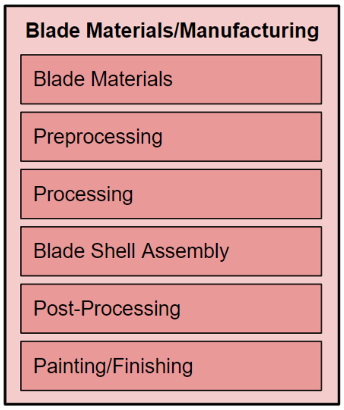

Figure 7.3.1 Overview of what is included in the blade materials and manufacturing section of the cost model

The blade material and manufacturing cost is assumed to be constant across all methods of mold manufacturing. The material cost, Mat_{blade}, includes the mass price of various materials used in blade construction as well as area price of the core foam used. Blade material cost is shown in Equation 7.3.1.

$$Mat_{blade} = (Uf + D) \times C_{Uf} + Er \times C_{Er} + Ec \times C_{Ec} + A \times C_{Cf} \tag{7.3.1}$$

Where Uf is uni-axial fiberglass mass in kg, D is double bias fiberglass mass in kg, C_{Uf} is uni-axial fiberglass and double bias fiberglass mass price in \$/kg, Er is epoxy resin mass in kg, C_{Er} is epoxy resin mass price in \$/kg, Ec is exterior coating mass in kg, C_{Ec} is exterior coating mass price in \$/kg, A is blade aerodynamic area, and C_{Cf} is core foam area price in \$/m^2.

The SNL Cost Tool User Manual provides a mass value for a 40 m blade and percent of blade mass values for various blade materials. This weight is scaled to a 100 m blade and the percentages are used to determine the mass of each material for a 100 m blade. This includes 11,901.12 kg of uni-axial fiberglass at \$2.97/kg, 3,233.13 kg of double bias fiberglass at \$2.97/kg, 16,531.37 kg of epoxy resin at \$4.65/kg, and 281.62 kg of exterior coating at \$14/kg. The area of core foam comes from blade aerodynamic area which is multiplied by an area price of \$32.7/m^2. These values are sourced from SNL Cost Tool User Manual (Johanns & Todd Griffith, n.d.).

Blade manufacturing cost, Man_{blade}, includes preprocessing, processing, blade shell assembly, post-processing, surface finishing, and painting. This is shown in Equations 7.3.2-7.3.7.

$$Pre = C_L \times (L + K + Cl) + C_M \times M \tag{7.3.2}$$

Where C_L is hourly labor cost in \$/hour, L is labor hours of loading fabric rolls and machine preparation, K is labor hours of kitting (organize parts into bundles to deliver), Cl is labor hours of clean up, C_M is hourly machine cost in \$/hour, and M is hours of material cutting.

$$Proc = C_L \times (Pr + In + Apsc + Apfc + Le + Ant + Afm + Aflr + Aflm + Avb + Pfv + Cvl + Ai + Cp + Rvb) \tag{7.3.3}$$

Where C_L is hourly labor cost in \$/hour, Pr is hours of preparing tools, In is hours of inserting root into the mold, $Apsc$ is hours of applying pre-fab spar caps, $Apfc$ is hours of applying pre-knitted foam and core, Le is hours of reinforcement during preparation, Ant is hours of applying nonsand tape and peel-ply, Afm is hours of applying flow medium, $Aflr$ is hours of applying feed lines for root preform, $Aflm$ is hours of applying feed lines for mold skins, Avb is hours of applying vacuum bag, Pfv is hours to pull full vacuum, Cvl is hours of checking for vacuum leaks, Ai is hours of actual infusion, Cp is hours of curing, and Rvb is hours of removing the vacuum bag.

$$Assem = C_L \times (Aswb + Cm) \tag{7.3.4}$$

Where C_L is hourly labor cost in \$/hour, $Aswb$ is hours to assemble shear web bonds, and Cm is hours to close the mold.

$$Post = C_L \times (Mbfa + Mbtb + Tpf + Mbotb + Mbs + Tbr) \tag{7.3.5}$$

Where C_L is hourly labor cost in \$/hour, $Mbfa$ is hours to move blade to finishing area, $Mbtb$ is hours to move blade to trim booth, Tpf is hours to trim perimeter flashing, $Mbotb$ is hours to move blade out of the trim booth, Mbs is hours to move blade in saddles for root cutting, and Tbr is hours to trim blade root.

$$Finish = C_L \times (Mbca + Psp + Mbpb + Ap + Cp + Ac + Cc + Mbs + Psf) \tag{7.3.6}$$

Where C_L is hourly labor cost in \$/hour, $Mbca$ is hours to move blade carts to finishing area, Psp is hours to perform surface preparation, $Mbpb$ is hours to move blade to paint booth, Ap is hours to apply primer, Cp is hours to cure/tackify the primer, Ac is hours to apply top coating, Cc is hours to cure the coating, Mbs is hours to move blade to surface finish area, and Psf is hours to perform surface inspection/finish.

$$Man_{blade} = Pre + Proc + Assem + Post + Finish \tag{7.3.7}$$

All values for blade manufacturing are sourced from an NREL report (Bortolotti et al., 2019).

7.4. Transportation

This section will cover the costs for the transportation of the plug, mold, and blade. This is shown in Figure 7.4.1.

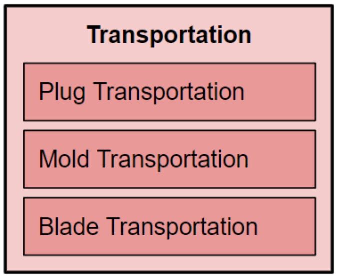

Figure 7.4.1 Overview of what is included in the transportation section of the cost model

The transportation section of the cost model was mainly derived from a website called oversize.io which attempts to output transportation cost based on route, load dimensions, and type of transport (Oversize.io, 2022). It also sources information from state laws for oversize and/or overweight permits from government websites. The model created considers the load dimensions, load weight, vehicle dimensions, vehicle weight, and distance traveled through each state along the route. It gives prices for permits, service fees, civilian escort cost, and trucking cost. It assumes a generic flatbed with five axles as the vehicle transporting each part.

The permit cost is calculated by deciding whether the overall transport is oversized or overweight. Figure 7.4.2 shows how the model calculates overall transport size and weight. The model uses regulations from each state to determine the cost of either/both oversize and overweight fees. These are found from state oversize permit pages. Some states have fees that scale with weight and/or miles traveled through said state. Typical values range from $15 to multiple hundred dollars. The number of escorts required is also determined by each state's regulations. The trucking cost is assumed to be $10/mile but can be altered if needed based on updated figures.

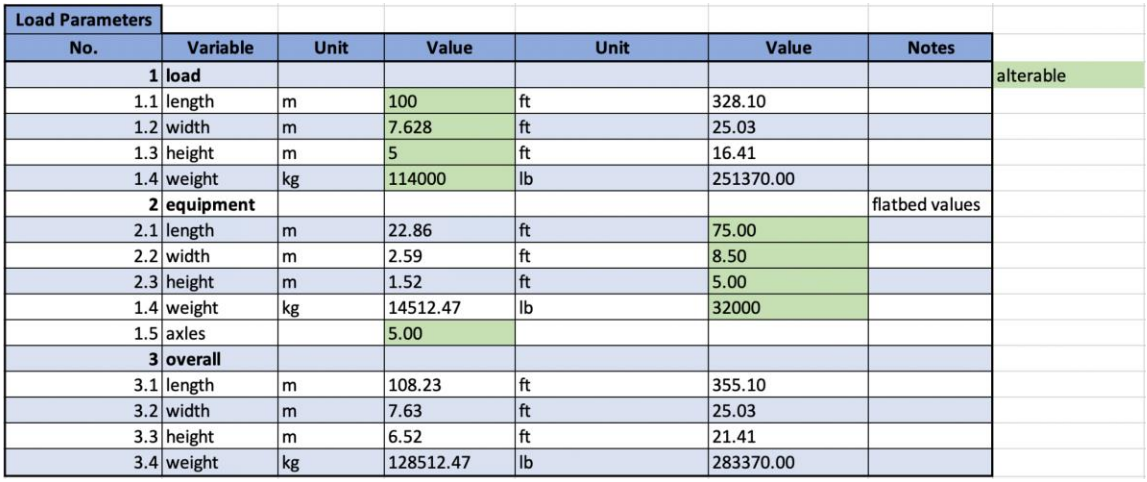

Load Parameters

No.	Variable	Unit	Value	Unit	Value	Notes	
1	**load**						alterable
1.1	length	m	100	ft	328.10		
1.2	width	m	7.628	ft	25.03		
1.3	height	m	5	ft	16.41		
1.4	weight	kg	114000	lb	251370.00		
2	**equipment**					flatbed values	
2.1	length	m	22.86	ft	75.00		
2.2	width	m	2.59	ft	8.50		
2.3	height	m	1.52	ft	5.00		
1.4	weight	kg	14512.47	lb	32000		
1.5	axles		5.00				
3	**overall**						
3.1	length	m	108.23	ft	355.10		
3.2	width	m	7.63	ft	25.03		
3.3	height	m	6.52	ft	21.41		
3.4	weight	kg	128512.47	lb	283370.00		

Figure 4.4.2 Load parameters section of transportation model

7.5. *Outputs of cost model*

This section will cover the outputs of the cost model as summarized in Figure 7.5.1. See Section 7.9 for numerical results.

Outputs

- conventional cost per blade
- BAAM cost per blade
- DMD cost per blade
- cost relative to number of blades per mold
- cost by category

Figure 7.5.1: Overview of outputs of the cost model

The output section of the cost model collects the values from all the previous sections and combines them for each manufacturing process. It includes replications per part, or how many times the cost value needs to be repeated for a single blade. For example, plug transportation has a value of 5 for replications per part, which indicates that 5 20m plug segments are needed for each blade. Therefore, the cost value for transporting a plug segment from the transportation section is multiplied by 5 to give the total cost. The outputs section also includes blades per replication or how many blades you can make with the cost value. For example, each mold can make more than one blade. The final value for each process is the sum of mold material, mold manufacture, blade material, blade manufacture, and transportation cost per blade.

7.6. Time model framework: conventional, BAAM, and DMD

The assumptions and variables from the cost model sections for each of the processes are also applied to the time models as detailed below. Figure 7.6.1 shows a time to market timeline for each mold production process.

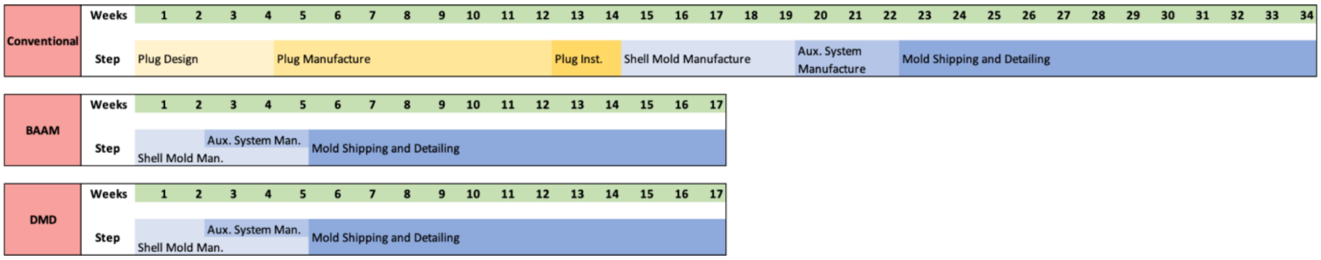

Figure 7.6.1 Gantt chart for each of the mold production processes; assumed that BAAM uses five machines in parallel with 2 heads each and DMD uses four machines in parallel with one head each

The timeline for blade manufacturing using the conventional mold manufacturing process includes the time associated with plug manufacture, mold manufacture, blade manufacture, and transportation of each. The plug manufacturing process general timeline is as follows: 4 weeks for plug design, 8 weeks for plug manufacture, and 2 weeks for shipping and installation for testing. This is a total of 14 weeks with a typical range of 12-16 weeks. The mold manufacturing process general timeline includes 4-6 weeks for shell mold manufacture, 2-4 weeks for axillary system manufacture (spar caps, shear webs, flanges, etc.), and 10-14 weeks for transportation and detailing with customers. This is an average of 20 weeks for mold manufacture with a typical range of 16-24 weeks. The blade manufacturing process is held to a 24-hour blade replication cycle once in full production. This is always enforced, and larger blades require a larger crew to keep this timeline. In total, the timeline for creating a blade using the conventional mold manufacturing process is 34 weeks on average with a typical range of 28-40 weeks. These values come from TPI communication and documentation.

The timeline for blade manufacturing using the BAAM mold manufacturing process includes the time associated with mold manufacture, blade manufacture, and the transportation of each. The mold manufacturing process general timeline varies depending on the number of machines and number of heads per machine used. If only one head on one machine is used in continuous operation, a 100 m mold (for a 100 m blade) would take 50 weeks to print. This value can be reduced linearly by adding heads to machines and/or running multiple machines in parallel. For example, if using five machines to make five segments in parallel, the time reduces to 10 weeks. If each of those machines has two heads instead of one, the time reduces further to 5 weeks, and so on. The blade manufacturing process is assumed to be identical to the conventional process and held to a 24-hour blade replication cycle once in full production.

The timeline for blade manufacturing using the DMD mold manufacturing process includes the time associated with mold manufacture, blade manufacture, and the transportation of each. The mold manufacturing process general timeline varies like the BAAM process depending on the number of heads/machines used. If only one head on one machine is used in continuous operation, a 100 m mold would take 20 weeks to print. This value can be reduced linearly by adding head to machines and/or running multiple machines in parallel. For example, if using five machines to make five segments in parallel, the time reduces to 4 weeks. If each of those machines has two heads instead of one, the time reduces further to 2 weeks, and so on. The blade manufacturing process is identical to the conventional process and held to a 24-hour blade replication cycle once in full production.

7.7. Direct energy model framework: BAAM and DMD

The direct energy consumption to produce a mold using BAAM and DMD processes is described in this section. This is the energy required to operate the machines during printing.

The direct energy consumption of the BAAM mold manufacturing process, $Energy_{BAAM}$, is modeled using Equation 7.7.1.

$$Energy_{BAAM} = Mass_{BAAM} \times I_{BAAM} \tag{7.7.1}$$

Where $Mass_{BAAM}$ is the mass of the BAAM mold in kg and I_{BAAM} is the energy intensity of the BAAM process in kWh/kg.

The direct energy consumption of the DMD mold manufacturing process, $Energy_{DMD}$, is modeled using Equation 7.7.2.

$$Energy_{DMD} = Mass_{DMD} \times I_{DMD} \tag{7.7.2}$$

Where $Mass_{DMD}$ is the mass of the DMD mold in kg and I_{DMD} is the energy intensity of the DMD process in kWh/kg.

7.7.1. DED energy consumption rate

An additional investigation of the costs and energy requirement of aluminum DED was undertaken. There is limited literature on the costs, energy requirements, and potential scale-up of aluminum DED; therefore, the UM team worked closely with DM3D on their existing practices and costs and conducted a case study on the electrical energy requirements using a prototype system at UM.

DM3D’s estimate of DED energy consumption is 32 kWh/kg, although this is not measured by DM3D. The UM team found a source in the literature (Ehmsen et al. [13]) which estimates aluminum DED energy consumption at 47 kWh/kg, which was measured on a DMG MORI Lasertec 65 3D DED machine using a power meter. The UM team then conducted a case study at UM on an experimental DED setup at UM which resulted in an estimated energy consumption rate of 341 kWh/kg, measured using two power meters linked to the laser and the CNC machine, Figure 7.7.1. As this was measured on an experimental setup, the machine parameters were not optimized. A group at UM (Morrow et al. [12]) that used a similar experimental setup estimated that industrial equivalents to experimental setups would have an order of magnitude reduction in energy consumption rate due to machine parameter optimization. Therefore, the industrial equivalent to the experimental setup used in this case study would have an estimated energy consumption rate of about 34 kWh/kg. Considering the three sources gathered for aluminum DED energy consumption rate, our estimate of aluminum DED energy consumption is 50 kWh/kg ± 20 kWh/kg uncertainty with a uniform distribution.

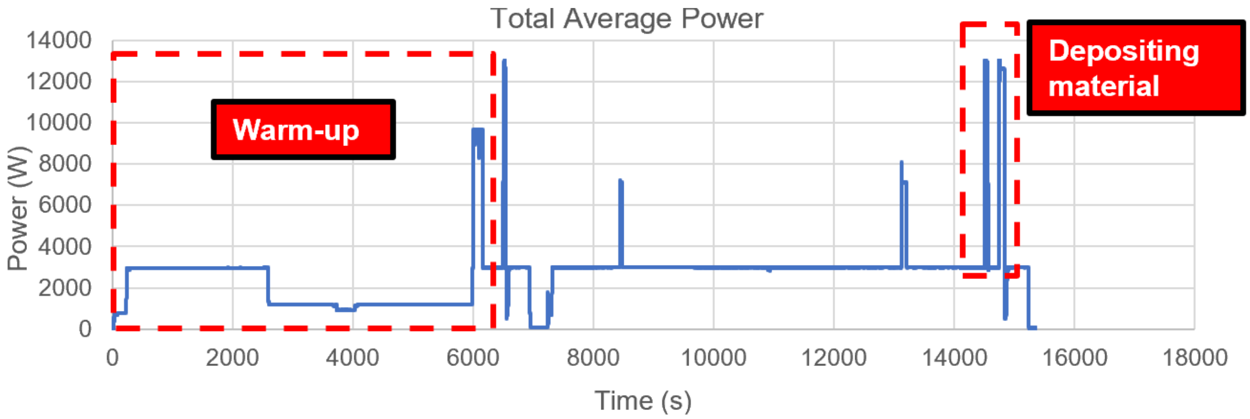

Figure 7.7.1 Total average power of CNC machine and laser during DED Case Study

7.8. *Uncertainty in data collection and expert elicitation*

This section will cover the process of gathering information about the blade manufacturing process from industry professionals as well as how uncertainties in the values provided were determined. In addition to using literature reviews during the process of creating the models, we were in communication with industry professionals who provided valuable insight and information about steps in the blade production process. To validate the conventional mold manufacturing model and add uncertainty, we met with Alexander Segala of TPI. We asked him various questions about the manufacturing process, both directly related to the model and ones that would indirectly help inform us. These questions were structured in a way that he would provide typical averages for numerical values along with upper and lower bounds. Some of the questions included plug and mold segment lengths, material price, and labor unit cost. The questions posed and values provided by TPI can be found in the related excel document.

7.8.1. *Uncertainty analysis for conventional, BAAM, and DMD*

The uncertainty of the cost values for conventional, BAAM, and DMD mold production methods was performed using Monte Carlo analysis with Python. For each mold manufacturing process, uncertainty was assigned to intrinsic values (e.g., mold materials) which influence the overall uncertainty of the calculated costs and time. Monte Carlo analysis draws samples from each uncertainty distribution assigned to these values and creates a histogram with 10,000 samples for the cost of one wind turbine blade. See Figure 7.9.10 for a representative graph. The specific variables which were assigned uncertainty for each process are detailed in Sections 7.9 below. For the following sections, unless otherwise stated, the range of uncertainty is assumed to be +/- 10% from the mean with a normal distribution.

For the conventional manufacturing process, uncertainty was assigned to the following values: mold and plug material cost (e.g., mold resin), blade material cost (e.g., fiberglass, resin, and coating), hourly labor cost and machine depreciation rate for blade manufacturing, and costs associated with transportation (e.g., mileage). Most of the uncertainty ranges used come from expert elicitation with TPI.

For the BAAM manufacturing process, uncertainty was assigned similarly to conventional (Section 3.2.1) with the modification of mold cost. Uncertainties for build sheet cost, mold manufacturing labor cost, and machine preparation cost were all included.

For the DMD manufacturing process, uncertainty was assigned similarly to conventional and BAAM (Sections 3.2.1 and 3.2.2) with the modification of mold cost. The model includes uncertainties for the scrap material cost, energy and gas consumption of the mold manufacturing, and mold manufacturing labor cost.

7.9. Results

The results are organized by each section of the model: cost, time, and energy. They are further divided by manufacturing process (conventional, BAAM, and DMD) where appropriate.

7.9.1. Cost model

This section will cover the results of the cost model including a cost breakdown by manufacturing step for each process, transportation cost breakdown by process, total cost comparison, how cost changes as the number of blades produced per mold increases, and the uncertainty of total blade manufacturing cost.

The output of the model for each mold manufacturing process is shown in the sections below. Each process (conventional, BAAM, and DMD) has a cost value that is divided by step along the blade manufacturing process. The values assume that each mold is used for a singular blade as a baseline and the blade is 100 m long. For this reason, the price of the mold materials and manufacturing is high compared to blade materials and manufacturing. Section 7.9.7 covers how this value changes with respect to the number of blades produced per mold.

These costs include values for plug materials, plug manufacturing, mold materials, mold manufacturing, blade materials, blade manufacturing, and transportation.

7.9.2. Conventional cost breakdown

The cost breakdown of blade manufacturing using the conventional mold manufacturing process is shown in Figure 7.9.1 below. The total cost for producing one blade is $3,431,490. This includes costs for plug materials/manufacturing ($549,827), mold materials ($1,902,147), mold manufacturing ($659,793), blade materials ($161,721), blade manufacturing ($94,780), and total transportation ($63,223). The blade materials and manufacturing are 7.47% of the total cost. The mold materials and manufacturing (including plug costs) are 90.69% of the total cost. The transportation costs (plug, mold, and blade) are 1.84% of the total cost.

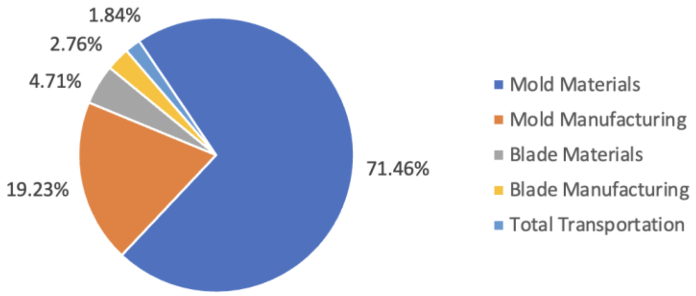

Figure 7.9.1 Conventional manufacturing blade cost breakdown

7.9.3. BAAM cost breakdown

The cost breakdown of blade manufacturing using the BAAM mold manufacturing process is shown in Figure 7.9.2 below. The total cost for producing one blade is $4,682,083. This includes costs for mold materials ($3,430,002), mold manufacturing ($973,742), blade materials ($161,721), blade manufacturing ($94,780), and total transportation ($21,839). The blade materials and manufacturing are 5.47% of the total cost. The mold materials and manufacturing are 94.06% of the total cost. The transportation costs (mold and blade) are 0.47% of the total cost.

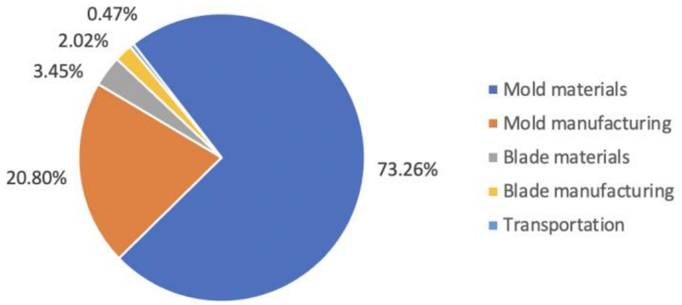

Figure 7.9.2: BAAM manufacturing blade cost breakdown

7.9.4. DMD cost breakdown

The cost breakdown of blade manufacturing using the DMD mold manufacturing process is shown in Figure 7.9.3 below. The total cost for producing one blade is $3,446,887. This includes costs for mold materials ($2,486,100), mold manufacturing ($682,449), blade materials ($161,721), blade manufacturing ($94,780), and total transportation ($21,839). The blade materials and manufacturing are 7.44% of the total cost. The mold materials and manufacturing are 91.93% of the total cost. The transportation costs (mold and blade) are 0.63% of the total cost.

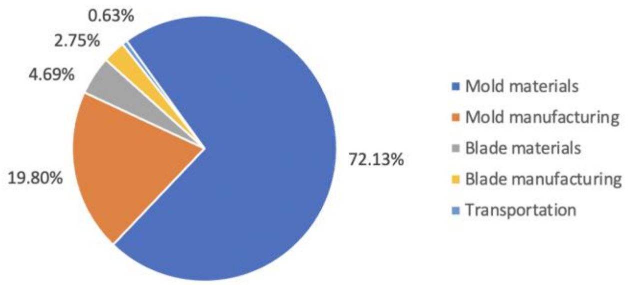

Figure 7.9.3 DMD manufacturing blade cost breakdown

Furthermore, the cost breakdown of mold manufacturing using the DMD process is shown in Figure 7.9.4 below. The total cost is divided into costs for electrical energy, gas consumption, machine, and labor. The DMD process is very energy intensive (1051 kWh/kg) which explains why 80.81% of the cost is due to electrical energy consumption.

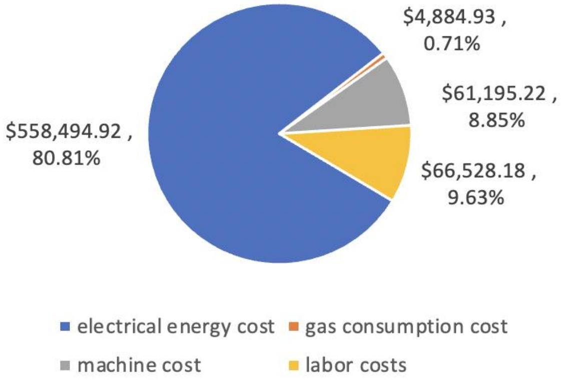

Figure 7.9.4 DMD mold manufacturing cost breakdown

7.9.5. Transportation cost per blade comparison

The transportation cost are compared step by step and across mold manufacturing processes in Figure 7.9.5. This considers the advantage of modularity for BAAM and DMD processes by using the routes as stated. Mold transportation cost is modeled as zero in the conventional manufacturing scenario because the blades and molds are manufactured in Juarez, Mexico for this process. The reduction in total transportation cost from $63,223/blade for conventional to $21,839/blade for BAAM and DMD is a 65% decrease compared to the 30% reduction as stated in the project proposal.

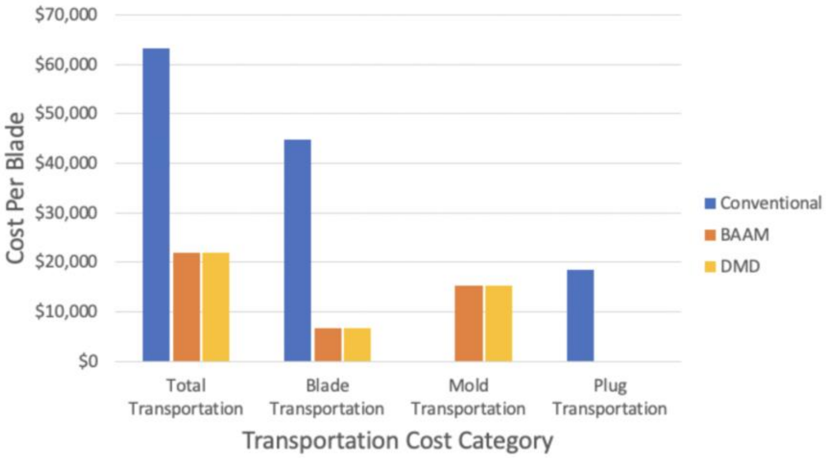

Figure 7.9.5 Transportation cost per blade comparison by category

7.9.6. Total cost comparison

The total cost for producing a blade is compared between mold manufacturing processes in Figure 7.9.6 and further broken down by step in Figure 7.9.7 below. The total cost is $3,431,490 for conventional manufacturing, $4,682,083 for BAAM manufacturing, and $3,446,887 for DMD manufacturing.

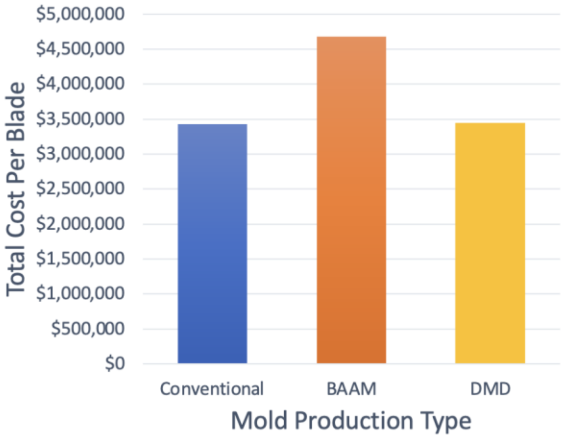

Figure 7.9.6 Total cost comparison between mold manufacturing processes

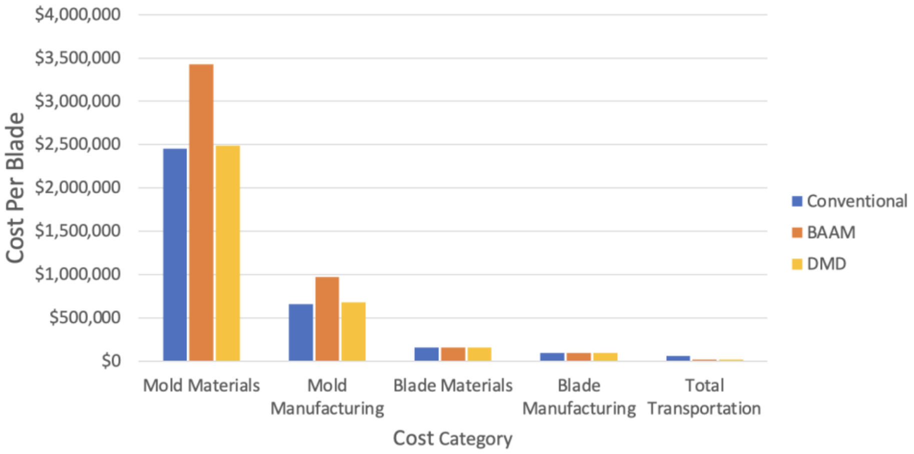

Figure 7.9.7: Total cost comparison by category

7.9.7. Cost relative to number of blades per mold

While the results so far have been the cost to produce a singular blade from one mold, in reality more than one blade is produced per mold. The industry warranty for conventional molds is 1,000 blades per mold. Figure 7.9.8 shows how the price per blade changes as the number of blades per mold is increased. This is achieved by dividing the mold material and manufacturing cost by the number of blades per mold and adding that to a constant blade material, blade manufacturing, and transportation cost. For this reason, the cost per blade value approaches an asymptote that corresponds to the combined cost of blade materials, blade manufacturing, and transportation. The value for 1,000 blades per mold is $322,836/blade for conventional, $282,743/blade for BAAM, and $281,508/blade for DMD. The conventional process has a higher transportation cost which accounts for the higher asymptote value.

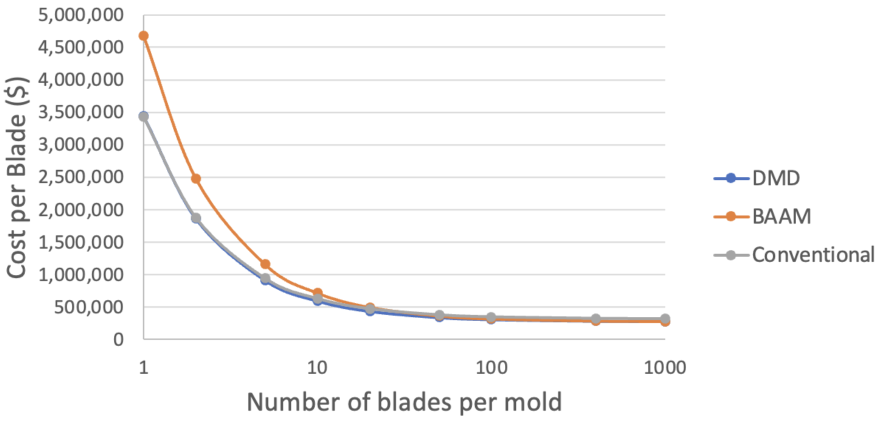

Figure 7.9.8 Influence of blades produced per mold on cost per blade; the DMD and conventional lines are almost overlapping

7.9.8. Commonality model

Although it has been shown that mold cost per blade decreases with the number of blades produced per mold, mold modularity will enable more blades to be produced per mold segment (module), resulting in increased savings, but will require mold module storage, which could result in increased costs. Metal wind turbine molds are predicted to have a greater physical lifespan than the current conventional wind turbine molds, which would result in a longer storage period. We have constructed parametric models with realistic industry values to give us a sense of the degree of savings a modular mold would bring, Figure 7.9.9. The best- and worst-case scenarios were evaluated to bound the analysis of the model. High commonality leads to a high utilization, low production, and low storage due to the ability of the modules to reconfigure into any mold required, while low commonality leads to low utilization, high production, and high storage since modules are less able to be reconfigured. Therefore, the model predicts that the highest commonality results in the highest savings, given that there will be a large reduction in storage and production costs.

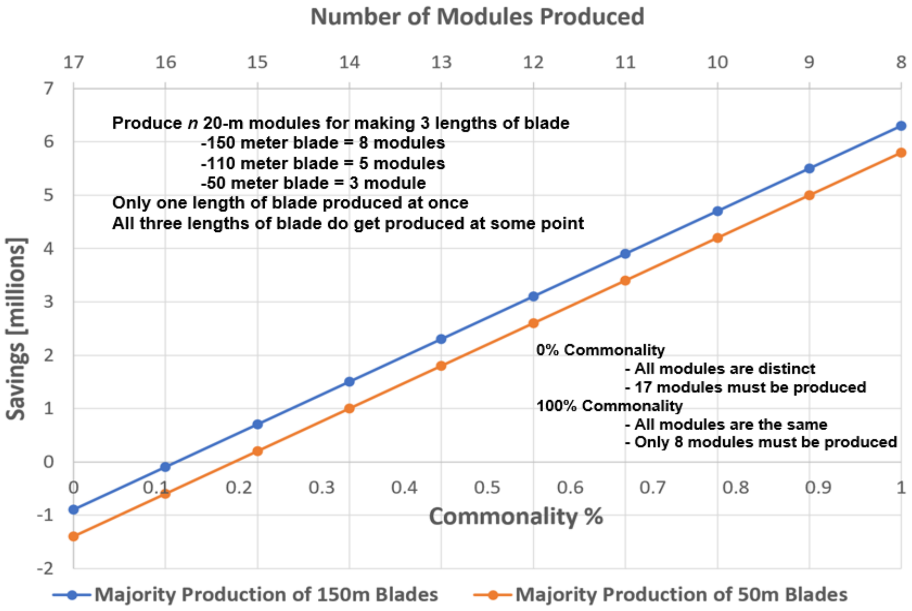

Figure 7.9.9 Savings from modular mold concept as a function of commonality

The degree of commonality across molds for varying blade lengths, the cost of storing the modular molds, the cost of reconfiguring the molds, and the lead time on mold construction have all been identified as critically important.

7.9.9. Total cost uncertainty

The results of the Monte Carlo analysis on the cost of producing one blade for each mold manufacturing process is shown in Figure 7.9.10 below. For conventional manufacturing, the mean cost is $3,431,335 with a standard deviation of $53,837. For BAAM manufacturing, the mean cost is $4,682,817 with a standard deviation of $268,639. For DMD manufacturing, the mean cost is $3,469,644 with a standard deviation of $167,872. These costs include values for plug materials, plug manufacturing, mold materials, mold manufacturing, blade materials, blade manufacturing, and transportation for a 100 m blade.

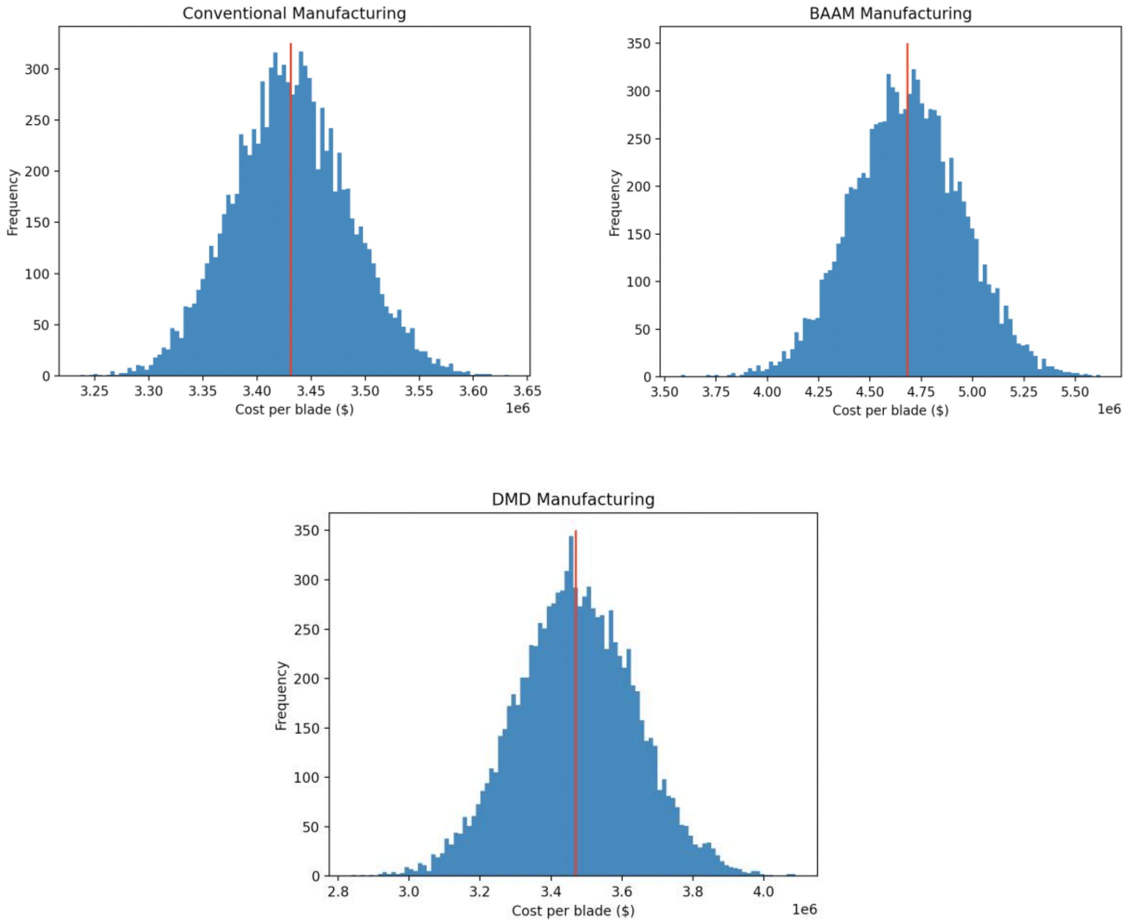

Figure 7.9.10 Monte Carlo uncertainty analysis results for each mold manufacturing process

7.9.10. Energy model

The total direct energy usage of each process as calculated is as follows: 308,344 kWh for BAAM and 8,740,137 kWh for DMD. The DMD process is much more energy intensive than the BAAM process (1051 kWh/kg compared to 1.17 kWh/kg). The analysis indicates that, assuming blade production is identical across the different molds, then the conventional mold production process is the least energy intensive but also the least reconfigurable and with the highest transport energy requirements. The BAAM process has a significantly higher primary energy requirement due to the use of energy-intensive carbon fiber filled polymer as the mold material. For the DMD mold, energy requirements are very sensitive to the lightweighting achieved because of the energy intensity of both the aluminum powder and the DMD process itself.

In the Figure 7.9.11 below, DMD Original refers to the case of using DMD to print the whole mold (base plate, mold face, and the optimized internal structure); whereas, DMD refers to a hybrid approach where the DMD process is only used to make the topologically optimized internal structure and not the solid base and face of the mold which might feasibly be made using aluminum plate shaped on reconfigurable segmented stretch forming dies. The DMD molds do have the advantage of being reconfigurable and therefore can be used to produce a larger number of blades than the conventional process before replacement. This reconfigurability means that the high upfront energy requirements of making the DMD mold can be amortized over a greater number of blades. For example, if the DMD (DMD original) mold depicted in the figure below were used to produce 800 (3200) blades, then the primary energy requirements per blade would be lower than a conventional mold that was only used to produce 100 blades.

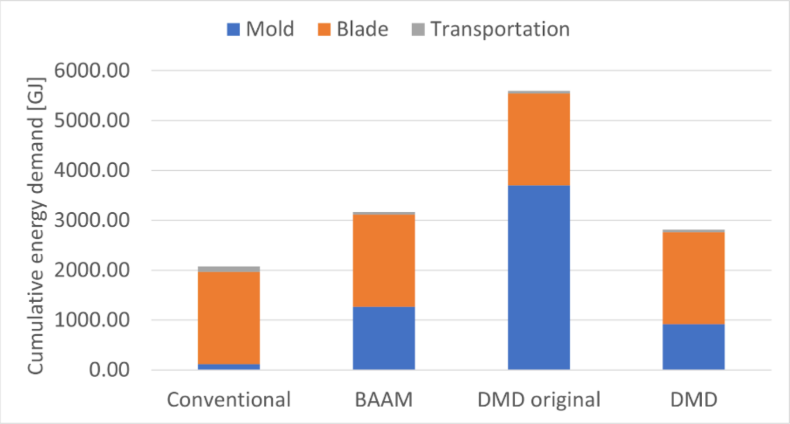

Figure 7.9.11 Energy requirements per blade if 100 blades are produced on each mold

7.10. Summary of cost savings

This section includes a comparison of the results to the goals, the variables that have the most impact on the results of the models. Information used in the detailed cost, time, and energy models are sourced either from direct communications with industry professionals, documentation from industry companies, or related papers online. This is to ensure that the results presented are accurate within a reasonable amount of uncertainty. Assumptions and sources of information are stated where appropriate.

Potential savings as stated in the proposal:

- A 30% cost saving of the tooling for 120m blades comparing with polymer composite additive manufactured molds
- A 50% reduction time of mold fabrication (printing and polishing) and time to market
- A 30% reduction in transportation cost of molds and blades based on the modularity design

As achieved:

- A 30% cost saving of the tooling compared to BAAM ($973,742 for BAAM and $682,449 for DMD)

- A 77% reduction time of mold fabrication (22 weeks to 5 weeks) and 50% reduction in time to market (34 weeks to 17 weeks)
- A 65% reduction in transportation cost of molds and blades based on modular design ($63,223/blade for conventional and $21,839/blade for DMD)

In relation to the cost model, the factor that affects the conventional process the most is the blade span. It determines the blade aerodynamic area which is the basis of much of the mold material cost and the cost for mold manufacturing. For the BAAM process, the blade span, mold shell thickness, and deposition rate per head all affect the mold material and manufacturing price significantly. For the DMD process, blade span, mold shell thickness, deposition rate per head, and energy intensity all have a great effect on the mold material and manufacturing cost. The time model is most significantly impacted by the number of machines operating in parallel and the number of heads per machine for BAAM and DMD. The time for mold printing can be reduced linearly by increasing either of those factors. For the energy model, the energy intensity of the process, blade span, and mold shell thickness are important to consider. They either affect energy consumption or the mass of the part.

7.11. Sensitivity analysis on mold process economics

A sensitivity analysis on mold process economics was conducted by varying molding operational parameters in consultation with TPI/RTRC. This includes examining curing and cooling time, aerodynamic efficiency, integrating market demand and engineering sub-models, DMD scale-up, and modeling the required stock and production flow of molds/modules given capacity projections.

7.11.1. Curing and cooling time

In collaboration with TPI, we identified the main variable in blade manufacturing to be curing time, Figure 7.11.1. An aluminum DED modular mold should be able to provide significant scheduling and scale up benefits due to the reduction in curing and cooling time. Per our colleagues at TPI, the thermal conductivity of the fiberglass laminate makes higher watt density dangerous since higher local heating (rate limited to 0.5 C/min) surrounding the resistance wire can be damaging to the current fiberglass tooling. However, metal-based tooling is able to have higher cure temperatures without any adverse effects due to a different heating mode (forced air). According to TPI, for every 10°C increase in dwell temperature (the temperature at which the resin cures, currently 80°C), the cure time is cut in half from its current value of ~3.5 to 4 hours. We can save time due to active cooling as well; blades cannot be “de-molded” until the hottest part of the blade falls below 50°C (to ensure structural integrity of the blade), so active cooling will result in shorter time to complete blade manufacturing. Blade assembly and cooling takes around 3 to 4 hours to complete. From previous conversations with TPI, the cooling takes about an hour to cool from 80°C to 50°C. At this stage, we are assuming that a 10°C reduction in cooling temperature could reduce cooling times by 50% (same as curing time reduction), which would lead to a decrease of 0.5 hours in cooling times.

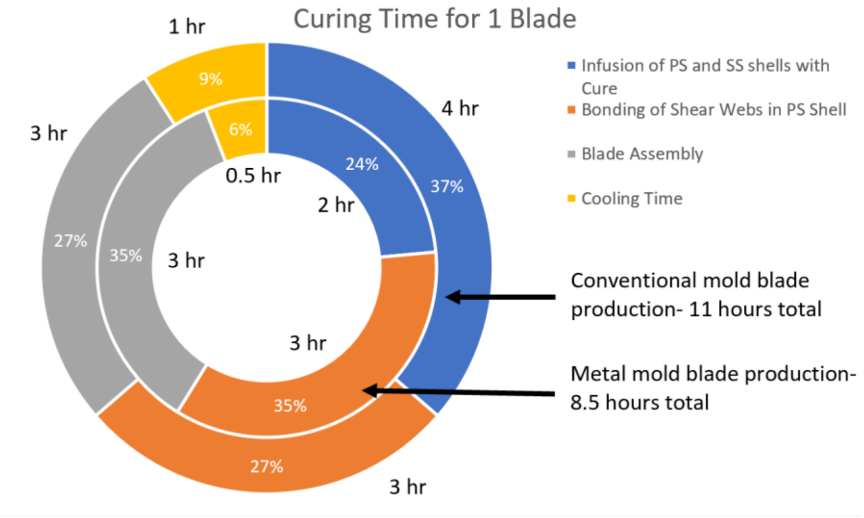

Figure 7.11.1 Curing and cooling time for production of a single blade [PS= Pressure Side, SS= Suction Side]

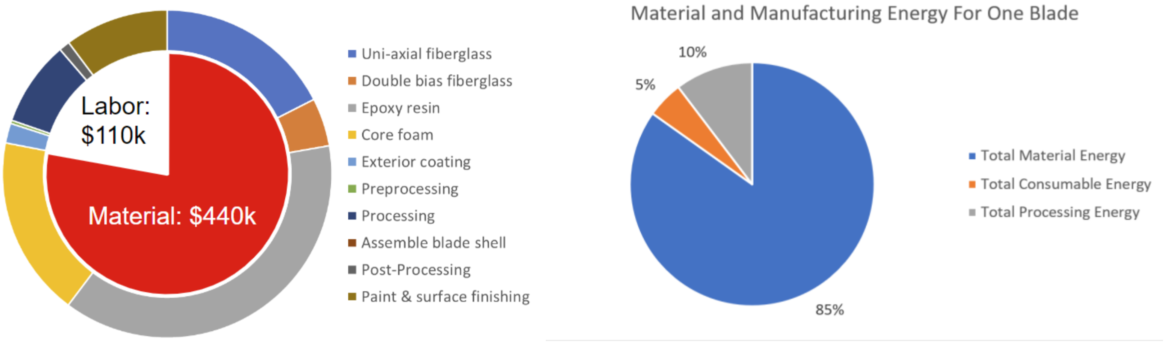

Figure 7.11.2 Overall cost and primary energy for production of a single blade

A reduction in curing time will lead to a reduction in time and cost, but this comes with a currently unknown change in power/energy. It is likely to be an overall modest benefit in total production cost and energy/power per blade as processing cost and energy are not large portions of overall blade production cost and energy as shown in Figure 7.11.2. However, as stated above, this could have significant potential scheduling and scale-up benefits as production flow is increased. Given the significant challenge of scaling up renewable generator manufacturing, this is arguably more important than modest changes in per blade production costs.

7.11.2. Aerodynamic efficiency trade-off

Modular design of the mold means there must be a compromise between the commonality between blades of different sizes and the retention in aerodynamic efficiency of the turbine blades of different profiles. Our aim is to investigate how the profitability and net energy yield (NEY) are sensitive to changes in blade production cost/energy intensity and turbine efficiency due to changes in mold types, manufacturing technologies, logistics, etc. Net energy yield (NEY) is the energy generated by a wind turbine blade during its lifespan minus the energy that was required to make and install the blade. In this analysis, the baseline for turbine aerodynamic efficiency is benchmarked to an index of value 1 for a 100 m conventionally manufactured blade (according to SNL100-00 model, this corresponds to a 13.2 MW max power per turbine of 3 blades, of which according to Sandia National Laboratories, the average capacity factor will be about 40% for land-based turbines over its lifespan). The baseline profit and Net Energy Yield (NEY) per blade (per ⅓ turbine profit/NEY assuming a typical three-blade rotor) are obtained based on our model for conventionally manufactured turbine blade and calculated for the lifetime of the turbine (assumed as 20 years according to Alsaleh and Sattler, 2019).

Any design changes (in blade, mold, production and transportation involved in production) are assumed to only influence the production cost and the production energy intensity without changing the lifecycle revenue and energy generation. Therefore, only the production cost and the production energy intensity are modeled as variables. Figure 7.11.3 shows the dependence of profitability on production cost and aerodynamic efficiency. The range where the modular mold design should target at is marked in the green triangle. The targeted region is built on an anticipated aerodynamic efficiency loss. With a limited aerodynamic efficiency loss and a decrease in blade production cost within the marked region, we can achieve a profitability which is the same as or above the baseline profit. However, the allowance for turbine aerodynamic efficiency loss is limited. It is anticipated that every 16% decrease in production cost can allow 1% decrease in turbine efficiency to retain the same profit. The revenue is calculated based on the electricity price where the electricity was produced (Vermont, 17 cents per kWh, June 2023).

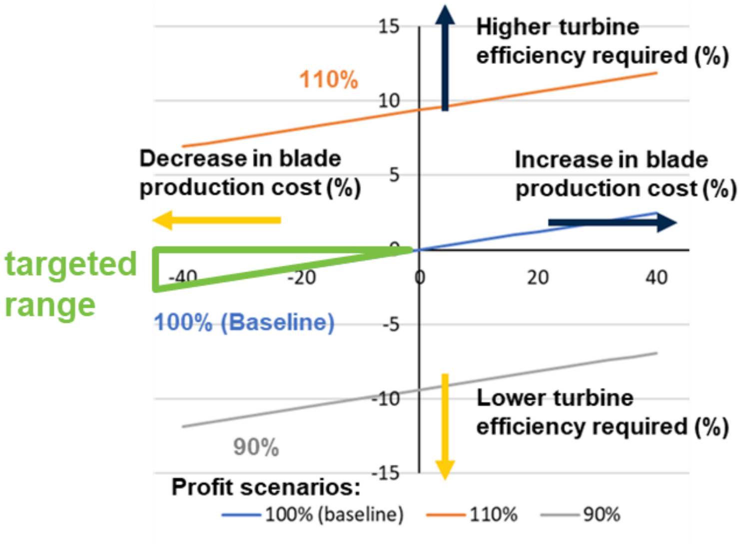

Figure 7.11.3 Sensitivity of Profitability to Blade Production Cost and Turbine Aerodynamic Efficiency

In the above model, production cost includes plug, mold and blade production and transportation during production. The lifecycle costs include the production cost, the operation and maintenance cost but not the decommissioning cost.

The NEY per blade can be subjected to changes in blade production energy intensity as well as aerodynamic efficiency, and its sensitivity to the blade production energy intensity and aerodynamic efficiency is presented in Figure 7.12.4. It is found that changes in the blade production energy intensity have little impact on the NEY. Every 28% decrease in blade production energy intensity will only spare 0.05% decrease in efficiency to retain the same NEY. On the other hand, change in NEY is almost equivalent to the change in the aerodynamic efficiency of the turbine, i.e., a 10% decrease in aerodynamic efficiency will result in a 10% decrease in NEY. To conclude, life cycle costing analysis suggests aerodynamic efficiency loss must be <<5% for costing and because lifecycle profitability is highly dependent on aerodynamic efficiency of the turbine, and a reasonable profitability (>95% baseline) requires the aerodynamic efficiency loss to be kept within the limited allowance. Life cycle energy analysis suggests aerodynamic efficiency loss must be < 1% because NEY is highly sensitive to changes in aerodynamic efficiency. However, reduced blade production cost and lead time is likely needed for rapid deployment.

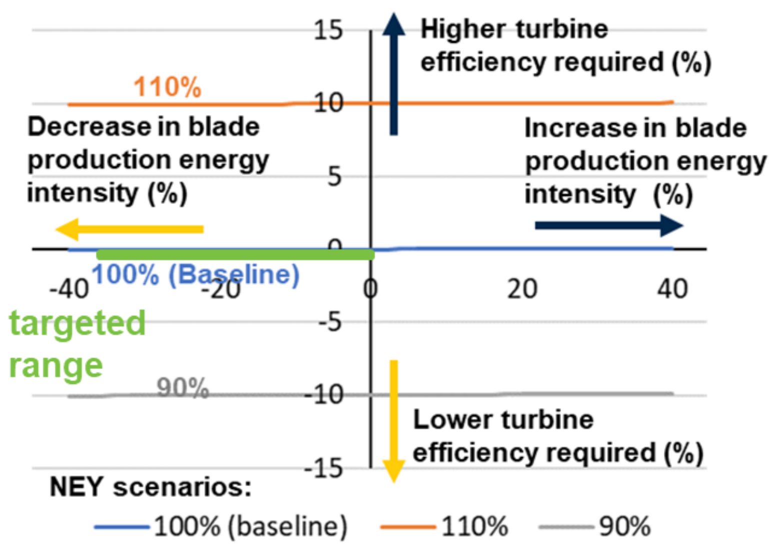

Figure 7.11.4 Sensitivity of Net Energy Yield (NEY) to Blade Production Energy Intensity and Turbine Aerodynamic Efficiency

In the above model, the production energy intensity includes plug, mold and blade production and transportation during production. The NEY includes the production energy intensity (negative) and lifecycle electricity generation (positive) but not decommissioning energy intensity.

7.11.3. Integrating market demand and engineering sub-Models

Figure 7.11.5 shows the overall integration of our estimated cost, energy, and time impacts models. We can use these models to estimate the savings across the U.S. wind sector using the outlook (projected capacity) of the sector.

The annual blade demand model, Figure 7.11.6, takes the projected generation capacity required per year and uses that along with the estimated average blade length and average specific power to estimate the number of turbines (and therefore number of blades) needed to satisfy the projected demand. We then take the historical data of the blade geometry distribution and apply it to the number of blades required per year to estimate the number of blades for each blade length/geometry.

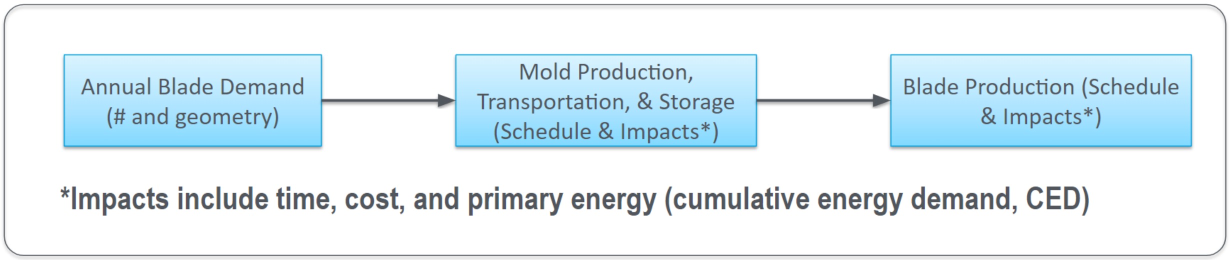

Figure 7.11.5 Overview of model integration

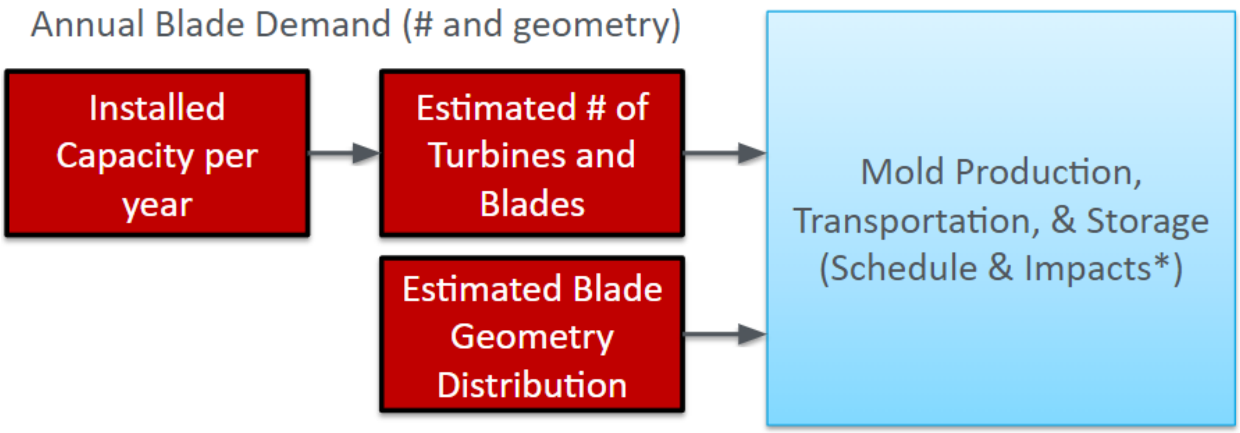

Figure 7.11.6 Structure of annual blade demand model

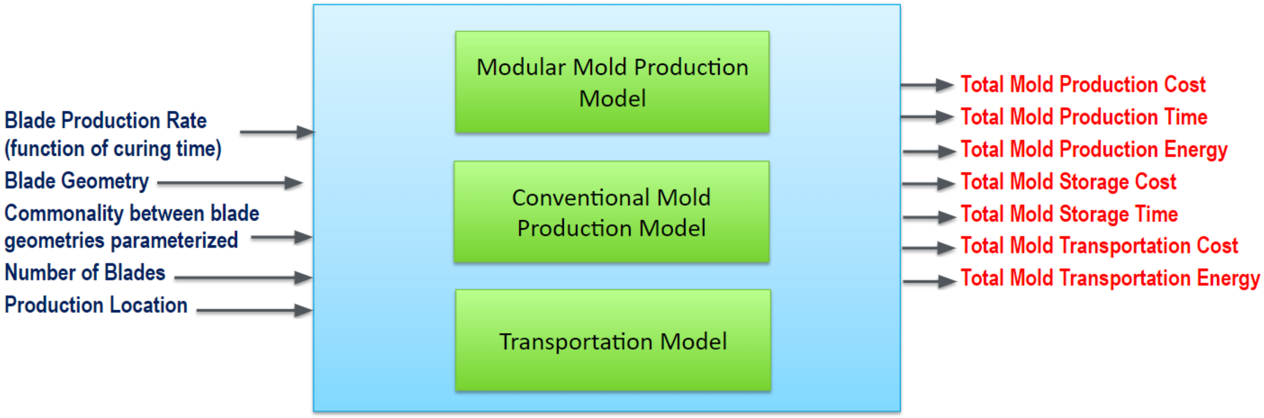

Figure 7.11.7 Structure of mold production, transportation, & storage model

The mold production, transportation, & storage model, Figure 7.11.7, has inputs of number of blades and blade geometry from the annual blade demand model, as well as additional inputs of blade production rate, the commonality between different blade geometries, and the production location. The impacts of time, cost, and primary energy are marked in red on the right (will be marked in red for following figures as well).

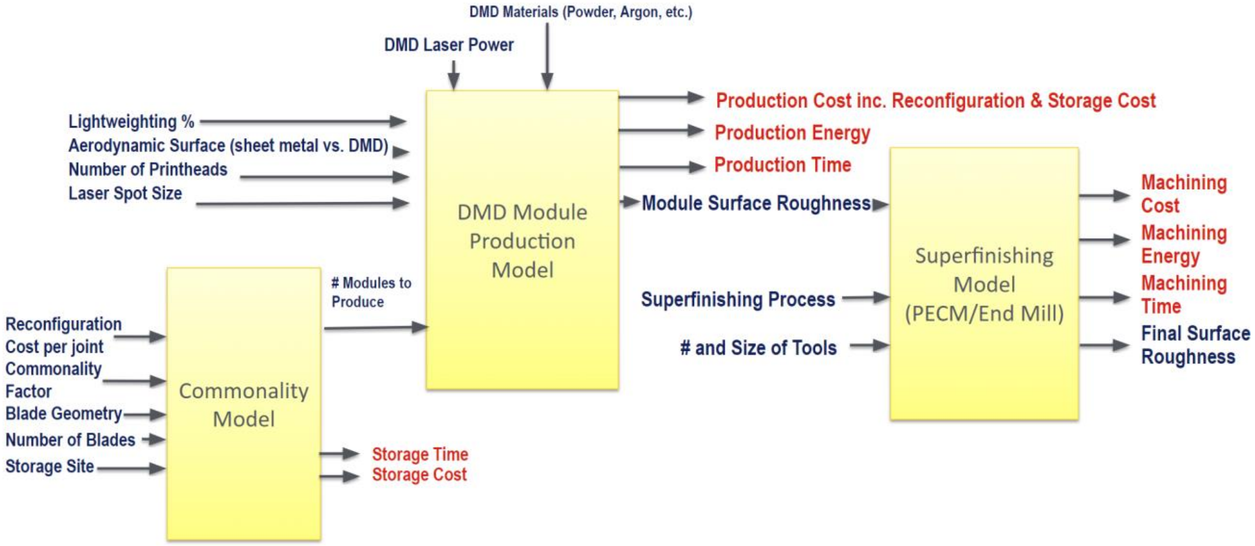

Figure 7.11.8 Structure of modular mold production model

The modular mold production model is shown in Figure 7.11.8. The commonality model takes in inputs of reconfiguration cost, blade geometry and number of blades from the annual blade demand model, and a parameterized commonality factor. This model then outputs the flow of modules to be produced to the DMD module production model, as well as the storage time and cost (calculated from the size and number of stored modules). The DMD module production model also takes in inputs such as the lightweighting percentage desired, the aerodynamic surface material (currently set as DMD), the number of printheads, and the laser spot size. It uses the inputs as well as parameters such as the laser power and the materials consumed during the DMD process to determine the production cost, time, and primary energy, as well as the surface roughness of the aerodynamic surface, which is an input to the superfinishing model. The number and size of tools used to superfinish the aerodynamic surface of the module is an input to the superfinishing model as well, with the outputs being the impacts of superfinishing (cost, time, and primary energy) as well as the final surface roughness of the aerodynamic surface.

The structure of the superfinishing model can be seen in Figure 7.11.9. The top model shows the PECM superfinishing model, which is modeling the process being developed by our colleagues at PSU. The main inputs being considered are current density, voltage, cathode type (moving, fixed), cathode size, overlap factore, and energy density per unit area. The model outputs are the impacts of PECM and the final surface roughness as stated above.

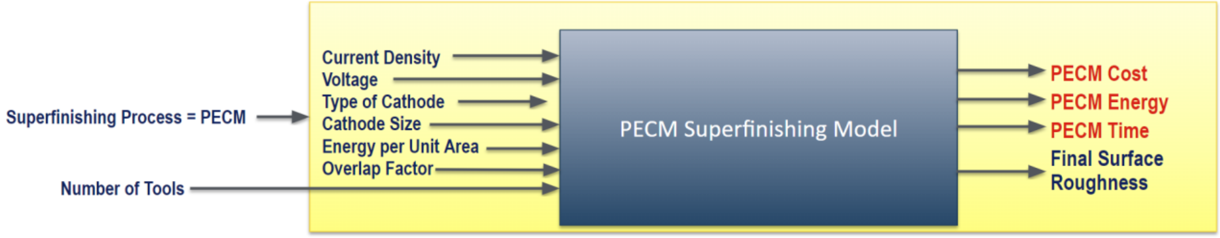

Figure 7.11.9 Structure of PECM superfinishing model

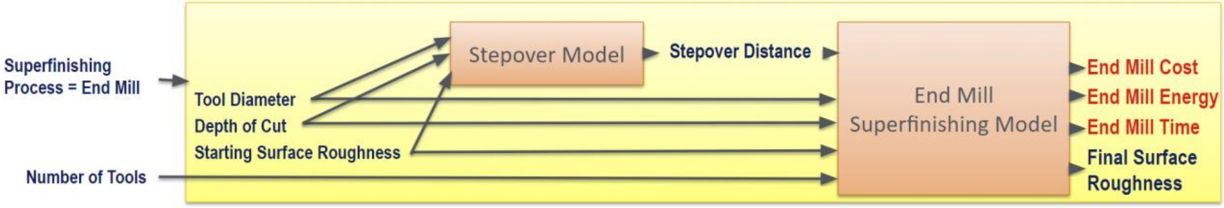

Figure 7.11.10 Structure of end mill superfinishing model

The end mill superfinishing model, Figure 7.13.10, was created to compare the PECM process to a more traditional ball end milling process to investigate the benefits of PECM. The inputs to the end mill model are the number of tools, tool diameter, depth of cut, and the starting surface roughness of the surface being machined. The tool diameter, depth of cut, and the starting surface roughness inputs are inputted into both the stepover model which calculates the required stepover to achieve the final surface roughness desired and the end mill superfinishing model which calculates the impacts of the end milling as well as the final surface roughness. This end mill model can also be used to estimate the impacts of the current process of machining scallops into the aerodynamic surface of the module before the PECM process.

7.11.4. DMD scale-up

As stated in the previously, the UM team has been closely working with DM3D to consider aluminum DMD scale-up to 1:1 production. Some strategies that could be used to decrease printing time are to increase the spot size of the laser to increase the powder deposition rate and increase the number of printheads (the number of printheads decreases printing time in a linear fashion). Some downsides to increasing the spot size of the laser is reducing the resolution of the print, although this is likely not a significant issue for 1:1 production, and increasing the power of the laser, although a higher-powered laser is a small percentage of the overall machine cost according to DM3D. A downside to increasing the number of printheads is the significant engineering cost; the printheads are essentially all different machines working in the same system and must be integrated at the machine design phase and cannot be added in at a later date.

The UM team has been consulting with Dr. Rajiv Malhotra, an associate professor at Rutgers University who is working on a Wire-Arc Additive Manufacturing (WAAM) system with a modified gantry. After consultation with both Dr. Malhotra and DM3D, the UM team has compiled a list of system components required for a full scale, totally enclosed powder-blown DMD machine for wind turbine blade mold module production.

- Aluminum Bed
- Robot Arm
- Powder Delivery System
- Gantry system/Motion system
- Sealing enclosure with powder suction

The modules are being built out of 6061 aluminum powder. DM3D will use a 6061-base plate (bed) or 5xxx series with the base plate being machined between builds. There are considerations that must be considered when printing, such as cooling off the build plate during operation of the DMD system to prevent warpage and leveling off the build plate. For such a large system, a 1° incline in the build plate could be about a foot difference in height, which is a large error and could be increased by having multiple pieces making up one bed. The robot arm would contain both the output of the powder delivery system and most likely a CNC router, due to the current need for scallops for the PECM process. The powder would have to be stored and heated elsewhere and pumped up to the nozzle on the robot arm. The gantry system would have to be a moving axes system, as a moving build plate of that size would have too many disturbances (vibrations) during the printing process. A cost analysis of this system is currently underway, with initial findings shown below. Figure 7.11.11 below shows the cost of tabletop CNC machines with a moving axis gantry system plotted against the area covered by the gantry system. We can use this data as a baseline to refine a cost estimate for this system.

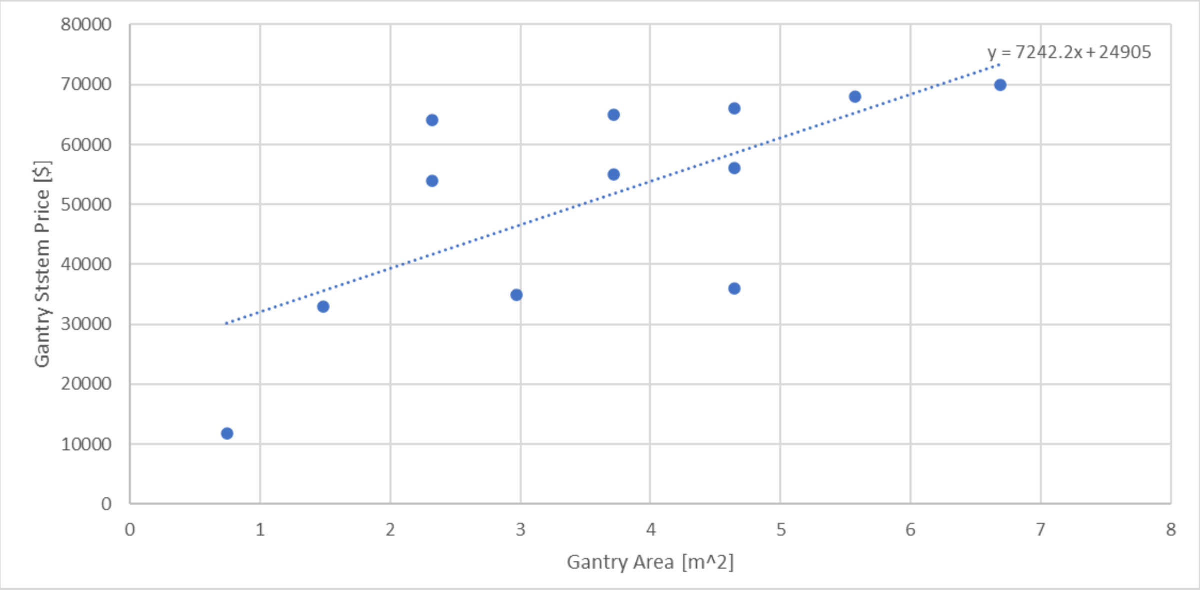

Figure 7.11.11 Gantry system cost vs. area for tabletop CNC machines

7.11.5. Modeling required stock and production flow of molds/modules given capacity projections

Figure 7.11.12 is the current model to determine the stock of molds required and the flow of molds produced given the generation capacity required per year, average blade length, and average turbine power/specific power. We take the power per blade (turbine power divided by 3) and use the capacity projection for a given scenario to determine the stock of blades required. We can then divide by the blade production rate, stated to be 250 blades/mold/year according to TPI, to determine the annual stock of molds required. This annual stock of molds is production rate determined; it only indicates the number of molds needed to produce the annual stock of blades required. We then take the year-to-year change in stock, the mold reuse factor (a number from 0-1 indicating how likely the mold is to be stored), and the commonality factor (a number from 0-1 indicating how common modules are across different molds) to determine the annual number of molds/modules produced. We can then apply historical data to determine the distribution of different blade geometries that will be produced.

$$Wind\ Swept\ Area\ \left[m^2\right] = \pi * \left(\frac{Rotor\ Diameter}{2}\right)^2$$

$$Turbine\ Power(nameplate\ capacity) = Specific\ Power\ \left[\frac{W}{m^2}\right] * Wind\ Swept\ Area\ \left[m^2\right]$$

$$Power\ per\ blade = \frac{Turbine\ Power}{3}$$

$$Annual\ Stock\ of\ Blades\ Required = \frac{Total\ Power\ in\ 1\ year}{Power\ per\ blade}$$

$$Annual\ Stock\ of\ Molds\ Required = \frac{Number\ of\ blades\ required\ per\ year\ [\frac{blades}{year}]}{Blade\ production\ rate\ [\frac{\frac{blades}{year}}{mold}]}$$

$$\Delta Stock = Annual\ Stock\ of\ Molds\ Required(t) - Annual\ Stock\ of\ Molds\ Required(t-1)$$

$$Annual\ Flow\ of\ Molds\ Produced(t) = [\Delta Stock(t) + Annual\ Stock\ of\ Molds\ Produced(t-1) * (1 - Mold\ Reuse\ Factor - Commonality\ Factor)]$$

$$Annual\ Flow\ of\ Modules\ Produced(t) = [\Delta Stock(t) + Annual\ Stock\ of\ Molds\ Produced(t-1) * (1 - Mold\ Reuse\ Factor - Commonality\ Factor)] * \frac{\#\ of\ Modules}{Mold}$$

$$Commonality\ Factor = \frac{Max\ Flow\ of\ modules\ produced - Flow\ of\ modules\ produced}{Max\ Flow\ of\ modules\ produced - Min\ Flow\ of\ modules\ produced}$$

Figure 7.11.12 Equations for stock and flow of molds/modules

7.12. Techno-economic challenges for scaling up mold fabrication

While working to refine our cost and energy models for the modular and conventional molds, we discovered an issue where the cost model had been using a shell thickness and the energy model had been using a mass multiplied by a weight reduction factor. Ee rectified this issue by equating the mold shell thickness and weight reduction factor, which can be seen in Figure 7.12.1. For example, the equivalent mold shell thickness for the conventional composite mold is 0.016 meters (16 mm), as the weight for a composite mold is ~52,000 kg. This figure allows us to see the scaling for the mold shell thickness (and weight reduction factor) for both the modular aluminum DMD mold cost and energy.

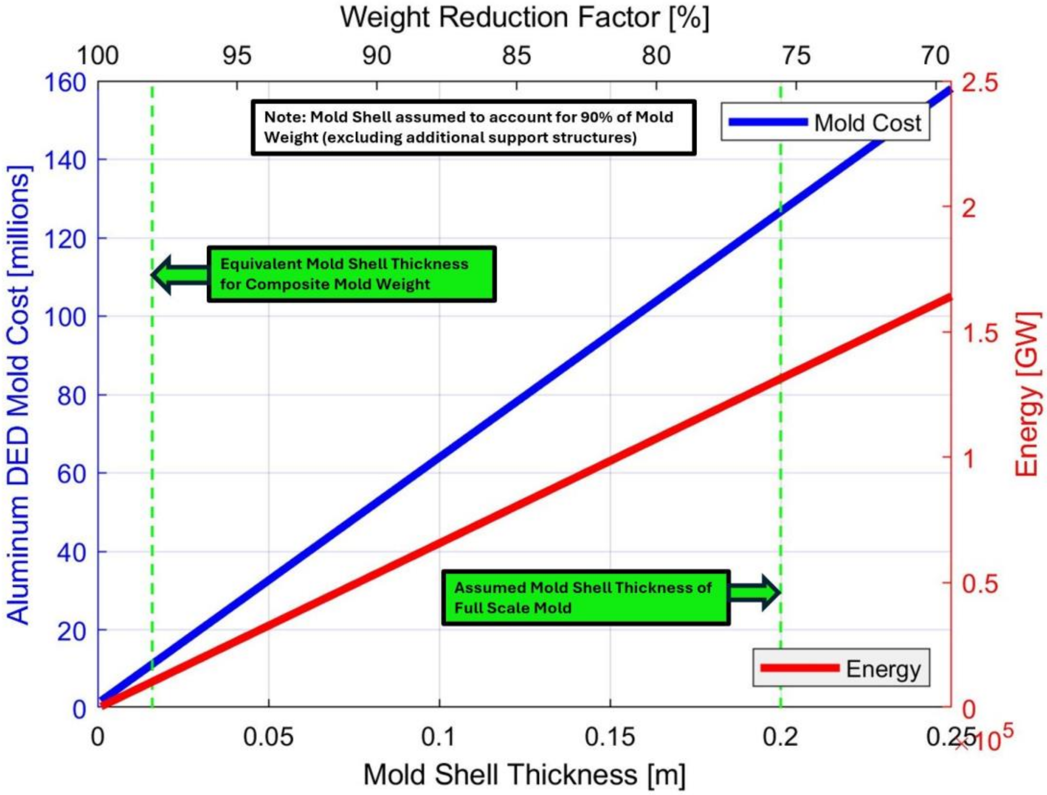

Figure 7.12.1 Equating Mold Shell Thickness and Weight Reduction Factor

In order to calculate the annual demand for wind turbine blade molds, we use the annual capacity projections to determine the annual demand for wind turbines and blades. The cumulative generation capacity for wind power as projected by NREL is about 779-1342 GW by 2035 to reach a 100% clean electricity system, with industry estimates projecting a much lower cumulative generation capacity of 223 GW by 2030. Therefore, the annual stock for wind turbines can be calculated using Equation (7.12.1),

$$Stock_{turbines}(t) = \frac{P_{total}\ (t)}{P_{turbine,avg}(t)} \qquad (7.12.1)$$

where $Stock_{turbines}(t)$ is an estimate of the number of turbines required to be installed in a given year t, $P_{total}\ (t)$ is the projected capacity in a year t in kW, and $P_{turbine,avg}$ is the average nameplate capacity of a wind turbine (the theoretical maximum amount of power the wind turbine produces) in kW. The annual stock of blades required for these turbines is three times the stock of turbines required, which can be seen below in Equation (7.12.2).

$$Stock_{blades}(t) = 3 \times Stock_{turbines}(t) \qquad (7.12.2)$$

The stock of blades in a year t can be used to calculate the flow of blades produced in the same year t, as shown in Equation (7.12.3),

$$Flow_{blades}(t)\ \approx\ Stock_{blades}(t) - Stock_{blades}(t-1) + Stock_{blades,EOL}\ (t) \qquad (7.12.3)$$

where $Flow_{blades}(t)$ is an estimate of the number of blades required to be produced in a given year t, $Stock_{blades}(t)$ is an estimate of the number of blades required to be installed in a given year t, $Stock_{blades}(t-1)$ is an estimate of the number of blades required to be installed the year prior to year t, and $Stock_{blades,EOL}(t)$ is an estimate of the number of blades that have reached their manufacturing warranty, which is assumed to be 30 years.

The annual flow of blades produced in a year *t* is then divided by the blade production rate to determine the annual stock of molds, shown in Equation (7.12.4) below,

$$Stock_{molds}(t) = \frac{Flow_{blades}(t)}{Blade\ Production\ Rate\ per\ Mold\ (t)} \qquad (7.12.4)$$

where $Stock_{molds}(t)$ is an estimate of the number of blades required to be installed in a given year t, and the *Blade Production Rate per Mold (t)* is the number of blades that can be produced on one mold per year, assumed to be 250 blades/mold/year. The annual stock of molds is production rate limited, meaning it is independent of any year-to-year reuse of molds or commonality between molds. It represents the minimum number of molds that must be produced to fulfill the stock of blades that will be required in a given year. More molds are likely to be produced as many molds will not be in production for an entire year.

Equation (7.12.5) below shows the calculation of the annual flow of molds produced,

$$Flow_{molds}(t) = Stock_{molds}(t) - Stock_{molds}(t-1) * RF \tag{7.12.5}$$

here $Flow_{molds}(t)$ is an estimate of the number of molds required to be produced in a given year t and *RF* is the mold reuse factor, a parameter from 0 to 1 that determines how often a mold is reused on an annual basis. Modular molds will have a higher *RF* than conventional molds as they are designed to be reused. *RF* is related to the commonality factor discussed in previous meetings and reports, but is presented as a parameter in this discussion due to the complexity of reuse between families of blades and year-to-year reuse.

Equations (7.12.6) and (7.12.7) show the calculation of a production split between conventional and modular molds for annual flow of molds produced,

$$Flow_{molds,con}(t) = p \times Flow_{molds}(t) \tag{7.12.6}$$

$$Flow_{molds,mod}(t) = (1-p) \times Flow_{molds}(t) \tag{7.12.7}$$

where $Flow_{molds,con}(t)$ is an estimate of the number of conventional molds required to be produced in a given year t, $Flow_{molds,mod}(t)$ is an estimate of the number of modular molds required to be produced in a given year t, and *p* is the percentage production split between modular and conventional production.

Equation (7.12.8) shows the calculation of the number of modules produced,

$$Flow_{Modules} = \frac{L_{mold}}{L_{module}} \times Flow_{molds,mod}(t) \tag{7.12.8}$$

where $Flow_{modules}(t)$ is an estimate of the number of modules required to be produced in a given year t, L_{mold} is the length of the mold, and L_{module} is the length of the module.

The following analysis was produced using:

1. A fixed blade length of 100 meters,
2. The historical data for average wind turbine nameplate capacity from 1997-2023 with a linear increase past 2023 (up to 2035) determined by the average increase in capacity from 1997-2023,
3. Industry consultant land-based wind power capacity projection by 2030 of 223 GW, which is an 87 GW increase in current capacity, with a linear increase till 2035 to equate to other projections,
4. NREL 100% clean electricity by 2035 lower bound projection of 779 GW by 2035, with a linear increase in capacity from 2024-2035,
5. NREL 100% clean electricity by 2035 upper bound projection of 1342 GW by 2035, with a linear increase in capacity from 2024-2035,
6. Internal data gathered on mold and module cost, production time, production CED, etc. adapted from a 100 meter mold (modular and conventional).

Figure 7.12.2 shows the cumulative U.S. wind energy capacity from 1997-2023, with the industry and two NREL projections for the 2024-2035 period. Figure 7.12.3 shows the model estimate and the reported data from the US Wind Turbine Database for turbines predicted by Equation (7.12.1) to demonstrate the high correlation between the model and reported data. This confirms Equation (7.12.1) should accurately predict the projected number of turbines required past 2023. Figure 7.12.4 shows an estimate of the number of turbines from 1997 to 2035 using Equation (7.12.1). A dynamic material flow analysis (DMFA) was conducted to quantify the end of life for wind turbines. This lifespan is modeled as a normal distribution with an average and maximum turbine lifespan of 20 and 30 years, respectively. Applying this DMFA to the capacity projections past 2023 will quantify the flow of blades to be produced according to Equation (7.12.3). The stock of molds can then be calculated using the flow of blades and the blade production rate of 250 blades/mold/year using Equation (7.12.4), as shown in Figure 7.12.5. The flow of molds produced, the production cost of those molds, and the production time of the molds are shown in Figures 7.12.6-7/12.8, where the production split between modular and conventional production is set to be 0.5.

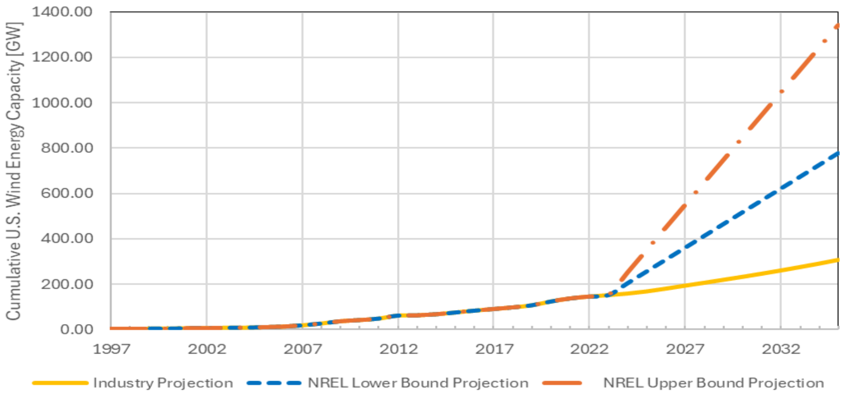

Figure 7.12.2 Cumulative U.S. wind energy capacity from 1997-2035 (projected past 2023)

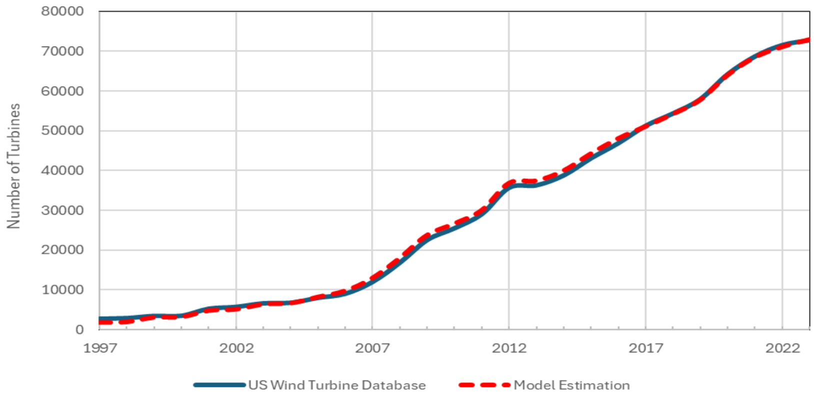

Figure 7.12.3 Cumulative stock of turbines 1997-2023 w/data from U.S. wind turbine database

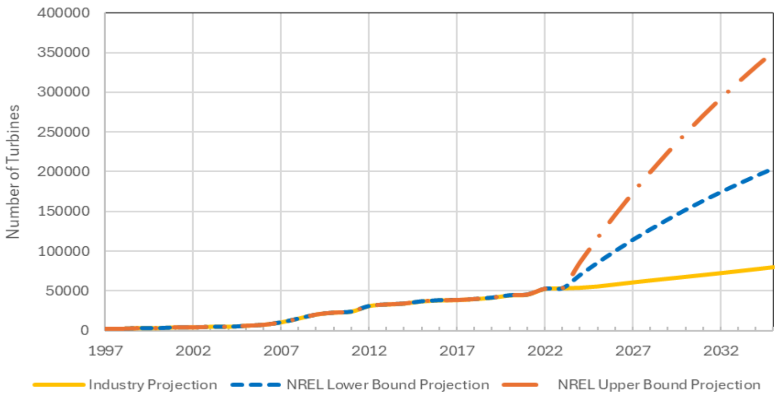

Figure 7.12.4 Cumulative stock of turbines 1997-2035 using U.S. wind energy capacity and turbine capacity

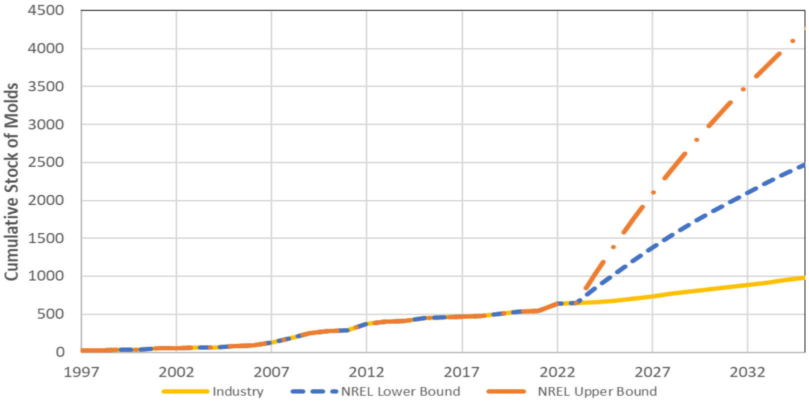

Figure 7.12.5 Cumulative stock of molds required 1997-2035

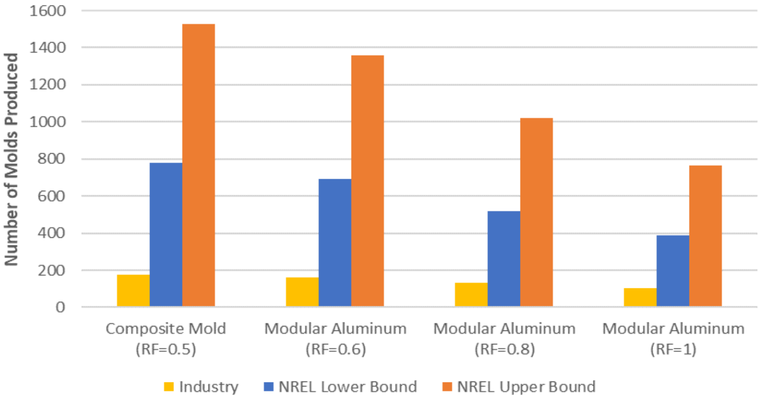

Figure 7.12.6 Total flow of molds produced 2024-2035

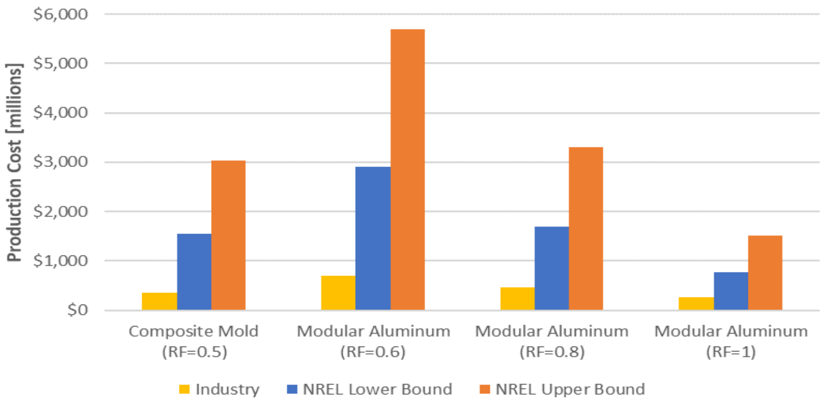

Figure 7.12.7 Total production cost 2024-2035 in Millions

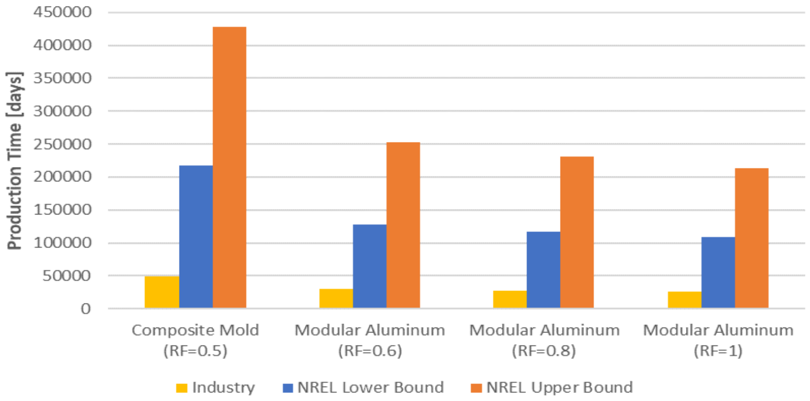

Figure 7.12.8 Total mold production time 2024-2035 assuming 5 DMD machines/plugs in parallel

7.13. Summary of market benefits and process commercialization study

Figure 7.13.1 shows the scope of our market benefits and process commercialization study. The middle of the diagram shows three of the models constructed: cost, energy, & time models for blade production using conventional and modular molds, superfinishing models for the modular mold, and system level models exploring the impact modular molds can have on the US Wind Sector. The design variables are the methods we choose for manufacturing and finishing the molds (like conventional or DMD mold manufacturing and mechanical versus electrochemical surface finishing methods), as well as the blade geometry (which determines the blade span and surface area) and mold geometry (including the mold thickness and segment length if we are talking about modular molds). The parameters incorporated are derived from expert elicitations with TPI for the manufacturing of conventional molds and blades, literature, published models like BAAM mold cost model from ORNL, and DMD experiments here at the University of Michigan. The results are all based on a blade span of 100 meters, but the model itself is able to take any blade span as input to obtain results.

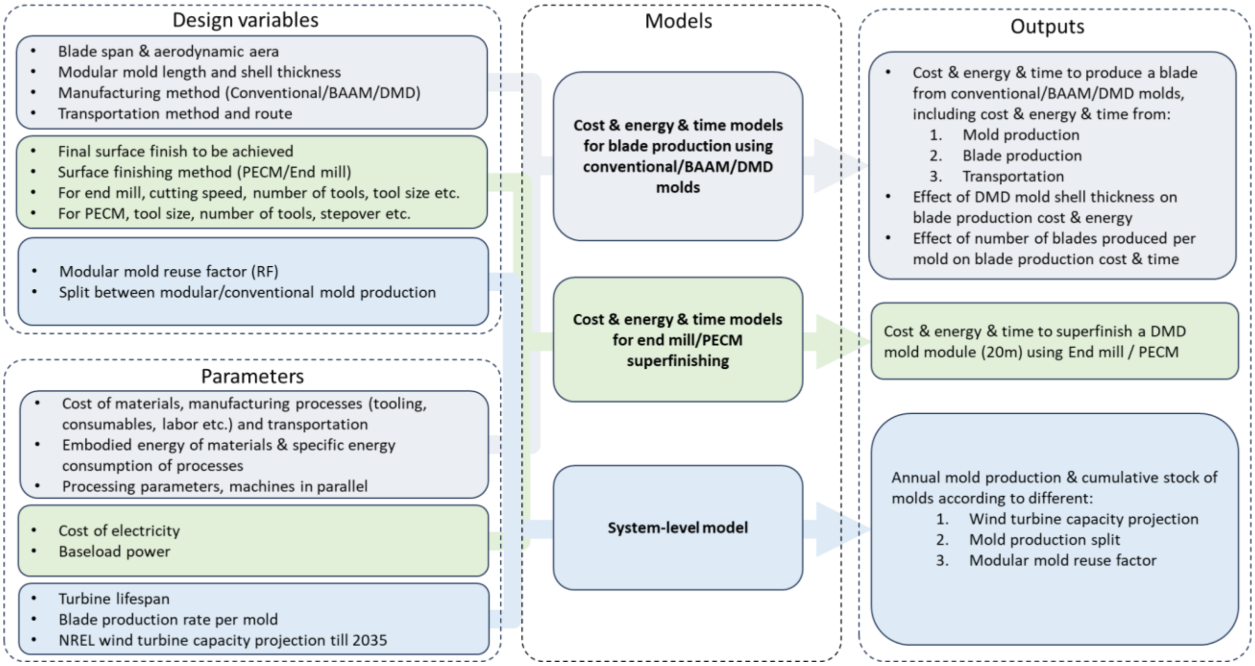

Figure 7.13.2 Diagram of framework for scope of study for market benefits and process commercialization study

8. References

1. *A6061-RAM2 Brochure*. (2021, April 16). https://www.elementum3d.com/a6061-ram2-brochure/
2. Abel Passos Dos Santos, J. (2018). *COST ESTIMATION MODEL FOR THE DIRECTED ENERGY DEPOSITION PROCESS ADOPTING AN ACTIVITY-BASED APPROACH*.
3. Bortolotti, P., Berry, D., Murray, R., Gaertner, E., Jenne, D., Damiani, R., Barter, G., & Dykes, K. (2019). *A Detailed Wind Turbine Blade Cost Model*. www.nrel.gov/publications.
4. *Cost Study for Large Wind Turbine Blades: WindPACT Blade System Design Studies*. (2003). http://www.doe.gov/bridge
5. Fischer, M. (2017, April 17). *How Additive Manufacturing Enables Fast Modification of Molds*. https://www.fabricatingandmetalworking.com/2017/04/additive-manufacturing-enables-fast-modification-molds/
6. Griffith, D. T. (2013). *Large Rotors: 100-meter Blade Research @ Sandia*. www.sandia.gov/wind
7. Johanns, W., & Todd Griffith, D. (n.d.). *SANDIA REPORT User Manual for Sandia Blade Manufacturing Cost Tool: Version 1.0*. http://www.ntis.gov/help/ordermethods.asp?loc=7-4-0#online
8. Love, L. J. (2015). *Oak Ridge National Laboratory Cincinnati Big Area Additive Manufacturing (BAAM) CRADA Final Report*. http://www.osti.gov/scitech/
9. Masood, S. (2022, July 20). *Direct Metal Deposition Facility*. https://www.swinburne.edu.au/research/strengths-achievements/specialist-facilities/direct-metal-deposition-facility/
10. *Oversize.io*. (2022). https://oversize.io
11. *Quick Guide to Metal AM*. (n.d.). Retrieved July 19, 2022, from https://optomec.com/wp-content/uploads/2019/06/Metal-AM-Selection-Guide.pdf
12. W.R. Morrow, H. Qi, I. Kim, J. Mazumder, S.J. Skerlos,Environmental aspects of laser-based and conventional tool and die manufacturing,Journal of Cleaner Production,Volume 15, Issue 10,2007,Pages 932-943,ISSN 0959-6526, https://doi.org/10.1016/j.jclepro.2005.11.030.
13. Ehmsen, S., Yi, L., Aurich, J.C. (2021). Evaluating the Cumulative Energy Demand of Additive Manufacturing Using Direct Energy Deposition. In: Behrens, BA., Brosius, A., Hintze, W., Ihlenfeldt, S., Wulfsberg, J.P. (eds) Production at the leading edge of technology. WGP 2020. Lecture Notes in Production Engineering. Springer, Berlin, Heidelberg. https://doi.org/10.1007/978-3-662-62138-7_36
14. Bourhis, F.L., Kerbrat, O., Hascoet, JY. et al. Sustainable manufacturing: evaluation and modeling of environmental impacts in additive manufacturing. Int J Adv Manuf Technol 69, 1927–1939 (2013). https://doi.org/10.1007/s00170-013-5151-2

9. Publications

The team has papers in progress to be finalized and submitted to journals. Once accepted and published, they will be uploaded on the OSTI website.